Langmuir-Blodgett Monolayer Studies of Mixed Gemini Surfactant-Phospholipid Monolayers System for Gene Therapy Applications

by

Taksim Ahmed

A thesis
presented to the University of Waterloo
in fulfillment of the
thesis requirement for the degree of
Master of Science
in
Pharmacy

Waterloo, Ontario, Canada, 2015

© Taksim Ahmed 2015

Author's Declaration

This thesis consists of material all of which I authored or co-authored: see Statement of Contributions included in the thesis. This is a true copy of the thesis, including any required final revisions, as accepted by my examiners.

I understand that my thesis may be made electronically available to the public.

Statement of Contributions

Taksim Ahmed: performed literature review related to the 'Interactions between DNA and Gemini surfactant: impact on gene therapy' (chapter I of the thesis); designed and performed all experiments using Brewster's Angle Microscopy (BAM) and Polarization Modulated Infrared Reflectance Absorption Spectroscopy (PM-IRRAS), analysed data (both chapter IV and V) and wrote the thesis/manuscript.

Amany O. Kamel: contributed substantially to the writing and revising of the thesis/manuscript.

Robert Henderson: performed all the Atomic force microscopy (AFM) and Kelvin Probe Force Microscopy (KPFM) experiments, and analysed data.

Jason Chau: performed experiments related to the characterization of the Gemini Surfactant-DNA system using the BAM (chapter IV of thesis), and contributed to the writing of the manuscript.

George Mekhail: performed experiments related to the model membrane using BAM and PM-IRRAS (chapter V of thesis) and contributed to the writing of the manuscript.

Shawn D. Wettig: supervised the project and finalized the thesis/manuscript; and is the corresponding author.

Abstract

Gene delivery relies upon the encapsulation of a gene of interest, which is then ideally delivered to target cells. For gene therapy applications, viral vectors are the most efficient vectors currently being studied, accounting for more than 67% of ongoing clinical trials, however, they have several potential disadvantages, chief among them being safety concerns. In contrary, non-viral vectors have advantages over viral vectors. In the first chapter we have reviewed non-viral gene therapy using gemini surfactants which is an unique approach to medicine that can be adapted towards the treatment of various diseases. The chemical structure of the surfactant (variations in the alkyl tail length and spacer/head group) and the resulting physicochemical properties of the lipoplexes are critical parameters for efficient gene transfection. Moreover, studying the interaction of the surfactant with DNA can help in designing an efficient vector and understanding how transfection complexes overcome various cellular barriers. This chapter provides an overview of the various types of gemini surfactants designed for gene therapy and their transfection efficiency, with a focus on the novel methods (Langmuir Blodgett monolayer studies, AFM, DSC, ITC, SAXS) used to understand their interaction with DNA.

The lack of understanding of how DNA influences the arrangement of vector components during the complexation of DNA, as well as their interaction with biological membranes is still a major barrier faced by non-viral vectors. Hence the aim of work in this project is to characterize the arrangement of the gemini surfactants and phospholipids that make up the transfection vector (both in the presence and absence of DNA) as well as the effect of these components on model biological membranes using Brewster's Angle Microscopy (BAM), Atomic force microscopy (AFM), Kelvin probe force microscopy (KPFM) and Polarization Modulated Infrared Reflectance Absorption Spectroscopy (PM-IRRAS).

Our current project focuses on gemini surfactants 16-7-16 and 16-7NH-16 or mixed gemini surfactant and helper lipid (DOPE) interaction at the air-water interface in the presence or absence of DNA. According to the surface pressure- area (π-A) isotherm, the 16-7NH-16 based systems formed the most stable monolayer in all pHs (pH 4, 7 and 9) compared to 16-7-16 based systems. The observed monolayer remained mostly in the liquid expanded (LE) or liquid expanded-liquid condensed (LE-LC) phase as evident from the compressibility modulus values. DOPE causes condensation in the mixed gemini/DOPE/DNA system in which antagonistic mixing behavior of DOPE is observed. Moreover, the BAM images showed fibril structures of the 16-7NH-16/DOPE/DNA system at pH 4, which was further confirmed by the AFM and KPFM studies. This

signifies the electrostatic interactions between the positively charged gemini quaternary amine head group with the negatively charged phosphate group of DNA molecules. The PM-IRRAS study revealed that the complex system (gemini/DOPE/DNA) undergoes several interactions, among them the electrostatic, ion-dipole and hydrophobic interaction is the major factor playing the role in the interactions.

In chapter V we have shown the interaction of the gemini/DOPE/DNA system on the model endosomal membrane (DPPC/cholesterol=75/25%). While mixing the DPPC and cholesterol, it forms a homogeneous film with the solid phase observed at the natural cell membrane surface pressure range (30-35 mN/m) at pH 4. The mixed 16-7-16 and 16-7NH-16 based system fluidized the model membrane at pH 4. The fluidization effect was strongly pH dependent for the 16-7NH-16 based system. This system undergoes protonation, and forms strong complex with the DOPE/DNA with a net positive charge, consequently adsorbing and penetrating into the model membrane. PM-IRRAS study revealed that the 16-7NH-16 based system was better than 16-7-16 in terms of enhanced membrane fluidization. This study suggests the idea that the gemini/DOPE/DNA based system may interact with the endosomal membrane, disrupt the membrane and release the DNA into the cytoplasm at low pH.

Acknowledgements

I take this opportunity to express my heartiest gratitude to my respected supervisor Dr. Shawn David Wettig for giving me the opportunity to pursue Master's degree under his mentorship. His guidance, support and encouragement throughout the project are invaluable. I was always fascinated by his in-depth knowledge, expertise, and passion for research! I have benefited enormously from his vast knowledge and experience. The enormous intellectual freedom that I have enjoyed in his laboratory during this course period will be long cherished. He granted constant encouragement, sound advice and many good ideas. All this broadens my thinking and thrust for research. Apart from science, Dr. Wettig has provided me huge mental support during all the stressful periods of my life. I am grateful to him for his patience during my graduation period.

My special thanks to advisory committee member, Dr. Jamie Joseph and Dr. Praveen Nekkar Rao for their guidance and helpful decision and evaluation of my thesis.

Apart from that, I would like to thank Dr. Amany O. Kamel for her direct and cordial supervision, encouragement and motivation for the best achievement and valuable editing in writing the thesis.

I would like to acknowledge Robert Henderson for conducting the AFM and KPFM experiments.

Special thanks to George Mekhail for his valuable time to help me in conducting the model membrane experiments in BAM and PM-IRRAS, and writing the manuscript. I really enjoyed his friendship and found him extremely generous, helpful and supportive all through my research period.

I am grateful to Jason Chau for his help in conducting the experiments related to characterization of the system in BAM and editing the thesis.

I have enjoyed great friendship from Osama Madkhali, warm thanks to him for everything he has done for me. He will remain in my heart all through my life!

I would like to specially thank Muhammad Shahidul Islam for his support in the lab and in my personal life. My special thanks to Samantha Shortall, who was extremely helpful and extended her helping hand whenever needed. Along with this, I would like to thank Aula al Muslim and Shannon Callender for their support and friendship. Additionally, I would like to thank Rony Eshaque, who has conducted some model membrane experiments.

Moreover, I have enjoyed the friendship of a large number of people in University Waterloo. I am grateful to all of them for their support and co-operation.

My special gratitude to my Uncle Mohammad Abdul Aziz, Ph.D., currently dean of science faculty, University of Dhaka. His tributes to my life for my research as well as motivation for enriching knowledge through study will be cherished.

I would like to thank Almighty ‘ALLAH’ for his blessings on me to carry on with my endeavors.

Thanks to my sweet parents who has always been supported me spiritually and prayed for my success. Their sacrifice and mental support strengthen my research motif, which is embedded to my heart.

Last but not the least, my heartiest thanks to my wife Sazeda Akter, for her understanding, mental support, love and pray for my success.

Dedication

To my parents …Abdul Kadir Miah and Anjumanara
&
Beloved Wife ….Sazeda Akter

Table of Contents

List of Figures

List of Tables

List of Abbreviation

Langmuir-Blodgett	LB
Gemini surfactant	GS
Reticuloendothelial system	RES
Critical micelle concentration	CMC
Dodecyltrimethylammonium bromide	DTAB
1,2-Dioleyl-sn-glycero-phosphatidyl-ethanolamine	DOPE
1,9-Bis(dodecyl)-1,1,9,9-tetramethyl-5-imino-1,9-nonanediammonium dibromide surfactant	12-7NH-12
(bis(guanidinium)-tris(2-aminoethyl)amine-cholesterol	BGTC
1,2-Dimyristoyl-sn-glycero-3-phosphocholine	DMPC
1,2-Dipalmitoyl-sn-glycero-3-phospho-(1′-rac-glycerol) (sodium salt)	DPPG
Brewster angle microscopy	BAM
Atomic force microscopy	AFM
Differential scanning calorimetry	DSC
Isothermal titration calorimetry	ITC
Small-angle x-ray scattering	SAXS
Transmission electron microscopy	TEM
Fourier transform infrared resonance	FTIR
Phosphatidylcholine	PC
Phosphatidylethanolamine	PE
Bimolecular lipid membranes	BLM
Supported Lipid Bilayers	SLB
Polarization modulation Infrared reflection absorption spectroscopy	PM-IRRAS
1,2-Dipalmitoyl-sn-glycero-3-phosphocholine	DPPC
1-Palmitoyl-2-oleoylphosphatidylcholine	POPC

Publications from this thesis

Article Type: **Review**

Status: **Accepted (August, 2015)**

1. *Taksim Ahmed, Amany O. Kamel and Shawn D. Wettig,* **Interactions between DNA and Gemini surfactant: impact on gene therapy. Part I.**

Journal: Nanomedicine (London), Impact Factor: 5.413 (2014); and 5.955 (5 year).

2. *Taksim Ahmed, Amany O. Kamel and Shawn D. Wettig,* **Interactions between DNA and Gemini surfactant: impact on gene therapy. Part II.**

Journal: Nanomedicine (London), Impact Factor: 5.413 (2014); and 5.955 (5 year).

Article type: **Conference Poster**

Conference details: *Taksim Ahmed, Jason Chau, Robert Henderson, Shawn D. Wettig*, **Characterization of the Novel Gene Transfection Formulations Consist of Gemini Surfactant-DNA Using Langmuir-Blodgett Monolayer Technique: Redefining the Role Helper Lipid**, The first Annual Meeting of the Biophysical Society of Canada, University of Waterloo, Waterloo, ON, Canada. June 17-19, 2015.

Plans to publish thesis data:

Article type: Research article

1. Taksim Ahmed, Jayson Chou, Robert Henderson, Amany O. Kamel and Shawn D. Wettig, **Characterization of Gemini surfactant and DNA monolayers at the air/water interface using Langmuir-Blodgett monolayer technique.** Research article to be submitted in '***Proceedings of the National Academy of Sciences of United Sates of America (PNAS)***'. (Chapter IV of the thesis).

2. Taksim Ahmed, George Mekhail, Amany O. Kamel and Shawn D. Wettig, **Interactions of Gemini surfactant-phospholipid based gene therapy formulation with the model cell membrane: understanding the endosomal release of lipoplexs.** Research article to be submitted in ***'Langmuir'***. (Chapter V of the thesis).

Chapter I

Interactions between DNA and Gemini surfactant: impact on gene therapy.

1.1. Introduction

1.1.1. Gene therapy

Gene therapy is a promising strategy for the treatment of various inherited and acquired diseases. Frederick Griffith discovered the bacterial transformation of a non-virulent R form of Type I pneumococcus into a heat inactivated virulent S form of type II pneumococcus in 1928 [1]. This discovery paved the way for the journey of modern gene therapy. The ultimate goal of gene therapy is to obtain a desired therapeutic effect in the treatment of a given disease, by delivery of a gene or genes in order to enable cells to generate therapeutic proteins [2, 3]. In general, gene therapy utilizes nucleic acids or oligonucleotides, which can be combined with a specific delivery vehicle (vector) to exert the desired therapeutic effect. The therapeutic effect(s) could be either 1) insertion of a normal or functional gene into the host cells to repair genetic disorders by replacing or correcting the defective gene; or 2) repression of an over expressing gene [4]. Gene therapy is a broad research arena and a detailed review is beyond the scope of this thesis; however the readers are referred to the recent review article on the history of gene therapy by Wirth et *al.* [5]; as well as a review on the different techniques and strategies for a successful non-viral gene therapy by Ibraheem et *al.* [6].

1.1.2. Classification of gene therapy

Gene therapy can be categorized into two broad classes: viral vector mediated and non-viral vector mediated gene therapy. To date viral vectors are considered to be the most efficient delivery vector in gene therapy. As of 2015, there are approximately 2142 gene therapy clinical trials either completed or under way in 36 countries in which most (approximately 67%) of the delivery systems utilize different viral vectors [7]. The breakdown of gene therapy clinical trials according to the delivery system used is depicted in Figure 1.1 [7]. Viruses have evolved themselves to efficiently gain access to host cells, and facilitate their replication by using the host cellular machineries. These features make the viral vectors superior and widely used vectors in gene delivery over its counterpart non-viral vectors. For gene delivery application, the viral vectors are designed in such a way that the vector utilizes the viral infection pathway but circumvent the expression of viral genes that lead to replication and toxicity. This is achieved by deleting or suppressing specific coding regions from the viral genome; and leaving intact those sequences necessary for functions such as packaging the vector genome into the virus capsid or the integration of vector DNA into the host chromatin [8].

Regardless of their high delivery efficiency, viral vectors suffer from several potential drawbacks such as toxicity, immunogenicity, limitations to the size of the therapeutic gene, production and packing problems, as well as high cost of production. Additionally, clinical trial failures led to the death of one patient in a clinical trial for the treatment of a rare metabolic disorder (ornithine transcarbamylase deficiency) in 1999, and the observation of a leukemia-like disease resulting from a genetic therapy in an early clinical trial for the treatment of severe combined immunodeficiency disorder (X-SCID) in 2002 [9, 10]. Therefore, the debate regarding the use of viral vectors in gene therapy applications has reached new levels, and delayed research in the field for several years [11].

Felgner and colleagues demonstrated the successful delivery of a gene using a non-viral cationic lipid-based vector, in 1987 [12]. Non-viral vector mediated gene therapy approaches are generally considered: safe (non-toxic and non-immunogenic with proper selection of vector components); cost-effective; and relative to viral vectors, they are easy to manufacture. The main disadvantage of non-viral vectors is their low transfection efficiency *in vivo* [13]. To overcome this challenge, substantial research has been carried out in the design of novel non-viral vector systems. A lack of consistency in how transfection efficiencies are reported significantly hampers the ability to compare not only vector systems, but also results obtained for different cell lines. In an attempt to address the transfection efficiency accurately, in this review we are reporting transfection efficiencies exactly as they were reported in the original research articles we cite. We have, where appropriate, tried to link results from different types of measurements in a qualitative fashion, and include the actual numeric values for transfection efficiency when these have been reported.

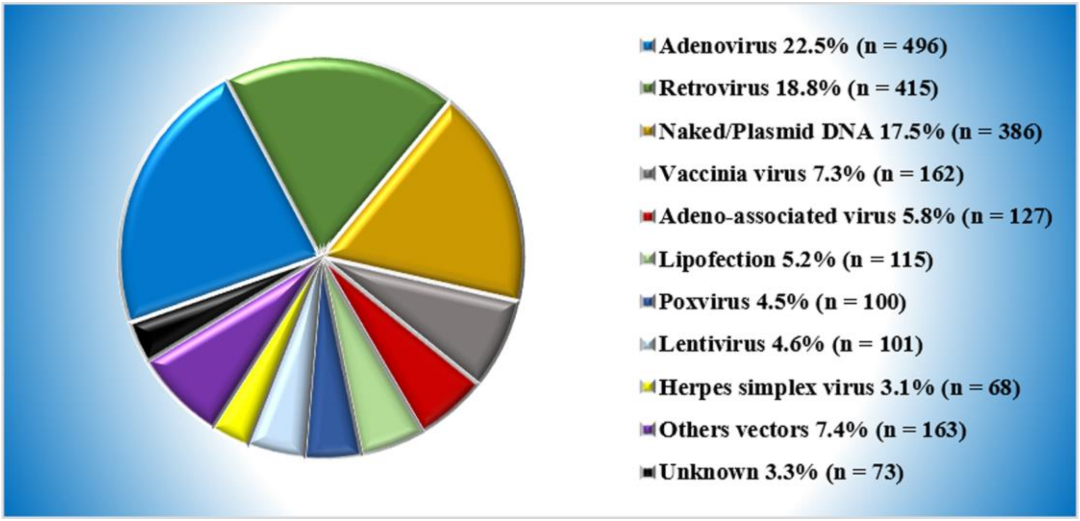

Figure 1.1. Vectors used in the current gene therapy clinical trials; adapted from reference [7].

1.1.3. Challenges in the design of an efficient non-viral gene therapy system

Transfection is the process by which the plasmids (DNA) are delivered to targeted cells. To achieve a successful gene therapy, expression of the delivered gene in the target cell is required. To do so, DNA has to travel across various extracellular, cellular, and intracellular barriers (Figure 1.2) [14]; several review articles have been published on this topic and are provided as references [15-22]. Briefly, the extracellular barriers include skin, blood cells, plasma components, the reticulo-endothelial system, and the immune system. The cell membrane itself is the main cellular barrier, and for the case of non-viral vectors it gets across primarily by endocytosis. Subsequently, the next major barrier is endosomal escape, which must occur before the endosome matures into the acidic lysosome, whose hostile environment would degrade the plasmid prior to nuclear uptake and expression. The trafficking within the cytosol, nuclear localization, and passage across the nuclear membrane are considered to be the additional intracellular barriers [15-22]. Figure 1.2 illustrates the various barriers to transfection. Over the past two decades the non-viral vector mediated clinical trials are minimal, for instance, only ~6 % of the ongoing clinical trials are based on the lipofection [7]. This is an indication that the knowledge from *in vitro* studies are not effectively translated into the *in vivo* models.

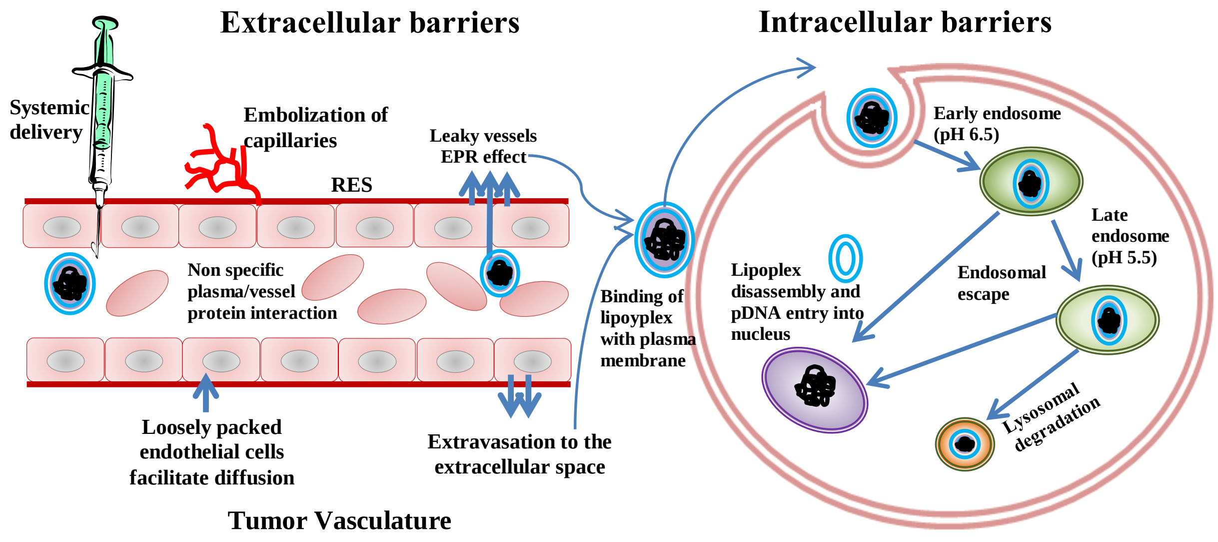

Figure 1.2. Summary of the extra- and intracellular barriers faced by non-viral gene therapies following systematic delivery. Adapted from the reference [14]. The lipoplex/polyplex is considered to be remained at the early endosome around 2-5 min (pH 6.5), late endosome around 10-15 min (pH 5-6) and in lysosome around 30-35 min (pH 4-5) [23].

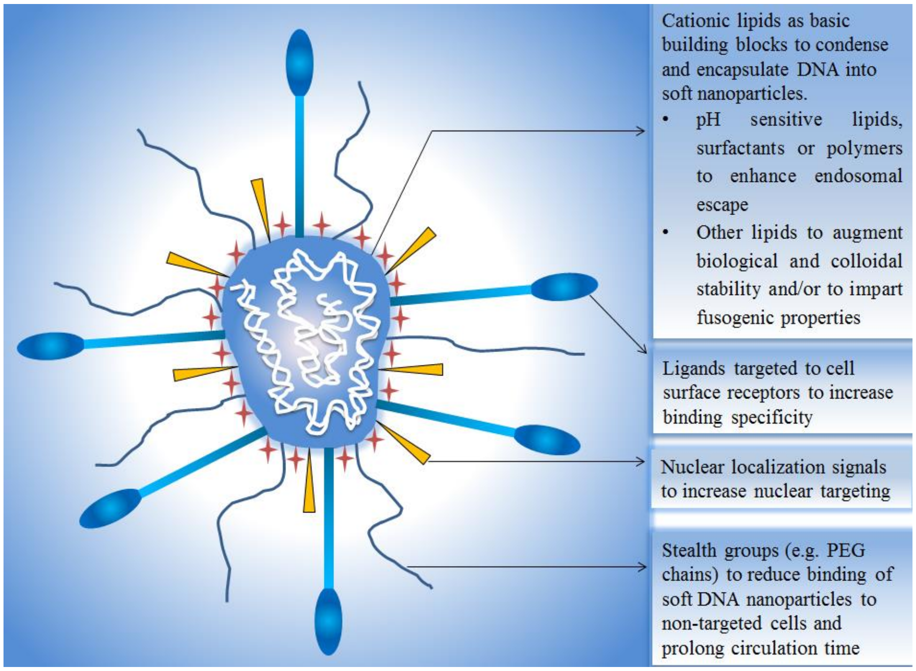

Cationic lipids as basic building blocks to condense and encapsulate DNA into soft nanoparticles.

- pH sensitive lipids, surfactants or polymers to enhance endosomal escape
- Other lipids to augment biological and colloidal stability and/or to impart fusogenic properties

Ligands targeted to cell surface receptors to increase binding specificity

Nuclear localization signals to increase nuclear targeting

Stealth groups (e.g. PEG chains) to reduce binding of soft DNA nanoparticles to non-targeted cells and prolong circulation time

Figure 1.3. Building blocks of multifunctional non-viral DNA delivery systems. Different types of cationic lipids can be used to create a lipid-based nanoparticulate system (soft nanoparticle) e.g. liposomes, lipoplexes and solid lipid particles. Introduction of pH-sensitive lipids, surfactants or polymers can facilitate the endosomal escape. Grafting of polyethylene glycol (PEG) lipids provides the inert, nonionic, hydrophilic and flexible polymer coating around the nanoparticles which facilitates the biological and colloidal stability of the nanoparticles. Cell specific binding of the nanoparticles can be achieved by incorporating specific ligands having the selective binding to the cell surface receptors. A nuclear localization signal moiety (ligand) can be anchored to the surface of the nanoparticle which will remain intact during the endosomal uptake as well as release, and enhance the nuclear localization of specific DNA. Adapted from reference [24].

Thus, an emerging question arises; specifically “How does one tailor an efficient delivery vector which can bypass the extracellular barriers, be readily absorbed via endocytosis followed by fast endosomal escape, facilitate trafficking through the intracellular matrix to the nucleus, facilitate nuclear import, finally resulting in expression of the desired protein encoded by the DNA?” To achieve this, researchers have developed an enormous variety of non-viral DNA vectors consisting of cationic lipids, surfactants, or polymers, where the cationic component serves to efficiently bind and compact the DNA plasmid, and the vector as a whole is able to deliver the gene of interest to a target cell population, where it can then be expressed producing the therapeutic protein of interest. Figure 1.3 demonstrates ideal building blocks of a non-viral gene delivery system with various functional properties that are important to enhance the overall efficiency of the system [24].

1.2. Cationic lipids and surfactants as non-viral gene delivery agents

Cationic lipid/DNA complexes (also known as lipoplexes) are extensively used systems in gene therapy and effectively absorbs to the predominantly anionic plasma membrane of mammalian cells via electrostatic interactions. In general, lipoplexes (and polyplexes for cationic polymer based vectors) possesses higher transfection efficiency in numerous cell lines when compared with other non-viral delivery systems, including niosomes (non-ionic surfactant vesicles) or anionic liposomes (due to the absence of positive charges) [25, 26]. Despite this fact, lack of knowledge about the interactions between the complexes and cellular components is a major challenge to overcome the poor transfection efficiency of lipoplex vectors, relative to viral vectors. To facilitate the development of improved lipoplex vectors, understanding the complex interactions that occur between the vector, the plasmid, and the cellular environment in which a lipoplex may be found, is crucial. Such studies will allow for the development of new systems that are specifically designed to overcome the various barriers to transfection, introduced above.

Several important physical and physicochemical parameter(s) to be considered while designing a lipoplex for gene delivery have been reviewed by Donkuru et *al.* [24]. Briefly, to facilitate the endocytosis a particle size of the lipoplexes of less than 200 nm is considered to be ideal. The charge ratio of lipoplex (+/-) and the zeta potential is another crucial parameter for gene transfection. For a complete charge neutralization of the negatively charged phosphate group of DNA, a minimum cationic lipid/surfactant to DNA of 1:1 is necessary. On the other hand, an overall positive zeta potential value is required for the strong electrostatic interaction of lipoplexes with the negatively charged cell membrane. The most commonly used charge ratios are 2:1, 5:1, and 10:1; nevertheless, there still does not appear to be any correlations between charge ratio and transfection efficiency that would apply across all cationic systems. Instead, the optimal charge ratio, while always greater than 1:1, is very dependent on the chemical structure of the cationic component in the vector system [27]. Additionally, variations in the charge ratio of lipoplexes can influence the various shapes non-viral systems assemble into [27], for example, rods, globules, spheres and toroids, filamentous or fibrous structures and netlike structures. Typically nanoparticles with smaller particle sizes (<500 nm) form spherical structures [24, 27, 28]. While there is no direct correlation between the lipoplex morphology and the transfection efficiency, the internal packing arrangement (i.e lamellar, hexagonal, cubic, etc.) of lipids/surfactants within the lipoplex is reported to have significant impact in gene transfection [29]. It is believed that the inverted hexagonal structure is preferable over the lamellar structure for efficient transfection [30-32], however, there are numerous exceptions to this conclusion reported in the literature [33-38].

1.2.1. Gemini surfactants as transfection vectors

Since Felgner's work in 1987 [12], tremendous effort has been made to design more efficient cationic lipid based vectors. Mintzer and Simanek in 2009 published a comprehensive review on this broad subject area to which readers are referred for an overview [39]. The focus of our current review is on a small subset of cationic lipid based vectors, those in which the cationic lipid has been replaced by a cationic "gemini" surfactant. In 1991, Menger [40, 41] was the first to use the term "Gemini surfactant" for the description of a family of amphiphilic (surfactant) molecules, consisting of two head groups (positively charged) and two aliphatic chains covalently linked by a flexible or rigid spacer group (Figure 1.4) [42, 43]. Since then the term gemini has been used to describe nearly every possible combination of multiple tail-multiple head group surfactant (including now gemini *lipids* having 4 tails and 2 head groups), even those which are non-symmetrical in nature; the reader is referred to the excellent text by Zana and Xia for a more complete discussion of the field of gemini surfactant research [44]. The unique structural features of the gemini surfactant results in a number of potential advantages in numerous industrial applications. For gene therapy applications, the structure results in lower critical micelle concentrations (CMCs) relative to the related monomer surfactant (for example, dodecyltrimethylammonium bromide (DTAB) is considered to be the monomer for the 12-s-12 series of gemini surfactants and has a cmc of approximately 12 mM compared to approximately 1 mM for the 12-3-12 surfactant), structural flexibility resulting in an ability to form various aggregate structures/morphologies, improved condensation of DNA, ease of manufacture, low production cost, and low toxicity [40-43]. Specific aspects of the gemini surfactant structure, relevant to gene therapy, are described in more detail, below. Additionally, the gemini surfactants used in this current project will be described in the section 1.6.4e.

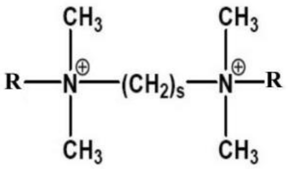

Figure 1.4. Chemical structure of the most commonly studied gemini surfactant, the N,N'-bis (dimethylalkyl)-alkane-diammonium-dibromide series, or "*m*-*s*-*m*", Two traditional monomeric surfactants with R= $C_{\mathbf{m}}H_{2m+1}$ alkyl tails are connected at their quarternary ammonium heads via a polymethylene chain containing "**s**"methylene units. Here, *m*= the number of carbon atoms in the alkyl tails, *s*= the number of atoms making up the spacer group. [42, 43]. For instance, a 12-s-12 series of gemini surfactants depicts that the surfactant has fixed 12 carbon length of alkyl chains, and a variable number of carbon spacer linked with the quaternary ammonium heads.

1.2.2. Variation in gemini surfactant structure

A large number of gemini surfactants with widely varied chemical structures have been shown to be efficient transfection vectors both *in vitro* and *in vivo*. In an earlier review article we have focused on describing the bulk of research having been carried out regarding the use of gemini surfactants as transfection vectors [42]. Thus, the remainder of this review will focus on specific structural features that may be important in modifying the interaction(s) between the surfactants and DNA, and therefore could be used to improve the transfection efficiency of the gemini surfactants.

1.2.3. Variations in tail length

Gemini surfactants possess different physicochemical properties brought about through variations in the tail lengths, which subsequently impact gene transfection. Detailed information can be found in recent review articles [42, 45, 46]. Badea et *al.* have synthesized gemini surfactants (spacer length n = 2–16; alkyl chain m = 12 or 16) (Figure 1.5A) to deliver the pGTmCMV.IFN-GFP plasmid (coding for the interferon γ (IFN) protein in murine keratinocytes (PAM 212) *in vitro* at various charge ratios of plasmid to gemini surfactant = 1:5, 1:10, 1:20, and 1:40. Additionally, the topical delivery of the same plasmid using liposomal and nanoemulsion systems (based on gemini surfactant 16-3-16) was investigated *in vivo* [47]. Their observation revealed that vectors with gemini surfactants (at a charge ratio, N^+/P^- of plasmid:gemini = 10:1 and a surfactant concentration of 1.5 mM) possessing long alkyl tails (16-3-16) are more efficient with respect to IFNγ expression (1.63 ng/5×10^4 cells) than those having short hydrocarbon tail (12-3-12, 1.1 ng/5×10^4 cells) *in vitro.* In further studies, Foldvari et *al.* have demonstrated the physicochemical (particle size, zeta potential) and structural features (effect of head group and tail lengths) of the 12-s-12 and 16-3-16 gemini surfactants necessary for cutaneous gene therapy [33]. It was found that the 12-s-12 series did not exhibit any transfection efficiency without the presence of the helper lipid dioleoylphosphatidyl-ethanolamine (DOPE). In the case of the 12-s-12 surfactants, increasing the spacer length substantially reduced the IFNγ expression level (from around 1200 pg/5x10^4 cells to around 500 pg/5x10^4] even though the particle size and the zeta potentials were similar. In a direct comparison of 12-3-12 and 16-3-16 (chemical structure in Figure 1.5A), both surfactants showed similar zeta potential value with a smaller particle size for 12-3-12 (140 nm) than 16-3-16 (210 nm) in a mixture of DNA-gemini-DOPE. The Small Angle X-ray Scattering (SAXS) studies revealed the presence of a complicated morphology of cubic packing arrangement with respect to the arrangement of surfactant and DOPE monomers, with both lamellar, and what was subsequently identified as (potentially) a cubic packing arrangement [33]. It was hypothesized that this ability to adopt multiple packing arrangements was responsible for the increase in transfection efficiencies observed by Badea et *al.* [47].

We have recently evaluated the delivery of pVGtelRL plasmid consisting of the green fluorescent protein (GFP) gene into human ovarian carcinoma cells (OVCAR-3) with a series of phytanyl substituted (Phy-3-m; m = 12, 16 and 18, Figure 1.5 B) and symmetric m-3-m (m = 12, 16 and 18) type gemini surfactants [48]. The transfection results revealed that the phy-3-m compounds showed higher GFP expression (~10-15%) as compared to the 16-3-16 gemini surfactant (~5%) at a N^+/P^- charge ratio of 10:1. This was attributed to the higher degree of micellization of phy-m-3 and the formation of higher order structures (i.e. inverse hexagonal and/or cubic) upon complexation with DNA [48]. Higher degree of micellization was observed due to the increased tail-tail interactions between the hydrocarbon chains of the surfactant molecules (because of increased hydrophobicity). Noteworthy, a higher degree of micellization (α) signifies that the head group repulsion might play a crucial role in determining the structure of micelle aggregate during the self-assembly process [48, 49]. A higher value of α, corresponds to greater dissociation of the counterions from the surface of the micelle, and indicates weaker ability of binding of the counterions to the micelles [50]. A cationic gemini surfactant with a higher α would be a better candidate to condense proteins or other polyelectrolytes, such as DNA, as anionic molecules may more easily be able to replace the counter ions at the surface of the micelle to form compact complexes of much smaller size [48]. Furthermore, phytanyl based gemini surfactants (phy-3-m, m = 12,16,18) along with DOPE (at molar ratio of DOPE:gemini = 1:1.5) were used to deliver the pVGtelRL vector (at charge ratio of DNA to gemini= 1:2, 1:5, 1:10) in OVCAR-3 cells [34]. The EGFP expression (~15 %) was higher for long tails (m=16 or 18) as compared to the short tail (m = 12) gemini series (~9 %). Phytanyl substituted compounds showed higher transfection efficiency (~ 9-15 % EGFP expression) than the symmetric 16-3-16 (~5%) which was correlated with our previous findings [48]. These results were further confirmed by a SAXS study which revealed the presence of multiple phase [34]. It should be noted that the OVCAR-3 cells are difficult to transfect, for instance the commercial positive control, Lipofectamine 2000 also exhibited only ~10-15% of cells expressing GFP [48].

In another study, Donkuru et *al.* utilized the m-3-m, m-7-m, and m-7NH-m (m = 12, 16, and 18) gemini surfactants to deliver a plasmid containing the luciferase gene (at N^+/P^- charge ratio of 10:1) in PAM 212 and COS-7 (African Green monkey kidney fibroblast) cells [35]. It was found that the transfection efficiency increased with an increase in alkyl tail length (m = 12 < m =16 < m =18). This was attributed to the increased hydrophobicity caused by the increase in the tail length of the surfactants and consequently enhanced DNA compaction. These results are in good agreement with our previous findings in which phy-3-12 exhibited the lowest level of GFP expression in OVCAR-3 cells [48].

The m-2-m (m = 12, 14, 16) type gemini surfactant with a pEGFP-C1 plasmid (encoding GFP; N^+/P^- charge ratios of 2:1, 4:1 and 8:1) and a mixed helper lipid component comprised of DOPE and cholesterol (molar ratio of gemini:DOPE:cholesterol was 3:2:1) was used for gene transfection in human epithelial cervical carcinoma (HeLa) cells by Cardoso et *al.* [51]. It was found that increasing the alkyl tail length of the gemini from 12 to 16 (without helper lipid), resulted in an increase in transfection from 6.6 % to ~32.1% GFP, respectively. Incorporating the mixed helper lipid substantially enhanced the transfection efficiency of these systems; for instance, 12-2-12 and 16-2-16 based vectors showed 45.7 % and 55 % GFP expression, respectively. It was hypothesized that the combined hydrophobic (increase in hydrocarbon tail provides better hydrophobic interaction) and electrostatic interaction (positively charged gemini and negatively charged DNA) were key factors for this enhanced transfection efficiency. It was further evident from video-enriched light microscopy analysis (VELM) and thermal analysis (DSC) data that both unilamellar and multilamellar vesicles of varying sizes were present for the m-2-m systems e.g. 16-2-16. In particular it was hypothesized that the 16-2-16 system may form two coexisting phases (one lamellar and a second, ambiguous phase), giving rise to the increase in transfection efficiency, consistent with previous results [33-38, 51].

Cardoso et *al.* have also investigated a series of serine-based gemini surfactants with variations in the alkyl chain length and in the chemical nature of the linker group bridging the spacer to the head groups (amine, amide and ester) [52]. The gemini surfactants were mixed with the pEGFP-C1 plasmid encoding GFP (N^+/P^- charge ratios ranging from 2:1 to 8:1), and with a mixed helper lipid component comprised of DOPE and cholesterol (molar ratio of DOPE: cholesterol = 2:1). The gemini to helper lipid added in various mole ratios ranging from 1:1 to 1:4. For instance, the molar ratio between $(12Ser)_2N5$: helper lipid = 1:4; and the $(14Ser)_2N$, $(16Ser)_2N$ and $(18Ser)_2N$: helper lipid=1:1. In the absence of helper lipids (N^+/P^- = 2:1), the transfection efficiency was increased while increasing the alkyl tail length from $(12Ser)_2N5$ (~2% of cells expressing GFP) to $(18Ser)_2N5$ (32% of cells expressing GFP). However, incorporating the helper lipid in these systems significantly enhanced the transfection efficiency, for instance, the maximum transfection efficiency was observed for $(12Ser)_2N5$ (N^+/P^- = 1:1), $(14Ser)_2N5$ (N^+/P^- = 4:1) , $(16Ser)_2N5$ (N^+/P^- = 8:1) and $(18Ser)_2N5$ (N^+/P^- = 2:1) were around 37%, 25%, 11% and 21% GFP, respectively. There were no clear trends observed relating variations in alkyl tail length and the transfection efficiency. It was found from a DNA protection experiment (DNA protection was expressed in terms of the level of intercalation of the PicoGreen dye; DNA complexed by surfactant is unable to intercalate the dye) that the $(16Ser)_2N5$-based complexes showed the lowest protection of DNA (high concentration of intercalated dye), and exhibited lowest transfection efficiency. Conversely, the 12, 14 or 18 alkyl tail surfactants showed higher levels of DNA protection (low concentration of intercalated dye) in both the presence and absence of the helper lipid component. The zeta potential values were changed from negative to positive values at the highest N^+/P^- charge ratios (4/1 or 8/1) for the C12-based systems (in addition of helper lipid mixture). It was suggested that the addition of helper lipid changed the internal structure of the complexes and consequently increased the zeta potential. In case of the C18 surfactant, which retains a negative zeta potential in the presence of the helper lipids, it is believed that the DOPE and cholesterol lipids remained at the surface level of the complex, with the combination of strong electrostatic and hydrophobic interactions between gemini and DNA preventing any internal rearrangement of the complexes. The lower transfection efficiency of the C18-based complexes was attributed to the lack of ability to adopt different morphologies by these systems. In support of this argument, it was observed that the C12-based system (both in presence or absence of helper lipid) showed the highest level of membrane (comprised of 1,2-dioleoyl-sn-glycero-3-phosphocholine, DOPC) destabilization as compared to the C18-based surfactant, which may be indicative of an enhanced ability of the C12 surfactant to interact with cellular membranes, possibly due to the ability of the components of the complex to adopt different morphologies. Again, this interpretation is in good agreement with previous observations for other gemini surfactant systems.

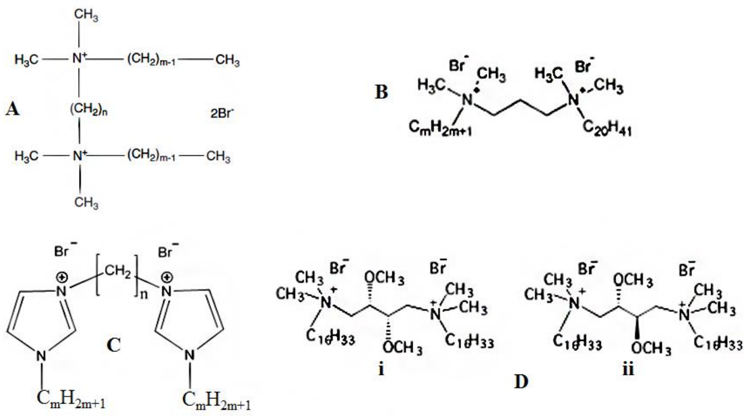

Figure 1.5. A. Molecular structure of the m-s-m type gemini surfactants. The head group is composed of two positively charged nitrogen atoms, separated by a spacer of n = 3, 4, 6, 8, 10, 12, or 16 carbon atoms and each containing two methyl groups. The tails consist of two saturated 12 or 16 carbon atom chains (m = 12 or 16) [33, 47, 53, 54] **B.** Phytanyl substituted gemini surfactants (Phy-3-m; m= 12, 16 and 18) [48] **C.** Molecular Structure of imidazolium gemini surfactants [1,2-Bis(hexadecyl imidazol) alkane], (CmH2m+1Im)2Cn, where n = 2, 3, 4 [55], 5, or 12, and m= 10, 12, 14 [55] or 16 [56]. **D.** (i) cationic gemini surfactants (S,S)-2,3-dimethoxy-1,4-bis(*N*-hexadecyl-*N*,*N*-dimethylammonium butane bromide; (ii) stereoisomer (S,R)-2,3-dimethoxy-1,4-bis(N-hexadecyl-*N*,*N*-dimethylammonium)butane bromide [57].

Zhou et *al.* have investigated DNA compaction and condensation induced by cationic imidazolium gemini surfactants ($[C_n\text{-}4\text{-}C_n\text{im}]Br_2$, $n = 10, 12, 14$) (Figure 1.5 C) at various charge ratios (N^+/P^- ratios of 20:1, 10:1, 5:1, 3.3:1, 2.5:1, 2:1, 1.4:1, 1.25:1 and 1:1; originally expressed as P^-/N^+ ratios of 1: 0.05, 0.1, 0.2, 0.3, 0.4, 0.5, 0.7, 0.8, and 1) [55]. Their study revealed that gemini surfactants with longer tail lengths facilitated hydrophobic interactions between the surfactant and DNA, resulting in enhanced DNA condensation (Figure 1.6). Subsequently, the increased compaction of DNA was responsible for the higher transfection efficiency of these and similar complexes.

In summary, the recent literature review clearly demonstrates that complexes containing gemini surfactants having longer alkyl tail lengths ($m \geq 12, 14, 16, 18$) exhibit increased *in vitro* transfection relative to those with shorter tail length ($m \leq 10, 12$).

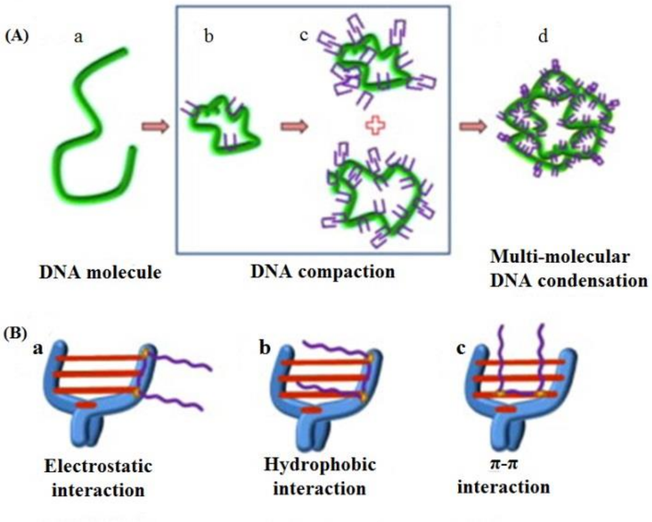

Figure 1.6. (A) Schematic illustration of DNA compaction to multi-molecular DNA condensation progress with the increasing of [Cn-4-Cnim]Br_2. (a) The free DNA strand with loose and flexible conformation. (b) Compacted DNA with minimum size. (c) Compacted DNA with slightly expanded size. (d) Multi-molecular DNA condensation. The purple "n"-shaped structures stand for the [Cn-4-Cnim]Br_2 molecules, the green string-like structures for DNA strands. **(B)** Schematic illustration of the three types of DNA and [Cn-4-Cnim]Br_2 interactions, electrostatic interaction (a), hydrophobic interaction (b), and π-π interaction (c). The blue "Y" shaped structures with attached red lines for the zoom-in view of the double-stranded DNA. Adapted from the reference [55].

1.2.4. Effect of spacer length/group

The composition and/or length of the spacer group in the region of the gemini surfactant head group has been shown to play a vital role in gene transfection. Zhi et *al.* have extensively reviewed the effect of spacer length, structure, and shape of the head group of various cationic lipids (including gemini surfactant), and their impact on gene transfection [58]. Briefly, the review examines cationic lipids possessing specific features in their head groups, including: amines and ammoniums (quaternary ammonium, primary, secondary and/or tertiary amine, polyamine lipids, linear-shaped polyamine compounds, globular and branched-shaped polyamines); guanidiniums; heterocyclic head groups; and some unusual head groups (cardiolipin analogues, nucleolipids, glycosylated cationic lipids, paramagnetic contrast agents or fluorophores). Varying the head group of the lipid/surfactant, one can design an efficient cationic lipid carrier to overcome the barriers of transfection efficiency both *in vitro* and *in vivo* [58].

Previous studies have shown efficient compaction of DNA for m-s-m type surfactants with spacer lengths of 2-12 methylene groups. When the gemini surfactant was combined with both plasmid DNA and the neutral lipid DOPE, the DNA was hypothesized to be compacted into a "ψ" form with resulting complexes having high positive surface charge, resulting in increased transfection efficiency [47, 59]. In the "ψ" form, DNA molecules possess tightly packed, highly condensed structures which exhibit negative ellipticity in a circular dichroism (CD) spectrum [60]. The CD spectrum of the "ψ" form DNA shows the presence of a band at ~260 nm, indicative of the increased negative ellipticity. In the "ψ" form the base pairs in the double helix of the DNA remain in opposite orientation in comparison to the backbone of B or A form of DNA. It has been reported that cationic lipids can neutralize the negative charge of the DNA molecule and induce the "ψ" form, and the resulting lipid-DNA complex may form an inverted hexagonal phase in which DNA has a spatial organization and a fixed directionality [59]. Further enhancements in transfection were observed upon the introduction of a pH-sensitive secondary amine group within the spacer of the gemini surfactant. An approximately 9-fold increase in transfection was observed using 1,9-bis(dodecyl)-1,1,9,9-tetramethyl-5-imino-1,9-nonanediammonium dibromide surfactant (12-7NH-12) compared to an unsubstituted gemini surfactant (12-7-12), and a 3-fold increase compared to the corresponding tertiary amine substituted compound. The pH-sensitive structural changes (pKa of the 12-7NH-12 surfactant was observed to be 5.0 [35]) and an ability for the surfactant/lipid bilayer to adopt multiple phases (lamellar and some undefined phases) within the resulting complexes induced this increase in the transfection efficiency. Both effects were hypothesized to increase fusion between the nanoparticles and endosomal membranes, thereby facilitating DNA release inside the cell [36].

In another study, Misra et *al.* have reported the improved transfection efficiency in human embryonic kidney 293 cells (HEK293T), HeLa and human lung squamous cell carcinoma (H1299) cells using gemini cationic lipids possessing imidazolium head groups [1, 2-bis(hexadecylimidazolium) alkanes; $(C_{16}Im)_2C_n$where C_n is the alkane spacer length (n = 2, 3, 5 or 12) between the imidazolium head groups] [56]. Complexes were prepared in combination with DOPE and pEGFP-C3 plasmid DNA (N^+/P^- = 0.5:1 to 4:1) and it was observed that complexes [$(C_{16}Im)_2C_n$/DOPE)] (Figure 1.5 C) where the gemini lipid had a shorter spacer length between the two imidazolium head groups exhibited better transfection efficiency (maximum 80% GFP cells) than the commercially available Lipofectamine-2000 (~60% GFP cells) in presence of serum in all three cell types [56]. In addition, the same research group demonstrated that 16-s-16 cationic gemini surfactants ($C_{16}C_sC_{16}$, where s = 2, 3, 5, or 12, Figure 1.5 A) in combination with DOPE and pEGFP-C3 plasmid (N^+/P^- = 2:l to 12:1) showed enhanced transfection efficiencies not only in HEK293T but also in human lung carcinoma (H460), Chinese hamster ovary (CHO), HeLa, and human glioma (U343) cells again compared to Lipofectamine-2000 [53]. The most significant observed increase in transfection were for surfactants having short spacer (s = 2 or 3) groups; approximately 80, 40, 50, 12, 15 % GFP cells was observed for the s = 2, 3, 5 and 12, respectively in HEK293T cells in presence of serum and similar results were reported for s = 2 spacer in the H460, CHO, HeLa and U343 cell lines. The results were attributed to the formation of two coexisting lamellar structures in the lipoplexes [53]. Several studies have reported that the existence of lamellar, inverted hexagonal or cubic phase in cationic lipid-DNA complexes are responsible for better transfection efficiency after the endocytosis [30, 61-63].

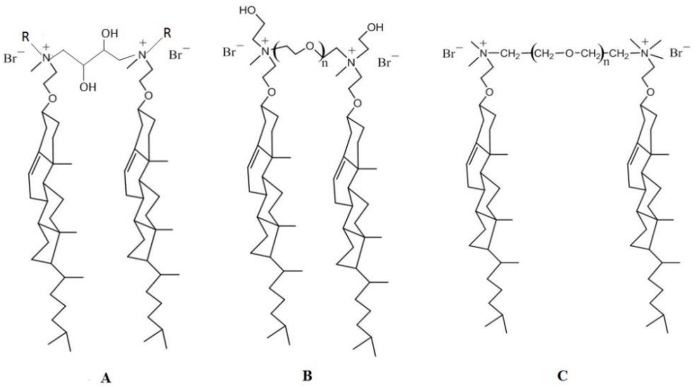

Figure 1.7. Molecular structures of cholesterol-based cationic gemini lipids A. hydroxyethyl spacer (R= $-CH_3$ or-CH_2CH_2OH) [64]; B. oligo-oxyethylene spacer n = 1-4 [64]; C. oxyethylene-type spacers n= 1-3,5 [65].

Misra et *al.* have investigated the cationic gemini surfactants based on cholesterol and possessing different positional combinations of hydroxyethyl ($-CH_2CH_2OH$) (Figure 1.7A) and oligo-oxyethylene-(CH_2CH_2O)n- moieties (Figure 1.7B) in the spacer group, as well as alkyl ($-CH_3$) and/or hydroxyethyl ($-CH_2CH_2OH$) moieties attached at the quaternary ammonium groups (Figure 1.7A and 7B) [64]. In presence of serum, these gemini surfactants (in combination with DOPE at the molar ratio of 1:1) enhanced or sustained the same level of transfection activity in the HeLa cells as compared to the one carried out without serum. Increasing the spacer length of oligo-oxyethylene (Figure 1.7B) from 1 to 4 decreased the transfection efficiency, which was further reduced upon introduction of a hydroxyethyl moiety ($-CH_2CH_2OH$, Figure 1.7A) in the spacer [64]. Enhanced transfection efficiency (~ 65% GFP expressing cells in the absence of serum, increasing to ~90 % GFP expressing cells in the presence of serum) was observed for the oligo-oxyethylene-$(CH_2CH_2O)_n$ with n = 1, (CholHG-1ox) compared to a hydroxyethyl spacer (~75 % GFP expressing cells in presence of serum) (Figure 1.7A) or other long chain oligo-oxyethylene-$(CH_2CH_2O)_n$ with n = 2, 3 and 4 (Figure 1.7B) in presence of serum, partly due to the presence of cholesterol moiety in their structure. The significant differences in the transfection efficiency among all the gemini surfactants were explained on the basis of their biophysical characteristics. In the presence of 10% fetal bovine serum (FBS), the CholHG-1ox showed improved lipoplex formation (zeta potential ~18 mV at $N^+/P^- = 0.5$) compared to CholHG-3ox (zeta potential ~12 mV at $N^+/P^- = 0.5$). Under the same serum condition, a DNA release study (ethidium bromide re-intercalation assay) from the lipoplex revealed that CholHG-1ox released approximately 50% DNA in the release medium (sodium dodecyl sulfate (SDS): cationic lipid molar ratio of 2), whereas the other gemini surfactants released only 30% DNA. Noteworthy, the anionic surfactant SDS is well known to induce the DNA release from various lipoplexes [64]. The exact mechanism for the enhanced transfection efficiency of CholHG-1ox is not clear; however, it is hypothesized that a shorter length oxyethylene spacer group in addition to the presence of cholesterol moiety in the tail group of the surfactant might play a crucial role to induce better DNA compaction in the lipoplex compared to other surfactants studied. The Dynamic Light Scattering (DLS) data suggested that the aggregates size for CholHG-1ox were ~137 nm whereas CholHG-3ox showed larger aggregates of approximately 220 nm. Thus, CholHG-1ox system caused more compaction and formed smaller complexes than the CholHG-3ox. Moreover, it was hypothesized that the presence of the cholesterol moieties may have rendered better stability of the CholHG-1ox lipoplexes. Recent studies reveal that the presence of serum protein helps the formation of cholesterol domains which can interact with the cellular membrane through lipid raft/membrane sorting mechanism, and consequently enhances the transfection efficiency of the lipoplexes [66]. Lipid raft of a biological membrane are enriched with different types of lipids and proteins e.g. cholesterol, long-chain saturated sphingo and phosphatidylcholine lipids and specific proteins, which are associated with the cell signaling and trafficking process. With respect to the head group of the surfactants, the presence of the hydroxyl groups on the head group of the CholHG-1ox undergoes interactions with serum protein (FBS), and enhanced lipoplex association in presence of serum. A DNase stability assay revealed that CholHG-1ox based lipoplexes had increased stability against DNase I than CholHG-3ox (in presence of serum (FBS), which may also account for some of the observed increases in transfection efficiency, and ultimately the combination of some or all of the above factors might play a significant role in inducing better transfection efficiency for the CholHG-1ox based lipoplexes.

Similar results were observed for four novel cholesterol-based gemini surfactant differing in the length of oxyethylene-type spacers $[-CH_2-(CH_2-O-CH_2)_n-CH_2-]$ between each ammonium head group (Figure 1.7C) [65]. It was observed that the incorporation of an oxyethylene spacer between the cationic ammonium head groups could significantly increase the transfection efficiency of the gemini surfactant as compared to their monomeric counterparts in HeLa cells [65]. In presence of 10% serum, the transfection efficiency for the short and longer spacer groups was ~75 % and ~20 % GFP cells, respectively; signifies that the shorter spacer are more efficient than the longer spacer groups. Barran-Berdon et *al.* have reported similar experimental results with the gemini surfactant [bis(hexadecyl dimethyl ammonium) oxyethylene], labeled as $(C_{16}Am)_2(C_2O)_s$, (where the oxyethylene spacer length varied from s = 1, 2 or 3) in combination with the pEGFP-C3 plasmid (at various N^+/P^- ratios between 1:1, 1.5:1, 2:1, 2.5:1, 4:1) and the helper lipid DOPE. The transfection efficiency was determined in HEK293T, HeLa, CaCO-2 (human epithelial colorectal adenocarcinoma), Hep3B (human hepatoma) and MDA-MB231 (human breast cancer) cells *in vitro* [37]. In the presence of serum, it was observed that a short polyoxyethylene spacer (s = 1) showed the highest transfection efficiency (ranging from ~50-75% GFP positive cells) in all cell lines except the HEK293T cells at the effective N^+/P^- = 2:1 and a molar ratio of gemini to DOPE of 0.7:1. In HEK293T cells, a longer spacer (s = 3), showed highest transfection efficiency (~45 % GFP positive cells) hypothesized to be due to the orientation of the polyoxyethylene region that may have occurred in such a way that the spacing between two cationic head group become smaller, and favors the transfection into this specific cells. The exact reason(s) for these enhanced transfection efficiency is not clear: however, the presence of coexisting lamellar phases (determined from SAXS studies) and the synergistic interaction between the polyoxyethylene moiety and serum protein might have played a crucial role [37]. Their conclusions again point to the potential importance for the lipids and surfactants to adopt multiple packing arrangements within the particle structure.

In further studies, Bajaj et *al.* [67], investigated the nature of the spacer between the head groups of thiocholesterol-derived gemini surfactants, having synthesized three gemini disulfide based surfactants with: 1) hydrophobic flexible polymethylene ($-(CH_2)_5$); 2) hydrophobic rigid aromatic ($-C_6H_4-$) spacer; and 3) hydrophilic flexible oligooxyethylene ($-CH_2-CH_2-O-CH_2-CH_2-$) spacer segments (Figure 1.8). A clear dependence on surfactant structure as well as on cell type was observed. Lipid formulations containing gemini surfactants with either hydrophobic polymethylene (Figure 1.8-1) and hydrophilic flexible oligooxyethylene (Figure 1.8-3) spacers were found to be effective in HeLa cells, whereas those incorporating gemini surfactants with only the hydrophilic oligooxyethylene (Figure 1.8-3) spacer were found to be more effective in human fibrosarcoma cells (HT1080) [67]. In prostate cancer cells (PC3AR), the hydrophobic rigid aromatic spacer (Figure 1.8-2) containing gemini was found to result in transfection efficiencies of up to 61% GFP expression.

Interestingly, this group of gemini surfactants was able to transfect the human keratinocyte cells (HaCat), which is believed to be “difficult to transfect” cells; although the actual reason for enhanced transfection with the novel disulfide possessing gemini lipids is not clear.

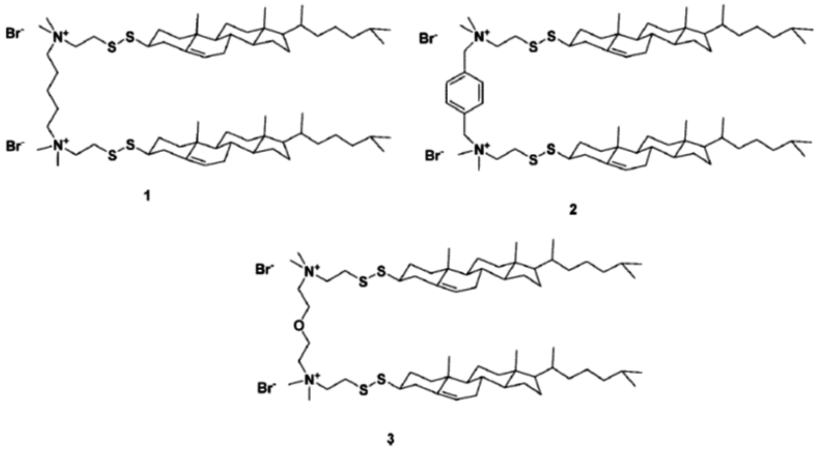

Figure 1.8. Chemical structures of thiocholesterol-derived cationic gemini lipids having -(CH$_2$)$_5$- (**1**), -C$_6$H$_4$- (**2**), and -CH$_2$-CH$_2$-O-CH$_2$-CH$_2$- (**3**) spacer. Adapted from the reference [67].

The spacer length between the head groups in pyridinium-based gemini surfactants impacted the DNA binding capability, stability, cytotoxicity and transfection efficiency [68-72]. Pyridinium-based surfactants along with the helper lipid DOPE (molar ratio of gemini:DOPE = 1:1) with pDNA (N$^+$/P$^-$ = 1:2.5) and having a C4 spacer between the head groups exhibited the highest transfection efficiency compared with the shorter C3 or longer C5 spacers in COS-7 cells [68]. The specific reason for the changes in the transfection efficiency was again not clarified; however, Cryo-TEM imaging revealed a vesicular structure of the lipoplexes with size less than 200 nm. Additionally, surfactants having a C8 spacing (~100,000 relative luminescence units (RLU)/µg protein) showed lower transfection efficiency than a C2 spacing (~120,000 RLU/µg protein) in lung carcinoma cells (NCI-H23) with a gemini surfactant to cholesterol helper lipid (molar ratio 1:1) and N$^+$/P$^-$ = 2:1 [69]. It is hypothesized that the pyridinium polar head groups are larger in size (relative to a quaternary ammonium group) and as a result a shorter spacer length might have bring the head groups closer than their desired (equilibrium) spacing, increasing charge density and therefore increasing electrostatic interactions with DNA and subsequently enhanced the DNA compaction [69].

Maslov et *al.* revealed that cationic liposomes composed of cholesterol, spermine-based polycationic gemini surfactant and DOPE (gemini: DOPE molar ratio 1:1) were able to deliver FITC labeled oligonucleotide (~70-274.5 mean fluorescenence, RFU), plasmids (~3.3-42 RFU), and siRNAs (~5-105 RFU) at the various charge ratio of gemini: pDNA = 2,4,6:1 into HEK293 cells with significantly higher efficiency than that of Lipofectamine-2000 (~1.4-34 RFU) in presence of 10% FBS serum. A gemini surfactant containing two cholesterol units, carbamate linker and spacer of six methylene groups showed the best transfection efficiency *in vitro* compared to the other tested analogues [73].

In summary, the literature review indicates that gemini surfactants having shorter spacer lengths ($s \leq 4$) OR longer spacer lengths ($s > 10$) exhibited better transfection efficiency than those with the intermediate spacer length. This was attributed to the fact that these features ($s \leq 4$ or $s > 10$) may induce structural and packing parameter changes of the complexes (gemini-DNA), for instance, lamellar, inverted hexagonal or cubic phase. Another important aspect is the introduction of specific functional groups within the spacer and/or head group region (extensively review by Zhi et *al.* [58]). For instance, cholesterol, spermine, pH-sensitive amide group (NH), guanidiniums, cardiolipin analogues, nucleolipids, glycosylated cationic lipids, pyridinium, etc. can impact compaction and condensation with negatively charged DNA molecules.

1.3. *In vitro* transfection efficiency

In recent years, more than 250 different types of gemini surfactants have been synthesized and their *in vitro* transfection efficiency have been determined by various research groups [43, 67, 73, 74]. The application of gemini surfactants for DNA transfection was extensively reviewed by Wettig et *al*; Bombelli et *al.*, Donkuru et *al.* and Kumar et *al.* [24, 42, 45, 46]. Only recent additions to the body of *in vitro* studies will be presented here.

Yang et *al.* utilized amino acid substituted (glycine or lysine; 12-7N(Gly)-12 or 12-7N(Lys)-12) and dipeptide substituted (glycine-lysine or lysine-lysine; 12-7 N(Lys-Lys)-12 or 12- 7N(Lys-Gly)-12) gemini compounds in the presence of helper lipid DOPE to prepare a lipoplex [75]. The gemini was combined with the DNA (encoding interferon gamma and GFP) ($N^+/P^- = 10:1$) to to transfect different epithelial cells, e.g., COS-7, PAM212 and cotton tail rabbit epithelial cells (Sf 1Ep). Results showed that the gene expression was substantially increased up to 72 h, and drastically declined by the 7th day. Overall, the glycine substituted gemini surfactant (12-7N(Gly)-12) exhibited higher gene expression (ranging from ~350-5000 pg IFN / 20000 cells at 72 h) in all three cell types.

Mohammed-Saeid et *al.* have investigated the effect of lyophilization (sucrose and trehalose as stabilizer) on gene transfection with the gemini surfactant (12-7NH-12) along with DOPE [76]. The gemini to plasmid (encoding for the murine interferon-γ and green fluorescent proteins (pGThCMV.IFN-GFP)) at an N^+/P^- charge ratio of 10:1 was used to transfect COS-7 cells. Sucrose and trehalose improved the stability of the lipoplex up to three months at 25ºC, and the transfection efficiency was enhanced by 2-3 magnitude higher than the fresh formulation (approximately 8.2±2.6 ng of IFNγ/1.5×10^4 COS-7 cells without lyophilization). It was hypothesized that the lyophilzation/rehydration cycles changes the lipoplex morphology (inverted hexagonal phase) which ultimately enhanced the transfection efficiency [76].

Perrone et *al.* synthesized a type of gemini surfactant containing melamine scaffolds connected by n-hexyl linker and functionalized with a 1-propylammonium polar head and a lipophilic chain having variable carbon length (from C8 to C16). GFP – expressing plasmid was used to transfect the adherent cell lines (A549 and U-87 MG), normal suspension cells (Bristol 8) and primary neuronal cells (DRG neurons) with. Significantly higher transfection efficiency was observed for the studied formulation and this was dependent on the gemini tail length. For instance, the C12 – tail surfactants showed significantly higher results (ranging from 45-80% GFP positive cells) than both C14 (15-20% GFP positive cells) and Lipofectamine 2000 (10-20% GFP positive cells) [77].

Sharma et *al.* have synthesized a series of pyridinium gemini surfactants, among them the gemini surfactant consisting of 3-oxapentane-1,5-diyl hydrophilic spacer showed significantly higher transfection efficiency (~500,000 RLU/µg protein) compared to Lipofectamine (~300,000 RLU/µg protein) in NCI-H23 lung cancer cells in presence of DOPE (gemini:DOPE at molar ratio of 1:2) [78]. This was attributed not only to the chain length but also to the presence of counter ions in the head group.

Donkuru et *al*. have introduced a a pH-sensitive spacer moiety in the gemini surfactant (1,9-bis(alkyl)-1,1,9,9-tetramethy l-5-amino-1,9-nonane-diammonium dibromide surfactants, m-7NH-m, m = 12, 16, 18) to facilitate the transfection efficiency [35]. The surfactants with pH – sensitive spacer groups (m-7NH-m) at a N^+/P^- charge ratio of 10:1 showed higher transfection efficiency in murine PAM 212 keratinocytes (~2.5-3.5 ng of luciferase/5×10^4 cells) compared to the unsubstituted compounds (m-7-m, m-3-m series, ~0.5-1 ng of luciferase/5×10^4 cells). This was attributed to the interactions between negatively charged phosphate groups of DNA and the (–NH–) groups of m-7NH-m gemini surfactants as well as trimethylene spacing between nitrogen centers and the polymorphic changes induced by acidic pH, better transfection results were obtained. Consequently, improved endosomal escape of the plasmid DNA occurred.

Maslov et *al.* synthesized gemini surfactant with polycationic lipids which consists of two cholesterol units, carbamate linker and spacer of 4 or 6 methylene groups, Figure 1.9. In presence of

DOPE, the transfection efficiency of FITC-labeled oligonucleotide, plasmid DNA and siRNA was evaluated in HEK293 cells. Their study showed substantially higher transfection efficiency than Lipofectamine 2000. The linker type, spacer length and the amount of cholesterol residues played a significant role in the results. The gemini surfactant containing two cholesterol units, carbamate linker and spacer of six methylene groups (with the 2X3-DOPE liposome, Figure 1.9) demonstrated the best *in vitro* transfection results among other analogues tested [73]. Additionally, we have mentioned in earlier section (‘effect of spacer length/group’) that gemini/DOPE system showed better transfection efficiency in a recent study compared with the Lipofectamine 2000 in HEK293T, HeLa and H1299 cell lines [56].

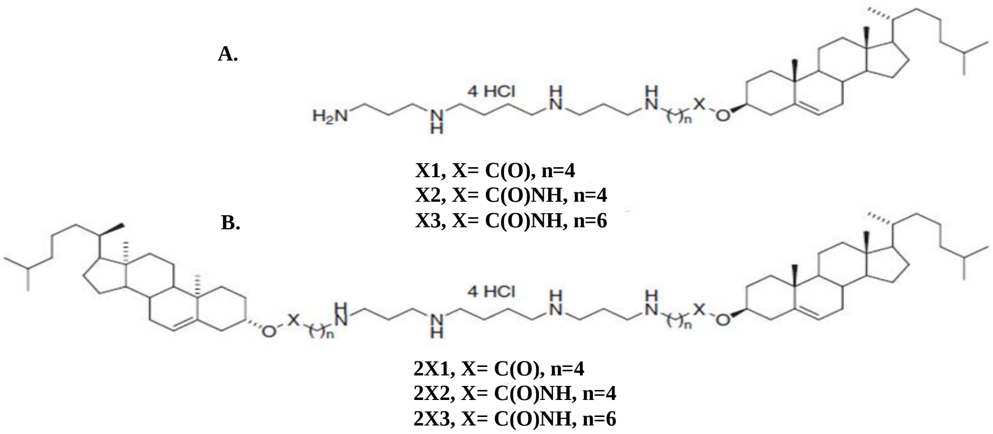

A.

X1, X= C(O), n=4
X2, X= C(O)NH, n=4
X3, X= C(O)NH, n=6

B.

2X1, X= C(O), n=4
2X2, X= C(O)NH, n=4
2X3, X= C(O)NH, n=6

Figure 1.9. Chemical structures of cholesterol based polycationic amphiphiles. Adapted from the reference [73].

In a recent study it was observed that using pyridinium gemini surfactants and cationic lipid mixtures (cholesterol, DOTAP and DOPE) (molar ratio of 1:2) along with plasmid DNA (gWiz Luc and gWiz GFP plasmid DNA) enhanced the transfection efficiency (~80000 RLU/µg of protein) in NCI-H23 cancer cells (in comparing with Lipofectamin-2000 (~20000 RLU/µg of protein)) [79]. This was obtained due to the blending of gemini surfactant into helper lipids, which causes fluidization of the supramolecular lipid bilayers.

Based on our previous review [42] and the current literature assessment, overall, there are no direct correlations observed between the different gemini surfactants and the transfection efficiency. Thus, multiple factors can be considered to interplay a pivotal role in these observed lack of correlations. For instance, variety of lipoplex formulations demonstrated by different research groups, use of varied vectors and co-lipids, lack of understanding of the lipoplexes internal structures, diverse cell lines, transfection efficiency determination method, choice of internal standard and presentation of the results [24, 42]. These are some of considerable factors to be addressed in near future to better understand the transfection efficiency governed by the cationic gemini based lipoplexes.

1.4. *In vivo* transfection efficiency

Intraperitoneal, intramuscular or subcutaneous injection strategies are well known for *in vivo* delivery of lipoplex [80]. Several studies showed topical application of lipoplexes containing gemini surfactant [81-83], *in vivo* ocular delivery for the treatment of glaucoma [84] and suppression of the B16 melanoma metastasis [85]. Badea et *al.* have shown the 16-3-16 gemini surfactant along with pGTm·CMV·IFN-GFP plasmid coding for interferon gamma (IFN-γ) and GFP for topical application for the treatment of localized scleroderma in normal, knock out and diseased animals [47, 81, 82]. Gemini–DNA formulations (nanoparticle and nanoemulsion) showed 3–5 fold increase in IFN-γ expression in the skin compared to the treatment with naked DNA, and 4–6 fold increase compared to the cholesteryl 3b-(-N-[dimethylaminoethyl] carbamate)[Dc-chol]–DNA complex [47].

In another study, Badea et *al.* have investigated cutaneous gene therapy with the gemini nanoparticles (16-3-16) as a topical formulation in IFN-γ deficient mouse model. Their results revealed significantly higher levels of IFN-γ in the skin (0.480 ng/cm^2) relative to treatment with naked DNA (0.167 ng/cm^2). No skin irritation was observed with the gemini based nanoparticle formulation compared to cationic lipid cholesteryl 3b-(-N-[dimethylaminoethyl] carbamate) [Dc-chol] (NPDc-DNA) nanoparticle [81].

Recently, the IFN-γ gene was used in Tsk/+ (tight-skin scleroderma) mouse model. The non-invasive topical nanoparticle formulation with gemini 16-3-16, in the treatment period of 20 days (once a day), resulted in a reduction of skin thickness. The DNA microarray, RT-PCR and histopathological results suggested that the IFN-γ induced inhibition of collagen production in the dermis [82].

Markov et *al.* have investigated the potential to study the antitumor effect (the suppression of B16 melanoma metastases) of gemini amphiphiles based on cholesterol (2X3, Figure 1.18) and long-chain hydrocarbon substituent (2D3) linked with spermine; along with the helper lipid DOPE and pEGFP-C2 plasmid DNA, *in vivo* [85]. The liposomes with 2X3-DOPE or 2D3-DOPE showed enhanced transfection efficiency in B16 (C57Bl/6J-derived melanoma) cells, and the results were substantially higher than the gold standard transfecting agent Lipofectamine 2000. In the antitumor model of murine B16 melanoma, 2X3-DOPE and 2D3-DOPE showed approximately 3-5 fold suppression of the metastasis, *in vivo.* It was observed that the 2D3-DOPE was efficient over the 2X3-DOPE liposomes *in vivo*. The exact reason for the enhanced gene transfection (both *in vitro* and *in vivo*) is not clear, notwithstanding, the endocytosis (in the dendritic cells) of these cationic gemini liposomes is believed to be mediated by the clathrine or caveolae pathway. This study is an indicative for the development of the antitumor dendritic cell based vaccine.

Alqawlaq et *al.* have used gemini surfactant (12-7NH-12) along with the helper lipid DOPE or helper lipid vesicle DOPE:DPPC system; and the Cy5 labeled pCMV6-GFP plasmid (at various charge ratio of gemini to DNA = 5, 7.5, 10, 12.5, and 15 :1 to treat glaucoma *in vitro* and *in vivo* [84]. After intravitreal administration of the gemini-DOPE-DNA, nanoparticles were localized in the nerve fiber layer of the retina. However, the topical administration was not as effective as the intravitreal in which the nanoparticles were localized within the limbus, iris and conjunctiva. It was reported that the nanoparticles prepared with gemini-DOPE-DPPC can induce coexisting lamellar and inverted hexagonal phase in lower pH (endosome or lysosome), these features are important for better gene transfection and release of DNA into the cytosol [33, 84]. Overall, this study demonstrates the applications of gemini-based lipoplexes for the treatment of glaucoma by intravitreal and topical ocular gene therapy.

1.5. Characterization of surfactant-lipid-DNA interactions

Transfection efficiency of cationic lipid-based vectors can be improved by incorporating various types of helper lipids in the system [86-96]. Gemini surfactants alone or in a mixture with helper lipids have showed enhanced transfection efficiency; however, the interaction mechanism(s) of cationic gemini surfactants (and/or helper lipids) with DNA remains mostly undefined. Among the various approaches, Langmuir Blodgett monolayer studies, atomic force microscopy (AFM) studies, fluorescence microscopy, zeta potential, particle size measurement, transmission electron microscopy, U.V. spectroscopy, thermodynamic binding studies, small-angle x-ray scattering (SAXS), and differential scanning calorimetry (DSC) studies have been carried out to study the complexation/condensation behavior of gemini surfactants-DNA, and subsequent gene expression. Among these techniques, we have presented two relevant approaches to our current thesis in the following sections. We will focus on some of the important insights gained from the use of these methods, the implication of these results on our understanding of the interactions between cationic lipids or surfactants and DNA, and the implication of these interactions on the mechanism(s) involved in transfection.

1.5.1. Langmuir Blodgett (LB) monolayer studies

The Langmuir-Blodgett (LB) monolayer technique is a relatively new approach towards understanding the interactions occurring in mixed surfactant/lipid/DNA complexes [97-102]. A Langmuir monolayer can be used as a model interface that allows the study of film chemistry and film structure with changes in either film compression or changes in sub-phase composition, pH, temperature etc. [103]. This could incorporate either a cell membrane model (this will be further discussed in the **section 1.6**) using the gemini surfactant [104-112] or the interaction between DNA and cationic lipid/ gemini surfactant at the air water interface [54]. The Langmuir trough is often coupled with Brewster angle microscopy (BAM) to determine the topography and domains of the floating monolayer at different phases. When p-polarized light shines incident to the air-water interface at or near 53^o (Brewster angle), no light is reflected. However, if a monolayer is spread on the surface, this changes the local refractive index and causes a small amount of light to be reflected and subsequently an image of the monolayer can be collected through a microscope objective by a CCD camera [113]. Thus, the image is obtained based on the differences between the refractive index of the pure surface and the surface with the monolayer. This technique provides information concerning the homogeneity of the monolayer, domain formation, phase transitions and adsorption of material from the aqueous phase.

To determine the surface pressure, the monolayer is compressed with the barriers present in the trough, this provides an isotherm of surface pressure as a function of mean molecular area (π-A) for the spread compounds. Surface pressure is the difference between the surface tension of pure sub-phase (γ_o) and the monolayer-covered sub-phase (γ). At 20°C pure water possess the surface pressure of about 72 mN/m. Figure 1.10 depicts an example of an ideal isotherm for a Langmuir monolayer [113]. As the surface pressure (π) of the two-dimensional monolayer increases, the molecules comprising the monolayer undergo different phase transitions and the molecules are packed more tightly with increasing surface pressure; i.e., in each phase, the molecules are found in different orientations. Thus, the theoretical isotherm (Figure 1.10) can be broken down into gaseous (G), liquid expanded (LE), coexisting LE and liquid condensed (LC), LC state, and solid-like (S) states or phases. In the G-phase, surfactant molecules remain far apart (Figure 1.10B), and consequently no interaction is observed. Increasing the surface pressure (by the compression of barriers) decreases the area per unit molecule. As the molecules comprising the monolayer are forced closer to one another, the liquid expanded (LE) phase can be observed. Further compression of the monolayer exhibits a steeper rise in surface pressure at slightly lower areas. This phase corresponds to the LC phase where molecules are closely packed compared with the LE phase (Figure 1.10B). Finally the monolayer reaches the S phase, where a very steep linear isotherm is obtained at low mean molecular areas; corresponding to a higher density of the molecules with low compressibility in the monolayer. Further compression of the monolayer causes monolayer collapse. The minimum cross sectional area (A_0) is obtained by extrapolating the isotherm at the steepest slope prior to collapse back to zero surface pressure (Figure 1.10). In practice, experimental monolayers may not exhibit all these phases due to the narrow ranges of temperature and surface pressure available.

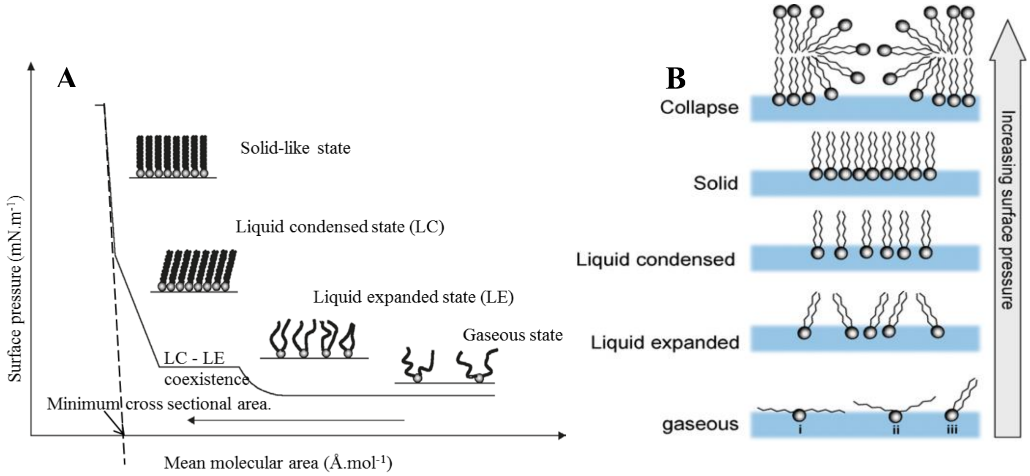

Figure 1.10. A. Theoretical π-A isotherm obtained by compressing an insoluble lipid monolayer formed at an air-water interface. Adapted from reference [113, 114]. **B.** Lipid packing at the various phases of monolayer (at gaseous phase molecules may be orientated flat on the interface (i), or their tails may remain out into the non-aqueous phase (ii and iii). Adapted from reference with permission [115].

Dupuy et *al.* have studied the surface properties of novel fluorinated gemini surfactants with a diamino- diethyl-oxide spacer and carboxylic acid or ester polar head groups [116]. Figure 1.11a shows the π–A isotherm for the interaction of a gemini surfactant containing an ester-based head group (Figure 1.12A) with DNA, the single stranded DNA (ss-DNA) concentrations were 0.1 mg/L and 1 mg/L at pH 7.4. When the ssDNA was added to the sub-phase, it was observed that the molecular area at the lift-off (A_0) remains constant, but the compressibility modulus decreased from 92 to 88 mN/m. Additionally, molecular area at collapse was 67 Å^2 and 73 Å^2 for the 1 mg/L as compared to 0.1 mg/L, respectively.

The changes in surface tension with respect to the area of the surface associated with a liquid film can be denoted as interfacial elasticity. For a Langmuir monolayer equilibrium elasticity is related to the compressibility of the monolayer [117]. Compressibility is indicated by the equation,

$$C = -\frac{1}{A}\left(\frac{dA}{d\pi}\right)_T \qquad \text{Equation 1.5.1-1}$$

where, A is the area per molecule at surface pressure π [117, 118]. The reciprocal of compressibility is denoted as compressibility modulus (C_s^{-1}). C_s^{-1} provides information on the phase transition(s) of a Langmuir monolayer, for instance, the more sharp the phase transition, the higher is the differential $d\pi/dA$ and stiffer the monolayer [104, 117, 119]. In contrast, carboxylic acid head groups (Figure 1.12B, Figure 1.10b) did not result in any significant interactions with ssDNA as observed from the similar compression isotherm curves. This was attributed to the electrostatic repulsions between carboxylate groups and DNA (Figure 1.13). These results signifies that the monolayer characteristics depend on the hydrophobic chain length, the polar-head, the pH of the sub-phase and the flexibility of the spacer. Figure 1.13 shows that the presence of ssDNA in the sub-phase seems to show a low interaction between the surfactants and the oligonucleotide. This study provides a platform to understand the interaction of gemini surfactant with DNA at the air/water interface using Langmuir monolayer technique.

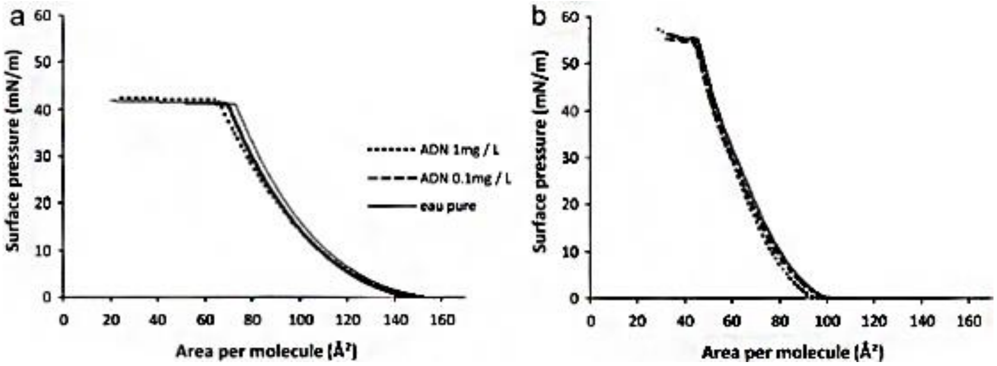

Figure 1.11. π-A isotherms of gemini surfactant with ester polar head groups (a) carboxylic acid head groups (b) with different concentrations of DNA in the sub-phase. Reproduced with permission [116].

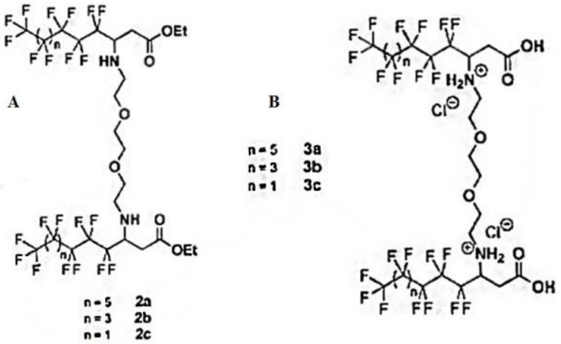

Figure 1.12. Chemical structure of the new fluorinated gemini surfactants. A. diester type gemini surfactant, B. diacids type gemini surfactants [116].

Castano et *al.* synthesized a derivative of cholesterol with guanidinium cationic head groups (bis(guanidinium)-tris(2-aminoethyl)amine-cholesterol, BGTC) and examined mixed monolayers of BGTC and DOPE with DNA to investigate the interactions between BGTC-DOPE and DNA in order to tailor an efficient gene therapy vector [120]. Figure 1.14 shows the DNA interactions with BGTC/DOPE (molar ratio 3:2) at charge ratio of BGTC:DNA = 1:5 at a surface pressure of 20 mN/m, and beyond the collapse pressure (surface pressure > 46 mN/m). It was hypothesized that due to the interactions of BGTC with DNA (in the sub-phase), the BGTC molecules remain in the layer facing towards the aqueous phase, in contrast, DOPE flip-flops (polar head group facing outside (air) and the alkyl tail resides towards the subphase (water), in Figure 1.14B the top DOPE layer) beyond compression to form a top layer. Polarization modulated infrared reflection absorption spectroscopy (PM-IRRAS) studies revealed that due to the adsorption of DNA under the BGTC monolayer, the intensity of the main band of the DNA phosphate group (1220 cm^{-1}) was increased. It was suggested that the BGTC molecules are stabilized by the DNA layer, and could not flip-flop like DOPE. This study signifies a systematic approach to understand the cationic lipid based gene delivery system and helps to explain the improved transfection efficiency both *in vitro* and *in vivo.*

Chen et *al.* conducted Langmuir monolayer studies with the cationic gemini surfactants, $[C_{18}H_{37}(CH_3)2N^{+}\text{-}(CH_2)s\text{-}N+(CH_3)_2C_{18}H_{37}],2Br^{-}$(18-s-18 with s = 3, 4, 6, 8, 10 and 12) (Figure 1.5A) in presence of ds-DNA or ss-DNA at the air/water interface [54]. It was observed from the $\pi-A$ isotherms along with FTIR, IRRAS, AFM and CD measurements, that for $s \leq 6$, a fibril structure was formed for the gemini/ds-DNA complex monolayer. For s > 6 the fibril structure collapsed to form a platform structure (Figure 1.15). For $s \leq 6$, the DNA remained intact in the complex; therefore, DNA undergoes a transition into the preferable ψ-phase with a supramolecular chiral order. This has been suggested to be important for efficient gene transfection [54] because in a ψ-phase, DNA molecules possess tightly packed highly condensed structures [60].

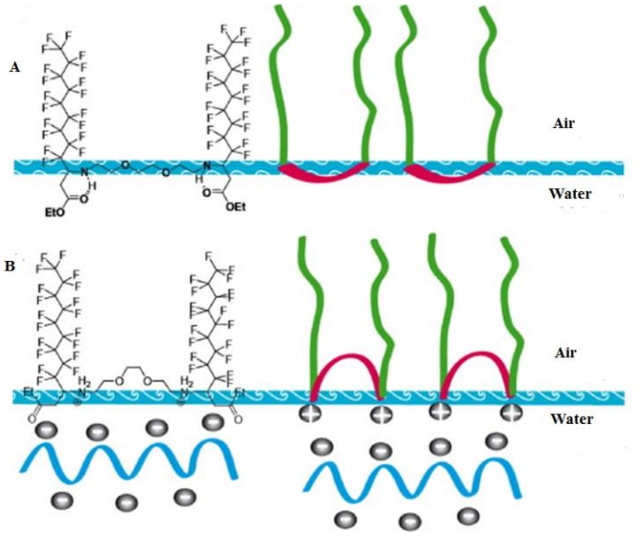

Figure 1.13. Schematic representation of monolayers of diester containing gemini surfactant compressed on an aqueous sub-phase with (**B**) and without DNA (**A**). **A**. at low surface pressure (small surface density of the molecules), ethyleneoxide moiety reside towards the subphase and intermolecular H-bond occurs in the NH group and no interaction with ssDNA. **B.** at higher surface pressure, the polar head group undergoes transition from an extended ethyleneoxide moiety to a U-shape and interacts with the negatively charged ssDNA molecule. Adapted from the reference with permission [116].

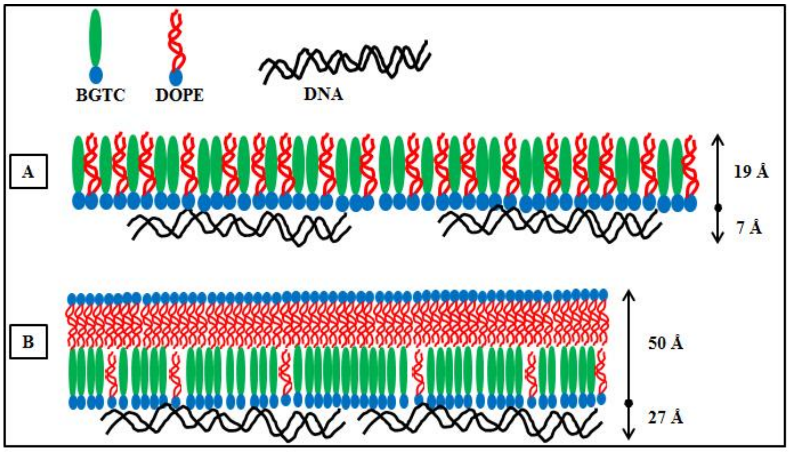

Figure 1.14. Scheme of the DNA (~200 base pairs) interactions with BGTC/DOPE. (**A**) At 20 mN/m, formation of an incomplete DNA layer (≈7 Å thick) under the BGTC/DOPE monolayer (≈19 Å thick). (**B**) Beyond the collapse pressure, formation of an asymmetric lipid bilayer (≈50 Å thick); DOPE on the top flip-flops to create a bilayer in which the polar head resides outward (air) and the alkyl tail toward the BGTC alkyl tail, and BGTC in contact with an organized DNA layer (≈27 Å thick). Adapted from reference [120].

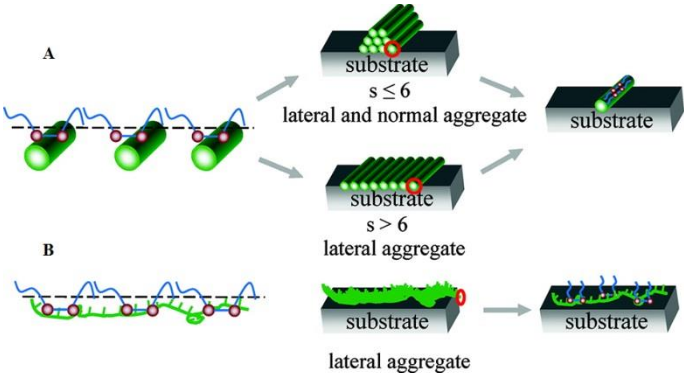

Figure 1.15. Schematic illustration of the monolayer of (**A**) gemini/ds-DNA complex; fibril (top) and platform structure (bottom) formation or (**B**) gemini/ss-DNA complex; fibril structure formation with the conservation of complex monolayer. A. the ds-DNA remains in the double-stranded helical conformation. For s ≤ 6 (top), at low surface pressure the gemini/ds-DNA complex is formed laterally and the fibril aggregate is achieved with the 2-7 nm height; at s > 6 (bottom), the complex formation occurs laterally and platform structure is achieved. Adapted from reference [54].

1.5.2. AFM studies

AFM is a widely used technique to investigate the interaction of gemini surfactants with other helper lipids or DNA [33, 34, 54, 121-125]. AFM studies were carried out to characterize the gemini surfactant – DNA monolayers (using 12-s-12 surfactants (s= 3, 4, 6, 8, 10, and 12) [125] and a series of asymmetric (m-s-n, m≠n) surfactants deposited from Langmuir films onto mica [126]. The formation of complex monolayers between gemini surfactants and DNA at the air-water interface was systematically investigated. The spacer length of the gemini surfactant had profound effect on the surface properties [125]. For surfactants with s = 6, electrostatic interactions between the phosphate groups of DNA and gemini led to a conformational change for the gemini compounds, resulting in the maximum extrapolated area (A_e) in presence of DNA in the subphase; whereas at s = 10, the maximum in the Gibbs area was observed in absence of DNA (surface tension measurement). Minimum surface area occupied by a surfactant molecule at the air/water interface can be determined from the concentration dependence of the surface tension using the Gibbs equation. The Gibbs surface excess concentration is derived from the equation:

$$\Gamma = -\frac{1}{2.303\,RT}\left(\frac{d\gamma}{d\log C}\right)_T \qquad \text{Equation 1.5.2-1}$$

where, dγ = change in surface tension, C = molar concentration of surfactant, R= ideal gas constant and T = absolute temperature. Using the equation 1.5.2-1 one can determine the surface area occupied by the surfactant molecules (Gibbs area) by the equation:

$$a = 1/(N_A \Gamma) \qquad \text{Equation 1.5.2-2}$$

where, N_A is the Avogadro's number [127]. The electrostatic interaction was further evident from the AFM topography which showed the presence of fiber like structures, and the thickness of the fibers were correlated with the spacer length of the gemini surfactants [125]. The asymmetric gemini surfactants also showed similar results. For instance, increase in the asymmetry of the alkyl tail increased the hydrophobicity and provided better condensation of DNA, and AFM topography showed an increase in the width of the fibrils [126]. Noteworthy, for compounds with s > 6, the compressed monolayer become more hydrophobic, resulting in the spacer group adopting a "U-shape" conformation which is an indication of bola amphiphile monolayers. This gemini surfactant tends to form a vertical wicket like conformation at the air-water interface like the other bola form quaternary ammonium surfactants [125].

The condensation effect of T4 DNA with the 12-3-12 gemini surfactant was observed using AFM microscopy and fluorescent microscopy (FM) was investigated by Miyazawa et *al.* [124]. It was found that upon increasing the surfactant concentration from 0 µM to 10 µM, DNA (0.1 µM) exhibited coil to partially folded to folded structure. A 'rings-on-a-string' structure or a network structure composed of many fused rings was observed with the gemini concentration of 0.2 µM and 1 µM, respectively. Specifically, many rings were observed and they were interconnected by elongated coil parts along a single DNA molecule (Figure 1.16). This study signifies that the electrostatic interactions between gemini surfactants and DNA induces condensation in the DNA molecule. It is hypothesized that the relatively smaller head group area of the 12-3-12 surfactant may lead to higher values of packing parameter indicative of the spherical structures, and the DNA molecule can be packed inside this surfactant collapse part and consequently forms the 'rings-on-a-string' structure [124]. Interestingly, studies have shown that gemini surfactant (12-3-12) can induce better transfection efficiency compared with other gemini surfactant 12-m-12, m=4, 6, 8, 10, 12, 16 in PAM212 cells [33]. Thus, the AFM study supports the transfection results of the 12-3-12 gemini surfactant.

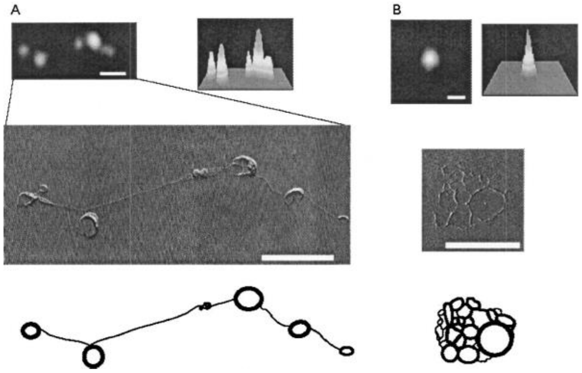

Figure 1.16. FM top and AFM middle images and schematic representations (bottom) of partially folded and folded DNA. The partially folded (**A**) rings-on-a-string structure in the AFM image. The folded (**B**) network structure composed of many fused rings in the AFM image. Reproduced with permission [124].

Foldvari et *al.* have utilized AFM to investigate the pGTmCMV.IFN-GFP plasmid /gemini surfactant (spacer n = 3–16; chain m = 12 or 16) complexes (1 : 10 charge ratio), in the presence or absence of DOPE [33]. In the absence of DOPE, a 'beads-on-a-string' structure was observed for the 16-3-16 surfactant. Interestingly, at 30 second incubation the 'beads-on-a-string' structure (Figure 1.17A) was formed; while increasing the incubation time to 15 min, formed more compact particles (Figure 1.17B) with a particle size of around 220 nm (determined from accompanying light scattering results). Conversely, introducing DOPE in the system resulted in substantial changes in the morphology of the complexes, for instance, both 12-3-12 and 16-3-16 exhibited clear vesicle formation. These findings were further confirmed by a SAXS study in which no polymorphic structures were observed for the gemini – DNA systems in the absence of DOPE [33]. Addition of DOPE to the gemini surfactant – plasmid complexes, for both 12-3-12 and 16-3-16 resulted in a lamellar morphology along with the presence of additional phases, and showed better transfection efficiency in PAM 212 keratinocytes *in vitro* over the system without DOPE. Hence, studying the morphology of the gemini based lipoplex with AFM, provided an insight as to how this could be correlated with the particles size and SAXS results; and ultimately to interpret the transfection efficiency results.

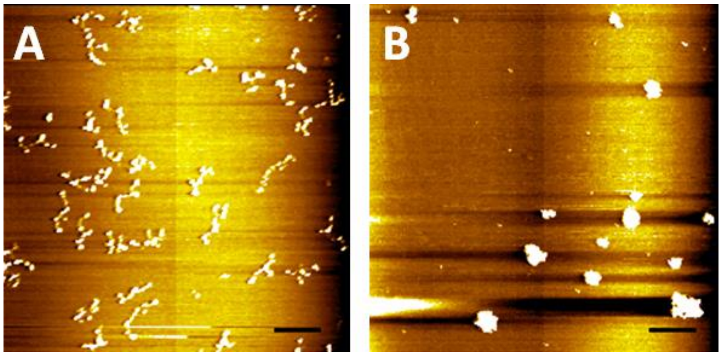

Figure 1.17. AFM images showing plasmid DNA compaction by the gemini surfactants on freshly cleaved mica surface (bar represents 400 nm). (**A**) plasmid-gemini complex after a 30-second incubation; (**B**) plasmid-gemini complex after a 15-minute incubation Adapted from reference [33].

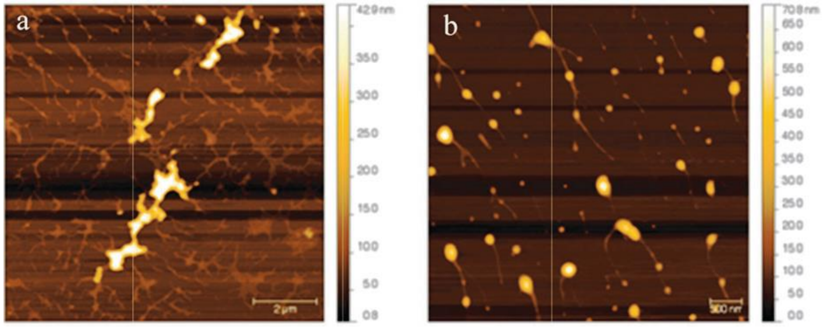

Figure 1.18. AFM images of the phy-3-12 containing complexes at different charge ratio of (a) 2:1 fibril structure; and (b) 10:1 compacted structure. Reproduced with permission [34].

Our recent study with phytanyl modified gemini surfactants (phy-3-m and phy-7NH-m, m = 12, 16, 18) along with helper lipid DOPE and pVGtelRL plasmid, exhibited improved transfection efficiency in OVCAR-3 cells [34]. The highest transfection efficiency was obtained at an N^+/P^- charge ratio of 5:1. The AFM study revealed that the phy-3-12 complexes at an $N^+/P^- = 2:1$ exhibit a large number of fibrils combined with larger aggregates (Figure 1.18). However, fibril formation was drastically decreased at an $N^+/P^- = 10:1$, and tightly compacted particles were formed. This was also evident from particle size analysis where particle sizes of 1220 nm and 188 nm, were observed for $N^+/P^- = 2:1$ and 10:1, respectively. Thus, AFM along with particle size measurement and SAXS study provided a better understanding of the interaction mechanism of lipoplex; and helped in correlating the enhanced transfection efficiency of gemini based lipoplexes with a better understanding of the morphology of the particle formation (larger aggregate or tightly condensed complex formation) [34].

1.6. Cell membrane model system

The biological membrane is a major component of living cells, and plays a significant role in most of the cellular phenomena. The following sections will describe the background of the proposed model membrane study. In the following sections we have presented various components of cell membranes and the importance model membrane system to study the interactions between the cationic lipoplex based and model membrane components.

1.6.1. Lipid raft formation in a biological membrane

A brief historical background of model membrane system development was reviewed by Sezgin and Schwille (2012) [128]. The liposome was discovered in 1964 [129] which led to the establishment of the Fluid mosaic model for the biological membrane by Singer and Nicolson in 1975. According to the fluid mosaic model it is believed that membrane proteins are like icebergs floating in a sea of lipids [130]. Recently, researchers have proposed the presence of ‘rafts’ and “caveole” at the cell surface [131-133]. According to this model, instead of being a random ocean of lipids, plasma membranes possess a certain lipid structure within this ocean of lipids. The lipid “structures” within the membrane ocean are called lipid rafts (Figure 1.19) [134, 135]. Lipid rafts (sizes ~10-200 nm) are enriched with cholesterol, long-chain saturated sphingolipids and phosphatidylcholine (PC) and specific proteins. These are associated with the cell signaling, membrane trafficking, endocytosis and are utilized by some viruses for budding [131, 135, 136]. It has been reported that sphingolipid/sterol assembly in lipid rafts can be modulated by glycosylphosphatidylinositol (GPI)-anchored proteins, certain transmembrane proteins, acylated cytosolic effectors, and cortical actin [135]. Lipid based formulations (lipoplexes) might influence the lipid rafts of cellular membranes, which in turn results in better endocytosis and endosomal escape of the lipoplex. There are several review articles published in the research area of lipid rafts [135, 137-139], and a detailed review of this broad field is beyond the scope of this thesis. Additionally, the outer leaflet of plasma membrane contains more sphingomyelin, phosphatidylcholine and cholesterol whereas the inner leaflet contains more phosphatidylserine and phosphatidylinositol [140]. There have been numerous review article published in the lipid composition of plasma membrane, lipids biosynthesis and lipid distribution at the different stages of endosome maturation [140-147]. The different endocytosis pathways and how the lipid based drug or gene delivery system may be uptake and released from the endocytosis process have been extensively reviewed by several researches [21, 148-152]. Readers are suggested to read above mentioned articles for better understanding of this broad research area.

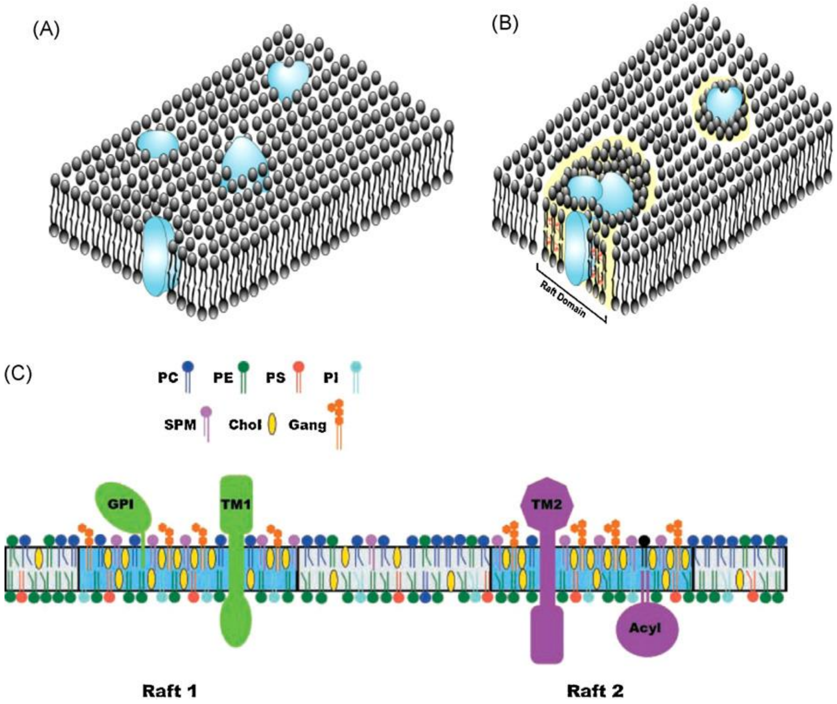

Figure 1.19 (A) Singer and Nicolson’s fluid mosaic model of the membrane; **(B)** lipid raft model of the membrane; **(C)** lipid raft structure in the membrane (blue bilayers) showing inserted transmembrane proteins (TM1, TM2); glycosylphosphatidylinositol anchored proteins; dually acylated proteins (Acyl); and phospholipids (PC), phosphatidylcholine (PE), phosphatidylethanolamine; PS, phosphatidylserine; PI = phosphatidylinositol; SPM = sphingomyelin; Chol = cholesterol; Gang = gangliosides (Figures are adopted from ref. [134] and [153]).

1.6.2a. Membrane lipid composition

Theoretically, the cellular membrane lipidome is composed of glycerophospholipids (9600 species), sphingolipids (more than 100,000 species), mono-, di-, or triglycerides variants (thousands) as well as fatty-acid and sterol-based structures (numerous) [154]. Cellular membrane lipids (Figure 1.20 and 1.21) are divided into three distinct groups such as phospholipids (glycerol-based lipids, 40-60 mol % of the total lipid fraction [114]), ceramide-based sphingolipids, and sterols. Phospholipids are subdivided into several groups according to their hydrophilic groups e.g. phosphatidylcholine (PC), phosphatidylethanolamine (PE), phosphatidylserine, phosphatidylinositol, and cardiolipin. The first three mentioned lipids are the principle lipids in the cellular membrane. Sphingolipids possess sphingoid base as a backbone; these lipids are responsible for the hydrophobicity of the core of the lipid bilayer. Cholesterol (30-50 mol % of the total lipid fraction) is responsible for the fluidity and packing of the lipid membrane [147, 155].

Figure 1.20. Modern view of biological membranes (adapted from the ref. [114]).The illustration shows the lateral heterogeneities, cluster and domain formation within the membrane plane. The 'green' color lipids forms the membrane bilayers, the 'red' color are the integral proteins, 'yellow' color are different domain formation.

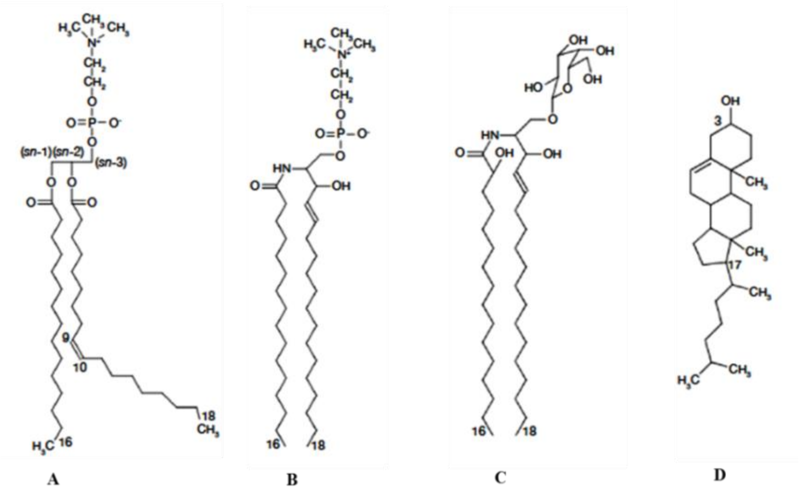

Figure 1.21. Chemical structure of some lipids present in biological membrane: **A.** Phosphatidylcholine (Glycerophospholipid), **B.** Sphingomyelin (sphingolipids), **C.** Glycosphingolipids (sphingolipids), **D.** Cholesterol (sterols).

1.6.2b. Model endosomal membranes

One method which can be used to investigate the interaction of different systems with cellular and endosomal membranes is by using model membranes. The real cell membrane is a bilayer formed by phospholipids molecules, in which sterols and proteins are embedded [156]. Model cell membranes are systems in which their lipid organization mimics the arrangement of lipids in natural cell membranes [106]. A mixture of different lipids like cholesterol, dipalmitoyl phosphatidylcholine (DPPC), dioleoyl phosphatidylcholine (DOPC) and 1-palmitoyl-2-oleoylphosphatidylcholine (POPC) are used to constitute these model membranes. The composition of different membranes inside the cell varies depending on the type of cell organelle and type of tissue [157]. Based on our literature survey, the exact composition of the endosomal membrane is not precisely defied. In mammalian liver, the plasma membrane, lysosomal membranes and nuclear membrane contains cholesterol at around 19.5%, 14% and 10% of total lipids, respectively [158]. Some molar ratios between cholesterol/phospholipid-p in human erythrocytes, thymocytes and lymphocytes are mentioned as 0.81, 0.75 and 0.69, respectively [158]. Therefore, for a normal plasma membrane the amount of cholesterol in the cell varies from 30% to 50% [147, 159]. Van Meer et *al*. have suggested that the early and late endosomes may have a cholesterol content of lower than 30 % or ~25-30% [147, 160]. Additionally, some recent Langmuir monolayer studies have utilized 30% cholesterol as a model mammalian cell membrane along with the DPPC lipid (70%) [156, 161]. Therefore, in our current study we have reduced the cholesterol concentration about 5% to mimic the endosomal membrane. To investigate the effect of our gemini based lipoplexes, a model membrane of DPPC and cholesterol with a molar ratio DPPC/cholesterol = 75/25 % will be used in our experiment to simulate the endosomal membrane.

1.6.3. Types of model membranes

In a model membrane system lipid organization mimics the arrangement of natural biological cell membrane. There are various types of model membrane systems including the Langmuir monolayer, supported lipid bilayers (SLB), bimolecular lipid membranes (BLM), and lipid bilayers (vesicles or liposomes) [106, 128, 153, 162]. The following sections will briefly describe the feature of these model membrane systems.

1.6.3a. Supported Lipid Bilayers (SLB)

SLBs are a model membrane system in which the lipid bilayers are formed on a solid support, mainly silicon or mica. In this model, the lipid monolayer exhibits specific characteristics such as the first layer of lipids polar head group remains at the support (mica/silicon), and the hydrophobic tails are in contact with the lipid chains of the second monolayer. SLBs possess a planner structure, and remain intact while subjected to high flow rate or vibration due to the coupling with underlying solid substrates. Therefore, SLBs are easy to produce, and exhibit higher stability than bimolecular lipid membranes [106, 114].

1.6.3b. Lipid monolayers: a Langmuir-Blodgett study

The simplest model by which to study the biological membrane is the lipid monolayer system. In chapter I we have introduced the Langmuir-Blodgett system. A lipid monolayer can be formed by spreading amphiphilic molecules on a sub-phase of water or different buffer systems using a Langmuir trough. By this technique temperature, surface pressure and sub-phase composition can be controlled to mimic a biological membrane [105]. It is believed that the surface pressure of biological cell membrane ranges from 30-35 mN/m [153, 163, 164], these surface pressures are readily accessible using the Langmuir method. The preparation of Langmuir monolayers will be discussed in the **section 3.2.3**.

1.6.3c. Liposomes/Lipid vesicles

A liposome is one of the model membrane systems having a lipid bilayer that surrounds a small internal aqueous compartment (Figure 1.22) [165, 166]. Liposomal model membrane systems are widely used because they mimic the organization of a biological membrane. There are three types of unilammelar system such as small unilammelar vesicle (SUV, 20-50 nm), large unilammelar vesicle (LUV, 50-100 nm), or giant unilammelar vesicle (GUV,10-100 μm) [106].

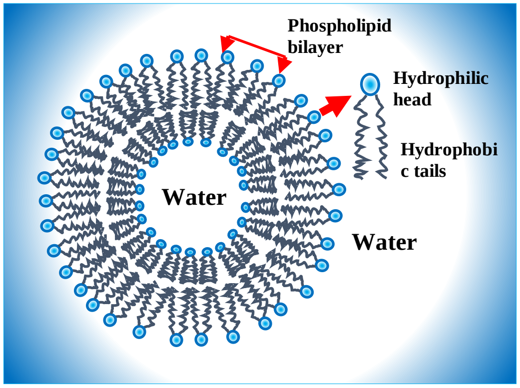

Figure 1.22. Illustration of the liposomal vesicles having phospholipids bilayer. Adapted from the reference [166].

1.6.4. Lipids and gemini surfactants used in the current project

1.6.4a. 1,2-dipalmitoyl-*sn*-glycero-3-phosphocholine (DPPC)

DPPC (Figure 1.23), a zwitterionic saturated phospholipid, consists of a polar head group (phosphate group and a choline), and non polar tail group of two fatty acid chains. DPPC is the most abundant lipid (30–45%) found in the lung, and forms stable monolayers in alveoli [167]. It can reduce the surface tension of water against air to approximately 3 mN/m, and maintains alveoli function during breathing. Therefore, DPPC is often denoted as lung surfactant [167, 168]. DPPC is a widely used lipid to study model biological membranes [169-183]. There have been few published articles which evaluated the effect of different types of gemini surfactant on DPPC model membrane [57, 184-188]. These studies provides an insight to use the DPPC as a major phospholipid component of model biological membrane in the Langmuir monolayer studies. Additionally, DPPC monolayer is easy to produce and already been well characterized in the literature as a model membrane.

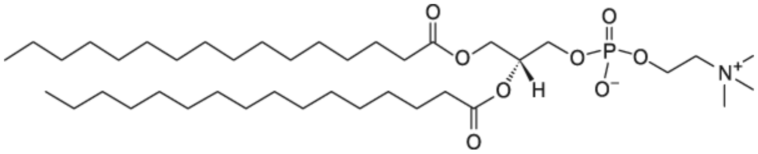

Figure 1.23. Chemical structure of 1,2-dihexadecanoyl-*sn*-glycero-3-phosphocholine (DPPC).

1.6.4b. 1-palmitoyl-2-oleoylphosphatidylcholine (POPC)

Tumor cell membranes are comprised of more unsaturated lipids (such as POPC) , whereas normal cells contain a higher amount of cholesterol and saturated phospholipids [189]. An extensive review has been published examining the biophysical changes with respect to cellular membrane composition, specifically for membranes in drug resistant cells [190]. Discussing all the features of cancer cell membranes is beyond the scope of this thesis. Readers are suggested to read the review by Nagoya (1993), for a detailed overview of cellular lipid composition of cancer cells [191]. In addition to cancer, alteration of cell membrane lipid composition may occur in other disease conditions such as diabetes, and cardiovascular disorders such as hypertension, atherosclerosis, coronary heart disease, sudden cardiac death, aneurism, and thrombosis. Therefore, biophysical investigations of lipid membrane structure, in order to understand the interaction of drugs or drug delivery systems with specific cell membrane lipids may provide insight with respect to cellular uptake mechanisms of such delivery systems [106].

POPC (Figure 1.24) is another most abundant phospholipids in cell membranes. POPC provides a good model to study the fluidic nature of the cancer cell membrane using the Langmuir technique. POPC has been reported to be more abundant lipid in leukemic cancer cell membranes than other cancers; and Wnetrzak el *al.* have studied a POPC/cholesterol monolayer as a model cancer cell membrane (leukemia) [180]. There have been few published articles which have used different gemini surfactant along with POPC monolayer system [192]. This study provides an insight to use the POPC as a model membrane component to investigate the interactions with the gemini-based lipoplexes in a Langmuir monolayer studies.

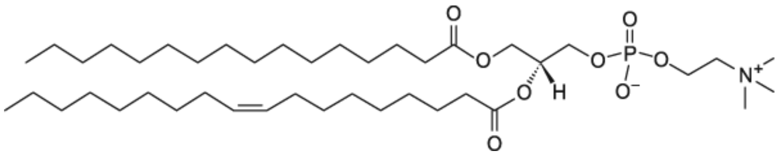

Figure 1.24. Chemical structure of 1-palmitoyl-2-oleoylphosphatidylcholine (POPC).

1.6.4c. Cholesterol

Cholesterol (Figure 1.25) is a vital component of mammalian cell membranes since it maintains membrane fluidity, and has significant role in lipid rafts [193]. Heczkova and Slott have synthesized new ether analogues of the phosphatidylcholine and lyso-phosphatidylcholine which possess properties of an anti-tumor agents. It was revealed that the ether lipids were strongly associated with the cholesterol– sphingomyelin domains (lipid rafts) of the plasma membrane due to the hydrophobic nature of the lipids, and stabilized the lipid rafts against the temperature induced melting. Thus, this study indicates that the anti-tumor agents can modulate the cholesterol portion of lipid raft [194]. Therefore, it is important to study cholesterol based model membrane system to have better understanding of the lipid raft. There have been several published articles which have reported different studies using cholesterol as a model membrane component. These include the comparative study between the Langmuir monolayer of the mixed DPPC-cholesterol system and the physical stability (particle size, polydispersity) of DPPC-cholesterol liposomes [182], 1,2-dimyristoyl-*sn*-glycero-3-phosphocholine (DMPC)-cholesterol monolayer [195], glycolipid–cholesterol monolayers [196], a lipid raft model of N-palmitoyl-D-erythro-sphingosylphosphorylcholine (PSM), 1,2-dioleoyl-sn-glycero-3-phosphocholine (DOPC), and cholesterol [197].These studies signifies the use of cholesterol as a model biological membrane component for the Langmuir monolayer study. In our current study, we have used cholesterol along with DPPC to mimic the model endosomal membrane.

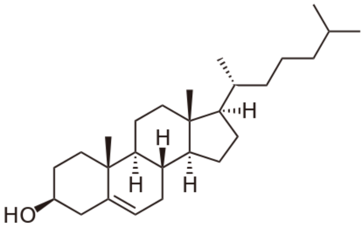

Figure 1.25. Chemical structure of cholesterol.

1.6.4d. 1,2-Dioleoyl-sn-glycero-3-phosphatidylethanolyamine(DOPE)

The transfection efficiency of cationic lipid based vectors can be improved by incorporating helper lipids in the system. One example includes the use of dioleoyl-phosphatidylethanolamine (DOPE, Figure 1.26) to increase transfection efficiency [86, 87]. In our current study we have used DOPE as a helper lipid in the formulation of our cationic gemini surfactant based transfection vectors. DOPE, as a helper lipid, is thought to increase transfection efficiency by formation of mixed aggregates with high (greater than unity) packing parameters. This leads to a transition from micelle-forming systems towards vesicles, and subsequently towards the formation of inverted hexagonal or cubic phases [198]. In addition, the fluidity of cellular membranes can be increased by incorporation of DOPE, which may further enhance transfection efficiency.

The co-existence of lamellar [32] and inverted hexagonal [31] structures as an important property for cationic lipid/DNA lipoplexes was first introduced by Safiniya's group [31, 32]. The inverted hexagonal phase of a lipoplex has been demonstrated to be preferable over the lamellar phase in terms of efficient gene transfection due to enhanced endosomal membrane fusion and release of the lipoplexes into the cytoplasm (this phenomena has been described in the section 1.2). Figure 1.27 depicts the conversion of lamellar to inverted hexagonal structure of lipoplexes. Lamellar lipoplexes generally bind with anionic lipids of cellular membranes and increase the packing parameter of the cationic surfactant which allows the formation of inverted hexagonal or cubic structures (Figure 1.27). However, these non-lamellar structures are not favorable for binding DNA; instead they are favorable for releasing DNA after cellular internalization. In this context some helper lipids are used in combination with the gemini surfactants; e.g. DOPE to aid in the formation of non-lamellar structures.

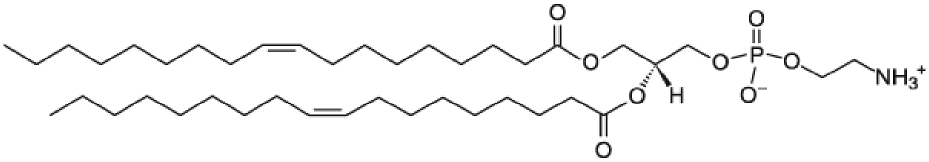

Figure 1.26. Chemical structure of 1,2-Dioleoyl-sn-glycero-3-phosphatidylethanolyamine (DOPE).

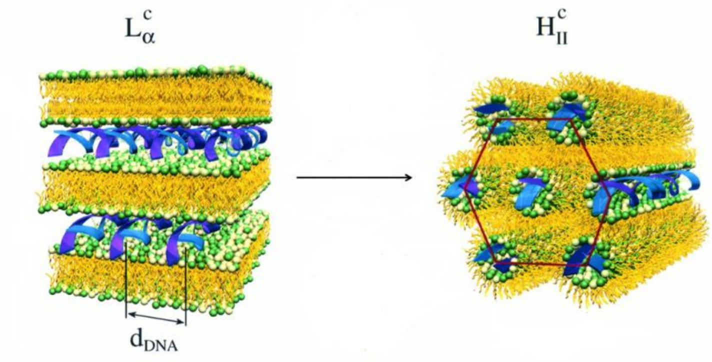

Figure 1.27. Schematic representation of the lamellar phase to the columnar inverted hexagonal phase of cationic lipid-DNA complexes. **A.** the cationic lipid-DNA complex in a lamellar phase. The DNA molecules reside between the lipid bilayers (in water) and are separated by a distance d_{DNA}. **B.** addition of the helper lipid DOPE with the DOTAP induces the phase transition from lamellar to inverted hexagonal phase in which the polar head group of the lipids are facing towards the DNA and the hydrophobic tails outward. Adapted from the reference [31].

1.6.4e. Cationic gemini surfactant used in the current project

The cellular uptake mechanism of a cationic lipid based nanoparticles can be governed by cell-type and nanoparticle properties, e.g. lipid raft-mediated uptake, macropinocytosis, clathrin and caveolae-dependent endocytosis [199]. Keeping this in mind, a novel class of pH sensitive gemini surfactant, m-7NH-m, m = 12, 16, 18 were synthesized (Figure 3.9) [200, 201]. In addition, 16-7NH-16 possess low CMC value as well its pKa value is 5.04 ± 0.3 [35]. This could provide better endosomal escape since the endosomal pH is around 5-6. The pH of the lysosome is around 4-5, which is more acidic compared to early endosomes [23]. Thus, the presence or absence of pH sensitive group (m-7-m) exhibits better structural activity relationship clues. As such, in this project we have used the gemini 16-7-16 and 16-7NH-16 surfactants (Figure 1.28) which have shown improved transfection efficiency in our previous study [35].

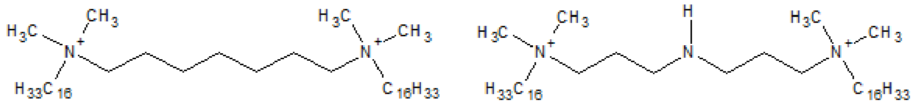

16-7-16 16-7NH-16

Figure 1.28. Typical gemini surfactant structures with a methylated spacer 16-7-16 and an amino-substituted spacer 16-7NH-16.

1.7. Summary

Overall, this literature review reveals that studying the interaction behavior of gemini surfactant with DNA in a lipoplex can aid in understanding the mechanism(s) involved in the condensation of DNA and the subsequent release of incorporated DNA from the lipoplex into the cytoplasm through endosomal escape. It is evident that the conformational changes in the lipoplex morphology will eventually facilitate enhanced cell penetration as well as transfection of the gene. In another aspect, in order to overcome the cellular barriers of a lipoplex, we need to understand how DNA influences the arrangement of vector components (lipids, surfactants, polymer etc.) during the complexion of DNA; as well as how these components interact with biological membranes. Moreover, ultimate usefulness of non-viral gene delivery systems will depend on the rate, extent and duration of transfection, the ability of the gene delivery systems to specifically interact with target cells *in vitro* as well as *in vivo*. Having been aware of the aforementioned features of a cationic lipoplex one can design an efficient non-viral gene delivery vector including gemini surfactant with appropriate modifications.

This chapter has demonstrated the impact of a wide number of variations within the structure of the gemini surfactant upon transfection efficiencies, and has identified a number of key features important for transfection, including structural polymorphism and stimuli responsive functional groups. Understanding of membrane fusion events, and overall a better understanding of the interaction of complexes with cellular membranes, and the eventual fate of complexes within the cytoplasm will continue to be critical for further optimization of these vectors. Studies should be carried out to locate/track the nanoparticles in the cell surface (membrane), cytoplasm or in the nucleus; allowing for correlation of the transfection efficiency results with the exact number of particles been taken up by a specific cells. Next generation gene transfection vectors could include gemini surfactant coupled with surface modification of the liposome for targeting, additional environmentally responsive stimulus, or the formation of other "smart" vectors to deliver the DNA cargo to the nucleus.

Moreover, the chemical nature of the transfection agent, the structure of the delivery system, cell types and transfection efficiency yet to be optimized for the gemini based gene delivery system. Next generation gene delivery method might include the cationic gemini surfactant along with the surface modification of liposome, utilizing the targeting ligands on them, using smart biomaterial (pH sensitive) and formation of different combination of smart biomaterial-gemini-DNA to deliver the DNA cargo to the nucleus. Keeping these important factors in mind we have designed the current project which will be discussed in **chapter IV**, and the interaction of novel gene transfection system on the model biological membrane in **chapter V**.

Chapter II

2.1 Objectives and Hypothesis

2.1.1 Hypothesis statement

We hypothesize that the interactions of the novel gene therapy formulations consists of gemini surfactant, DOPE and DNA may disrupt and destabilize the model endosomal membrane.

2.1.2 Overview of proposed project/rationale

Multicomponent lipid membranes form the majority of membrane barriers in living organisms, and their function is highly dependent on membrane composition. It is known that domains high in the concentration of a particular lipid component are formed in cellular membranes under specific conditions (e.g. lipid raft domains in endocytosis) and that these domains can be modified by lipid-based drug delivery systems [149]. On the other hand, major barriers faced by the non-viral transfection vectors to deliver DNA in gene therapy applications includes a lack of understanding of how DNA influences the arrangement of vector components (lipid, surfactants or polymers) during the complexation of DNA; as well as how they interact with biological membranes. Brewster's Angle Microscopy (BAM), Polarization Modulated Infrared Reflectance Absorption Spectroscopy (PM-IRRAS), Atomic Force Microscopy (AFM) and Kelvin probe force microscopy (KPFM) can be used to characterize the arrangement of the gemini surfactants and phospholipids that make up the transfection vector (both in the presence and absence of DNA) as well as the effect of these components on model biological membranes.

2.1.3 Objective / Short term goals

Characterization of gemini phospholipids transfection formulations in the presence and absence of DNA using BAM, PM-IRRAS, AFM and KPFM.

2.1.4 Long term goals

Characterization of model biological membranes

a. DPPC-Cholesterol or POPC-Cholesterol model membrane.

b. Model Membrane (DPPC-Cholesterol or POPC-Cholesterol) with gemini surfactants/phospholipids (16-7-16, 16-7NH-16 with DOPE or without DOPE).

c. Model Membrane with gemini surfactants/phospholipids/DNA system.

Chapter III

Material and Methods

3.1 Materials

Gemini surfactants 16-7-16 and 16-7NH-16 were synthesized in our laboratory according to procedures previously reported in the literature [35, 201, 202].. The degree of purity was determined by using NMR and surface tension measurements [200]. DOPE (1,2-dioleoyl-sn-glycero-3-phosphoethanolamine), 1,2-dipalmitoyl-*sn*-glycero-3-phosphocholine (DPPC) and cholesterol was purchased from Avanti Polar Lipids (Alabaster, USA). Double-stranded salmon sperm DNA was from Sigma-Aldrich, USA and was used without further purification. Sodium acetate was obtained from OmniPur (Darmstadt, Germany), acetic acid from Fischer Scientific (Ottawa, Canada). Chloroform, Sodium dihydrogen phosphate monohydrate and disodium phosphate heptahydrate were obtained from Sigma-Aldrich (Steinheim, Germany). Sodium acetate, acetic acid, and sodium bicarbonate were purchased from Sigma-Aldrich (Oakville, Ontario). In this investigation, deionized Millipore-Q water (18 mΩ cm and 72.6 mN/m at 20°C) was used.

3.2 Methods

3.2.1 Experimental procedures / Techniques

3.2.2 Characterization of gemini-DOPE-DNA nanoparticles

The gemini formulation used in the current project showed better transfection efficiency in PAM 212 keratinocyte cells and COS-7 cells [35], *in vitro*. However, our literature survey revealed that there is no report about the presence of specific types of lipids in ovarian cancer cells. Springer et *al* (2003) has characterized some plasma proteins in ovarian cancer cells [203], but they are not useful to study as model membrane system. As such, our current project aimed to evaluate DPPC-cholesterol based model membrane system to mimic a normal cell membrane or endosomal cell membrane. Additionally, the POPC-cholesterol system may be implemented to represent the model cancer (leukemia) cell membrane [180].

In our previous study we have synthesized, and characterized the gemini 16-7-16 and 16-7NH-16 along with helper lipid DOPE with or without the presence of DNA [35, 200]. This system showed smaller particle size with a positive zeta potential value, and improved transfection efficiency in PAM 212 and COS-7 cell line [35]. In our current project, we have used the gemini-DOPE system with or without the presence of DNA as a lipoplex combination to observe the interaction with model membrane systems.

3.2.3. Preparation of a Langmuir-Blodgett monolayer

We have already introduced the Langmuir-Blodgett monolayer system in chapter I, section 1.5.1. The preparation of the Langmuir monolayer is described in the following section 3.2.4. In addition to the LB technique, Brewster angle microscopy (BAM) is commonly used to determine the thickness and topography of the LB monolayer [113].

3.2.4. Monolayer formation and surface pressure measurements

Surfactant, lipid, and mixtures were dissolved in chloroform obtained at a concentration of 2.5 mmol/L. The mixtures of DOPE and gemini surfactants were prepared at a mole ratio of 3:2. DNA stock solution was prepared by dissolving DNA in Millipore-Q water for a stock concentration of 4 mg/L. The concentration of DNA and buffer used on the trough was 0.004 mg/mL [54]. Buffer solutions at pH = 4, 7, and 9 were prepared using acetate buffer (using 1% acetic acid), phosphate buffered saline (using Na_2HPO_4) and sodium bicarbonate (using $NaHCO_3$), respectively at 10 mM/L. The experiment was performed on a large (14.5 cm by 53 cm) Langmuir-Blodgett trough (KSV Instruments, Helsinki, Finland), with surface pressure monitored using the Wilhelmy plate method. Compressions of the monolayers on the trough were carried out at a rate of 15 mm/min. A volume of 20 µL of surfactant and/or lipid solution was placed onto the surface of the subphase using a micro-syringe (GASTIGHT®, Hamilton-Bonaduz, Schweiz, Switzerland). For experiments that involved only buffer subphase, the monolayer was allowed to equilibrate for 10 minutes. For experiments involving DNA and buffer, the sub-phase was given 60 minutes to equilibrate with DNA prior to adding surfactant. The monolayer was then allowed to equilibrate for 30 minutes on the DNA and buffer subphase before the isotherms were collected. Isotherms and BAM images of the following samples with or without DNA were collected: 16-7-16, 16-7NH-16, DOPE, DOPE and 16-7-16, DOPE and 16-7NH-16.

For the model membrane studies, the different buffer solutions (pH 4, 7 and 9) were spread as sub-phase in the Langmuir trough. Then a volume of 20 µL of surfactant and/or lipid solution was injected into the sub-phase using a micro-syringe (GASTIGHT®, Hamilton-Bonaduz, Schweiz, Switzerland). The injected samples were mixed with the sub-phase with the help of a glass rod and kept for 10 min to evaporate the solvent. However, for experiments involving DNA, the DNA solution was placed as a sub-phase in the though, and allowed 30 minutes to equilibrate prior to adding surfactant systems. Then, the gemini surfactant-DOPE systems were injected in the subphase, mixed with a glass rod, allowed 15 min for equilibration. Finally, DPPC: cholesterol = 75%:25% (the experimental concentration is 2.5 mM in which DPPC and cholesterol possess 1.875 mM and 0.625 mM, respectively) model membrane was spread on the DNA subphase. This monolayer was allowed to equilibrate for another 15 minutes on the DNA sub-phase before the isotherms were collected. Finally, the barriers were compressed at a rate of 15 mm/min to obtain the isotherm.

3.2.5. Brewster angle microscopy (BAM)

The Langmuir balance described in section 3.2.4 is equipped with a Brewster angle microscope (BAM) (KSV Instruments, Helsinki, Finland) which was used to visualize the morphology of the studied monolayers at the air–water interface. A standard He-Ne laser was used as a light source with the power of 50 mW, wave length of 658 nm and the spatial resolution of the device was 2 µm. Briefly the p-polarized light at 658 nm wave number was reflected at the air/water interface at the Brewster angle (53.1°) to an embedded CCD camera. During the compression of the monolayer, the images were collected at least every 0.2 mN/m surface pressure changes; and the images were processed by the ‘ACCURION Image 1.1.2’ software. The software automatically pings the surface pressure and mean molecular area at which the images were collected; consequently BAM images were presented according to the surface pressure values in the current studies.

3.2.6. Atomic Force Microscopy

Atomic Force Microscopy (AFM) was used to determine the nanoscale structure of a selected subset of the monolayers. The monolayers were deposited onto a solid, atomically flat substrate. In the current experiment, the standard Langmuir-Blodgett deposition onto freshly cleaved mica slides was used. Briefly, 15 µL of gemini surfactants and/or gemini-DOPE (stock solution of 1 mg/mL in chloroform) was spread onto the subphase containing buffer pH 4 (with DNA if applicable) in a small (approximately 15cm x 7cm) Langmuir trough (KSV Nima). The solvent was allowed to evaporate for 10 minutes, afterwards, the monolayer were compressed to reach and maintained the target pressure (15, 25 or 35 mN/m). The mica substrate (slide) was drawn up through the monolayer at a speed of 10 mm/min. The finished samples were allowed to dry overnight in a desiccator before imaging. AFM images were obtained with an AIST-NT Smart SPM loaded with a MikroMasch HQ:NSC15//Pt-15 cantilever tip (resonant frequency approximately 325 kHz). Height and phase images were obtained in AC mode.

Additionally, the Kelvin probe force microscopy (KPFM) technique was used to obtain the images of the contact surface potential difference (CPD) (between the tip and sample) in amplitude modulation (AM) mode. In the KPFM technique, a bias voltage is applied to the sample, and an additional AC voltage is applied to the tip to generate a vibrating capacitor system; the bias voltage is chosen to compensate for the signal arising from the electric surface potential, and thus the image of the CPD is obtained [204, 205]. The AFM and KPFM images were obtained in one step, with two sweeps per line (one for AFM, the second for KPFM). The AFM and KPFM data were processed with the program IAPro from AIST-NT, by first fitting each line to a horizontal polynomial of degree 2 (quadratic), and polynomial levelling, if required, to achieve a flat image. Cross sections are obtained by first smoothing the image with a Gaussian filter ($\sigma = 1$ pixel), for clarity.

3.2.7. PM-IRRAS

Polarization modulation Infrared reflection absorption spectroscopy (PM-IRRAS) is another technique used to determine the conformation, interaction and orientation of molecules in a Langmuir monolayer [120]. Dluhy and Conell (1985), obtained the first IRRAS spectra from fatty acids and phospholid Langmuir films [206, 207]. Blaudez et *al* (1993), reported the complete mid infrared monolayer spectra of deutorated arachidic acid on a water sub-phase using the polarization modulated IRRAS system [208]. There are several review articles published on this subject area that readers are referred to for more detailed information [209-212]. In the PM-IRRAS system, a goniometer holds two units, a spectrometer and polarization modulation unit in one arm and an MCT-detector on the other arm. Briefly, parallel (p)-polarized light or perpendicular (s)-polarized light passes through the monolayer formed on the Langmuir trough. These signals are processed by the detector unit and reflectance spectrum is observed [213]. The spectrometer and PM-unit are operated at different frequencies, thus, allowing separation of the two signals at the detector. Interference from water or CO_2 is removed by the polarization modulation method.

3.2.7 (a) Monolayer characterization by PM-IRRAS

In the current study, the PM-IRRAS measurements were carried out on a KSV NIMA PM-IRRAS instrument (KSV Instruments Ltd, Helsinki, Finland). The incident light angle beam was set at 76°. Initially, different buffer solutions (pH 4, 7 and 9) were spread on the medium Langmuir trough and the background spectrum was collected. The surfactant and DOPE mixture was prepared according to the procedure mentioned in section 3.2.4. Then, 12 µL of this chloroform solution was spread over the sub-phase (buffer pH = 4, 7, 9 with or without DNA) on the medium Langmuir trough to obtain an initial surface pressure of around 10 mN/m. For the PM-IRRAS measurements of the model membrane, after collecting the background spectrum of the buffer (pH 4, 7 and 9); 20 µL of the gemini surfactant/DOPE systems were injected in the subphase, mixed with a pipette, allowed

10 min for equilibration. However, for experiments involving DNA, the DNA solution was placed as a sub-phase in the trough, and allowed 5 minutes to equilibrate prior to adding surfactant systems. Finally, 12 µL of the DPPC: cholesterol = 75%:25% (the experimental concentration is 2.5 mM in which DPPC and cholesterol possess 1.875 mM and 0.625 mM, respectively) model membrane was spread on the DNA subphase. The monolayer was allowed to equilibrate for another 10 minutes on the DNA sub-phase.

The monolayer was compressed (5 mm/min) to surface pressures of 30 mN/m, 35 mN/m and the maximum compression of the barrier; PM-IRRAS spectra were collected at each surface pressure. The spectra was collected in the range of 800-4000 cm^{-1} and the resolution was 8 cm^{-1}. In a PM-IRRAS instrument, the polarization modulation unit modulates the signal reflected from the surface at 74 kHz between s- and p-polarization. The difference between the two polarizations provides the spectrum containing surface specific information, and the sum provides the reference spectrum [214].

Chapter IV

Characterization of Gemini surfactant and DNA monolayers at the air/buffer interface using Brewster angle microscopy

4.1. Analysis of the π - A isotherms

The compressibility modulus (C_s^{-1}) was calculated from the compression isotherm according to the equation:

$$C_s^{-1} = -A(\partial\pi/\partial A)_T \qquad \text{Equation 4.1}$$

where, A is the molecular area at a given surface pressure, π. The molecular area at collapse (A_c) and collapse pressure (π_c) were directly determined from the compression isotherms. According to Davis and Rideal [118, 215], the compressibility modulus is used to determine the phases of the monolayer; for instance, for the liquid-expanded phase (LE) C_s^{-1} = 12.5–50 mN/m, liquid phase (LE-LC) C_s^{-1} = 50–100 mN/m, liquid-condensed (LC) C_s^{-1} = 100–250 mN/m and solid (S) for $C_s^{-1} > 250$ mN/m. The higher the C_s^{-1} values, the less elastic the monolayer is. Apart from this, several other parameters are determined directly from the isotherm. For instance, the liftoff area (A_L) is the molecular area where the isotherm rising just emerges from the baseline, and provides useful insight about the molecular orientation at the onset of intermolecular contact in the gas –liquid phase region [216]. At the gas–liquid transition phase, liftoff occurs at larger molecular areas until all the molecules are compressed into a liquid phase. Fahey and Small have suggested that the liftoff from the base line is best estimated by eye since it is not always possible to get a sharp break from the base line [216]. The limiting area or minimum cross sectional area ($A\infty$) is obtained by extrapolating the isotherm at the steepest slope prior to collapse back to zero surface pressure. The smaller the value of limiting area, more closely packed the monolayer is [119, 216]. The collapse pressure (π_c) is determined from the 'y'-axis value of the isotherm at which the maximum surface pressure occurs; and the corresponding 'x'-axis value represents the molecular area at the collapse of the monolayer (A_c). The higher the surface pressure value at collapse, more stable the monolayer is [113].

4.2 Results and Discussion

4.2.1 Compression isotherms of the pure component films

The Langmuir monolayer studies of the pure gemini surfactants were carried out at pH 4, 7, and 9 buffers (Table 4.1, Figure 4.1). From Table 4.1 and Figure 4.1A, at pH 4 we see that 16-7-16 possesses a higher initial surface pressure (~5 mN/m) and the isotherm started rising at a higher molecular area (250 Å^2). The monolayer underwent a gas (G) to liquid expanded (LE) phase transition in the region of ~5-23 mN/m surface pressure followed by a plateau in surface pressure at around ~23 mN/m. The exact reason for this expanded monolayer is not clearly understood; however, the intermolecular forces (hydrophobic interaction) between the alkyl tail groups of two adjacent 16-7-16 molecules may be responsible. The probable mechanism(s) will be discussed in the following sections. For 16-7-16, the isotherm shows an initial higher surface pressure of ~5 mN/m which indicates that the isotherm started rising at a higher molecular area (lift off area) compared to the base line. This further indicates that the interaction between two adjacent 16-7-16 molecules occurred right after the monolayer was spread on the subphase, even without starting the compression of the monolayer. At the gas phase, the molecules were lying flat on the air/buffer interface (see for example Figure 1.10 B(i)), and provided much larger area, and better hydrophobic interaction between alkyl tails of two adjacent 16-7-16 molecules. Chen et *al*. have shown that 18-s-18, s = 6, 8, 10, 12 surfactant also showed higher lift off areas, attributed to the fact that these molecules were lying flat on the water surface compared to ones with smaller spacer length (s < 6) [119]. This is in agreement with results obtained for the 18-Ar-18 surfactant, which showed a liftoff area of approximately 245 Å^2 at 25°C [217]. Due to the smaller spacer group, the steric hindrance between the two alkyl chains of gemini surfactants would affect their rotation around C-C bonds of the spacer. This phenomena disappears when the spacer length increases. Thus, if the spacer is made more rigid, there is a higher chance that the alkyl tail of the surfactant may remain slightly tilted as opposed to directly lying flat on the surface. This could result in a smaller liftoff area for such a surfactant, as the molecule would now occupy a smaller area on the surface [119]. This phenomena is schematically presented in the Appendix (Figure A4.1). At low pH, 16-7-16 possesses two positive charges, which may have strong interactions with the buffer subphase (water molecules and the acetate buffer components). Additionally, after compressing the monolayer, it reaches a saturation point (at a surface pressure ~23 mN/m) which is an indication of continuous micelle formation. More 16-7-16 molecules are squeezed out from the monolayer to the buffer subphase, where they can form micelles. Thus, there was no further increase in the surface pressure, instead a plateau was observed. Interestingly, the CMC value of 16-7-16 is much smaller than 16-7NH-16, which favors micelle formation (16 ± 9 x 10^{-6} M vs 150 ± 50 x 10^{-6} M, respectively) [35]. Consistent with this explanation, Chen et *al*. reported for the 12-6-12 surfactant that there was no surface pressure increase at the air/water interface during the compression of the monolayer. This was attributed to the dissolution of the surfactant in the aqueous medium [125]. In our case, the observed plateau at pH 4 was absent at higher pHs (7 or 9) indicating the importance of buffer components as well as the solubility on the monolayer behavior. Overall, the buffer component may play a crucial role in determining the trend (relatively condensed or expanded) of the isotherm at different pHs. A similar effect was observed for the 18-2-18 gemini surfactant on an aqueous subphase containing anions of the Hofmeister series or different divalent cations by Alejo et *al* [218]. Their study revealed that the presence of specific ions in the subphase may induce changes in the monolayer in the form of condensation or expansion. Further investigation is needed to properly understand the effect of buffer components on the nature of the isotherm of the 16-7-16 surfactant. It is important to mention that 16-7-16 monolayer mainly remained in the G-LE or LE phase. Several studies have demonstrated similar results in which the monolayer remains in the LE phase. For instance, both 18-3-18 [219] and 18-2-18 [218] showed only the LE phase before collapse at air/water interface, which implies that there was no appearance of phase condensation.

Table 4.1: Monolayer properties for the 16-7-16 and 16-7NH-16 surfactants, and DOPE at pH 4, 7, and 9 at the air/buffer interface.

System	pH	A_L (Å^2)	A_c (Å^2)	A_∞ (Å^2)	π_c (mN/m)	C_s^{-1}
16-7-16	*4	-	17	-	23.1	34.6
	7	111.6	35	66.4	36.5	57.7
	9	-	32.4	183.6	31.7	51.7
16-7NH-16	4	218.8	35.7	74.1	39.4	47.5
	7	139.9	53.1	88.6	40.1	77.9
	9	163	70.1	112.0	35.9	76.0
DOPE	4	173	35.2	127	40.9	56.7
	7	125.3	38.7	79.2	41.6	74.6
	9	118	56.2	84.0	46.3	123.5

Parameters obtained from the π-A isotherms are liftoff area, A_L; molecular area at collapse, A_c; collapse pressure, π_c; minimum cross sectional area or limiting area, A_∞ and maximum compressibility modulus, C_s^{-1}.* At pH 4 the isotherm reaches a plateau after around 17 mN/m surface pressure, therefore, it was not possible to get A_L, A_c, A_∞ or π_c values accurately.

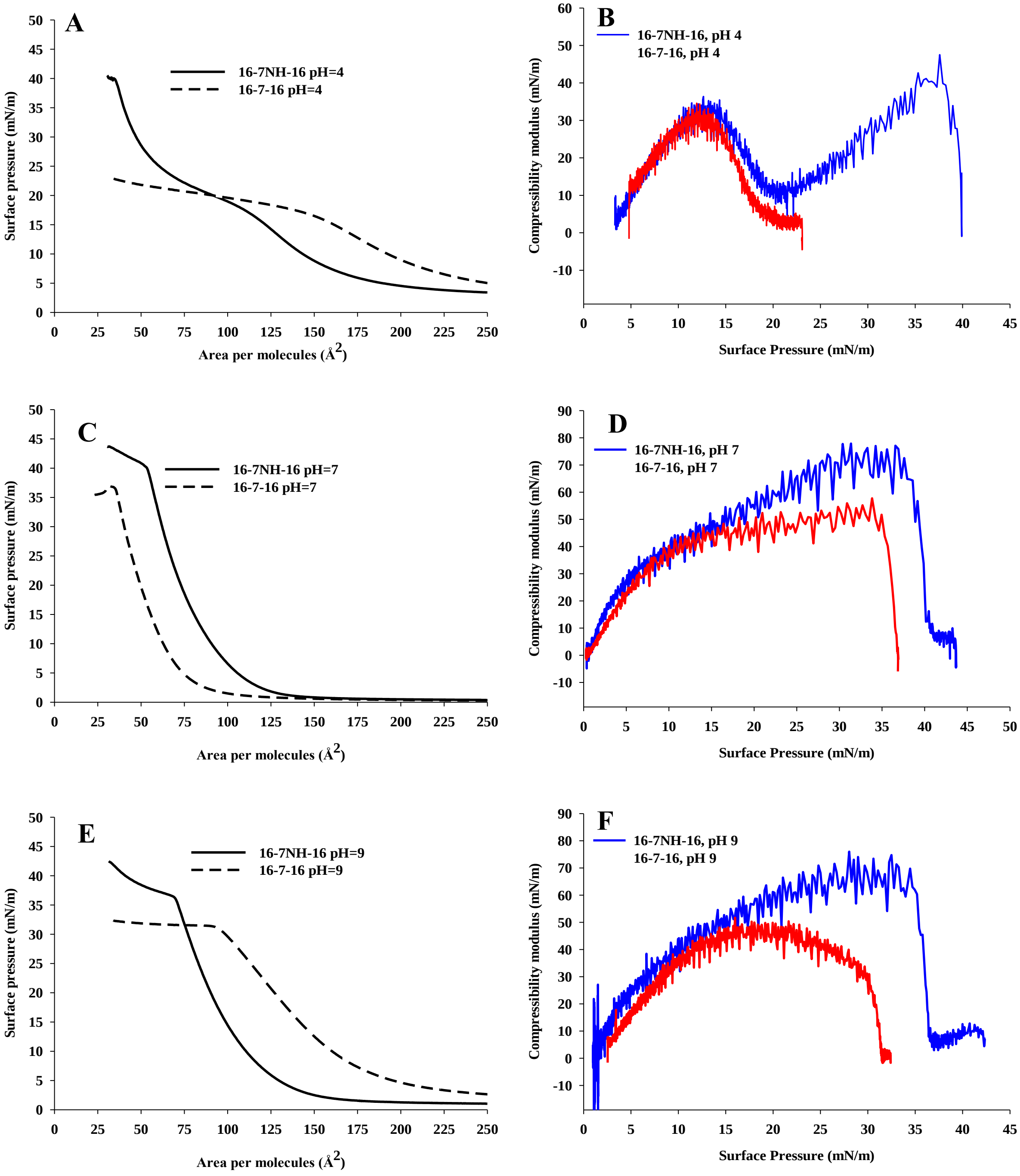

Figure 4.1. Comparison of π -A isotherm (A, C, and E) and compressibility modulus as a function of surface pressure (B, D, and F) for the gemini surfactant monolayers at pH 4 (A, B), pH 7 (C, D) and pH 9 (E, F) at 25°C.

On the other hand, 16-7NH-16 undergoes a gas to liquid expanded phase transition at a molecular area of ~218.8 Å^2 (Table 1 and Figure 4.1A). While further compressing the monolayer, 16-7NH-16 showed several phase transitions and reaches a maximum surface pressure of ~40 mN/m. We believe that 16-7NH-16 is protonated at pH 4, and contains three positive charges. This likely results in increased rigidity in the surfactant and forces the monolayer to adopt higher order phases i.e (LE, LC, etc.) reaching a surface pressure of 40 mN/m at collapse. Detailed explanation of this isotherm is mentioned in the following paragraph with compressibility modulus analysis.

As mentioned earlier the G and LE phases correspond to the $C_s^{-1} = \leq 12.5$, and 12.5-50 mN/m, respectively. As is observed from Figure 4.1B and 4.2A at pH 4, the 16-7-16 undergoes transition from a G to LE phase at around ~5-12 mN/m. Before the plateau of the isotherm, the monolayer reaches a LE phase (region A, Figure 4.2A). Then the monolayer returns to the gas phase and remains in gas phase until the maximum compression (region B, Figure 4.2A). Thus, 16-7-16 remains in G or G-LE phase. In contrast, from Figure 4.1B, it is observed that 16-7NH-16 exhibited distinct phase changes at various mean molecular area as well as surface pressure. To illustrate these phase changes more clearly, we can plot both compressibility modulus and surface pressure as a function of mean molecular area (Figure 4.2B), allowing a direct comparison between the two plots. We can divide the plot into 3 distinct regions, corresponding to different phases and phase transitions within the monolayer. In region A, the monolayer undergoes a G to LE phase with a maximum C_s^{-1} value of 36 mN/m at surface pressure around ~13 mN/m and molecular area of 131 Å^2. Afterwards, the compressibility modulus plot shows two distinct phase transition regions. For instance, at region B and region C shows the presence of LE→G and G→LE phase transitions, respectively. Additionally, comparing the 16-7-16 with 16-7NH-16 at pH 4 (in both Figures 4.1B and 4.2), both surfactants show similar phase transition up to the surface pressure of ~21 mN/m. Afterwards, the C_s^{-1} values for 16-7NH-16 increases with the increase in surface pressure and reaches a maximum surface pressure of 39.4 mN/m. However, 16-7-16 did not show this change in the surface pressure in the isotherm rather formed a plateau (Figure 4.1A and B). This result is consistent with the previously published results of 18-2-18 [218]. Overall, the results from the Figure 4.2 reveal that we cannot identify the phases accurately by relying only on the surface pressure isotherm. Based on a more detailed analysis of the compressibility modulus, it is apparent that there are alternative assignments of phases and transitions.

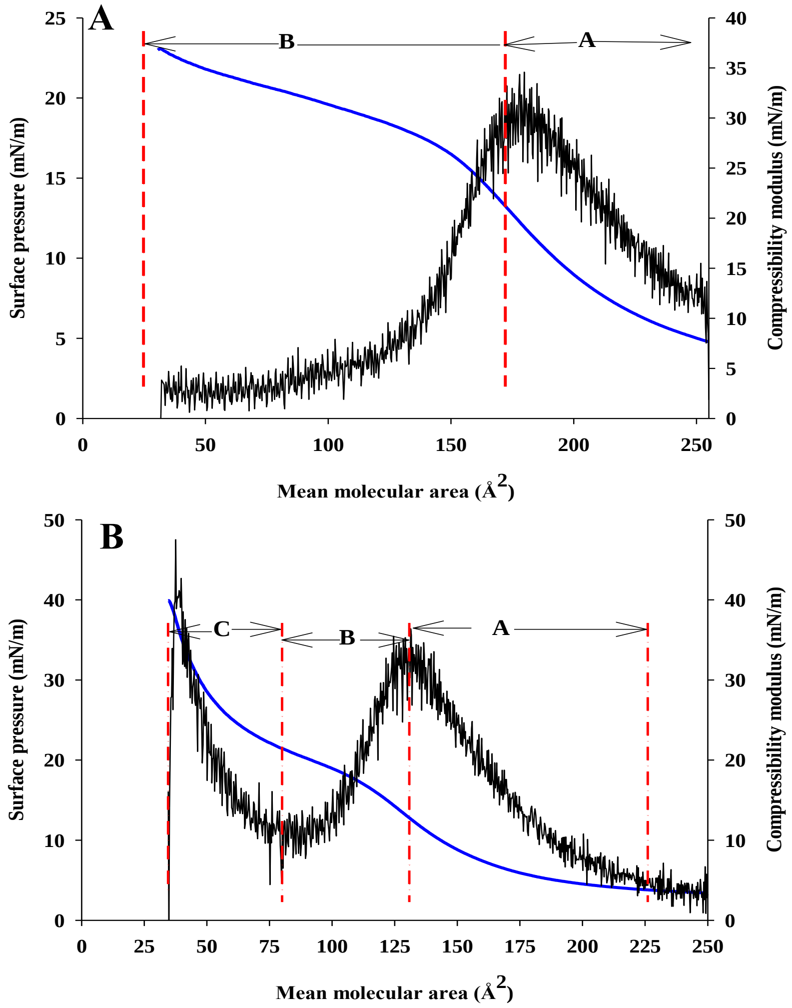

Figure 4.2. Surface pressure and compressibility modulus plotted as a function of mean molecular area of 16-7-16 (**A**) and 16-7NH-16 (**B**) monolayers at pH 4. The blue continuous line represents surface pressures and black line represent values of the compressibility modulus of both surfactants, respectively. The three regions of phase changes are indicated with A, B and C.

Precisely, from the Figure 4.2B it is observed that while compressing the 16-7NH-16 monolayer, it reaches a first maximum value of compressibility modulus (36 mN/m), and drops to a lower value afterwards (5 mN/m). This drop could be influenced by the negatively charged acetate (buffer component) which may have incorporated in between the 16-7NH-16 molecules to minimize the electrostatic repulsions (the phenomenon is schematically presented in the Appendix Figure A4.2). Until, a saturation point reaches between the charge neutralization by buffer component, the monolayer continues to change from LE → G phase, seen in region B of Figure 4.2B. At this point, a minimum in the compressibility modulus plot is observed. Due to the reduced repulsive forces brought about by neutralization of the head group charge by the presence of the acetate ions (CH_3COO^-) the 16-7NH-16 molecules are able to come closer to one another. This gives rise to the further increase in surface pressure and compressibility modulus shown in region C of Figure 4.2B. While this explanation can explain the features observed in the isotherm for 16-7NH-16 at pH 4, it is possible that the neutralization of head group charge is not complete. As such there is sufficient repulsion to keep the 16-7NH-16 monolayer from entering more compressed states, such as the LC or S phases. The same phenomena would not occur at higher pH values, or for the 16-7-16 surfactant, where the possibility of a third positive charge in the head group is not possible. Additionally, higher aqueous solubility of the 16-7-16 over 16-7NH-16 may also play a vital role in determining the isotherm behavior of the monolayers.

As can be seen from Table 4.1 and Figure 4.1C, 16-7-16 has a small liftoff area of ~ 111 Å^2 at pH 7, and an area at collapse (A_c) of 35 Å^2 at a collapse pressure of 36.5 mN/m. The monolayer undergoes G to LE phase transition at ~5 mN/m and remains in the LE phase until undergoing an LE-LC phase transition prior to collapse. The minimum cross sectional area (A_∞) is approximately 66.4 Å^2. This signifies a relatively condensed monolayer prior to collapse as compared to 183.6 Å^2, at pH 9. A_∞ is obtained by extrapolating the isotherm at the steepest slope prior to collapse back to zero surface pressure. This provides the cross sectional area of a hydrocarbon chain regardless of whether or not the compressed monolayer consists of close-packed vertically orientated chains. The smaller the value, the more closely packed the monolayer is [119]. At pH 9, the isotherm started rising at high molecular area, and then underwent a G to LE phase transition and remained mostly in the LE phase. At pH 9, the monolayer is more expanded than at pH 7. Several researchers have also reported similar expanded isotherms for the 18-s-18, s = 3,4,6,8,10,12 [54, 119]; 12-s-12, s = 3,4,6,8,10,12 [125]; 18-Ar-18 [217], gemini amphiphilic pseudopeptides [104], pH sensitive gemini amphiphiles of N,N_0-dialkyl-N,N_0-di(ethyl-phthalimide) ethylenediamines (Di-CnPh, n = 6, 8, 10, 12) [220], fluorinated gemini surfactants at different subphase pHs [116], and 18-2-18 with ions present in subphase [218]. Once again the buffer component (Na_2HPO_4) might have played a role in the relatively condensed monolayer at pH 7. Charge neutralization of the 16-7-16 molecules might have occurred which would have helped more molecules come closer together as a result of reduced repulsion. On top of that, the additional Na^+ ions present in the buffer subphase may induce repulsions between the N^+ atoms of the head group of the surfactant. Thus, 16-7-16 molecules remained at the air/buffer interface at pH 7 rather than undergoing rapid micellization (as observed at pH 4). Additionally, at pH 7 the maximum surface pressure of 36.5 mN/m is significantly higher than the values at pH 4 or 9, indicative of the stable monolayer formation. On the other hand, the 16-7NH-16 formed relatively condensed monolayers at both pH 7 and 9. At pH 7, the monolayer started rising at lower molecular area (139.9 Å^2) and reached a maximum surface pressure of 40.1 mN/m. The A_∞ for this isotherm is 88.6 Å^2, which is significantly smaller than at pH 9 (112 Å^2). The monolayer mostly remained at the LE-LC coexisting phase at pH 7 and 9. However, at pH 7, the monolayer is more condensed than at pH 9.

Monolayers having high values of surface pressure are generally observed to be more stable than those having low surface pressure [104, 113]. Overall, the surface pressure values obtained at collapse for the 16-7-16 follows the trend: pH7 > pH 9 > pH 4. Thus, the most stable monolayer was formed at pH 7 with a surface pressure of 36.5 mN/m. On the other hand, 16-7NH-16 follows the trend pH 7 ≥ pH 4 > pH 9, where both pH 4 and 7 produces the more stable monolayer with a surface pressure ~40 mN/m. At pH 4, the 16-7NH-16 underwent several phase changes which did not occur at other pHs. The exact reason for this is not clear; however, it can be hypothesized that at low pH, 16-7NH-16 becomes protonated, having 3 positive charges in the head-group, creating more electrostatic repulsion between the head groups of the 16-7NH-16 molecules at the air/buffer interface. Such an argument further supports that at pH 4, 16-7NH-16 forms a liquid expanded phase, and the rigidity of the monolayer is lower than that of pH 7 and 9.

While comparing the C_s^{-1} at pH 7, 16-7-16 remains mainly at LE phase (Figure 4.1D). To better understand the results we have presented the compressibility modulus as a function of the mean molecular area in Appendix Figure A4.3(a). However, before the collapse pressure the monolayer showed the LE-LC coexisting phase (at the surface pressure of ~29-34 mN/m). The maximum C_s^{-1} values for this surfactant at pH 7 is 57.7 mN/m (Table 4.1). This value is slightly higher than the values of indicative LE phase (12.5-50 mN/m) [118, 215]. This implies that even at higher pH, 16-7-16 still remains at expanded state with less compaction of the monolayer. On the other hand, 16-7NH-16 showed LE phase at ~2-15 mN/m (Figure 4.1D, Appendix Figure A4.3(a)). And after this surface pressure, the monolayer remains in the LE-LC coexistence phase with the C_s^{-1} values ranges from 50-77.9 mN/m. The higher compressibility modulus values for 16-7NH-16 compared to 16-7-16 signifies that 16-7NH-16 forms a more rigid, and compacted monolayer. At pH 7 the 16-7NH-16 molecule possesses two positive charges compared to three positive charges at pH 4. Thus, the net repulsion between two adjacent 16-7NH-16 molecules reduced and allows for more molecules to come closer and form a relatively rigid monolayer.

At pH 9, the maximum C_s^{-1} was observed to be 51 mN/m at a surface pressure of 16 mN/m for 16-7-16 (Figure 4.1F and Appendix Figure A4.3(b)). As for pH 7, the 16-7-16 monolayer only appears to reach the LE phase, with no significant transition to more compressed phases. Above a surface pressure of ~16 mN/m the compressibility modulus drops until collapse of the monolayer, which signifies that monolayer undergoes LE-LC→LE phase transition and remained at the LE phase (Appendix Figure A4.3(b)). Thus, 16-7-16 showed a steady LE phase throughout the compression of the monolayer. In comparison, 16-7NH-16 showed LE-LC coexisting phase transition at the surface pressure ranging from 14 mN/m toward collapse (Figure 4.1F and Appendix Figure A4.3(b)). C_s^{-1} values are similar at pH 7 and 9. Thus, the presence of two positive charge at 16-7NH-16 exhibits less repulsion forces between two 16-7NH-16 molecules, and formed more condensed monolayer compared with the values at pH 4 (protonation). Overall, the C_s^{-1} for 16-7NH-16 follows the trend pH 7 ≥ pH9 > pH4.

4.2.2. Minimum cross sectional area or limiting area of the pure system

As mentioned earlier, the smaller the value of limiting area, more closely packed the monolayer is [119]. It is observed from our studies that the 16-7NH-16 monolayer mostly remains in LE or LE-LC phase, and the limiting area is high in all cases. This signifies that most of the molecules are not oriented vertically to the subphase, rather tilted towards the subphase, giving rise to the higher values of mean molecular area. Similar phenomena is also observed for 16-7-16 monolayers. The head group area (a_0) for the 16-7-16 and 16-7NH-16 are 8.9 and 13.3 Å^2, respectively, and the alkyl tail length (*l*) is calculated at around 21.74 Å^2 for these surfactants [200]. Therefore, if the surfactant molecules remain perfectly vertical to the subphase, one could expect that the molecular size of the experimental 16-7-16 or 16-7NH-16 to be less than 30 Å^2. Moreover, if the monolayer is in a true LC or solid phase, the limiting area would also be near that value. Therefore, our compressibility modulus results (Figure 4.1B, D and F) correlates with the mean molecular area results. Similar results were observed for 18-2-18 series with a limiting area of 124 Å^2 in air/water interface [218]. With the 18-s-18 surfactants, increasing the spacer length from 18-3-18 to 18-10-18 increased the liming area from 128 Å^2 to 236 Å^2, respectively in air/water interface [54]. It was further reported that presence of DNA in the subphase substantially changed the limiting area. This was attributed to the expansion or contraction of the isotherm depending on the length of the spacer. Overall, their study suggests that there was complex monolayer formation between the gemini surfactant and the DNA on subphase which will be further discussed in later section.

4.2.3. Isotherm of the pure DOPE

From Figure 4.3A it can be seen that, similar to the gemini surfactants discussed in the previous section, pure DOPE also exhibits pH dependent monolayer formation. The liftoff area (Table 4.1) was much higher at pH 4 than at pH 7 or 9. At pH 4, the monolayer reaches a maximum surface pressure of ~40.9 mN/m with large minimum cross sectional area of ~127 Å^2 (Table 4.1). This signifies that the monolayer is relatively expanded than with the higher pHs. At pH 7, the maximum surface pressure of the monolayer is similar with pH 4. However, the minimum cross sectional area was ~79.2 Å^2. This signifies that DOPE forms a more condensed monolayer at pH 7. At pH 9, the monolayer reaches a maximum surface pressure of ~46.3 mN/m, which is relatively higher than pH 4 and 7. The minimum cross sectional area for this monolayer is ~84 Å^2, which is comparable with pH 7.

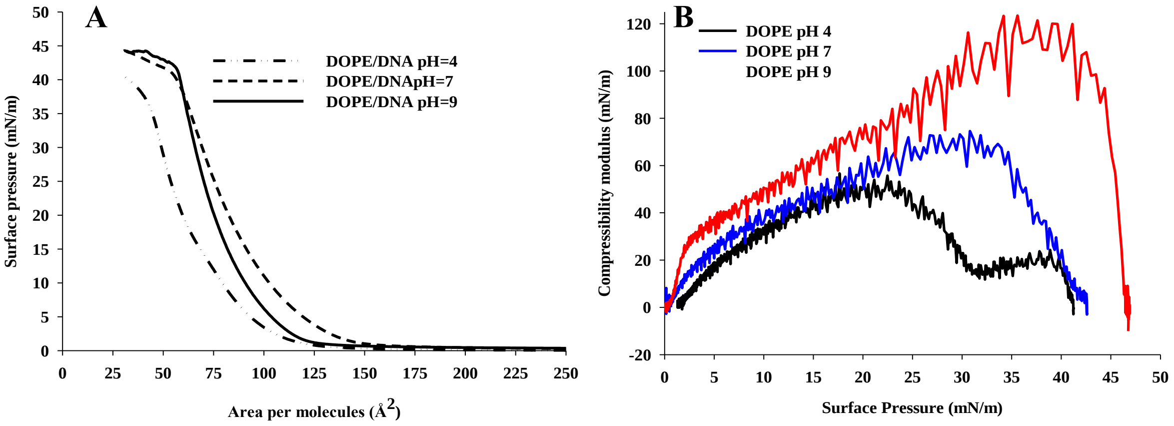

Figure 4.3. Comparison of π-A isotherm (A) and compressibility modulus as a function of surface pressure (B) of pure DOPE monolayers at different pHs at buffers at 25°C.

From the compressibility modulus results for DOPE (Figure 4.3B), at pH 4 we observe a G-LE phase transition at a surface pressure between ~1 to 5 mN/m, followed by an LE-LC coexistence phase, can be inferred at the maximum of the peak in C_s^{-1} (i.e. an approximately constant compressibility modulus), at surface pressures of ~19 – 23 mN/m, followed by a return to the LE phase. At pH 7, no decrease in compressibility modulus is observed, and the DOPE monolayer remains in the LE phase, evidenced by the maximum C_s^{-1} value of ~74.6 mN/m. Interestingly, at pH 9, the monolayer undergoes a sharp G to LE phase in the range of ~0-10 mN/m surface pressure followed by a transition from LE → LE-LC phase up to a surface pressure of ~27 mN/m. At higher surface pressures this monolayer reaches a LC phase with a maximum C_s^{-1} values of 123.5 mN/m.

Based on the compressibility modulus values, the overall rigidity of the monolayer was governed at the following trend pH 4 < pH 7 < pH 9 with monolayers found in the LE phase, the LE-LC phase, or the LC phase, respectively.

From the chemical structure (chapter I, Figure 1.26), it is evident that DOPE is a neutral, zwitterionic phospholipid with an amphiphilic character [221]. Therefore, at different pHs it can participate in equilibrium reactions with both hydrogen ions and hydroxyl anions. As a result of adsorption of H^+ and OH^- ions on the surface of DOPE layer, the DOPE molecule can exist in three different forms:

$$\mathrm{DOPE} + \mathrm{H}^+ \leftrightarrow \mathrm{DOPE\text{-}H}^+$$

$$\mathrm{DOPE} + \mathrm{OH}^- \leftrightarrow \mathrm{DOPE\text{-}OH}^-$$

$$\mathrm{DOPE} + \mathrm{HOH} \leftrightarrow \mathrm{DOPE\text{-}HOH}$$

A similar mechanism was reported for the phosphatidylethanolamine monolayer at air/water interface [222]. Thus, in our case, at pH 4, DOPE can have an additional positive charge on the amine group, resulting in increased electrostatic repulsions and expanded monolayer formation. At pH 7 this charge would not be present, allowing for formation of a less expanded monolayer, in our case, one likely in an LE-LC coexistence phase.

The exact reason for the condensed monolayer formation at pH 9 is not clear. However, we hypothesized that at pH 9, DOPE may possess a negative charge. Additionally, we have used $NaHCO_3$ as buffer component to prepare the pH 9 buffer. Apart from the production of OH^- anions, the buffer also contains a large amount of Na^+ ions. If DOPE is negatively charged at pH 9 due to the adsorption of the OH^- ions, it is possible that the Na^+ ions are adsorbed at the monolayer. This combined effect of cations and anions present in the sub-phase may have reduced the overall repulsion forces allowing DOPE molecules to come closer together. The exact extent of the effect of buffer species on the formation of DOPE monolayers is unknown. Further studies are required to understand this effect by varying the buffer components (using different anions and cations). In support of this argument, Alejo et *al* have previously reported that the 18-2-18 gemini surfactant showed condensed monolayer as the anions of the buffer subphase compensated the electric charges of the surfactant adsorbed at the air-water interface [218]. Additionally, the size of the divalent cations impacted the overall monolayer trend. As the size of the divalent cations increased from $Mg^{2+} < Ca^{2+} < Sr^{2+} < Ba^{2+}$, a more condensed monolayer was formed. Their results further indicate the importance of cations on the subphase with respect to changes in monolayer phase behavior. Additionally, Xu et *al.* have reported the importance of cations on the structural behavior of molecules at the air/water interface [223, 224]. Overall, these studies signifies that buffer components have substantial impact on the monolayer phase behavior.

In general, the effect of pH on the conformation changes of DOPE is well known. Interestingly, our experimental results also shows that at lower pH values of C_s^{-1} values are relatively small indicating more fluidic monolayer. Moreover, DOPE has similar collapse pressures (π_c) at pH 4 and 7, with a higher value at pH 9. This suggests DOPE forms a more stable monolayer at pH 9 and relatively less stable monolayers at lower pHs.

4.2.4. Brewster Angle Microscopy (BAM) of the pure components

BAM is an effective technique to determine the surface structure of monolayers spread on an aqueous subphase at various surface pressures. BAM images at various surface pressures and pH values are shown in Figure 4.4 for the 16-7-16 surfactant; additional images can be found in Appendix Figure A4.4, 4.5 and 4.6. In Figure 4.4, it can be seen that at all surface pressures and pHs, no significant domain formation occurred for the 16-7-16 surfactant. It has previously been reported that these types of images, combined with the Langmuir isotherms obtained for 16-7-16, are indicative of the LE or G-LE phase (dark images) [220, 225]. Similar BAM images were obtained for the 18-2-18 surfactant in the G or G-LE phase [218]. Images obtained for 16-7NH-16, again at representative surface pressures at each pH, show evidence of much more interesting phase behaviour (Figures 4.5 and 4.6; additional images found in Appendix Figure A4.7, 4.8 and 4.9). At pH 4 the images are again generally featureless and dark, consistent with the G-LE or LE phase [220]. In some images very bright, large spots can be observed; these types of features are typically associated with dust particles and are not representative of any specific domain formation. Interestingly, at pH 4, no evidence of the higher order phase transitions seen in the surface pressure isotherm (Figure 4.1B) are detected using BAM. Thus, the BAM images at pH 4 is consistent with the compressibility modulus values presented in Figure 4.1B and Figure 4.2a (presence of LE or G-LE phases).

At higher pHs and higher surface pressures, i.e. ≥ 35 mN/m at pH 7 and ≥ 40 mN/m at pH 9, significant and heterogeneous domains are observed for 16-7NH-16 (Figure 4.6) as evidenced by the bright ribbon and dot-like or island features observed in the BAM images. These bright domains are consistent with more ordered structures (possessing a greater difference in refractive index as compared to water), and are consistent with the higher compressibility modulus values obtained for 16-7NH-16 (Figure 4.1 and Table 4.1). From these results, we conclude that the 16-7NH-16 surfactant, at higher pH values, is forming more organized monolayers, likely the LE-LC coexistence or LC phases.

Finally, images for pure DOPE monolayers at pH 4, 7 and 9 are shown in Figure 4.7 (additional images found in Appendix Figure A4.10, 4.11 and 4.12). At very low surface pressures (0.11-2 mN/m), at all pH values, small bright domains consistent with a mixed G – LE phase can be observed. Given that DOPE has very limited solubility in water, and does not form micelles, but rather vesicles (with some energy input), the DOPE molecules have no other means of minimizing unfavourable solvation energies, other than film formation. As such, domains are observed at these low surface pressures. This is in contrast to the case for the surfactants, where some of the observed dark images may be due not only to a very heterogeneous G-LE phase, but also to a depletion of the monolayer by micelle formation occurring in the bulk. As the DOPE film is further compressed additional domain formation can be observed, consistent with the formation of LE and/or LC phases, as observed from the compressibility modulus results (Figure 4.3B).

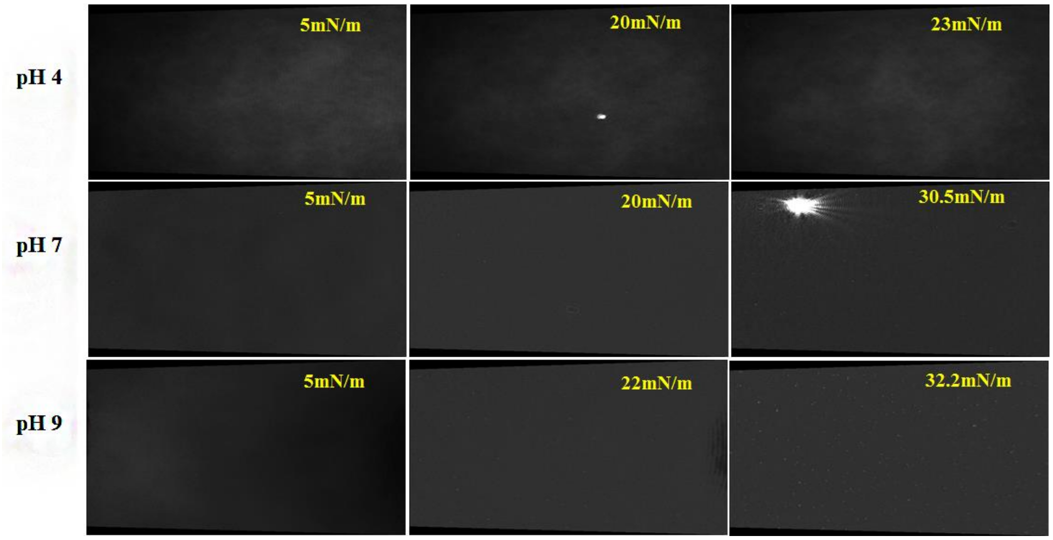

Figure 4.4. BAM image of 16-7-16 in different pHs at selected surface pressures.

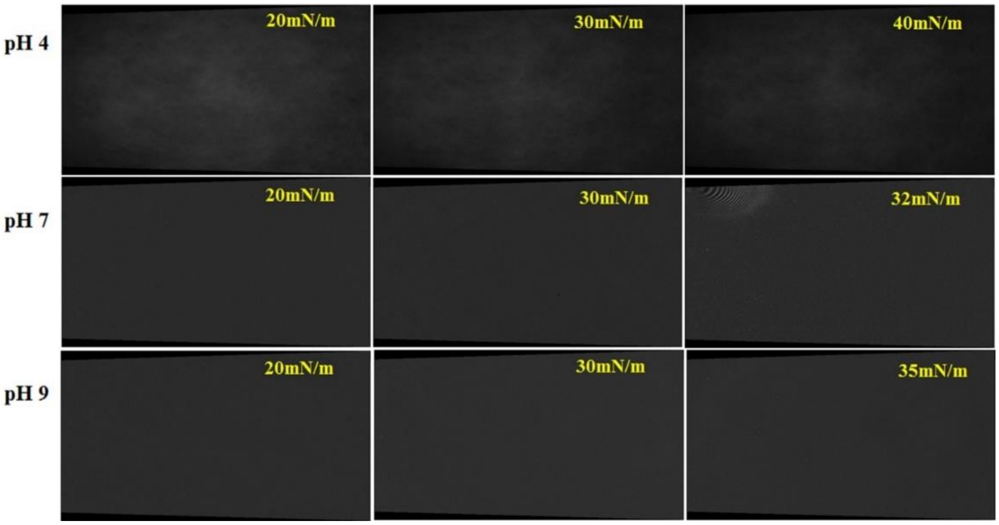

Figure 4.5. BAM image of 16-7NH-16 in different pHs at selected surface pressures.

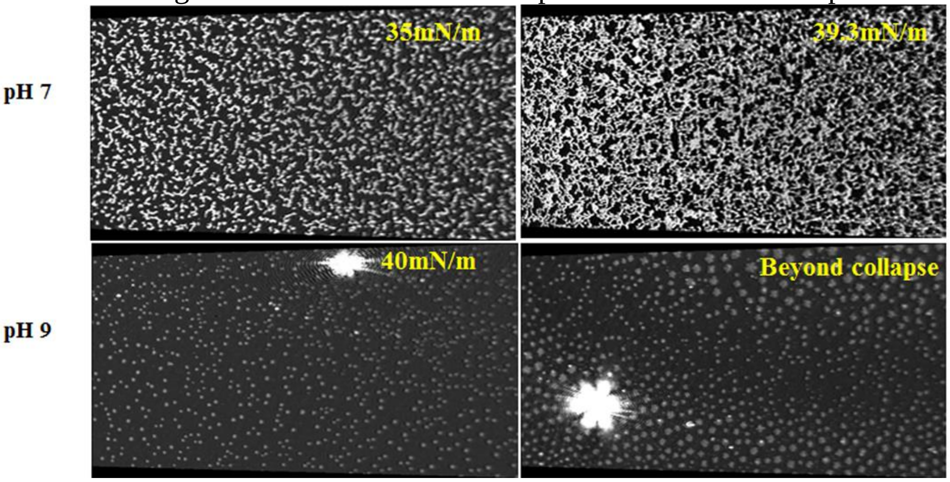

Figure 4.6. BAM image of 16-7NH-16 in pH 7 and 9 at selected surface pressures.

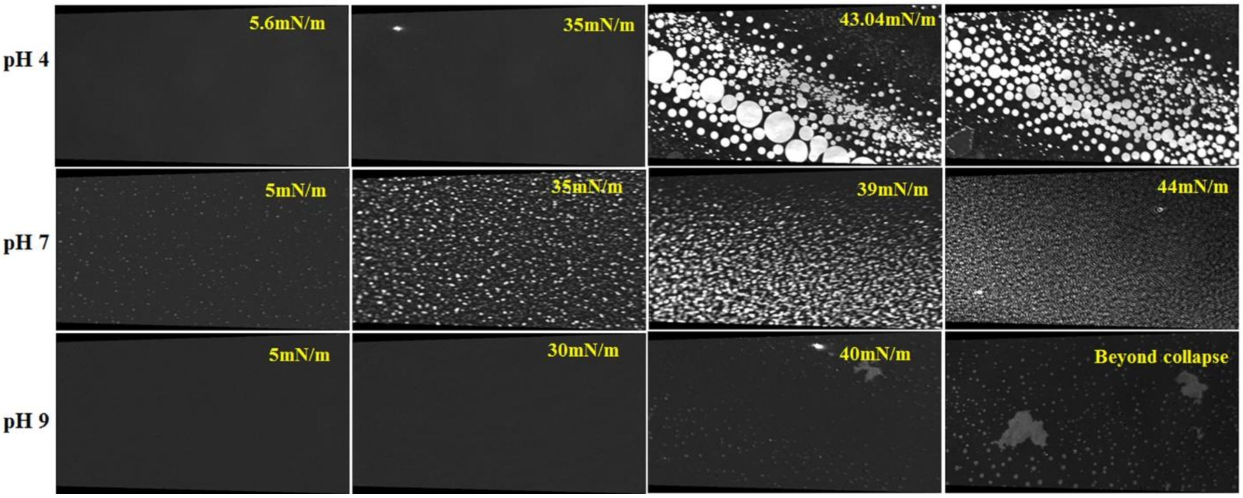

Figure 4.7. BAM image of DOPE in different pHs at selected surface pressures.

4.2.5. Gemini Surfactant/DOPE mixed monolayers

Studies have shown that the presence of the helper lipid DOPE may increase the transfection efficiency of gemini based lipoplexes by approximately 10 fold [35] . This is attributed to the fact that the addition of pure DOPE causes formation of mixed aggregates with higher (greater than unity) packing parameter; shifting micelle systems towards vesicles, and vesicle systems toward the inverted hexagonal or even cubic phases [35]. In addition, DOPE is thought to increase the fluidity of cellular membranes and thus facilitates the penetration of genetic materials into the cell. Furthermore, DOPE has been reported to help in disruption of the endosomal membrane, again by increasing membrane fluidity, at the endosomal escape phase leading to increased transfection efficiency [226-231].

Table 4.2: Monolayer properties for the mixed gemini surfactant/DOPE monolayers, at pH 4, 7, and 9 at 25°C at the air/water interface.

	pH	A_L (Å^2)	A_c (Å^2)	A_∞ (Å^2)	π_c (mN/m)	C_s^{-1}
16-7-16/DOPE	4	156	39.8	128	41.3	59.6
	7	136.7	57	92	42.5	101
	9	147	61.8	100	42.1	90.7
16-7NH-16/DOPE	4	123.5	45.6	96	43.5	74.9
	7	116.7	55.4	88	45.3	109.1
	9	117.2	56	88	43.7	101.9
DOPE/DNA	4	120.4	33	76	40	65.0
	7	146.8	54	104	41.1	71.0
	9	127.9	55.6	89	42	93.3
DOPE	4	173	35.2	127	40.9	56.7
	7	125.3	38.7	79.2	41.6	74.6
	9	118	56.2	84.0	46.3	123.5

Parameters obtained from the π-A isotherms are liftoff area, A_L; molecular area at collapse, A_c, collapse pressure, π_c, minimum cross sectional area or limiting area, A_∞ and maximum compressibility modulus, C_s^{-1}.

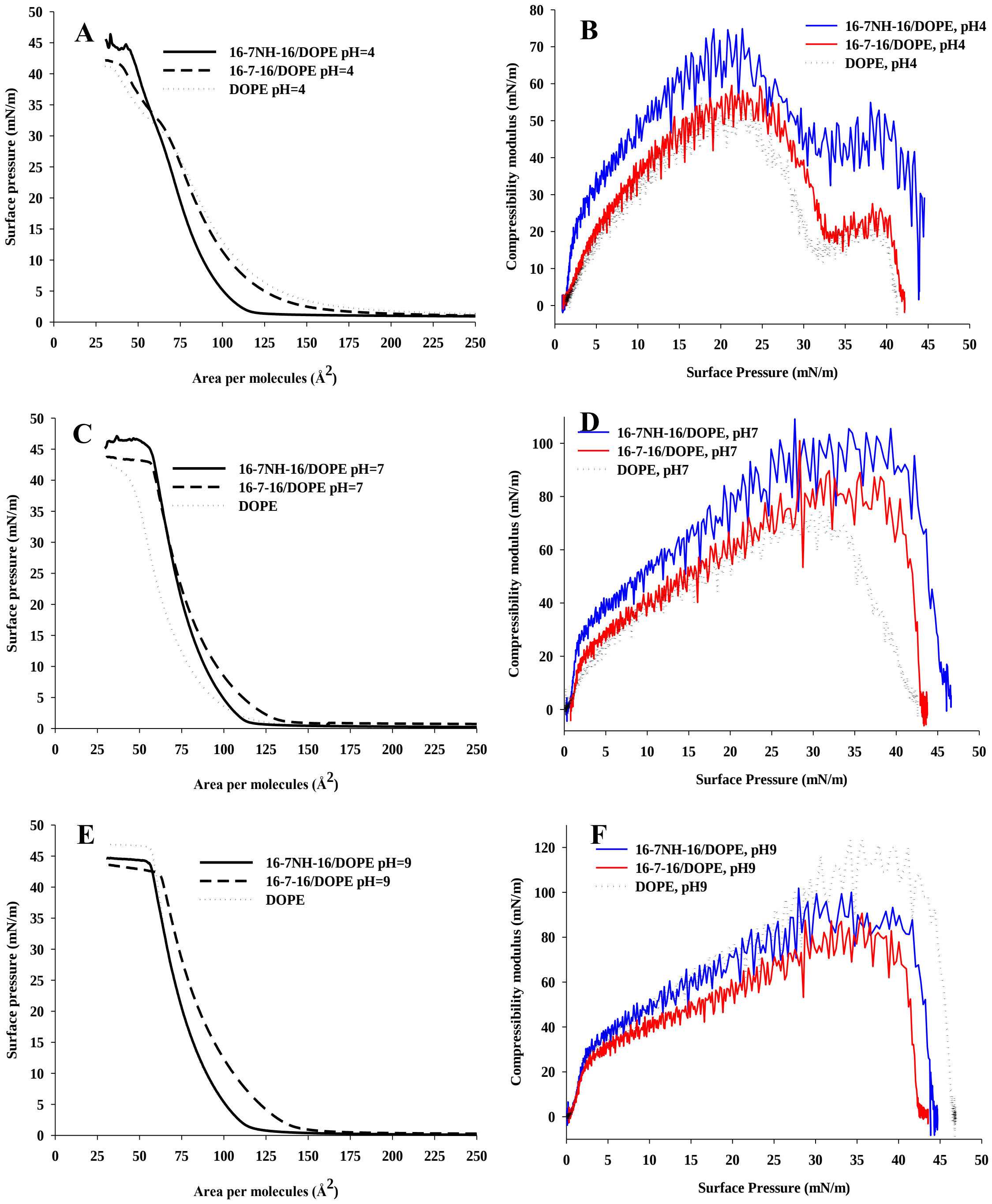

Figure 4.8. π -A isotherms (A, C, and E) and compressibility modulus as a function of surface pressure (B, D, and F) for the mixed gemini surfactant/DOPE monolayers at pH 4 (A, B); pH 7 (C, D); and pH 9 (E, F) at 25°C.

Figure 4.8 shows the isotherms and compressibility moduli for the mixed gemini surfactant/DOPE monolayers. In all cases, very different behaviour is observed as compared to the gemini surfactant monolayers alone (described in the previous section), with the isotherms now looking very similar to those obtained for pure DOPE. It would appear, at first glance, that the monolayer structure is being defined by DOPE and not the gemini surfactant. At pH 4, the lift off area and collapse pressure for the 16-7-16/DOPE are approximately 156 Å^2 and 41.3 mN/n which are comparable to values for pure DOPE; 173 Å^2 and 40.9 mN/m. The observed isotherm and the C_s^{-1} plots reveal that the mixed monolayer undergoes similar G-LE →LE→LE-LC phase transitions that are seen for pure DOPE at pH 4. This indicates that there is in fact no substantial interaction between DOPE and 16-7-16 at pH 4. This is consistent with previous work in our lab, where an analysis of mixed aggregate formation between gemini surfactants and DOPE demonstrated that they interact antagonistically, i.e. the molecules prefer to form pure surfactant and pure lipid aggregates, rather than mixed aggregates [200]. The 16-7NH-16 surfactant appears to have somewhat more of an effect on the DOPE monolayer, at pH 4, with a smaller lift off area (123.5 Å^2) and a higher collapse pressure (43.5 mN/m) that for the pure DOPE monolayer. Both the isotherm and the compressibility modulus show subtle changes that signifies that 16-7NH-16/DOPE forms a more condensed monolayer than 16-7-16/DOPE system at pH 4. At pH 7 and 9, the similarities between the mixed monolayers, and the pure DOPE monolayer are even more pronounced, with the 16-7-16/DOPE isotherm and compressibility modulus plots nearly overlapping those for the pure DOPE system (Figures 4.8 C, D, E, and F). For both mixed surfactant/DOPE monolayers, the isotherms and compressibility moduli suggest the systems remain mostly within the LE, LE-LC, or LC phases, depending upon pH and surface pressure.

The BAM images for the 16-7-16/DOPE system show homogeneous film formation at pH 4 without any substantial domain formation at higher surface pressure (Figure 4.9, additional images are in Appendix Figure A4.13). Similar BAM images was observed for the 16-7NH-16/DOPE system at pH 4 (Figure 4.9, additional images are in Appendix Figure A4.14). In general, the BAM images at pH 4 are indicative of LE or LE-LC phase transition. 16-7-16/DOPE at pH 7 and 9, showed similar BAM images (Figure 4.10 and 4.11, Appendix Figure A4.15 and A4.17). At higher surface pressure the monolayer showed some small domains. On the other hand, 16-7NH-16/DOPE showed some interesting domains at higher surface pressure (Figure 4.10 and Appendix Figure A4.16) at pH 7. If we compare the pure DOPE BAM images (Figure 4.7) and this mixed system, it is apparent that both of them showed bright domains at higher surface pressure in pH 7. Thus, domains might be formed from the DOPE system. At pH 9, 16-7NH-16/DOPE showed initial network like domains at the G-LE phase, which was merged together and formed homogeneous film until collapse (Figure 4.11 and Appendix Figure A4.18).

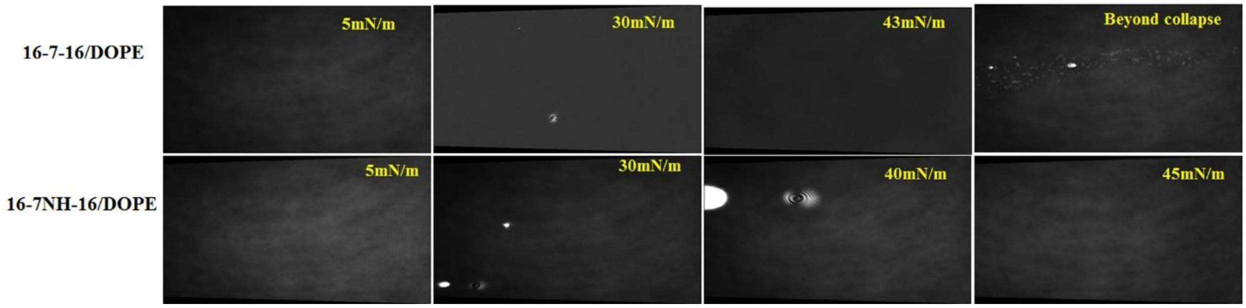

Figure 4.9. BAM image of 16-7-16 and 16-7NH-16/DOPE at pH 4 at selected surface pressures.

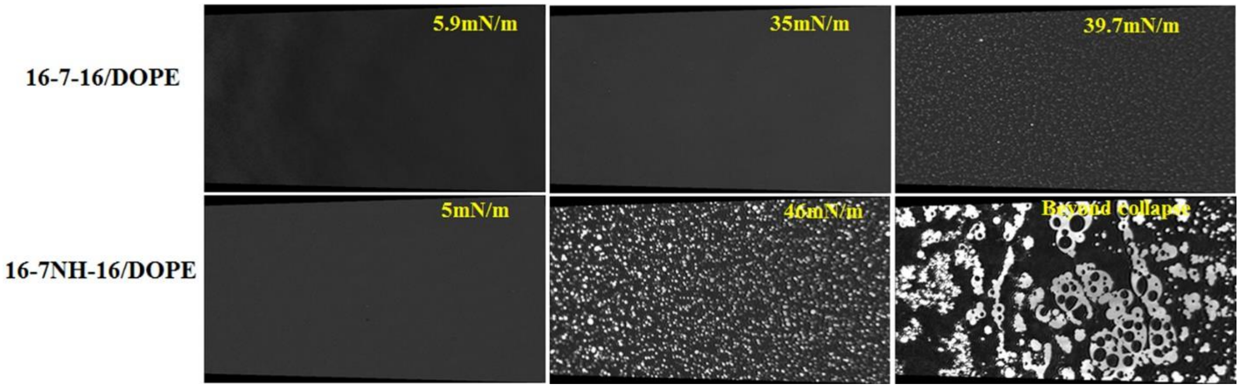

Figure 4.10. BAM image of 16-7-16 and 16-7NH-16/DOPE at pH 7 at selected surface pressures.

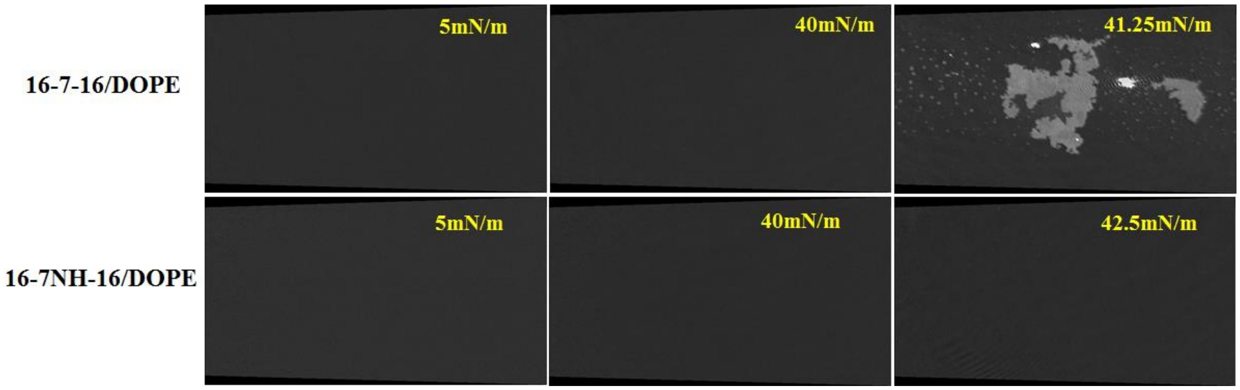

Figure 4.11. BAM image of 16-7-16 and 16-7NH-16/DOPE in pH 9 at selected surface pressures.

4.2.6. Gemini surfactant/DNA mixed monolayers

The π -A isotherms and compressibility modulus plots for the mixed gemini surfactant/DNA monolayers indicate that DNA has a pronounced effect on the nature of monolayer, with distinct differences again observed as a function of pH. At pH 4, it is observed that 16-7-16/DNA monolayer has a non-zero initial surface pressure (similar to what was observed for the pure 16-7-16 monolayer, Figure 4.1A) and reaches a maximum value of around 36.6 mN/m. The monolayer undergoes a G to LE phase transition in the surface pressure range of ~2-21 mN/m at which point the behaviour becomes quite different from that for the pure 16-7-16 isotherm. At a surface pressure of ~ 25 mN/m, a distinct plateau is observed over a molecular area range of ~118 to 52 Å^2 (Figure 4.12 A). From compressibility modulus (Figure 4.12 B) this corresponds to a sudden drop in C_s^{-1}. This sudden drop might be explained based on the equation 4.1. (compressibility modulus); which signifies that if there is no changes in surface pressure the compressibility modulus values becomes zero. Noteworthy, the compressibility modulus value may be misleading at the plateau region and the results are artifact obtained from the equation. At this stage only change one can expect is the mean molecular area. Thus, to explain the plateau we have to assign the mean molecular area as a determining factor of monolayer behavior without any substantial changes in the surface pressure. Since the mean molecular area at this plateau decreased from 118 to 52 Å^2, this indicates much compacted monolayer formation at this range. Thus we hypothesized that the plateau is LE-LC coexisting phase. With the exception of minor differences in the surface pressure associated with the transitions, the same behaviour is observed for the 16-7NH-16/DNA monolayer, and a key difference in that the 16-7NH-16/DNA monolayer does enter an LE-LC phase with the compressibility modulus value of ~64 mN/m before collapse (Table 4.3).

Unsurprisingly, we believe that the observed plateau is likely due to the strong electrostatic interactions between the positive charge of the nitrogen atoms of the gemini surfactant and the negative charge of the phosphate groups of the DNA molecules. We hypothesized that in the plateau region, the DNA molecules are adsorbed at the positively charged gemini monolayer due to the electrostatic interaction. Further compressing the monolayer, the gemini molecules come closer and provides increased interaction with the DNA molecules. However, the adsorption of DNA reaches a saturation point, beyond which no more interaction is possible. This could be induced by the mechanical forces of the barrier which surpasses the electrostatic interaction between gemini and DNA; consequently, the isotherm started rising to reach to the collapse. Similar results were observed for the 16-3-16 system at air/water interface (data not shown). Interestingly, no plateaus are observed at pH 7 for either the 16-7-16/DNA or 16-7NH-16/DNA monolayers, and they appear to transition smoothly from the gas phase (G) through the LE phase to remain at the LE or possibly LE-LC phase with a maximum compressibility modulus value of around 65.4 and 75.5 mN/m (Table 4.3), respectively (Figure 4.12C and D). The BAM images obtained for both the 16-7-16/DNA and 16-7NH-16/DNA at pH 4 are again consistent with the system remaining in a G – LE transition state (Figure 4.13), while those at pH 7 are show the more highly ordered domains indicated by the isotherm and compressibility modulus data.

At pH 9, the 16-7-16/DNA system appears to undergo multiple, small, phase transitions between ~20 mN/m to 33 mN/m surface pressure (Figure 4.12 E and F). The monolayer mainly remains in a G – LE or LE phase at these surface pressures. While the BAM images (Figure 4.15) are consistent with this, they unfortunately offer no insight into the multiple, weak, transitions seen in both the isotherm and compressibility plots. The 16-7NH-16/DNA monolayer appears to have a phase behaviour very similar to what was observed at pH 4 (comparing Figure 4.12 A and B with E and F), again possibly reaching an LE–LC coexistence phase. With the 18-s-18 surfactants, increasing the spacer length from 18-3-18 to 18-10-18 increased the limiting area from 12.8 Å^2 to 3.6 Å^2, respectively in air/water interface [54]. It was further reported that presence of DNA in the subphase substantially changed the limiting area. This was attributed to the expansion or contraction of the isotherm depending on the length of the spacer. Overall, their study suggests that there was a complex monolayer formation with the gemini surfactant and the DNA on subphase which will be further discussed in later section. Additionally, Chen et *al.* shows the expansion of the gemini monolayer upon addition of DNA [125]. Relatively, expanded monolayer was also reported for the ester polar head group containing fluorinated gemini surfactant than the carboxylic acid head group containing gemini surfactant in presence of DNA on the subphase [116]. As can be seen from Figure 4.13 (additional images are provided in Appendix Figure A4.19 and A4.20), BAM images illustrates the presence of LE phase transition for the 16-7-16/DNA system in pH 4 which is consistent with the observed isotherm and compressibility modulus results (Figure 4.12A and B). Similar BAM images are observed for the 16-7NH-16/DNA monolayer at pH 4 (Figure 4.13). From Figure 4.14 (additional images are presented in Appendix Figure A4.21 and A4.22), it can be seen for the 16-7-16/DNA system that at higher surface pressure around > 25 mN/m, the smaller domains increased in size and brightness are observed which is an indication of the LE-LC phase. In the same pH, 16-7NH-16/DNA system also formed homogeneous film with the presence of LE-LC phase at higher surface pressure (Figure 4.14). Likewise, the presence of LE phase is observed for the 16-7-16/DNA monolayer at pH 9 (Figure 4.15, additional images are in Appendix Figure A4.23 and A4.24). For the 16-7NH-16/DNA system a homogenous film with LE-LC phase was observed at higher surface pressure at pH 9 (Figure 4.15). Overall the BAM images are consistent with the observed isotherm and compressibility modulus results (Figure 4.12).

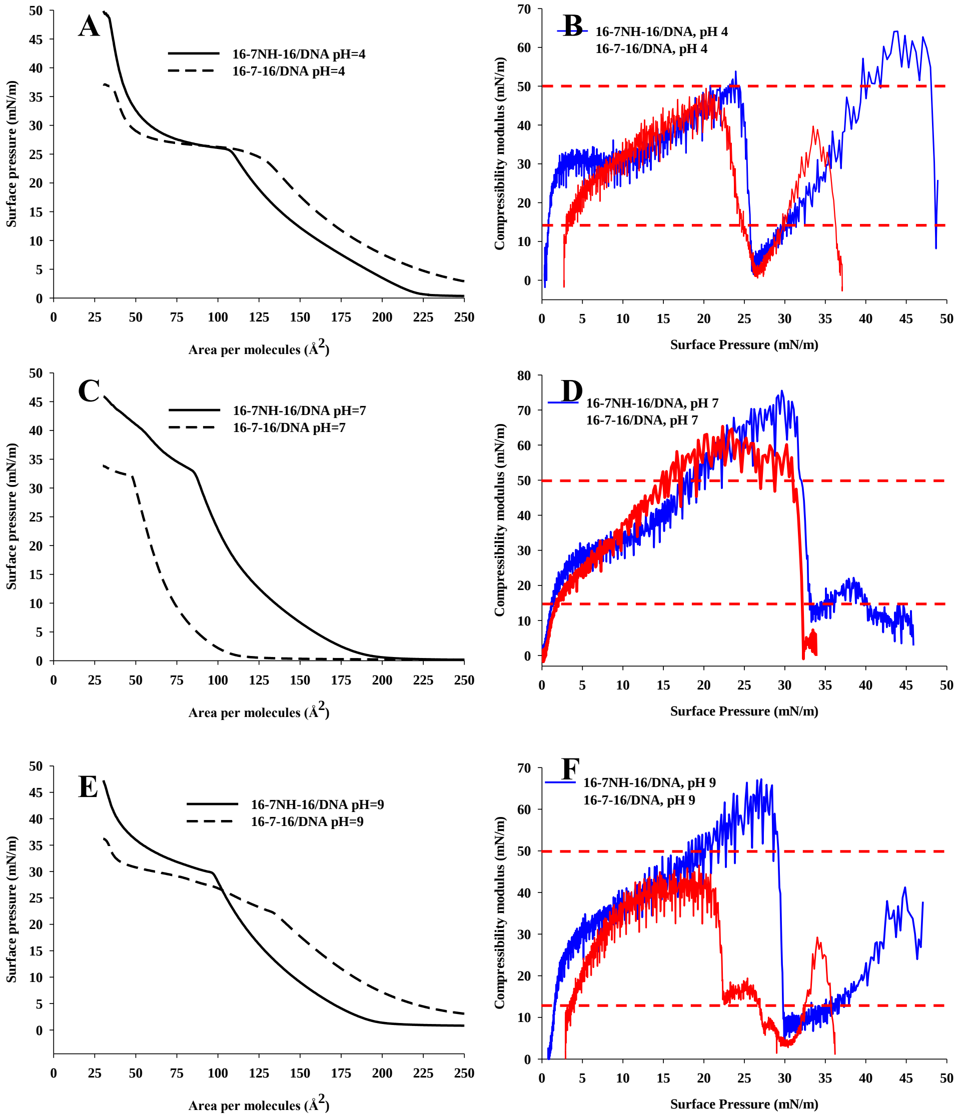

Figure 4.12. π-A isotherms (A, C and E) and compressibility modulus as a function of surface pressure (B, D, and F) for the mixed gemini surfactant/DNA monolayers at pH 4 (A, B); pH 7 (C, D); and pH 9 (E, F) at 25°C. The red dashed line in B, D and F indicates the region of LE phase.

Table 4.3: Monolayer properties for the mixed gemini surfactant/DNA monolayers at various pHs.

System	pH	A_L (Å^2)	A_c (Å^2)	A_∞ (Å^2)	π_c (mN/m)	C_s^{-1}
16-7-16+DNA	4	-	35.2	79.8	36.6	49.5
	7	112.9	47.7	77.9	32.1	65.4
	9	-	32.2	94.6	35.8	46.5
16-7NH-16+DNA	4	171.3	34.1	66.6	48.4	64.2
	7	193.4	84.9	130.3	32.9	75.5
	9	201.6	30.8	77.2	46.8	67.2
DOPE+DNA	4	120.4	33	76	40	65.0
	7	146.8	54	104	41.1	71.0
	9	127.9	55.6	89	42	93.3
16-7-16+DOPE+DNA	4	170.4	62.4	96	31.5	78.1
	7	142.8	51.9	86	34	66.4
	9	147.5	54.4	92	30.3	66.4
16-7NH-16+DOPE+DNA	4	165	36	128	43.3	81
	7	134.5	61.9	92	43.7	112.2
	9	129.3	54.8	88	41	98.8

Parameters obtained from the π-A isotherms are liftoff area, A_L; molecular area at collapse, A_c; collapse pressure, π_c; minimum cross sectional area or limiting area, A_∞ and maximum compressibility modulus, C_s^{-1}.

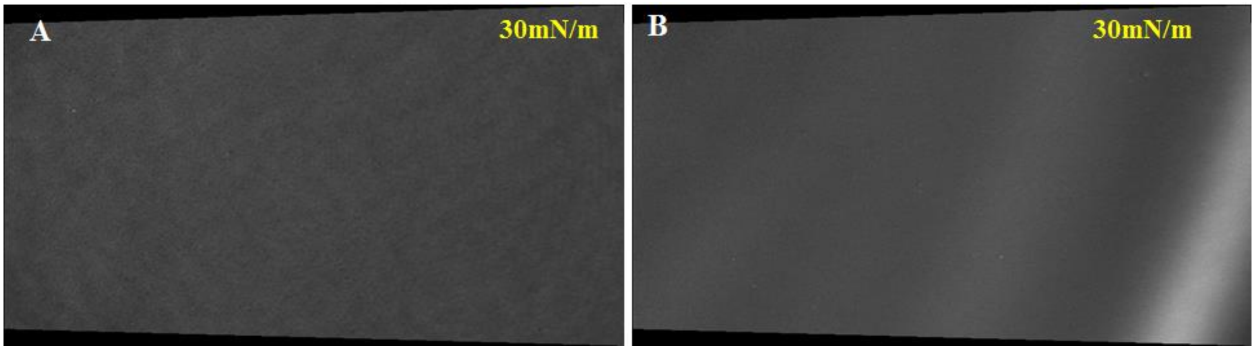

Figure 4.13. BAM image of (A) 16-7-16/DNA and (B) 16-7NH-16/DNA in pH 4 buffer.

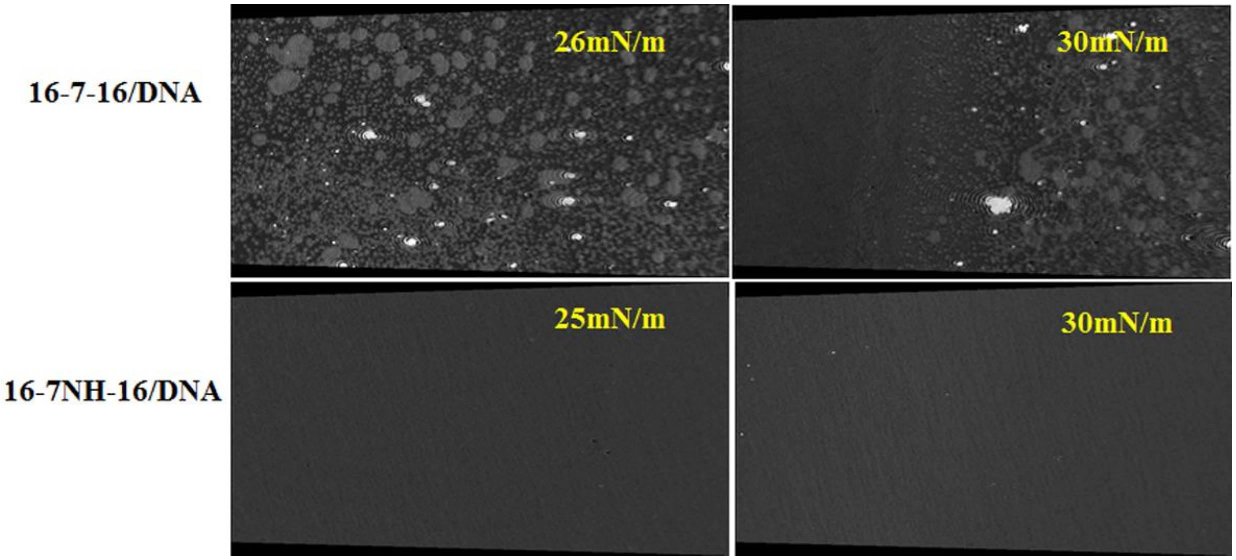

Figure 4.14. BAM image of gemini/DNA system in pH 7 at selected surface pressures.

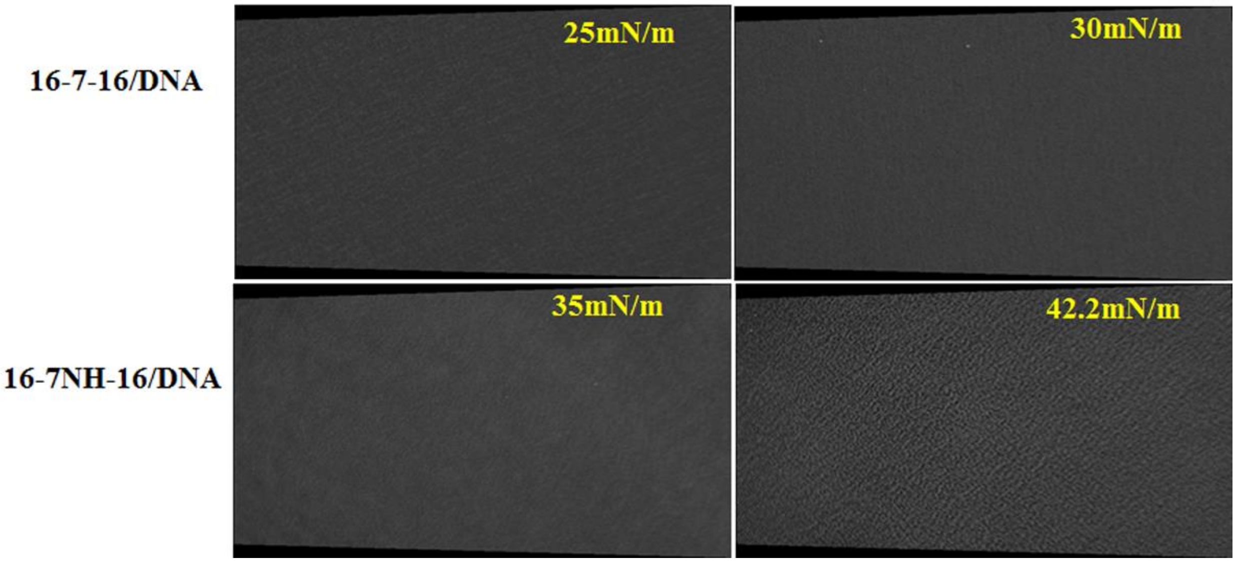

Figure 4.15. BAM image of gemini/DNA system in pH 9 at selected surface pressures.

4.2.7. Effect of DNA on DOPE monolayer

It can be seen in Figure 4.16 that the monolayer behavior was at both pH 4 and 7, but clearly NOT at pH 9, influenced by the pH of the subphase. At pH 4, the DOPE seems to have some interactions with the DNA molecules. The minimum cross sectional area decreased from 127 for pure DOPE to 76 Å^2/molecule for the DOPE/DNA system, respectively (Table 4.1 and 4.3, respectively). This implies that the presence of DNA induced condensation of the DOPE monolayer at pH 4.

As mentioned earlier, zwitterionic DOPE may carry positive charges at low pH, which can undergo electrostatic interactions with the DNA molecules. This can reduce repulsions between the adjacent DOPE molecules, and induce enhanced compaction of the monolayer upon compression. This observation is further supported by the behaviour of the monolayer at pH 9, in which presence of negative charge at the head group of DOPE causes repulsions to the negatively charged DNA molecules. Therefore, at pH 9, and do not observe any substantial interactions between DOPE and DNA. In this case and the monolayer isotherm and compressibility modulus data is nearly identical to that for pure DOPE (Figure 4.16 E and F). At pH 7, both the pure DOPE and DOPE/DNA systems showed identical similar phase behavior; (Figure 4.16 C and D). However, the monolayer is expanded in the presence of DNA compared with the pure DOPE, as the based on the minimum cross sectional areas are (~79.2 and 104 Å^2/molecule for the DOPE and DOPE/DNA monolayers, respectively). Castano et *al.* have investigated the interactions of bis(guanidinium)-tris(2-aminoethyl)amine-cholesterol (BGTC) with DNA in presence or absence of DOPE using BAM and PM-IRRAS. Their study revealed that, where they determined that DOPE does not directly interact with the DNA at air/water interface [120]. The BAM images of the DOPE/DNA system show homogeneous film with the presence of LE-LC phase (Figure 4.17, Appendix Figure A4.25). At higher surface pressure (≥41 mN/m), BAM images shows the presence of LE-LC coexisting domains (bright domain with dark spaces). These results are in good agreement with the observed isotherm and compressibility modulus for this system (Figure 4.16). On the other hand at pH 7, BAM images shows similar domain formation at higher surface pressure (>25 mN/m) (Figure 4.17, Appendix Figure A4.26). We have observed earlier that the pure DOPE monolayer at pH 7 shows more domains formation than other pH 4 or 9 (Figure 4.7). However, at pH 9, the DOPE/DNA system exhibited (Figure 4.17 and Appendix Figure A4.27) less domain formation compared to the pure DOPE (Figure 4.7) indicative of the LE-LC phase.

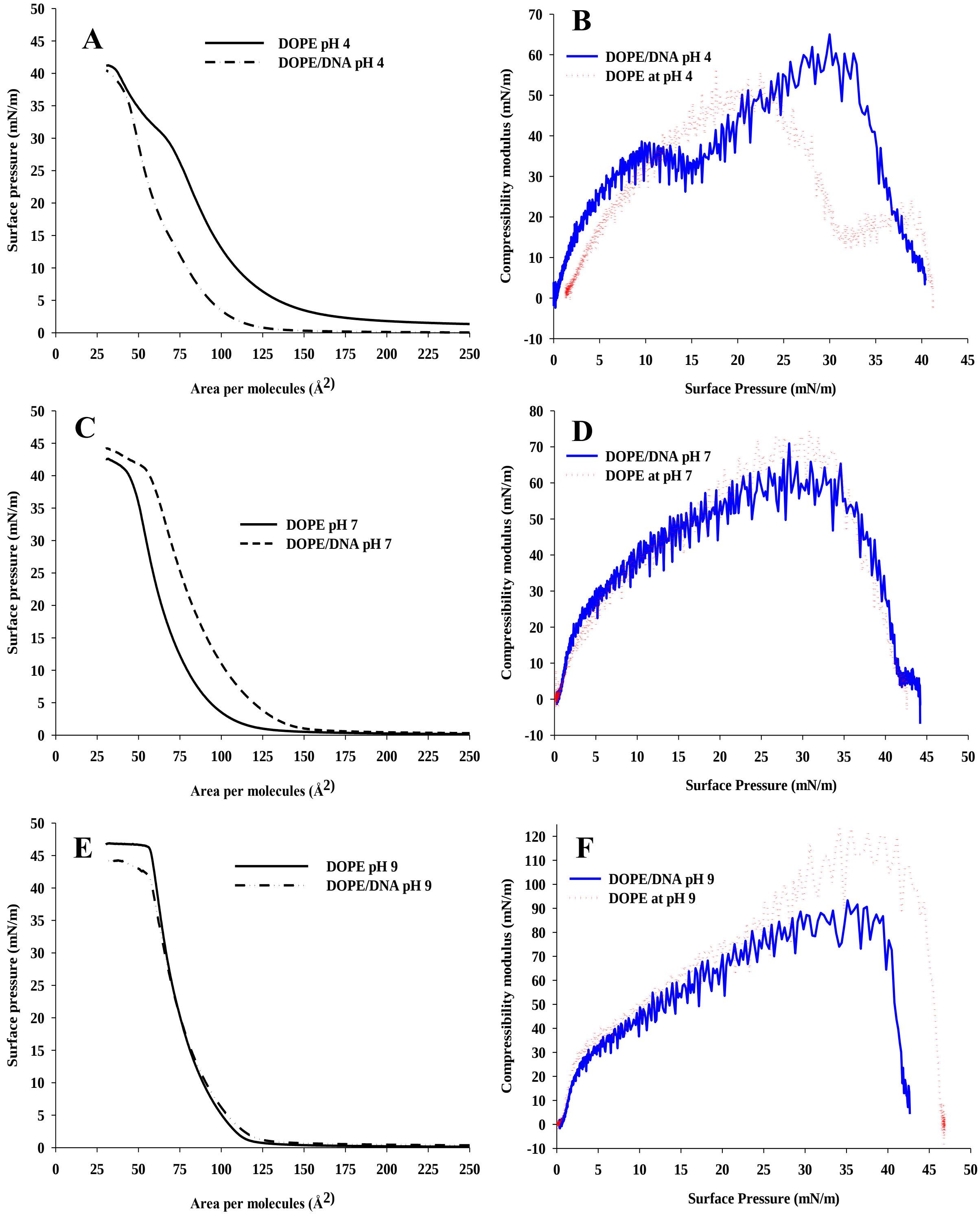

Figure 4.16. π -A isotherms (A, C and E) and compressibility modulus as a function of surface pressure (B, D, and F) for the DOPE/DNA monolayers at pH 4 (A, B); pH 7 (C, D); and pH 9 (E, F) at 25°C.

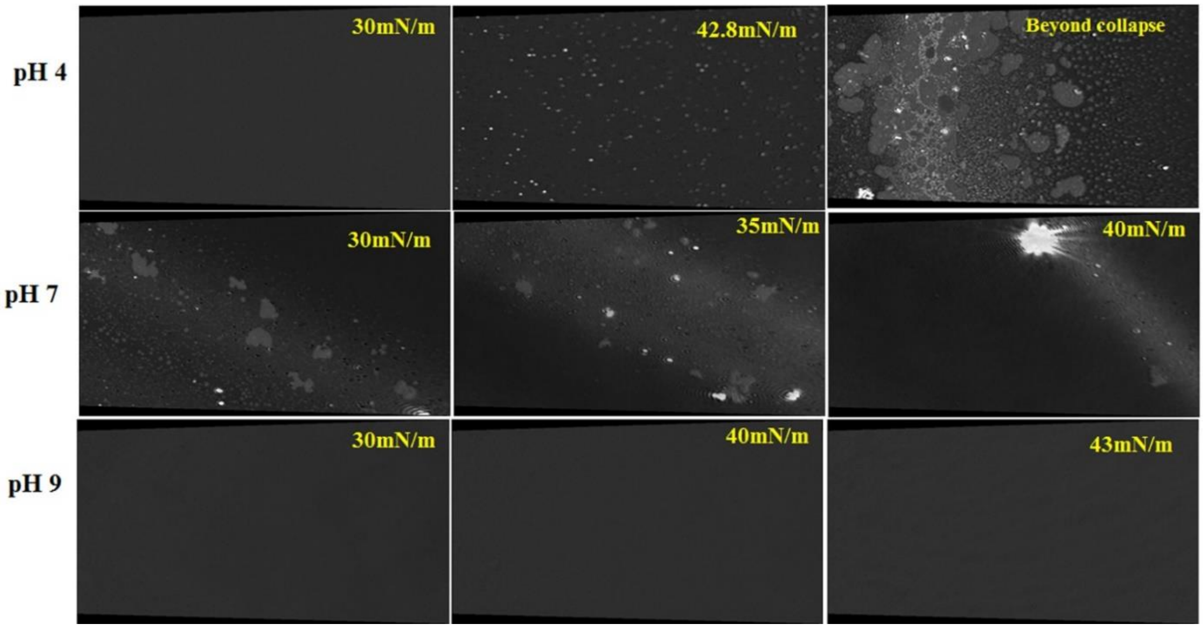

Figure 4.17. BAM image of DOPE/DNA in different pHs at selected surface pressures.

4.2.8. Mixed gemini surfactant/DOPE/DNA monolayers

The isotherms for the complete gemini surfactant/DOPE/DNA mixed monolayers are shown in Figure 4.18, along with the compressibility modulus plots; monolayer properties are listed in Table 4.3. From Figure 4.18 A and B, we observe that the 16-7-16/DOPE/DNA monolayer at pH 4 undergoes a G to LE phase transition at a molecular area of approximately 170.4 Å^2 and undergoes a smooth transition into an LE – LC coexistence phase, confirmed by the compressibility modulus, and reaches a maximum surface pressure of ~31.5 mN/m. If we recall from previous sections that the 16-7-16/DNA without DOPE (Figure 4.12A and B) reached only the LE phase at pH 4, while pure DOPE reached an LE – LC coexistence phase, or possibly an LC phase. Looking at the shape of the isotherm and compressibility modulus plots, it seems that again the nature of the monolayer is governed to a great extent by the absence or presence of DOPE; although from comparison of Tables 4.1 to 4.3, it is clear that all 3 components are involved in the overall structure of the monolayer.

Similar results are observed for the 16-7NH-16/DOPE/DNA system at pH 4 (Figure 4.18 A and B and Figure 4.19). As can be seen from Figure 4.19, the monolayer undergoes a G→LE phase transition with a parabola like appearance in the compressibility modulus in the range of molecular areas of ~175 to 116 Å^2. The lift off area for this system is similar to that of 16-7-16/DOPE/DNA at pH 4; however, the monolayer reaches a maximum surface pressure of ~43.3 mN/m (Table 4.3). Again, the monolayer mostly remains in the LE-LC phase for surface pressures in the range of ~15 mN/m to collapse (Figure 4.18 B and 4.19). Clear differences are observed between 16-7NH-16/DNA and the 16-7NH-16/DNA/DOPE monolayers, where DOPE induces condensation in the monolayer. Seemingly contrary to this, the minimum cross sectional area for 16-7NH-16/DNA/DOPE and 16-7NH-16/DNA system are 128 and 66.6 Å^2/molecules, respectively (Table 4.3). The higher value of cross sectional area for the 16-7NH-16/DNA/DOPE monolayer can be explained based on their electrostatic interaction phenomena. 16-7NH-16 will have three positive charges at pH 4, and DOPE may also carry a net positive charge. Therefore, gemini and DOPE may electrostatically repel one another at the air/buffer interface. This electrostatic repulsion likely inhibits the possibility for compressing this monolayer to a small molecular area. Since, DNA molecules are present at the subphase, it will undergo electrostatic interactions with the gemini as well as slightly with DOPE molecules. Moreover, the interaction behavior of the mixed system can be further explained based on the mixing behavior of the DOPE with the GS based system in presence of DNA. In our previous studies by Akbar et *al*, we have shown that the mixing behavior between the DOPE and a series of GS (16-3-16, 16-7-16, 16-7NH-16) is antagonistic in nature, because the DOPE tends to form inverted or bilayer structures whereas GS forms micellar structures in the aqueous phase [200]. This factor may also have caused the overall repulsion of the molecules subsequently formed expanded monolayer.

At pH 7, 16-7NH-16/DOPE/DNA system formed the most rigid monolayer, with indications of the LC phase at higher surface pressure (Figure 4.18 C and D, Table 4.3). The phase transition for the 16-7-16/DOPE/DNA is again similar to that for pure DOPE. At pH 9, the 16-7-16/DOPE/DNA monolayer remained at the LE phase whereas the 16-7NH-16/DOPE/DNA monolayer reaches a LE-LC coexisting phase (Figure 4.18 E and F, Table 4.3). Both of these systems showed C_s^{-1} values lower than for pure DOPE indicating that the condensation effect of DOPE is less prominent at pH 9 than at pH 4. Interestingly, the C_s^{-1} values exhibits clear differences between 16-7NH-16/DNA and the 16-7NH-16/DNA/DOPE monolayers at pH 9, where DOPE induces condensation in the monolayer. Similar results are observed at pH 7 for this systems. In general, our results suggests that presence of DOPE induces condensation in the 16-7NH-16/DOPE/DNA system regardless of the pHs. Conversely, comparing the 16-7-16/DNA with 16-7-16/DOPE/DNA system, DOPE induces condensation effect at pH 4 and 9 (relatively lower than pH 4), however, at pH 7 compressibility modulus values were similar indicative of no effect. In general, the rigidity of the 16-7NH-16/DOPE/DNA monolayer follows the trend: pH4 < pH9 < pH7; whereas the 16-7-16/DOPE/DNA system follows the trend: pH9 < pH7 < pH4.

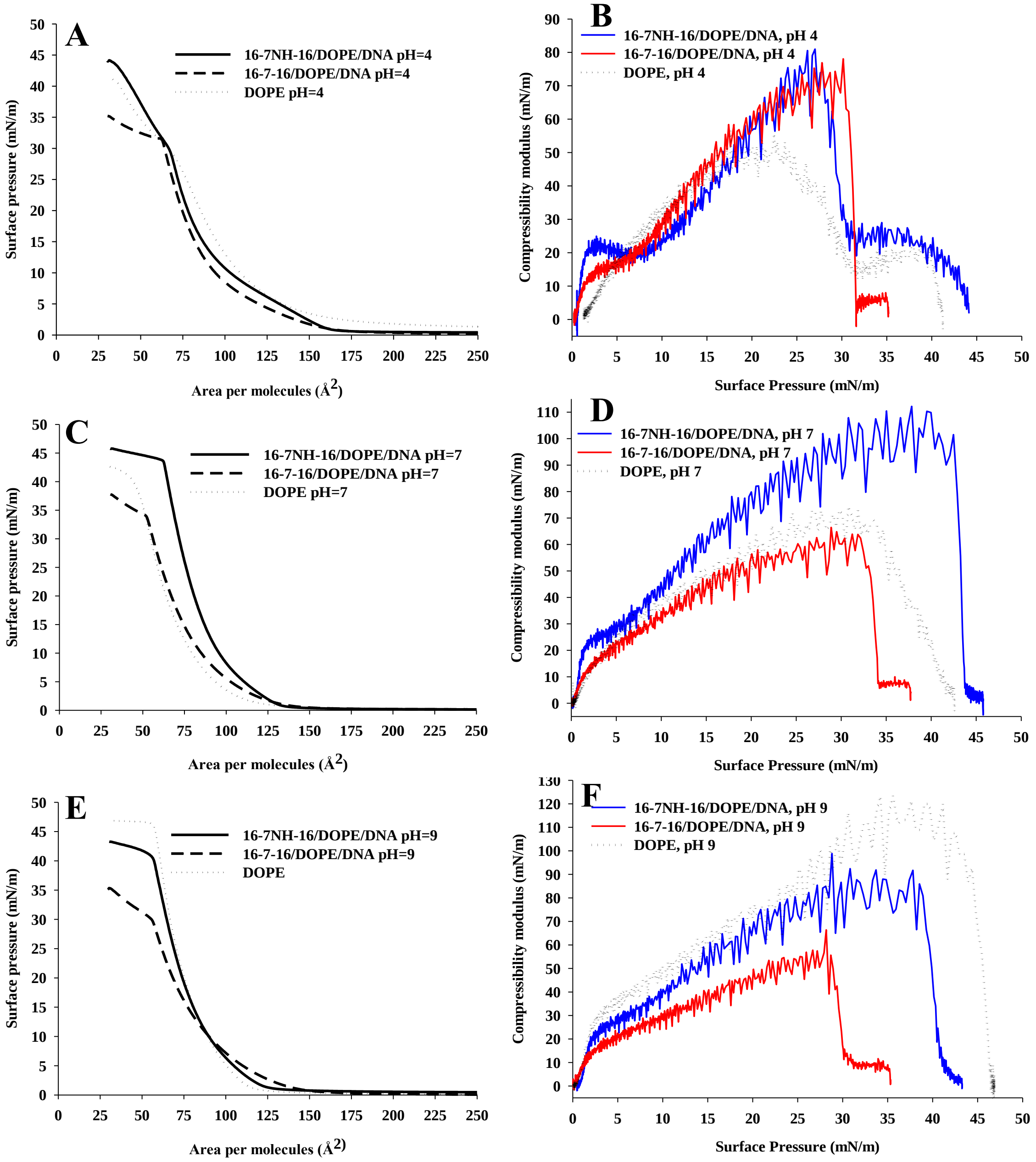

Figure 4.18. π -A isotherms (A, C and E) and compressibility modulus as a function of surface pressure (B, D, and F) for the mixed gemini surfactant/DOPE/DNA monolayers at pH 4 (A, B); pH 7 (C, D); and pH 9 (E, F) at 25°C.

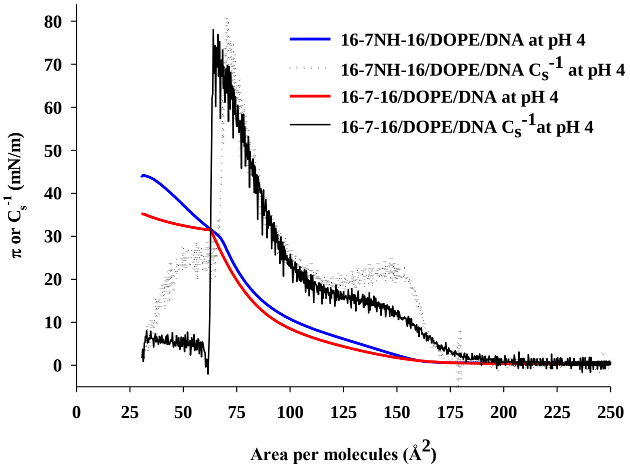

Figure 4.19. Compressibility modulus and surface pressure as a function of mean molecular area of the GS/DOPE/DNA at pH 4.

At pH 4, the 16-7-16/DOPE/DNA system formed a homogeneous film with mostly dark BAM images, indicative of the LE or LE-LC phase (Figure 4.20, additional images are presented in Appendix Figure A4.28). The results are in good agreement with the surface pressure isotherm and compressibility modulus values as presented in Figure 4.18 A and B. The 16-7NH-16/DOPE/DNA system surface pressure >30 mN/m exhibited fibril type domains which is indicative of the LE or LE-LC phase. The fibril or network like structure is presented in Figure 4.22 for better understanding. The fibril structure contains numerous 'white dot' like domains. If we recall the 16-7NH-16/DNA monolayer which shows a plateau region (Figure 4.12) at around ~30 mN/m (due to the electrostatic interactions between the gemini and DNA), and the BAM images of the 16-7NH-16/DOPE/DNA system also exhibits the complex fibril structure ~33 mN/m. Thus, combining the BAM images with the surface pressure area isotherm, there is a strong interaction present in the 16-7NH-16/DOPE/DNA system at pH4. Interestingly, Chen at *al.* have shown the presence of DNA with the 18-s-18, s = 3-10 gemini surfactant formed complex monolayer with fibril structures [54]. Their results are consistent with our observations. The exact role of DOPE in this system is not clearly understood, however, the condensation effect of DOPE is seen from the surface pressure isotherm data. This further signifies that DOPE may reside on top of the fibrils or attached to the fibril structures due to the hydrophobic interactions at pH 4. This phenomena will be further explained at the AFM and KPFM section. The BAM images of the 16-7-16/DOPE/DNA system at pH 7 and 9 is indicative of the LE-LC phase (Figure 4.20, additional images are in Appendix Figure A4.29 and A4.30) which is consistent with the isotherm and compressibility modulus results (Figure 4.18 C, D, E and F). However, 16-7NH-16/DOPE/DNA showed domain formation at the LC phase of the monolayer (~42 mN/m), Figure 4.23. The 16-7NH-16/DOPE/DNA monolayer showed small domains at surface pressure > 40 mN/m which is an indication of LE-LC or LC phase (Figure 4.24). Thus the BAM images are in consistent with the isotherm and compressibility modulus observed for this system.

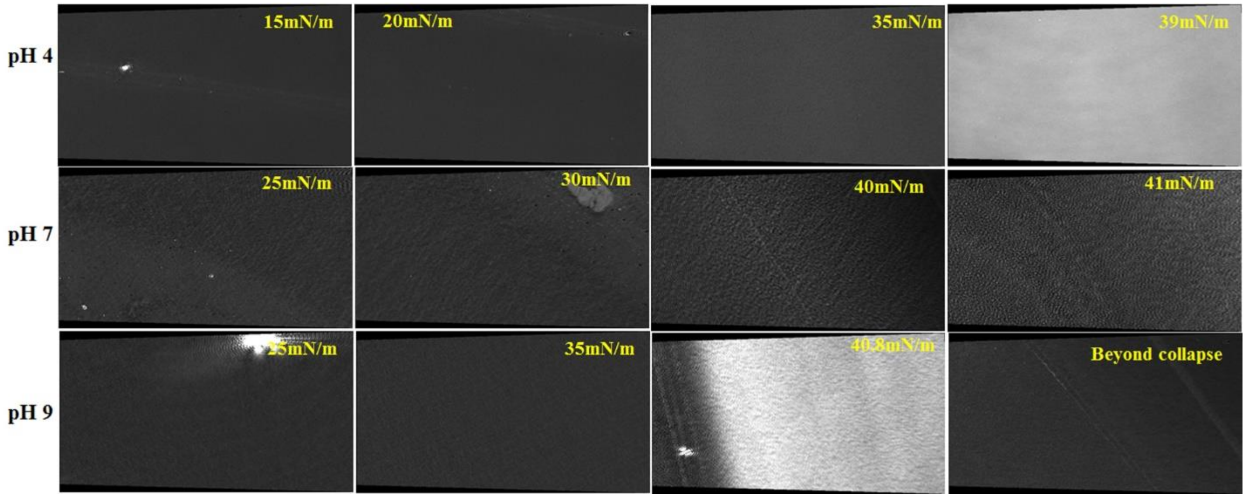

Figure 4.20. BAM image of 16-7-16/DOPE/DNA in pH 4 buffer.

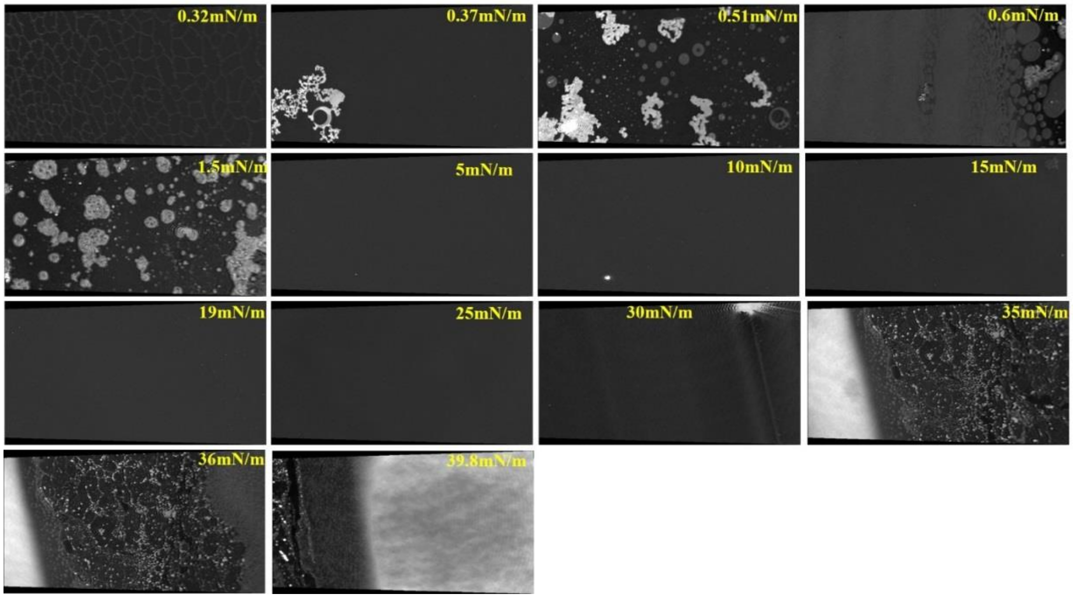

Figure 4.21. BAM image of 16-7NH-16/DOPE/DNA in pH 4 buffer.

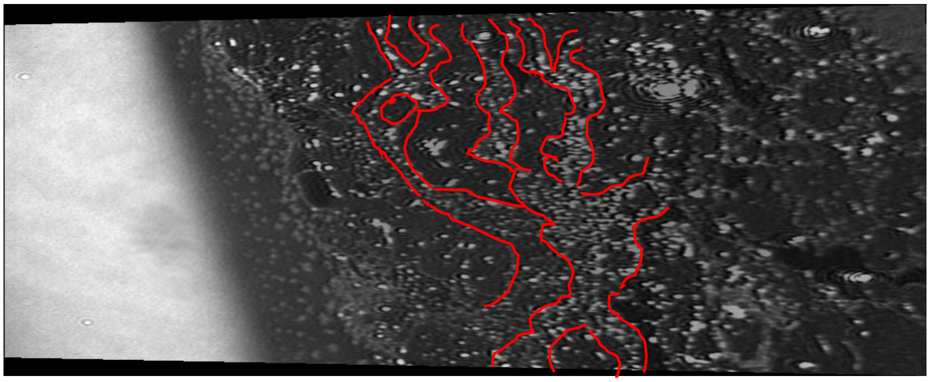

Figure 4.22. BAM image of 16-7NH-16/DOPE/DNA in pH 4 buffer at surface pressure of 35 mN/m. The red lines indicate the fibril or platform structures in the monolayer.

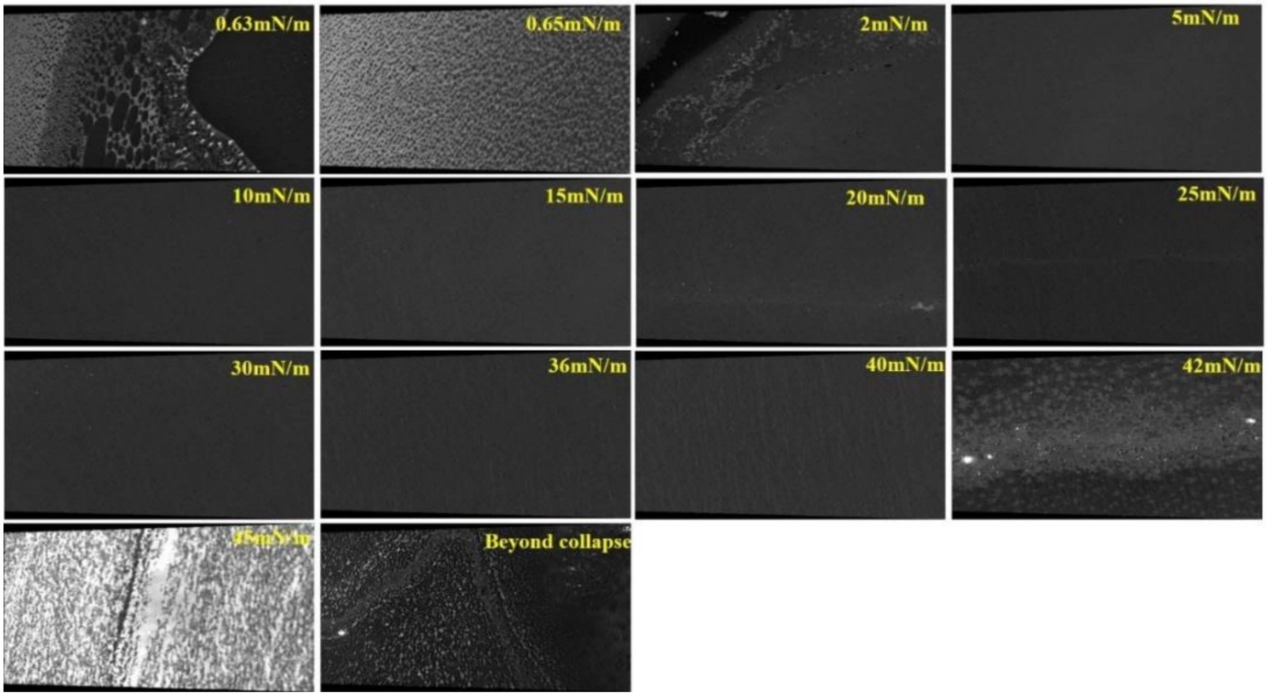

Figure 4.23. BAM image of 16-7NH-16/DOPE/DNA in pH 7 buffer.

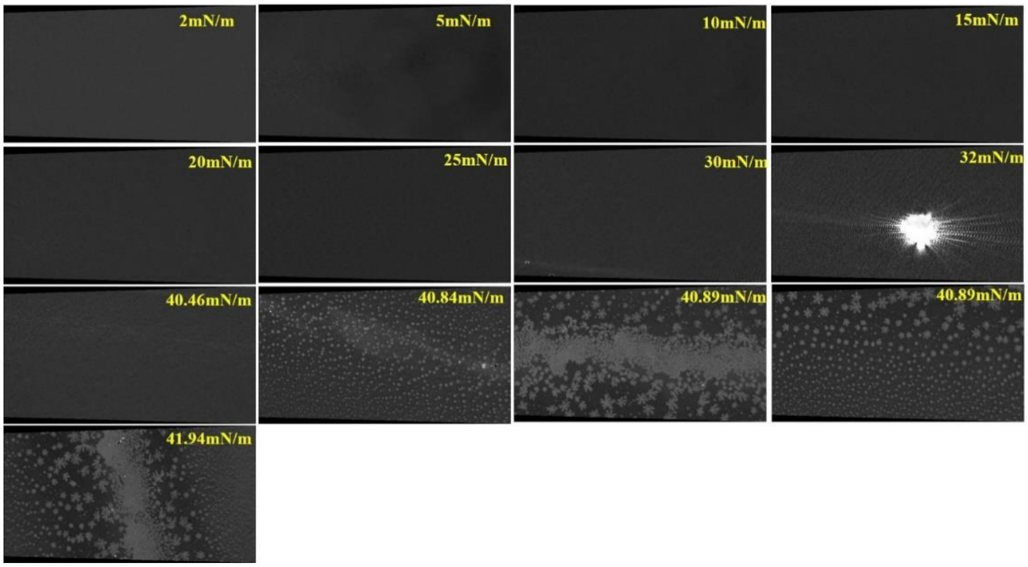

Figure 4.24. BAM image of 16-7NH-16/DOPE/DNA in pH 9 buffer.

4.2.9. AFM and KPFM studies of the gemini/DOPE/DNA systems

To better understand the interaction mechanism of the gemini/DOPE/DNA system, AFM and KPFM studies have been conducted. For the 16-7NH-16/DOPE monolayers, the AFM images show the presence of vesicle or donut (round) shape complexes. KPFM images for the same monolayers indicate that these vesicles are positively charged at the outer layer, with the core being neutral (Figure 4.25A). In an AFM studies of the 18-10-18 gemini surfactant monolayer, Chen et *al.* showed the presence of surface micelle [119]. Thus, we hypothesized that at pH 4 DOPE possesses one and the 16-7NH-16 three positive charge, and may be present in the outer layer of the round shape complex and the alkyl tail may reside in the core (a micelle formation). Nevertheless, the exact role of DOPE in this vesicle or donaut shape structure formation is not clear, which might need further investigation.

As can be seen from the AFM images (Figure 4.26), the 16-7NH-16-DOPE system with DNA (at 15 mN/m surface pressure) shows branched or relatively irregular fibrils (yellow color arrow), parallel fibrils (red color arrow), and the main platform (blue color arrow) with few fibrils structures. Chen et *al.* have observed similar AFM images for the 18-s-18, s = 3,4,6,8,10,12 gemini surfactant in presence of DNA [54, 125]. Similar structural features are observed from the monolayer deposited at higher surface pressure (35 mN/m) (Figure 4.26 A and B). The AFM images can interpreted if we assume that the positively charged gemini surfactants are interacting with negatively charged DNA molecules that have been deposited as a layer on the substrate. The 16-7NH-16 molecule are bound to this layer, forming the fibril structures. This gives rise to charge neutralization in the region of the fibrils, showing up as black regions of zero charge in the KPFM images. This implies that the GS is solely interacting with DNA, and DOPE remains unaffected. Additionally, the KPFM shows the background area (other than the fibril structure) as net positive charges. We hypothesized that the free GS or DOPE molecules which have not undergone any interactions with DNA, are present in the background or there could be DOPE/DNA system in the background. Again at pH 4, 16-7NH-16 should have three positive charges, whereas DOPE should be having one positive charge. Therefore, there should be some kind of repulsions between these two head groups (GS and DOPE) which was evident from the isotherm of these systems (Figure 4.8). The only interaction between these two systems could be the hydrophobic interaction between the tail groups of 16-7NH-16 and DOPE. Interestingly, it is observed from the isotherm of 16-7NH-16-DOPE-DNA (Figure 4.18) that the DOPE is dominating the shape of isotherm. Our previous findings also showed the antagonistic interactions between gemini surfactant and DOPE system characterized by surface tensiometry and Clint's, Rubingh's, and Motomura's theories for mixed micellar formation [200]. Additionally, from the DOPE-DNA isotherm (Figure 4.16), we can observe that the isotherm is more like DOPE, a minor change have been observed in terms of maximum surface pressure, collapse pressure or the mean molecular area (Table 4.1 and 4.3). For instance, the maximum compressibility modulus for the pure DOPE and DOPE-DNA at pH 4 is ~ 56.7 and 65 mN/m, respectively. And the collapse pressure (π_c) is ~40.9 mN/m and 40 mN/m; molecular area at collapse (A_c) is around 35.2 Å^2 and 33 Å^2. Thus, the complex structure formation in AFM studies are in good agreement with the BAM images for the 16-7NH-16/DOPE/DNA at pH 4, in which we have seen similar fibril structure (Figure 4.21 and 4.22).

From Figure 4.27, the 16-7-16-DOPE-DNA system also shows the fibril formation. KFPM image exhibits the dominant positive charge on the image. Increasing the surface pressure form 15 mN/m to 25 mN/m, the fibril structure increased. We hypothesized that the charge neutralization is less in this case, and we observed thread like fibril structure and less platform structure than that of the 16-7NH-16-DOPE-DNA system (Figure 4.26). This indicates that the 16-7-16 is not as effective as 16-7NH-16 for interacting with negatively charged DNA. This is also evident from the weak interaction of 16-7-16-DOPE system with DNA in comparison to the 16-7NH-16-DOPE in terms of π_c (~ 31.5 mN/m and 43.3 mN/m, respectively); and A_c (~62.4 and 36 Å^2, respectively) (Table 4.3). That means more compacted monolayer with higher surface pressure is formed with the 16-7NH-16/DOPE/DNA system at pH 4 than 16-7-16/DOPE/DNA system. Thus, AFM images further justified that DOPE caused condensation in the mixed gemini/DOPE/DNA monolayer.

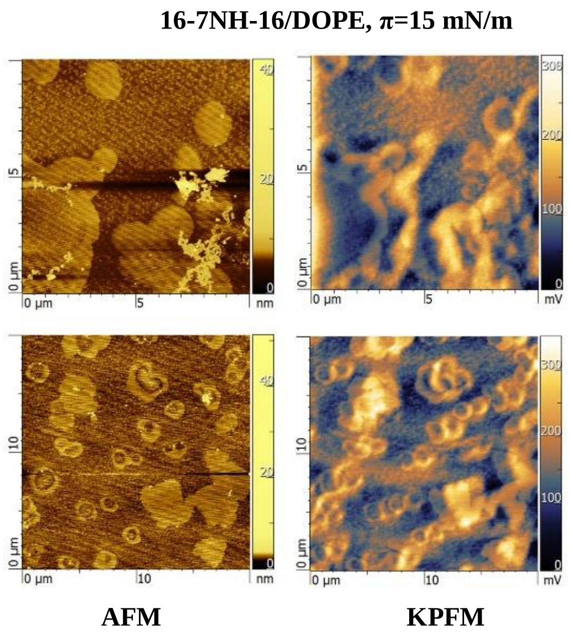

Figure 4.25. Small-scale AFM and KPFM images of 16-7NH-16/DOPE monolayers, with cross sections. The top and bottom two figures are in the scale bar of 10x10 and 20x20μm. In all cases, the deposition pressure was = 15 mN/m.

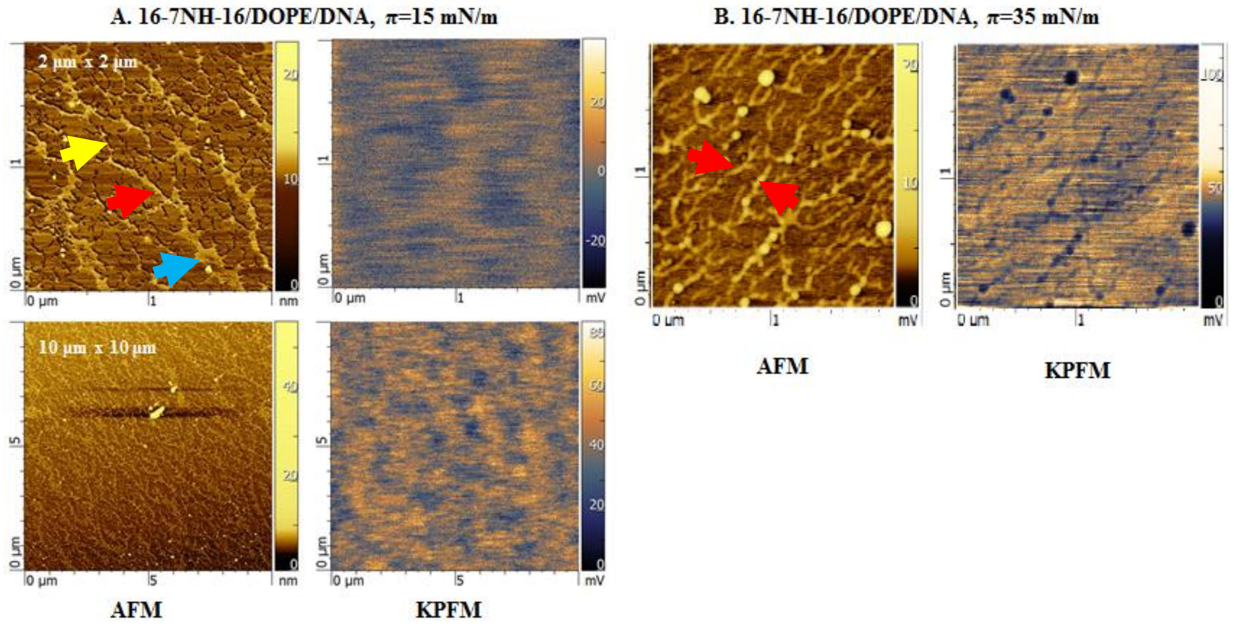

Figure 4.26. Small-scale AFM and KPFM images of **A.** 16-7NH-16/DOPE/DNA monolayers at surface pressure 15 mN/m, **B.** 16-7NH-16/DOPE/DNA monolayers at surface pressure 35 mN/m, with cross sections (adapted from the reference with permission [232]). The top row figures are at the scale bar of 2x2 μm and the bottom row figures are 10x10 μm scale. The Yellow, Red and Blue color arrow in indicates the irregular fibrils, parallel fibrils, and the main platform, respectively.

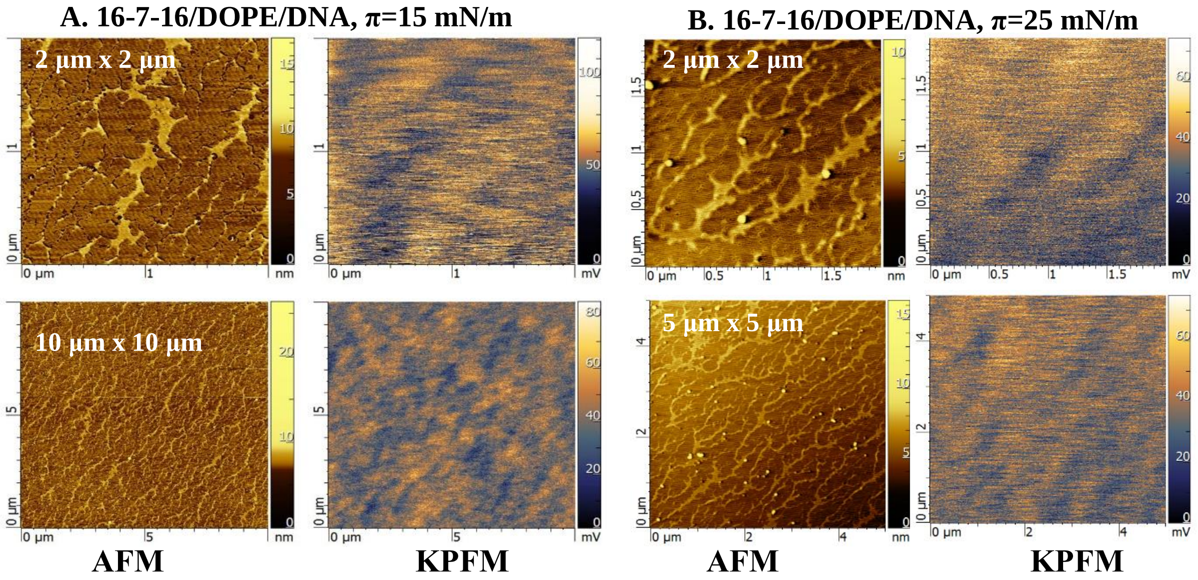

Figure 4.27. Small-scale AFM and KPFM images of **A.** 16-7-16/DOPE/DNA monolayers at surface pressure 15 mN/m, **B.** 16-7-16/DOPE/DNA monolayers at surface pressure 25 mN/m, with cross sections.

4.2.10. PM-IRRAS characterization of the mixed monolayers

To further investigate the effect of DNA on the monolayer of gemini-DOPE mixed system, PM-IRRAS was used. Initially, we have determined the attenuated total reflection (ATR) spectrum for the pure gemini surfactant to determine the IR bands. It is observed from Figure 4.28 that both gemini surfactants possesses a CH_2 symmetric stretch ($v_s(CH_2)$) at 2850 cm^{-1} and a CH_2 asymmetric stretch ($v_a(CH_2)$) at 2917 cm^{-1} attributed to the methylene groups present in the alkyl tails of the surfactants [54, 120]. The observed band at ~1470 cm^{-1} is indicative of a CH_2 bending vibration, again from the alkyl tail [233]. We next attempted to find the same bands in the PM-IRRAS spectrum for the pure gemini surfactant monolayers. Unfortunately, we were unable to separate the bands due to the surfactants from the noise arising from the aqueous subphase (data not shown). This could be due to the higher solubility of the gemini surfactant in subphase, as compared to the mixed monolayer; this is consistent with our isotherm and BAM characterizations of the pure gemini surfactant monolayers.

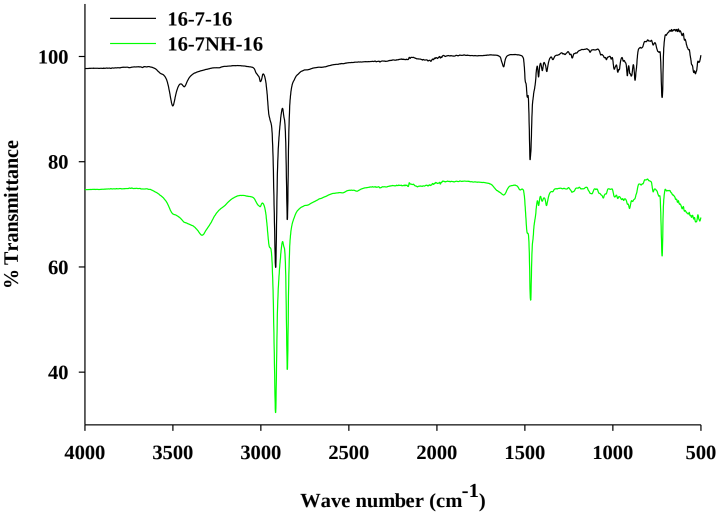

Figure 4.28. ATR spectra of 16-7-16 and 16-7NH-16. Both gemini surfactants have similar transmittance value, hence, 16-7NH-16 was subtracted (value of 25) from the original value for better representation in the graph.

The gemini/DOPE monolayers provided clear spectra; specific regions of the IRRAS spectra are presented in Figure 4.29. As can be seen, the characteristic $\nu_s(CH_2)$ signal is observed at 2851cm^{-1} and the $\nu_a(CH_2)$ signal at 2926 cm^{-1} at surface pressure of 30 mN/m; this surface pressure corresponds to that of cellular membranes which vary in surface pressure from 30-35 mN/m). The frequencies of these bands are sensitive to the conformation of the phospholipid acyl chains. Therefore, these bands provide substantial information about the molecular orientation of the lipid acyl chains at the air/water interface [210, 234-237]. In general, if the peaks are shifted to values lower than 2920 and 2850 cm^{-1} (i.e. red shifted), this indicates higher chain ordering in the film. Higher values (i.e. blue shifted) indicates chain disordering [238, 239]. Our literature review suggests that $\nu_a(CH_2)$ is often found in a narrow range from 2915 to 2918 cm^{-1}, and $\nu_s(CH_2)$ from 2846 to 2850 cm^{-1} for all-trans conformations of the fully extended tail chains [54]. Noteworthy, a red shift is an indicative of an ordered all-trans conformation of the chain, whereas a blue shift is indicative of chain disordering associated with the gauche conformation [238]. As can be seen from Figure 4.29, the $\nu_a(CH_2)$ and $\nu_s(CH_2)$ bands have moved slightly to higher values of 2926 cm^{-1} and 2851 cm^{-1} from the ideal 2920 and 2850 cm^{-1} values, respectively. This is an indication of the disordered acyl chains that would be associated with the liquid expanded monolayer film, an interpretation that is consistent with our isotherm and compressibility modulus data. Rubio-Magnieto et *al.* have reported similar results for gemini amphiphilic pseudopeptides at the air/water interface [104], in which pure lipid monolayer exhibited wavenumber higher than the 2920 and 2850 cm^{-1}, and corresponded to the LE phase of the film with disordered acyl chain. The IRRAS study of gemini surfactant (18-s-18, s = 3 ,6 ,8) in presence of DNA in the subphase, revealed the presence of $\nu_a(CH_2)$ and $\nu_s(CH_2)$ bands at around 2924 and 2854 cm^{-1} at the air/water interface [54], which is comparable to our results.

DOPE possesses similar $\delta(CH_2)$ acyl chains bands, a band characteristic of ester groups $\nu(C{=}O)$ at 1737 cm^{-1}, and the asymmetric ($\nu_a(PO_2^-)$) and symmetric phosphate ($\nu_s(PO_2^-)$) stretches at 1220 and 1080 cm^{-1}, respectively [120, 240]. The ester $\nu(C{=}O)$ stretch band of lipids may range from 1710 to 1740 cm^{-1} [235], as such the observed band at 1726 cm^{-1} can be attributed to DOPE (Figure 4.48). The $\nu_a(PO_2^-)$ is observed at 1231 cm^{-1} at 30 mN/m surface pressure. This band was further shifted to higher values upon increase of the surface pressure. The exact reason for the shifts of this band to higher values is not clear; however, $\nu_a(PO_2^-)$ is sensitive to hydration and ion binding [235]. It is possible that some structural or orientation changes in the DOPE head group resulted in increased access of water molecules to the phosphate group. This could be an indication that, at pH 4, the phosphate group might have formed hydrogen bonding with water molecules, resulting in a shift of the band higher values at higher surface pressure. An IRRAS study of the diphosphoryl Lipid A (a precursor of lipopolysaccharide) revealed the presence of three overlapped features in the asymmetric phosphate band region. The bands at 1225, 1238 1258 cm^{-1} corresponded to dihydrated, monohydrated, and unhydrated phosphate groups, respectively. These multiple bands were attributed to the accessibility of Lipid A molecules to nearby water molecules [235].

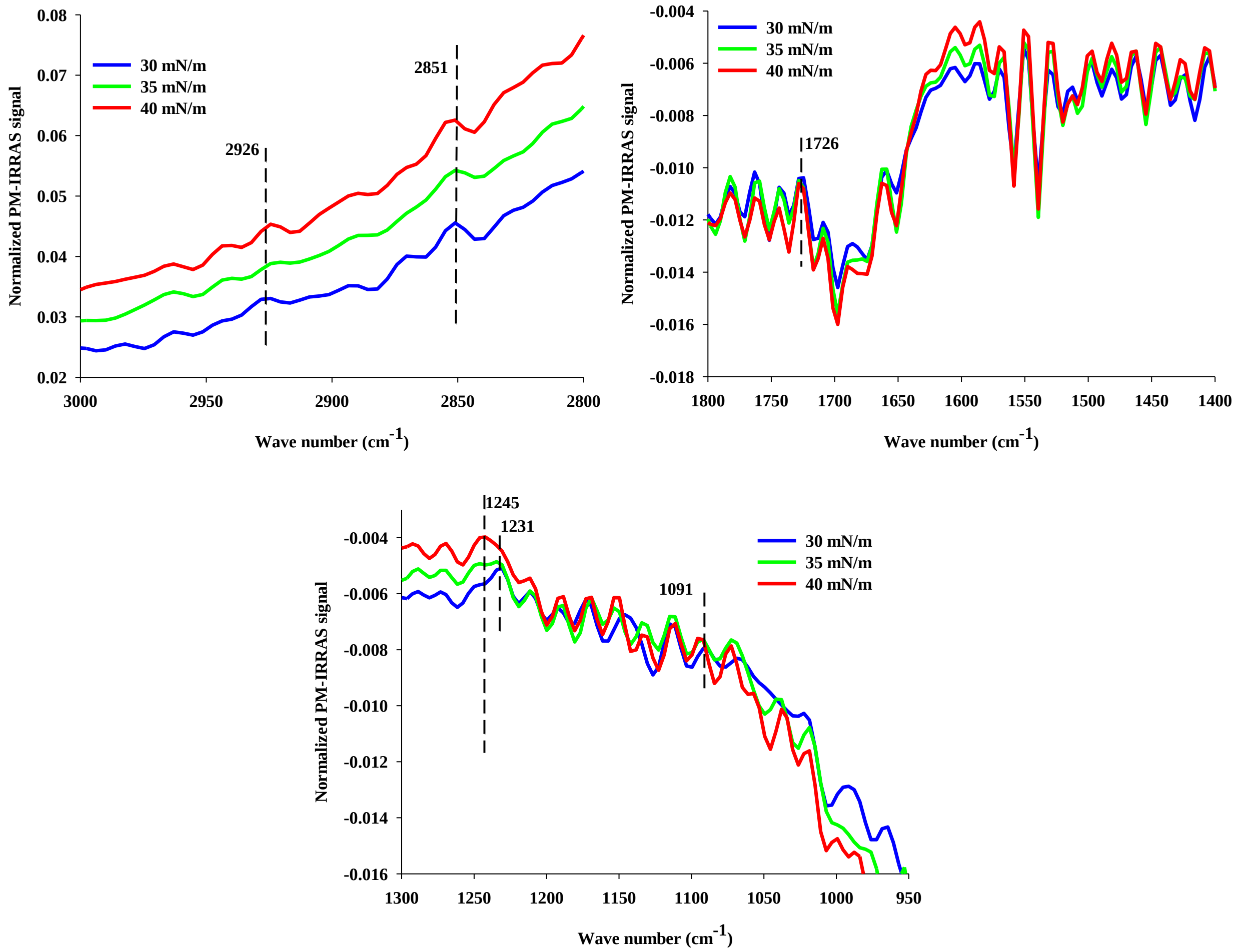

Figure 4.29. PM-IRRAS spectra of the 16-7NH-16/DOPE monolayer at pH 4 and various surface pressures.

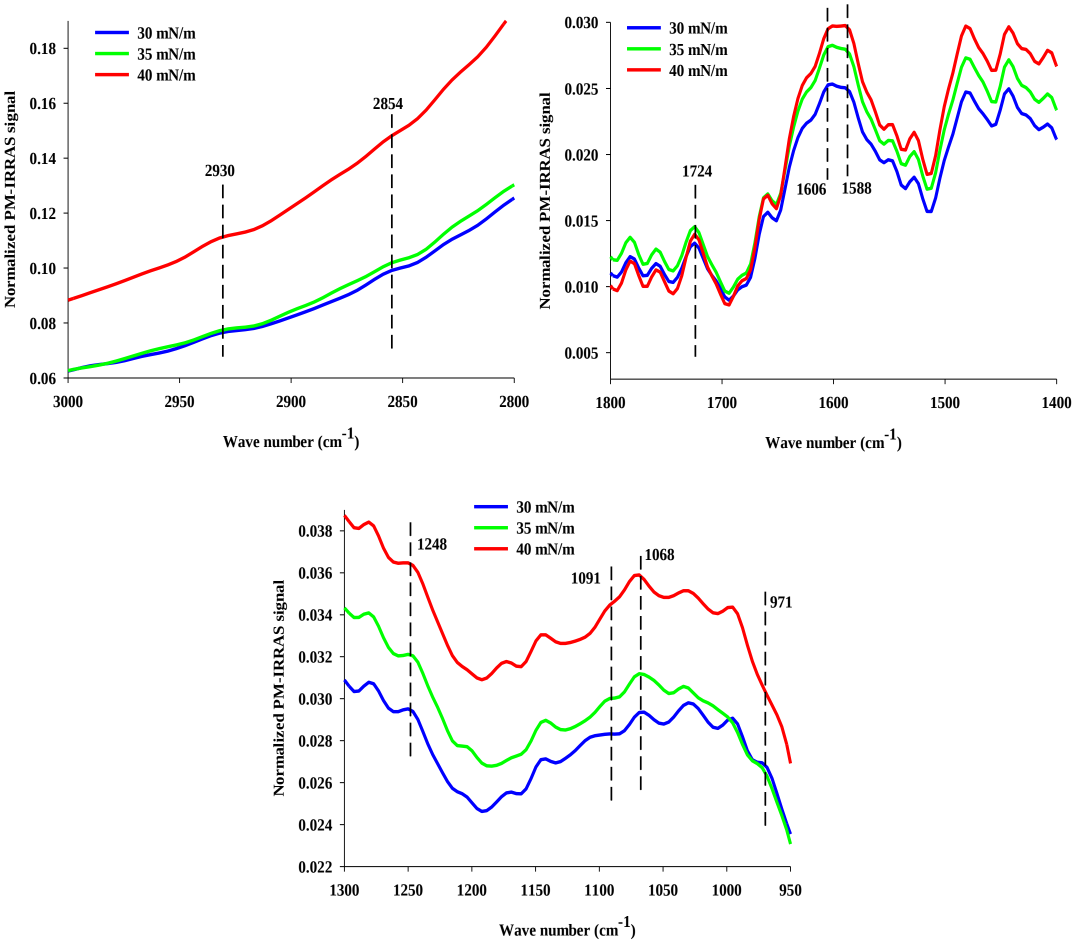

Figure 4.30. PM-IRRAS spectra of the 16-7NH-16/DOPE in presence of DNA at pH 4 at different surface pressures.

Braun et *al.* have showed the FT-IR spectra of the B form DNA has bands due to the guanine/thymine carbonyl (C=O) stretch at 1715 cm^{-1}, the thymine aromatic amine stretch (1328 cm^{-1}), $v_s(PO_2^-)$ and $v_a(PO_2^-)$ stretches at around 1088 and 1222 cm^{-1}, respectively; and a strongly coupled sugar-phosphodiester signal at around 970 cm^{-1} [241]. Thus we can expect to see the similar bands in the PM-IRRAS spectrum in presence of DNA in our systems. Figure 4.30 shows that for 16-7NH-16/DOPE in the presence of DNA at pH 4 the $v_a(CH_2)$ and $v_s(CH_2)$ bands are red shifted to 2930 and 2854 cm^{-1}, respectively, similar to the red shift observed with increases in pressure for the 16-7NH-16/DOPE system at higher surface pressures but greater in magnitude. This is again an indication that the alkyl chains of the 16-7NH-16/DOPE/DNA complex monolayer remain in a more disordered state with a greater number of gauche conformations. Again these results are consistent with the both the isotherm and compressibility modulus results for the 16-7NH-16/DOPE/DNA system (Figure 4.18 A and B) at pH 4.

With respect to the bands associated with DNA, we have not observed any changes in the C=O band at 1724 cm^{-1}. Interestingly, Marty et *al.* have reported that cationic ion−base interactions can induce changes in the vibrational band of adenine at 1609-1606 cm^{-1} towards lower values [242]. Neault et *al.* showed that the bands observed at 1606 and 1590 cm^{-1} were attributed to an aspirin-DNA interaction [243]. The drug was mainly bound through the backbone of the PO_2^- group and the A-T bases (DNA). The interaction was mediated through the guanine and adenine N7 atoms and thymine O2 in the major and minor grooves of DNA duplex [243]. Given this, the band we observe at 1606 and 1588 cm^{-1} (Figure 4.30) may be due to the interactions of the quaternary ammonium head groups of the gemini surfactant with the adenine N7 or thymine O2 atoms. Therefore, this spectral feature is suggestive of the presence of ion−dipole interactions in the gemini/DOPE/DNA complex monolayers. The addition of DNA on the sub-phase substantially shifted the phosphate asymmetric band to 1248 cm^{-1} (Figure 4.30). Both DOPE and DNA can contribute to this phosphate group region of the PM-IRRAS spectra, and the shift in the $v_a(PO_2^-)$ stretches to higher values is a further indication of the gemini-PO_2^- interaction. This interpretation is also consistent with FT-IR studies 18-s-18 (s = 3,6,8) gemini surfactant/DNA deposited LB films which showed a similar shift of the $v_a(PO_2^-)$ band to higher values corresponding to the gemini-PO_2^- interaction [54].

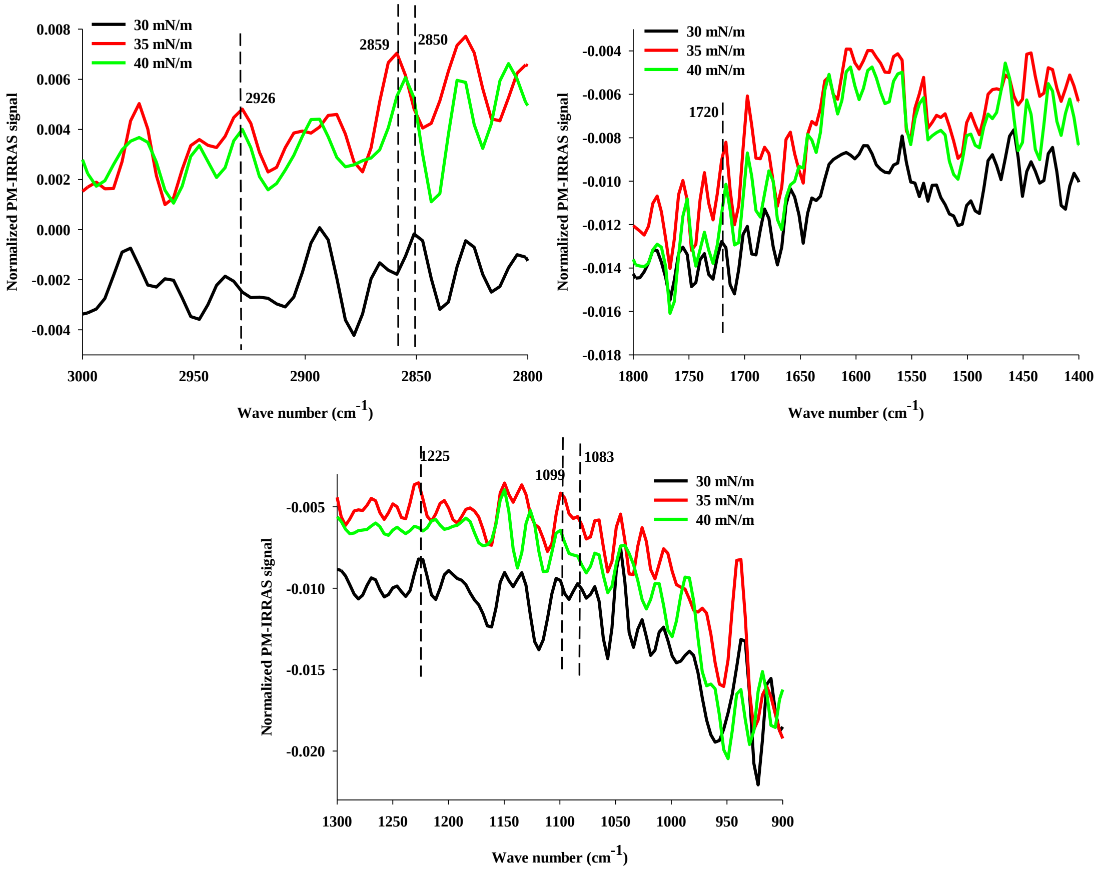

Figure 4.31. PM-IRRAS spectra of the 16-7NH-16/DOPE without DNA at pH 7 at different surface pressures.

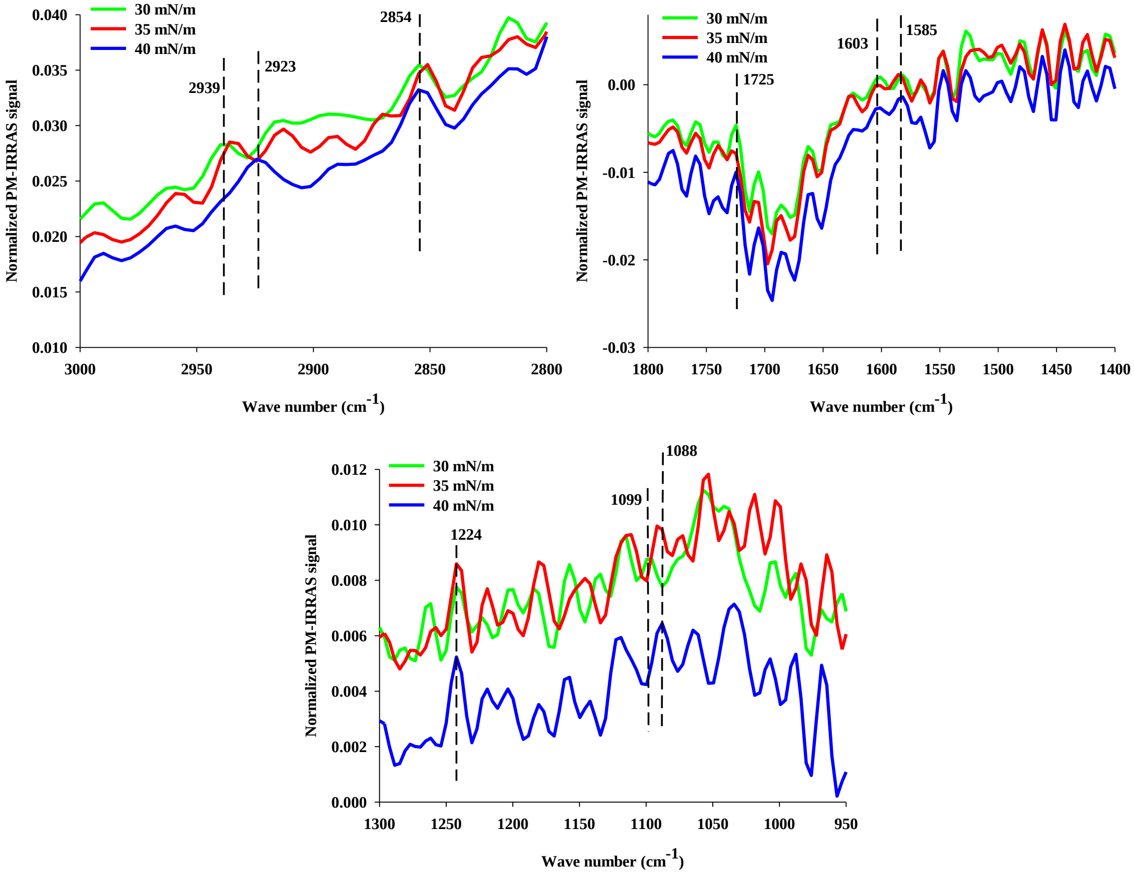

Figure 4.32. PM-IRRAS spectra of the 16-7NH-16/DOPE with DNA at pH 7 at different surface pressures.

The PM-IRRAS spectrum of the 16-7NH-16/DOPE system at pH 7, showed similar bands at the 3000-2800 cm^{-1} region (Figure 4.31). There were some changes of the $v_s(CH_2)$ from 2850 cm^{-1} to higher values. Thus at both pH 7 and 4, the results shows similar disordered alkyl tails at the air/buffer interface consistent with an LE-LC or LC phase for the monolayer. All other spectra at pH 7 are similar to the bands observed at pH 4 (Figure 4.31). It is observed from the Figure 4.32 that the 16-7NH-16/DOPE in presence of DNA at pH7 shows similar characteristics peaks as observed in Figure 4.30 (pH 4). Interesting changes are observed in the 3000-2800 cm^{-1} region with relatively higher values for the symmetric and asymmetric bands of the alkyl tails. At higher surface pressure (40 mN/m), more ordering of the alkyl tails are observed, with a blue shift from 2939 to 2923 cm^{-1}). It was observed from the compressibility modulus values that the 16-7NH-16/DOPE/DNA monolayer is found in the LC phase at higher surface pressures 35 mN/m (Figure 4.18 B), consistent with the observed blue shift in the IRRAS spectrum. Similar changes in the spectra are observed for pH 4 in the region 1300-950 cm^{-1} are seen at pH 7. At pH 9, the 16-7NH-16/DOPE IRRAS spectrum is consistent with a relatively ordered monolayer since the alkyl tail bands have not shifted significantly to higher values (Figure 4.33). In the presence of DNA (Figure 4.34), increased disorder in the alkyl tails is again observed as a red shift in the asymmetric CH_2 stretch band. The spectra region at the 1800 to 1400 cm^{-1} and 1300 to 950 cm^{-1} is again similar to the spectra observed at pH 4.

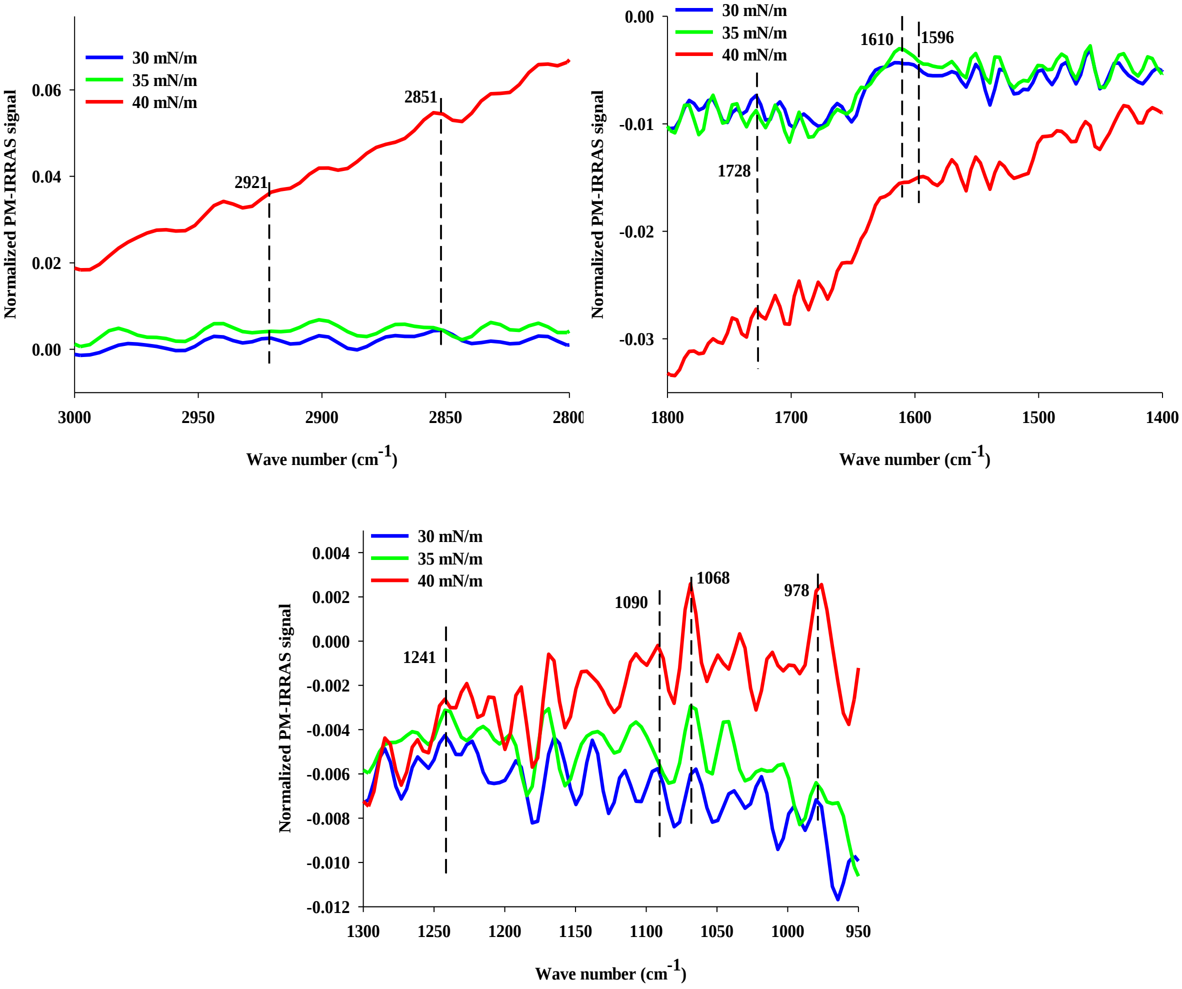

Figure 4.33. PM-IRRAS spectra of the 16-7NH-16/DOPE without DNA at pH 9 at different surface pressures.

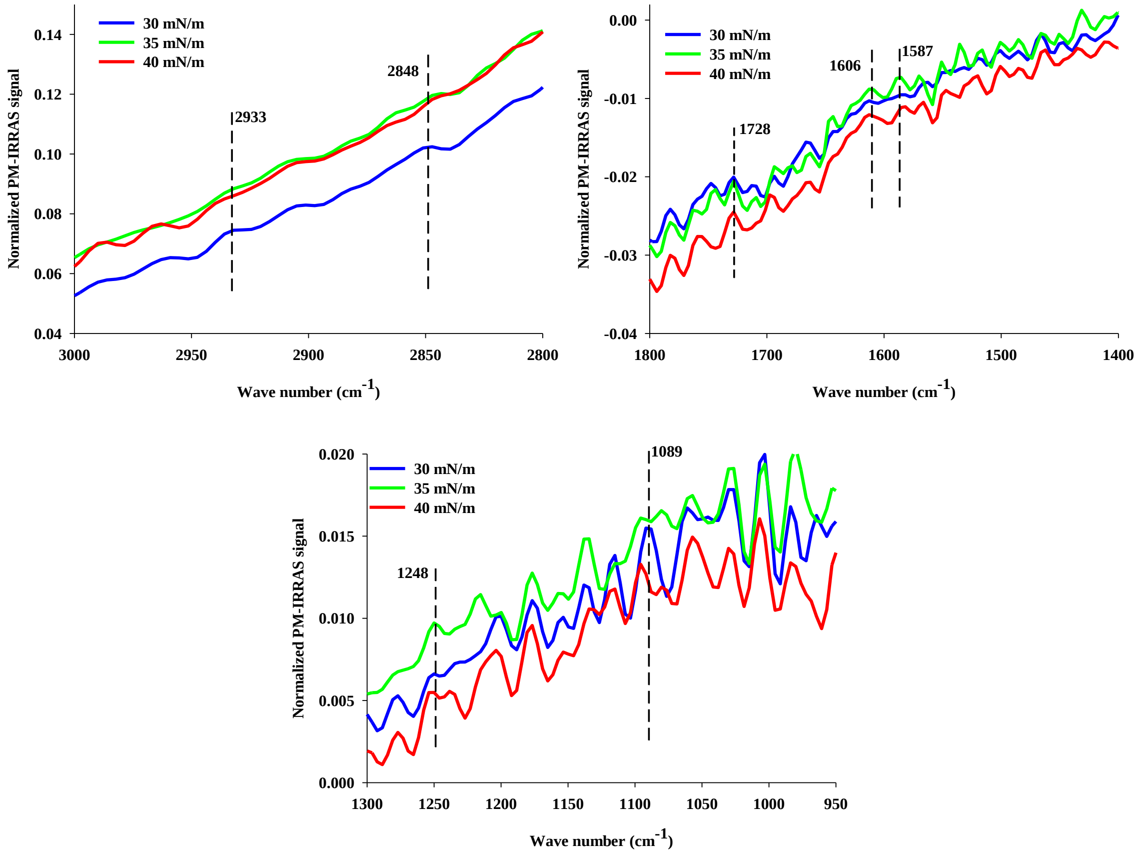

Figure 4.34. PM-IRRAS spectra of the 16-7NH-16/DOPE with DNA at pH 9 at different surface pressures.

We have further investigated the PM-IRRAS spectra of the 16-7-16/DOPE system in presence or absence of DNA. As can be seen from the Figure 4.35 at pH 4, that the CH_2 band regions of the alkyl tails resembles the disoriented structure (LE or LE-LC phase). The asymmetric PO_2^- shifted to higher value (around 1239 cm^{-1}) indicative of the interaction at the gemini- PO_2^- interaction. We have observed similar PM-IRRAS spectra at pH 7 (Figure 4.36) and pH 9 (data not shown). In general, the presence of the LE or LE-LC phase is observed for the 16-7-16/DOPE/DNA system in all pHs. These results are in good agreement with the isotherm and compressibility modulus results (Figure 4.18).

Several models have been proposed to elucidate the complex properties of the cationic lipid/DNA complex:

1. Electrostatic interactions between the lipid head group and phosphate group of DNA;

2. Base binding between lipid polar groups and the bases donor atoms; and
3. Hydrophobic interactions between aliphatic tails [54, 244, 245].

In general, the PM-IRRAS spectra revealed that the complex monolayer of 16-7NH-16/DOPE/DNA undergoes electrostatic, ion-dipole as well as hydrophobic interactions among the components.

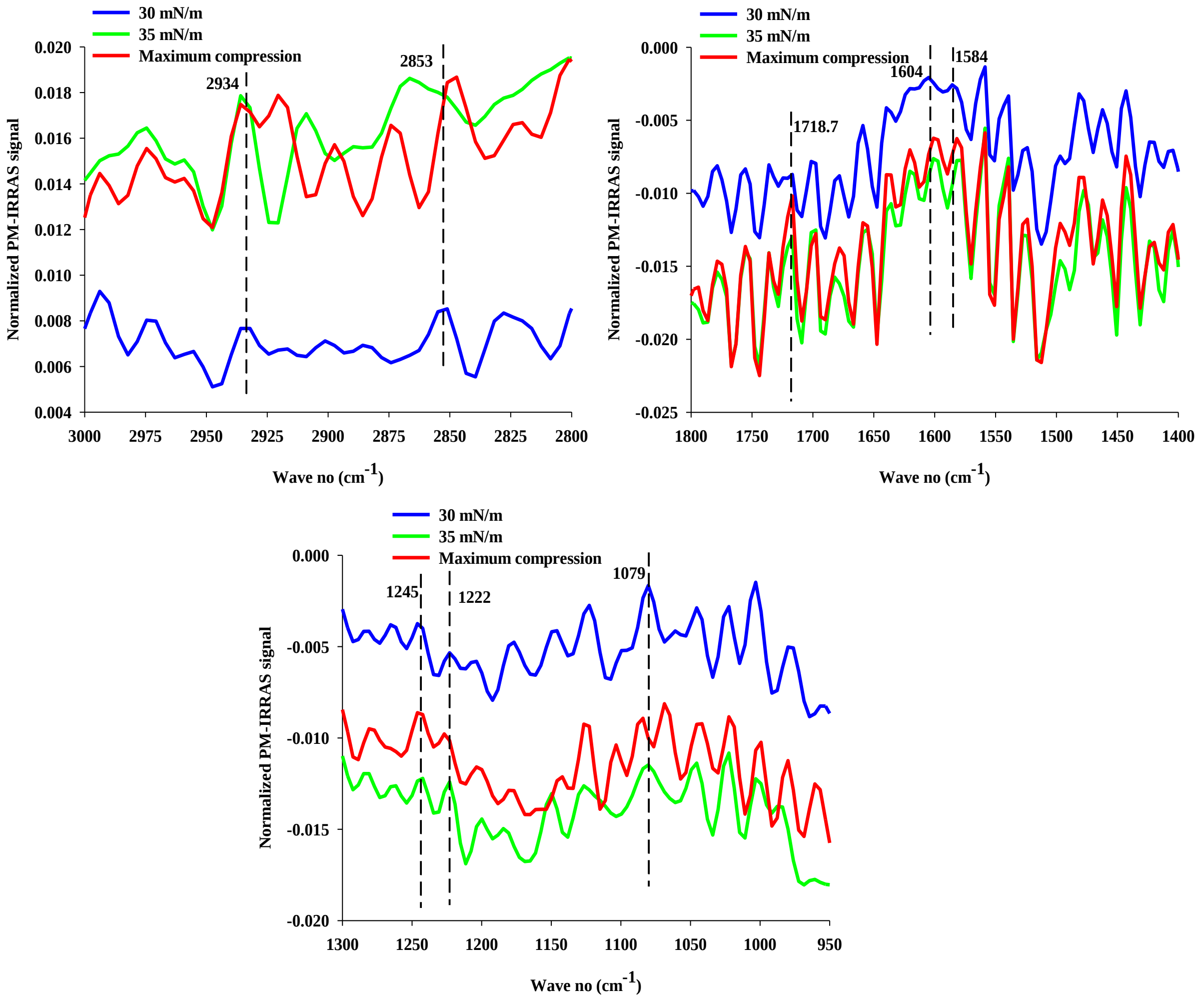

Figure 4.35. PM-IRRAS spectra of the 16-7-16/DOPE with DNA at pH 4 at different surface pressures.

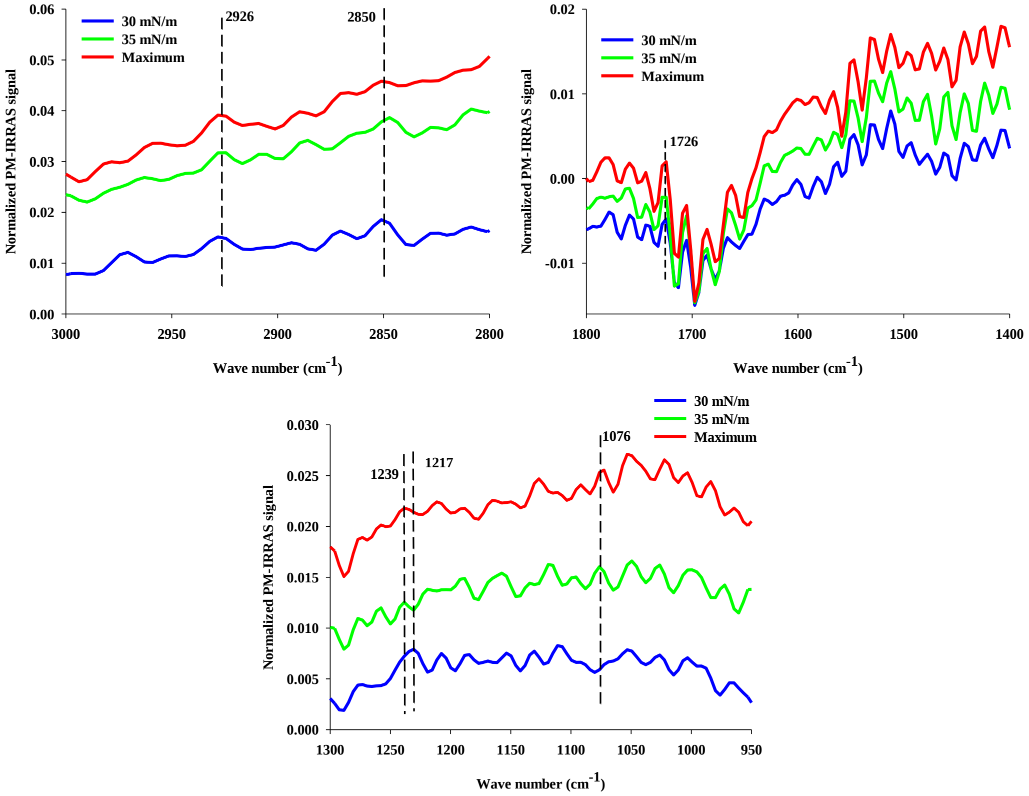

Figure 4.36. PM-IRRAS spectra of the 16-7-16/DOPE with DNA at pH 7 at different surface pressures.

4.3. Summary

Based upon our detailed characterization of the mixed gemini surfactant/DOPE/DNA systems, we can conclude that both the DOPE and DNA play important roles in defining the nature of the monolayers formed. The DOPE tends to condense the monolayers formed by gemini surfactants, both in the presence or absence of DNA. In the presence of DNA, KPFM demonstrates that the gemini surfactant strongly undergoes electrostatic interactions with DNA, fibril type complex structures. We believe that the DOPE may not participate in this gemini/DNA complex but rather resides outside of this complex (based upon our interpretation of the AFM results). The exact role of DOPE in this transfection complex is not clear, other than the described condensation effect. Further investigation is required to completely elucidate the role of DOPE in the system, and importantly it’s effect on model biological membranes. Thus, in the following chapter (Chapter V), we have evaluated the effect of the gemini/DOPE/DNA system on monolayers that represent a model endosomal membrane.

Chapter V

Interactions of Gemini surfactant-phospholipid based transfection system with model endosomal cell membrane.

5. 1. Results and Discussion

5.1.1. π-A isotherm and compressibility modulus of the model membrane components

The surface pressure-area (π–A) isotherms at different pHs are shown in Figure 5.1 A, C, and E, for pure DPPC, pure cholesterol and a 75/25% mixture of DPPC/cholesterol, which is used as a representative model for the endosomal membrane. As can be seen, pure cholesterol forms a typical condensed monolayer with liftoff areas of ~52.4, 43.2, 37.8 Å^2 at pH 4, 7 and 9, respectively. Regardless of the pH, the collapse pressure of the monolayer is ~45 mN/m, and the minimum cross sectional area for cholesterol in the monolayer ranges from 31 to 49 Å^2 /molecule (Table 5.1). All of the parameters determined in this work for the cholesterol monolayers are consistent with the results described in the literature [156, 246-249]. Cholesterol forms a condensed monolayer in which molecules arrange themselves in a vertical position or slightly tilted towards the surface.

To fully understand the monolayer phase behavior, the compressibility moduli (C_s^{-1}) were evaluated [215] and are presented in the Table 5.1 and Figure 5.1 B, D, and F. The higher the compressibility modulus values, the lower the interfacial elasticity of the monolayer. At pH 4, the cholesterol monolayer remains in the G phase from ~250 Å^2 to 52 Å^2 molecular area (Figures 5.1A and 5.2B). Liftoff occurs (at a molecular area of approximately 52 Å^2) in which the monolayer undergoes a sharp change from the G to LC phase over a narrow surface pressure range (0-5 mN/m). Between 5 and 20 mN/m, the monolayer remains in the LC phase before finally reaching the S phase at ~21 mN/m (pH 4). Both pH 7 and 9 showed similar phase behavior to that at pH 4. Interestingly, at pH 9, the monolayer exhibited the greatest rigidity based on the maximum C_s^{-1} values (593 mN/m). The maximum C_s^{-1} value of cholesterol monolayer has been observed to reach values of between 650 to 693 mN/m on a water subphase [156, 249]. Under surface pressure conditions consistent with natural cellular membranes (30–35 mN/m), cholesterol is found in a solid or S phase for all pH conditions.

BAM images of the cholesterol monolayer at the air/buffer (pH 4) are presented in Figure 5.3. At low surface pressures, where the cholesterol monolayer is in the G phase, circular or ovoid solid domains are observed (0.27 mN/m). Upon increasing the surface pressure, the domains merged together, and mixed G-S phase domains are observed (3.86 mN/m). As the monolayer is further compressed, the domains merged together and formed a homogeneous solid film (> 20 mN/m), indicative of the solid S phase. Here the steroid rings of cholesterol are likely to be oriented vertically toward the air side of the air/buffer interface. At higher surface pressures, and beyond collapse, bright domains begin to appear, consistent with aggregate or multilayer formation. Similar BAM images are observed at pH 7 and pH 9, and are provided as Appendix Figure A5.1 and A5.2. Our results are similar to the results obtained by Miñones et *al.* [156].

At pH 4, the DPPC monolayer exhibits a G-LE phase transition in the surface pressure range of 0 to ~0.8 mN/m (Figures 5.1 A and B). An LE phase is observed for surface pressures between 0.9 and ~5 mN/m (shown as a loop in Figure 5.2A), followed by an LE-LC phase transition at surface pressures between 6 and 16 mN/m, with C_s^{-1} values increasing to ~100 mN/m. The monolayer remains in the LC phase until collapse (~52 mN/m). There is a distinct plateau observed in the isotherm in the region of ~5.2 to 6.6 mN/m surface pressure (Figure 5.1A, indicated with arrow 'LE-LC'), which is a characteristic feature of the DPPC monolayer. The same plateau is observed at approximately the same region of surface pressures at pH 7, and at slightly higher surface pressures of ~6.2 to 7.0 mN/m at 9 (Figure 5.1 C and D). This plateau is attributed to changes in the orientations of the DPPC molecules upon compression. It has been previously reported the DPPC monolayer exhibits first order phase transition from the LE to LC state (also referred as gel to liquid crystal transition) over a similar range of surface pressures as the plateau observed in this work (i.e. 5 – 7 mN/m) [113]. In our case the transition is not first order since the surface pressure does not remain constant. Similar results are reported by Minones et *al.*[156]. Our results of DPPC monolayer behavior at air/buffer interface are in good agreement with the published data [156, 180, 249-251]. Regardless of the pH, the DPPC monolayer displayed similar cross sectional area (~60 $Å^2$) as well as maximum surface pressure (53 mN/m; Table 5.1); however, the monolayer is relatively expanded at pH 4 compared to pH 7 or 9 (Figure 5.1 and Table 5.1). In the range of natural membrane surface pressures the DPPC monolayer remained in the LC phase (enclosed with the dotted lines in Figure 5.1 B, D, and F); although at pH 9, C_s^{-1} is closer to values associated with a solid phase. Figure 5.4 shows BAM images of the pure DPPC monolayer at pH 4. At low surface pressures (0.07 mN/m), when the monolayer is found in the G phase, network like domains are observed. As the surface pressure increases in the range of 0.21 to 4 mN/m, the monolayer is observed as a fairly homogenous film with minor defects and corresponds to the G-LE phase transition and the LE phase (1-4 mN/m). In the LE phase, the acyl tails of the lipids are neither ordered nor protruding vertically from the surface, resulting in less reflection of the incident light and dark BAM images. At the phase transition of LE-LC ($\pi \geq 5$ mN/m), small bright circular and irregular, lobed domains suspended in a darker phase are observed. These domains increased in size as the monolayer undergoes LE to LC phase transition with higher surface pressure. At the LE-LC phase transition the different tilt of the alkyl chain of the DPPC molecules induces differing reflectivity (anisotropy) with respect to the plane of incident [156, 252]. As the surface pressure further increases, the domains merge together and gradually blur, giving rise to relatively homogenous BAM images prior to monolayer collapse. BAM images are similar regardless of the pH of the subphase (images at pH 7 and 9 are provided as Appendix Figure A5.3 and A5.4) and are consistent with the published results [156, 253].

Table 5.1. Monolayer properties of the DPPC, Cholesterol and their mixture at air/buffer interface.

System	pH	A_L (Å^2)	A_c (Å^2)	π_c (mN/m)	A_∞ (Å^2)	C_s^{-1} (mN/m)		
						30 mN/m	35 mN/m	Max
DPPC	4	97.0	36.5	52.6	53.6	135.8	134.7	163.4
	7	117.7	47.3	53.3	60.2	191.8	193.6	235.7
	9	130.8	50.4	52.8	62.9	238.3	220.6	271.4
Cholesterol	4	52.4	39.5	44.8	49.2	253.8	207.9	265.9
	7	43.2	34.4	45.2	39.7	238.4	337.7	376.0
	9	37.8	28.4	45.9	31.3	503.9	581.3	593.6
DPPC/Cholesterol	4	74.2	37.6	52.3	48.1	287.3	256.6	315.2
	7	74.3	38.2	52.1	49.0	174.8	191.1	222.4
	9	64.4	34.3	52.3	41.4	249.0	252.9	338.5

Parameters obtained from the π-A isotherms are liftoff area, A_L; molecular area at collapse, A_c; collapse pressure, π_c; minimum cross sectional area or limiting area, A_∞. Compressibility modulus (C_s^{-1}) at 30 mN/m, 35 mN/m surface pressure and the maximum compressibility modulus values.

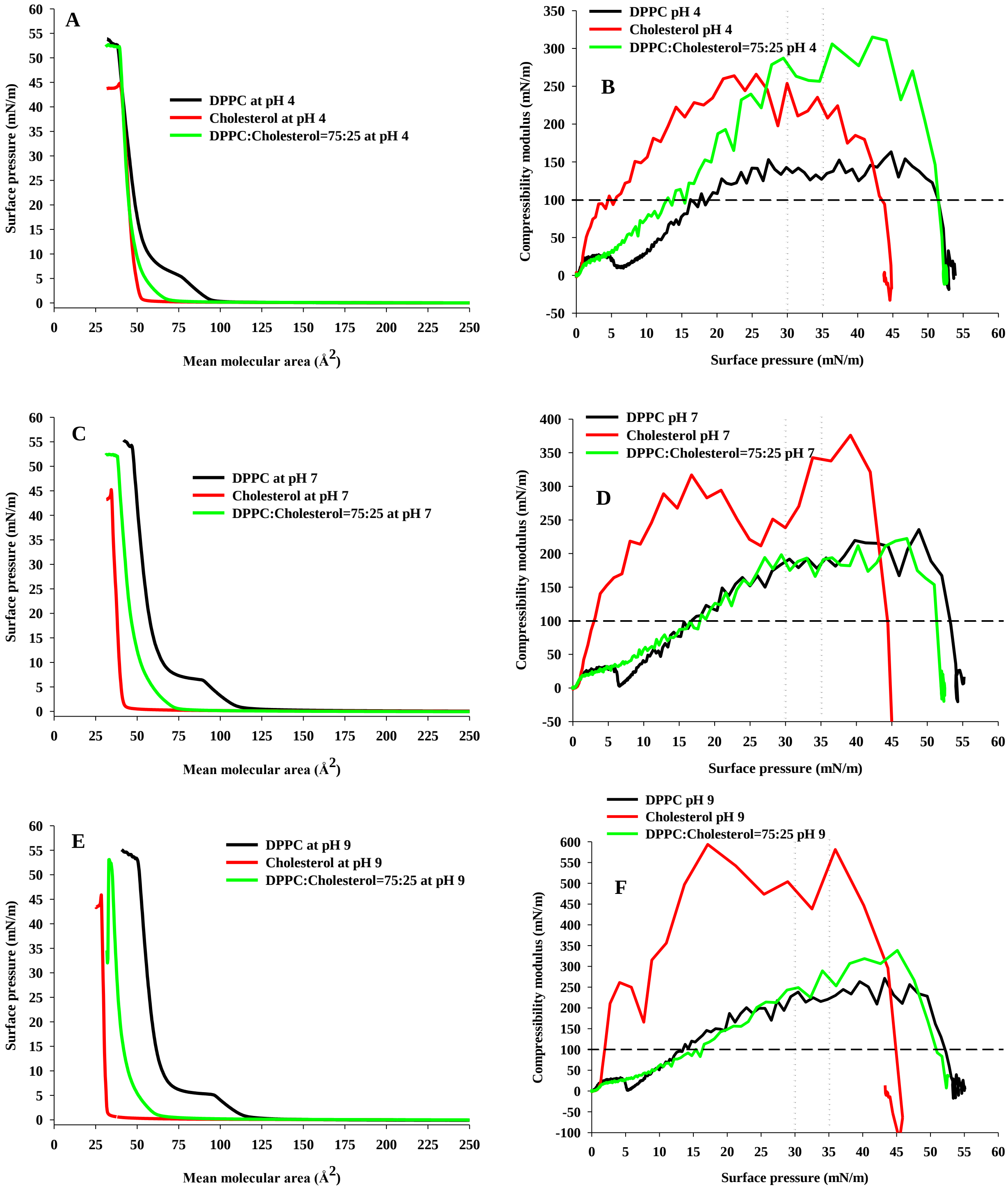

Figure 5.1. π-A isotherm (A, C, and E) and compressibility modulus (B, D, and F) of the DPPC, Cholesterol, their mixture (DPPC: cholesterol = 75:25 %) at pH 4 (A, B), 7(C, D) and 9 (E, F). The LE-LC phase is shown in Figure A. The dotted line encloses the compressibility modulus values at the 30-35 mN/m.

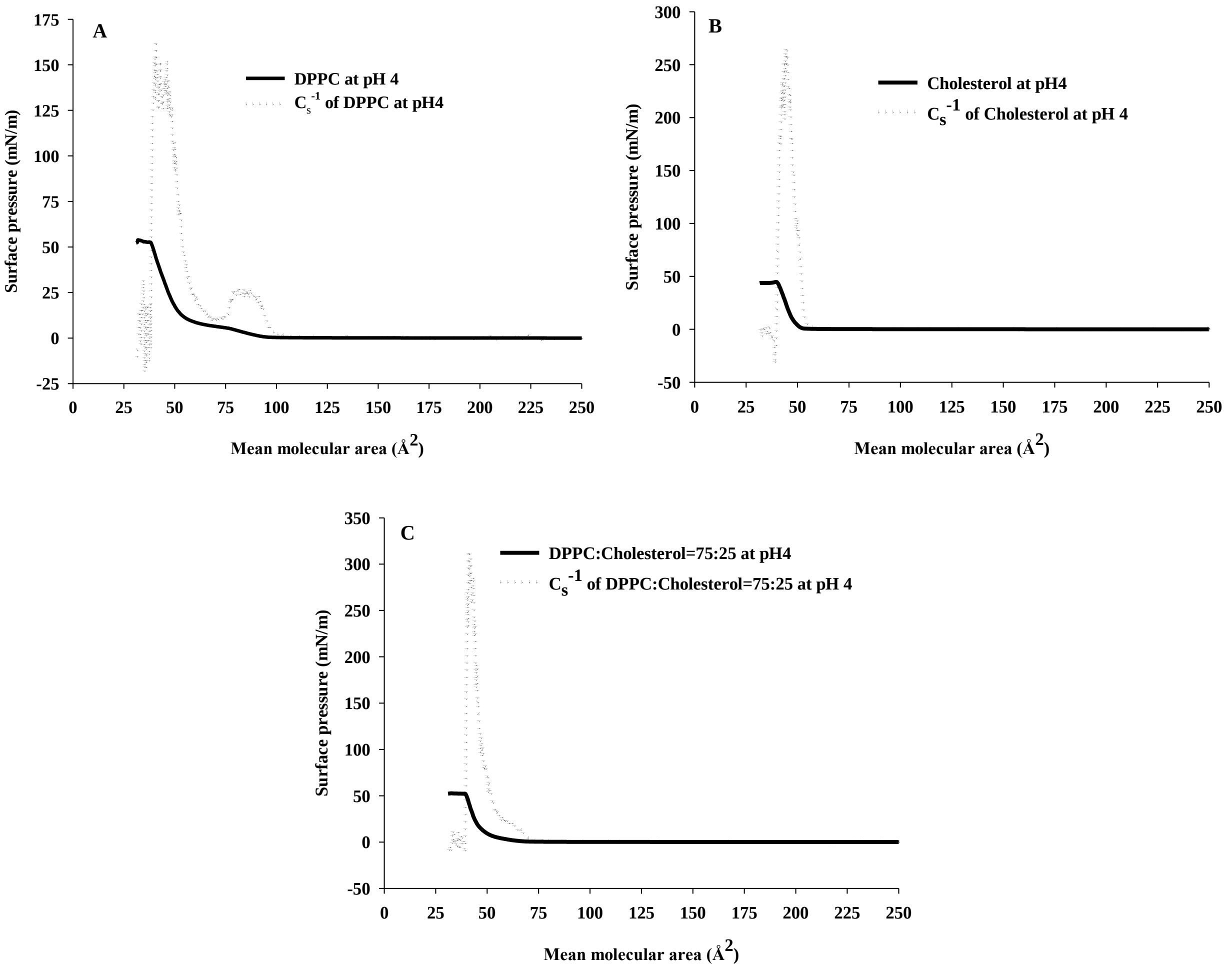

Figure 5.2. Compressibility modulus values of the DPPC (A), Cholesterol (B) and model membrane (DPPC: cholesterol= 75:25 %) (C) at air /buffer (pH 4) interface.

As mentioned earlier in Section 1.6.2b the amount of cholesterol in the plasma membrane varies from 30% to 50% [147, 159]. Van Meer et *al.* have suggested that the early and late endosomes may have a cholesterol content lower than 30% [147] or it may vary from 25 to 30% [160]. Additionally, some recent Langmuir monolayer studies have utilized 30% cholesterol as model mammalian cell membrane along with the DPPC (70%) [156, 161]. We have used the molar ratio of DPPC/cholesterol =75/25 % for our experiment to simulate the endosomal membrane. The DPPC/cholesterol mixed monolayer system along with their corresponding compressibility modulus values is presented in Figure 5.1 and Table 5.1. As can be seen from Figure 5.1A and B, and 5.2C, the monolayer undergoes a G-LE phase transition at ~0.6 mN/m surface pressure at pH 4, then an LE-LC phase transition is observed between 0.6 to 13 mN/m. The monolayer reaches the S phase at

~27 mN/m surface pressure. At the cell membrane surface pressure range, the DPPC/cholesterol monolayer is in an S phase (Figure 5.1B), indicative of rigid monolayer formation. Similar rigid monolayer behaviour can be seen at pH 9 (Figure 5.1F); however, at pH 7, the monolayer is found in the LC phase indicating a relatively less rigid monolayer. Noteworthy, there is no plateau formation observed for the DPPC/cholesterol system at surface pressures where the DPPC monolayer underwent the LE-LC transition. This indicates that addition of cholesterol in the system causes condensation of the monolayer. The condensation effect of cholesterol is well known and our results are consistent with the published results of other research groups [156, 180, 254-258]. The condensation effect of cholesterol is observed at low surface pressure regardless of the pH of the subphase [254]. Additionally, the minimum cross sectional area of the mixed system ranges from 41 to 49 Å^2/molecules, indicating relatively vertical orientation of the molecules at the air/buffer interface (Table 5.1).

BAM images for the mixed DPPC/cholesterol monolayer are presented in Figure 5.5 at the air/buffer (pH 4) interface. At low surface pressure (~0.27 to 1.22 mN/m), where DPPC/cholesterol monolayer is in the G-LE phase transition, exhibits circular or ovoid domains. Upon compressing the monolayer, the LE phase undergoes LC phase transition and a blur images are observed at 2.34 mN/m. As the monolayer is further compressed, the domains merged together and formed solid film (> ~25mN/m) Interestingly, the lobbed domains of pure DPPC at low surface pressure (Figure 5.4, below 10 mN/m) in not observed in the DPPC/cholesterol mixture, which is indicative of the condensing effect of cholesterol [156, 249]. Similar BAM images are observed at pH 7 and 9 (images are provided as Appendix Figure A5.5 and A5.6) are similar to the pH 4.

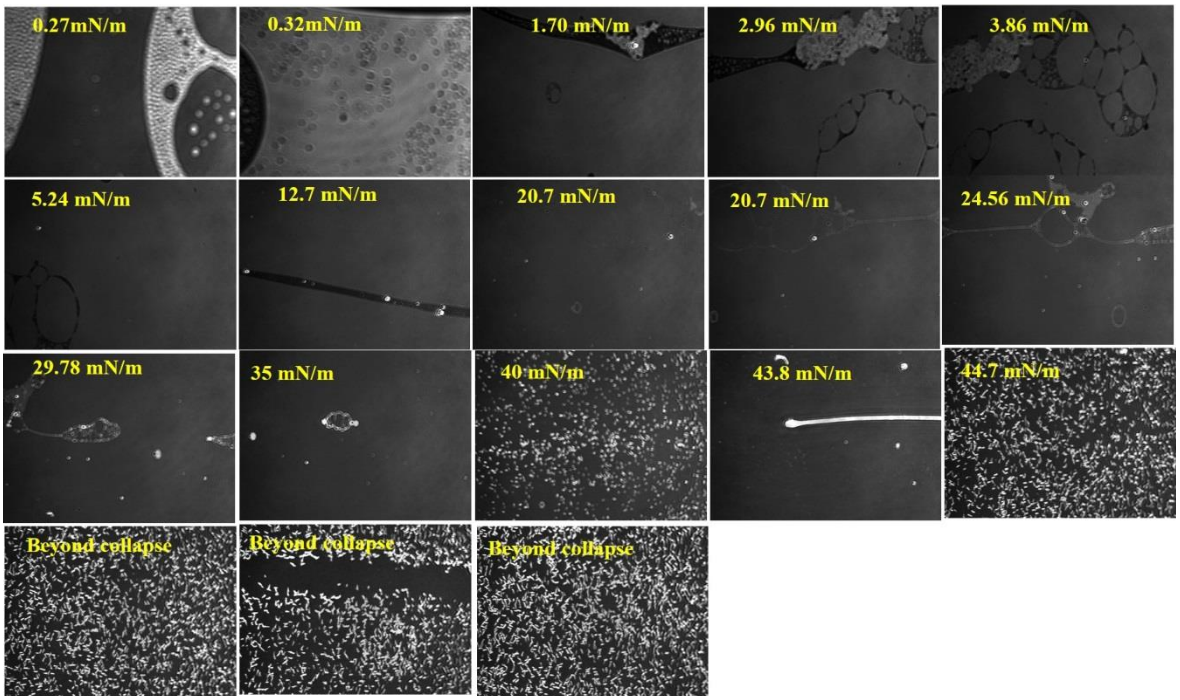

Figure 5.3. BAM image of the pure cholesterol monolayer at the air/buffer (pH 4) interface at various surface pressures.

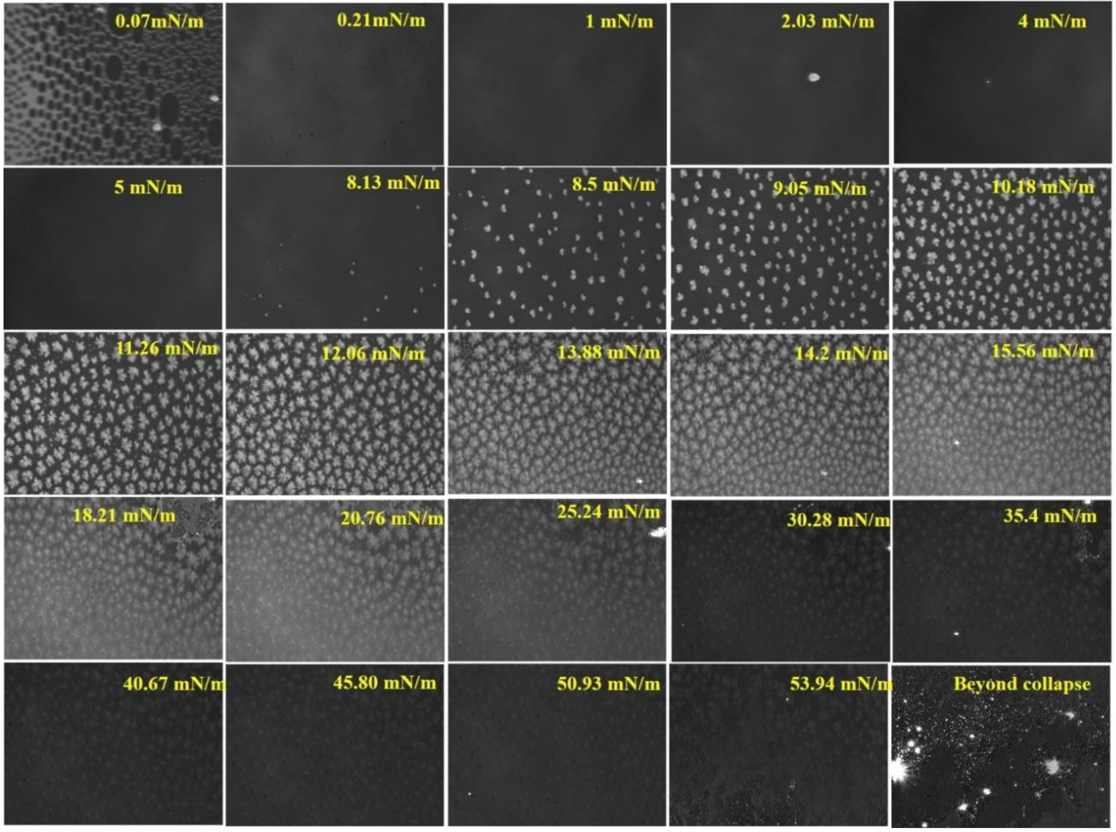

Figure 5.4. BAM images of the pure DPPC monolayer at the air/buffer (pH 4) interface at various surface pressures.

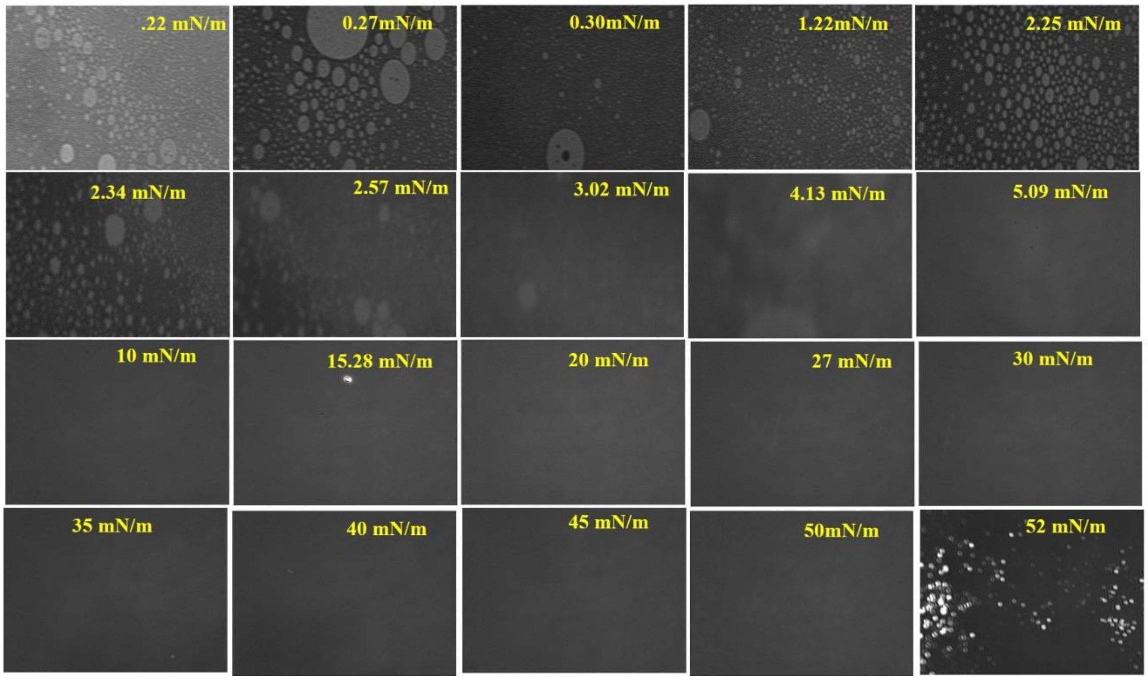

Figure 5.5. BAM images of the model membrane (DPPC/cholesterol=75/25 %) monolayer at the air/buffer (pH 4) interface at various surface pressures.

5.1.2. Effect of pure gemini surfactants on the model membrane

To the best of our knowledge, the interactions of gemini/DOPE/DNA system with the model membrane (DPPC/cholesterol) has not yet been reported. To get a better insight of the interactions, we have injected the surfactant systems under the subphase at each pH, mixed them and subsequently spread the DPPC/cholesterol model membrane monolayer on top of this subphase that now contains the components of the gene delivery system. We believe that this unique study design will provide insight with respect to the relevance of our systems in a real biological system (for example an intravenous injection of lipoplexes into the aqueous environment of the blood stream where they can eventually interact with cell membranes at the site of action[14]). Several researchers have used the DPPC/cholesterol based system to evaluate drug-membrane interactions [249], phospholipid-model membrane interactions [180], or sterol-phospholipid interactions [156]. Since the surface pressure of the actual cell membrane ranges from around 30-35 mN/m, we will take a closer look at this surface pressure range along with the detailed analysis of the isotherm in the following discussions.

The effect of 16-7-16 based systems with the model DPPC/cholesterol membrane are shown in Figure 5.6. At first we have determined the 16-7-16 with the DPPC/cholesterol system at pH 4. As can be seen from Figure 5.6A and 5.7A that the 16-7-16 induces fluidization in the model membrane at pH 4. The C_s^{-1} values revealed the presence of LE-LC phase up to the surface pressure of 30 mN/m (Figure 5.7A). At the cell membrane surface pressure range (30-35 mN/m), the 16-7-16/DPPC/cholesterol system shows the presence of LE phase whereas the pure DPPC/cholesterol exhibits S phase (C_s^{-1} values ranges from ~287 to 256 mN/m) (Figure 5.7B, Table 5.1 and 5.2). Thus, 16-7-16 substantially changed the rigidity of the model membrane which corresponds to the fluidization. The fluidization effect of the drug to the model membrane has been evaluated by several researchers, for instance, paclitaxel [259], prazosin [169], and natamycin [249] with the DPPC/cholesterol, tetracaine with the 1,2-dimyristoyl-*sn*-glycero-3-phosphocholine (DMPC)/ cholesterol [260], hexadecylphosphocholine and erucylphosphocholine with the POPC/cholesterol [261], and toremifene with the dipalmitoyl-phosphatidyl-glycerol (DPPG) model membrane [262]. In all cases, presence of the drug molecule substantially reduced the compressibility modulus of the pure model membrane, which was considered to be the fluidizing effect of drug to the model membrane.

At pH 7, DPPC/cholesterol monolayer exhibits a LC phase transition (C_s^{-1} values ranges from ~131 to 120 mN/m) in presence of the pure 16-7-16 (Figure 5.7 D). In comparison with the 16-7-16/DPPC/cholesterol with the pure DPPC/cholesterol monolayer (Figure 5.7D), it is found that the 16-7-16 reduced the rigidity of model membrane. However, this reduction in rigidity is not as prominent as was observed at pH 4. At pH 9, similar LC phases are observed at the 30-35 mN/m surface pressure (Figure 5.7F). Overall, the 16-7-16 system induced fluidization at the model membrane regardless of the pHs, and the observed trend is pH4 > pH7 > pH9. The BAM images (Figure 5.12) in presence of pure 16-7-16 system revealed that the DPPC/cholesterol monolayer exhibits the G-LE phase transition at the low surface pressure (~1-10 mN/m), with the presence of dot like domains in dark background. At 30-35 mN/m, the image is suggestive of the LC phase transition with bright dots in a homogeneous film. However, this feature are not observed at the pure DPPC/cholesterol monolayer (Figure 5.5). Thus, 16-7-16 induced some domain formation which might be due to the penetration of the surfactant or adsorption of the surfactant to the DPPC/cholesterol monolayer. In the LC phase, the acyl tails of the lipids are relatively ordered, however, not perfectly vertical to the plane; thus, increased reflection of the incident light occurs and results in the formation of small bright domains at the BAM images. In our case, adsorption might have disoriented the alkyl tail group of the lipids and BAM images shows smaller domains instead of homogenous film (as observed for the pure DPPC/cholesterol). Similar BAM images were observed for the DPPC/cholesterol monolayer in presence of pure 16-7-16 at pH 7 or 9 (data not shown). Thus, the BAM images are clear indication of the fluidization of the monolayer in presence of the surfactant.

On the other hand, it is observed form Figure 5.8 and Table 5.2, 5.3 and 5.4, the DPPC/cholesterol in presence of 16-7NH-16 system formed more expanded monolayer at pH 4 (A_L = 105 Å^2) than at pH 7 (A_L = 96.4 Å^2) and 9 (A_L = 88.7 Å^2). A_∞ is approximately 85.4, 73.4 and 67.4 Å^2/molecules at pH 4, 7 and 9, respectively; indicating relatively condensed monolayer formation at higher pHs. In presence of 16-7NH-16 the DPPC/cholesterol monolayer remained at LE-LC phase transition at pH 4, whereas the monolayer exhibits LC phase transition >15 mN/m at pH 7 and 9 (Figure 5.7 A, C, and E). In the cell membrane surface pressure range, the pure DPPC/cholesterol possess S phase (C_s^{-1} = >250 mN/m) (Figure 5.7B) at pH 4, which was substantially reduced (C_s^{-1} = < ~100 mN/m) in the presence of 16-7NH-16 (Figure 5.7B). This is a clear indication of substantial membrane fluidization effect by the 16-7NH-16 at pH 4. However, at pH 7 and 9, the DPPC/cholesterol monolayer was not influenced by the 16-7NH-16 (Figure 5.7 D, and F). These results are in good agreement of our hypothesis that at pH 4, the 16-7NH-16 possess three positive charge, and undergoes strong electrostatic interaction with the negatively charged model membrane. Whereas at pH 7 or 9, 16-7NH-16 may possess two positive charges in their head group and causes less interaction comparing to pH 4. The negative charge of the DPPC/cholesterol model membrane may be attributed to the presence of phosphate or hydroxyl group at the DPPC and cholesterol polar head groups, respectively. Comparing the monolayer with of 16-7-16/DPPC/cholesterol, 16-7NH-16 induced relatively more rigidity than the 16-7-16 system in all pHs. This could be explained based on the phase behavior of the pure 16-7NH-16 which shows the presence of LE-LC or LC phase whereas the 16-7-16 shows LE phase (Figure 5.7 B, D, and F).

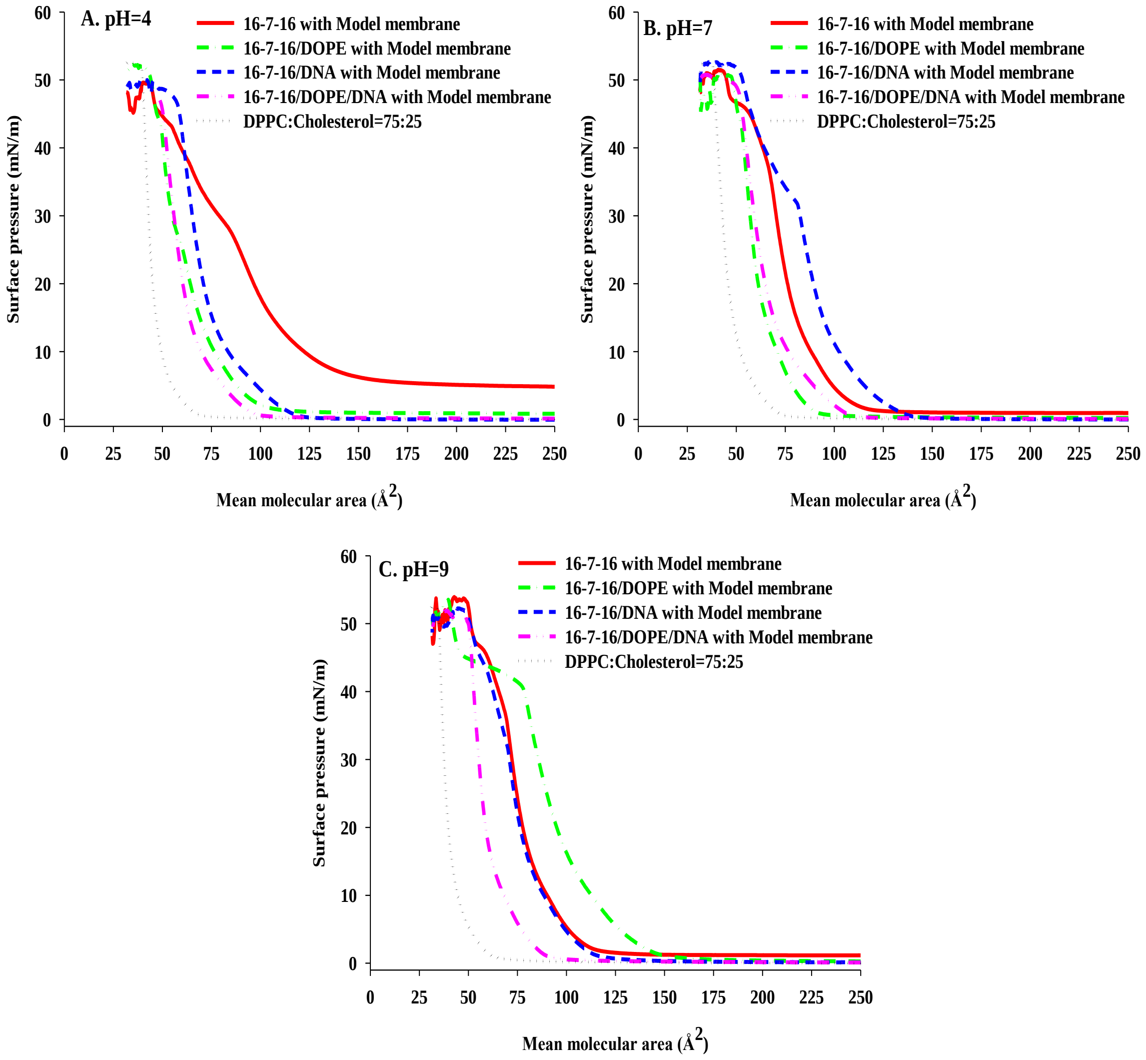

Figure 5.6. π-A isotherm of the 16-7-16 based systems with the model membrane (DPPC/cholesterol = 75/25 %) at pH 4 (A), 7 (B) and 9 (C).

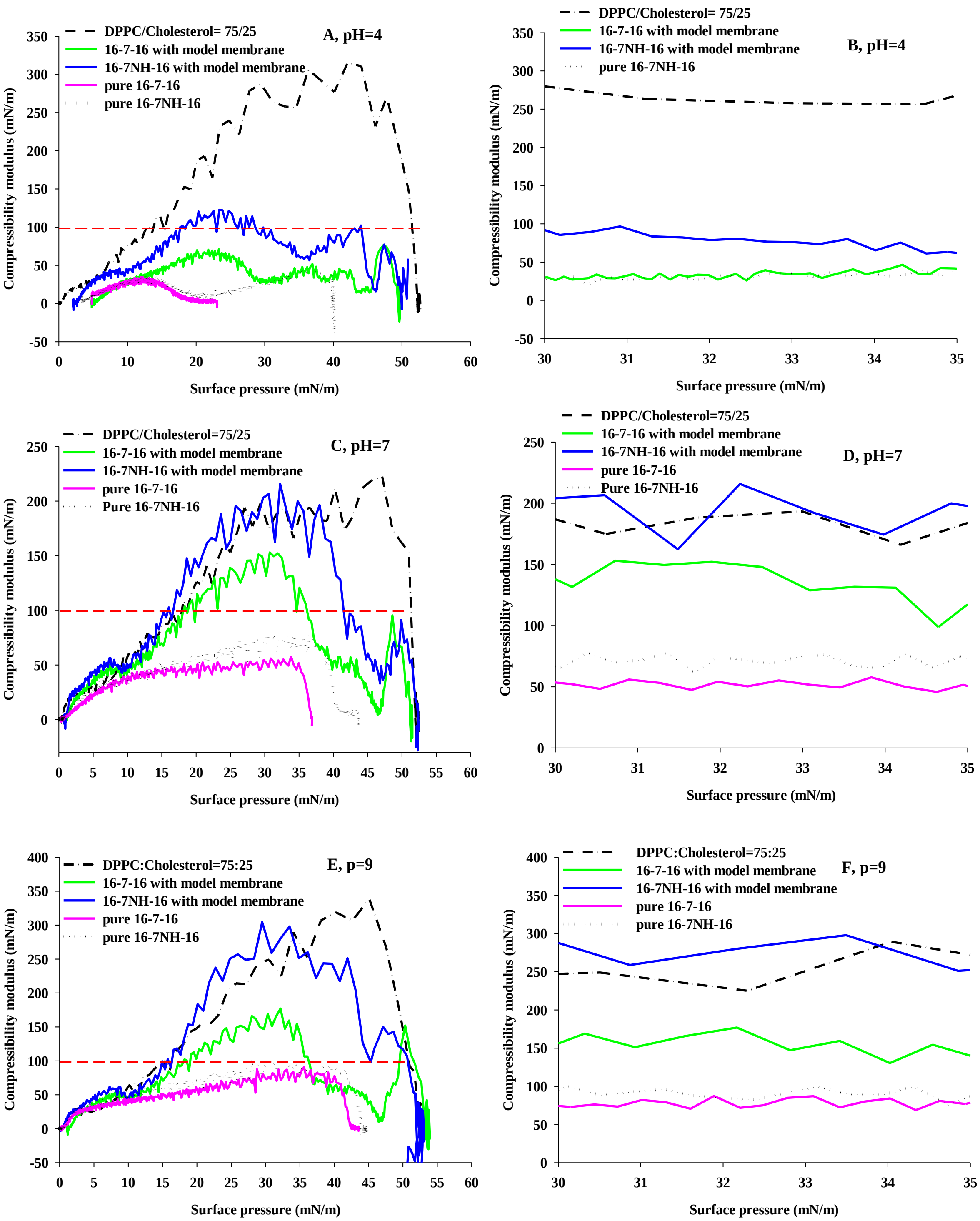

Figure 5.7. Compressibility modulus of the pure components at various pHs (A, C, and E) and at 30-35 mN/m surface pressure range (B, D, and F).

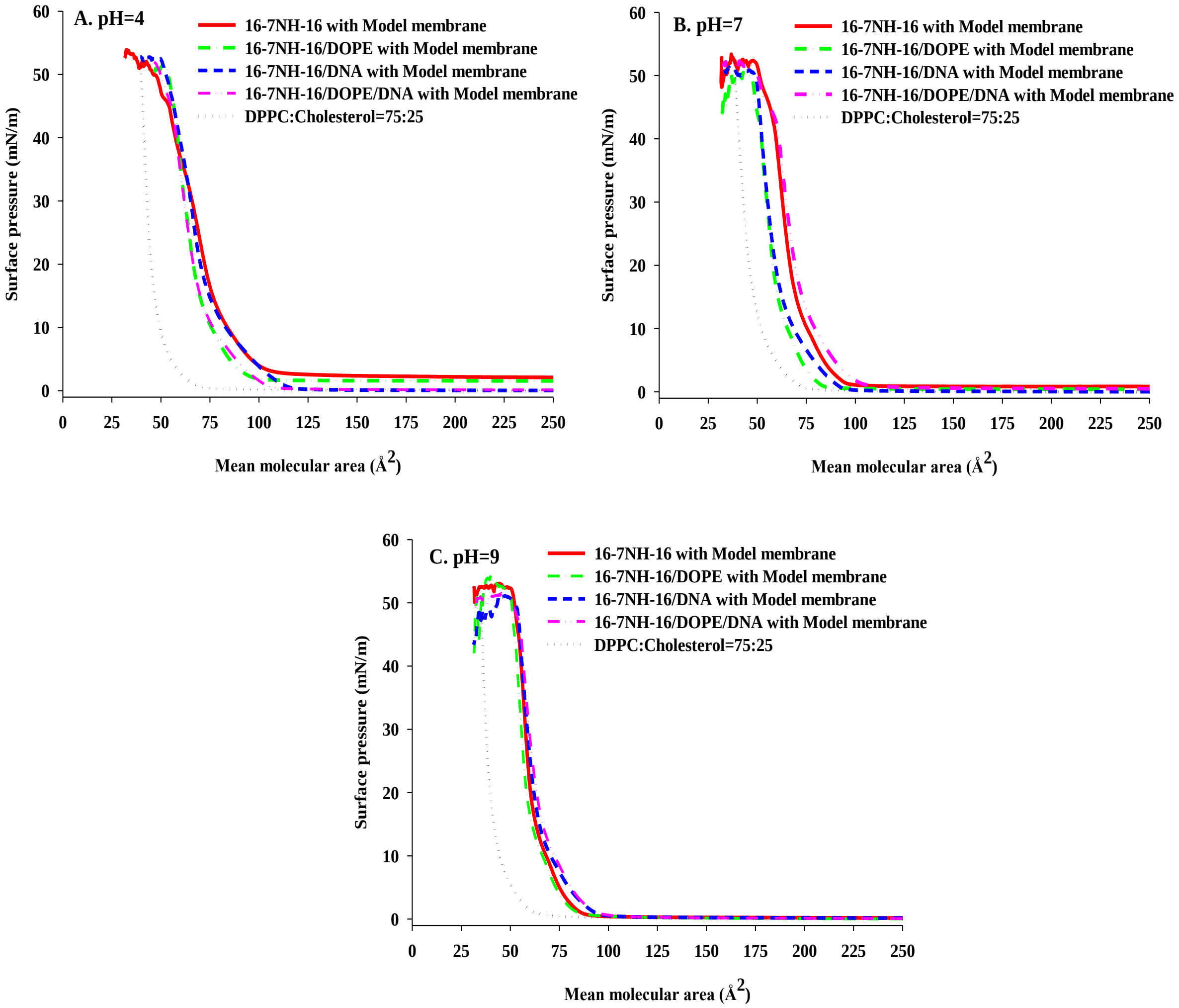

Figure 5.8. π-A isotherm of the 16-7NH-16 based systems with the model membrane (DPPC/cholesterol = 75/25 %) at pH 4 (A), 7 (B) and 9 (C).

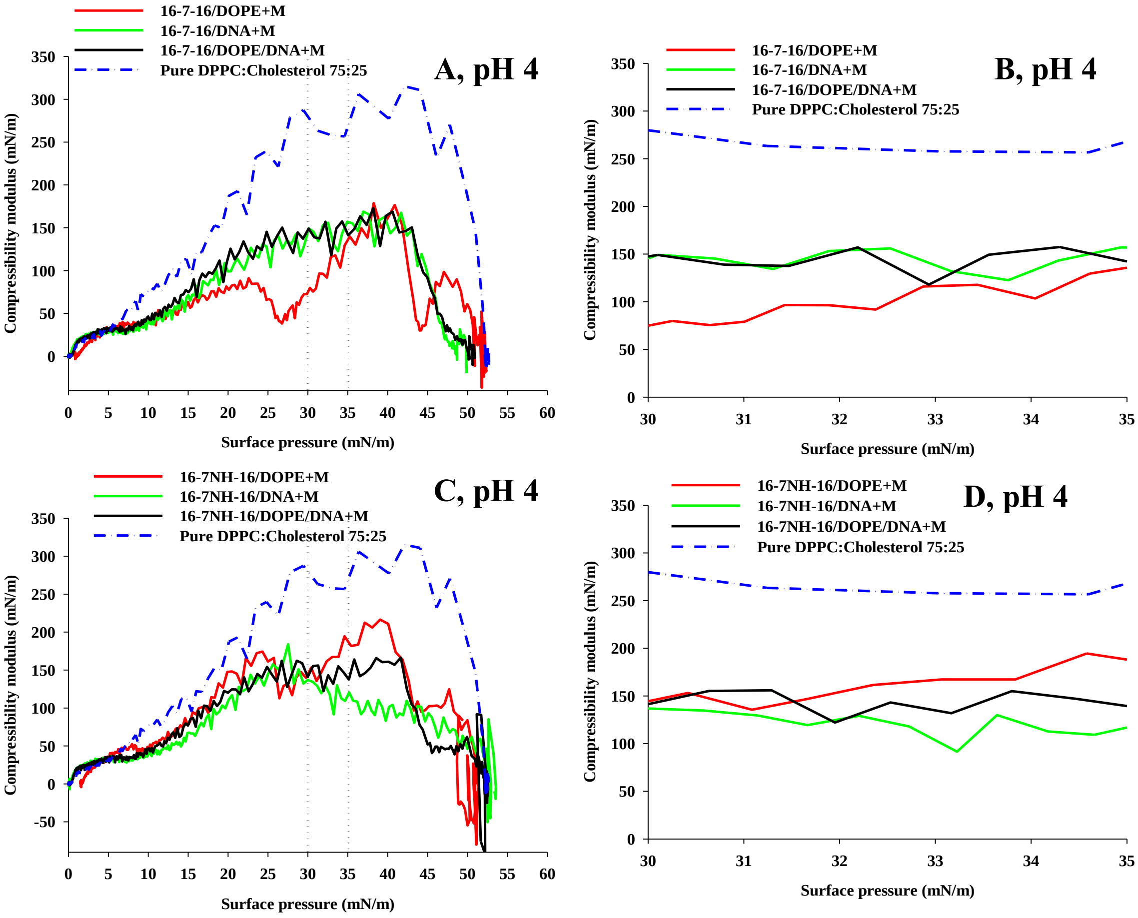

Figure 5.9. Compressibility modulus for the 16-7-16-based system (A, B) and 16-7NH-16-based system (C, D) in pH 4. M = model membrane (DPPC/cholesterol = 75/25 %).

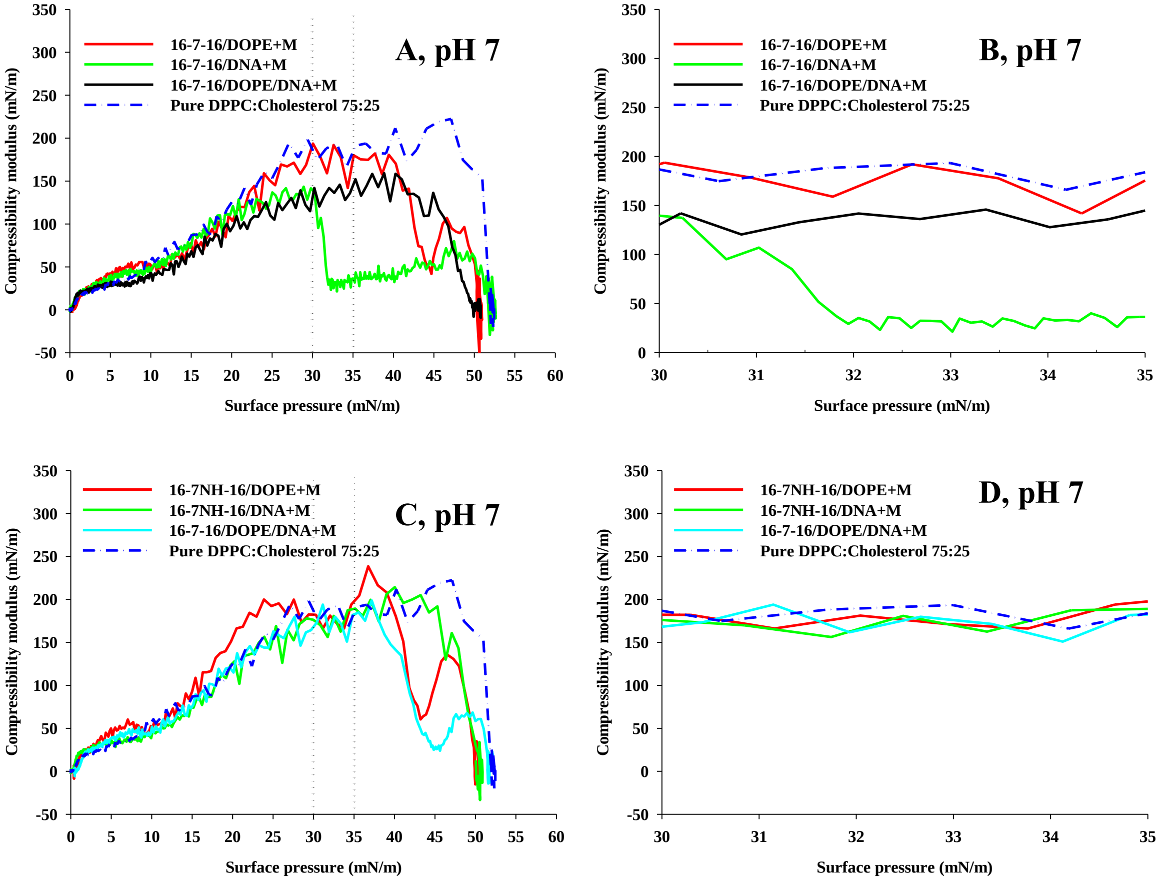

Figure 5.10. Compressibility modulus for the 16-7-16-based system (A, B) and 16-7NH-16-based system (C, D) in pH 7. M = model membrane (DPPC/cholesterol = 75/25 %).

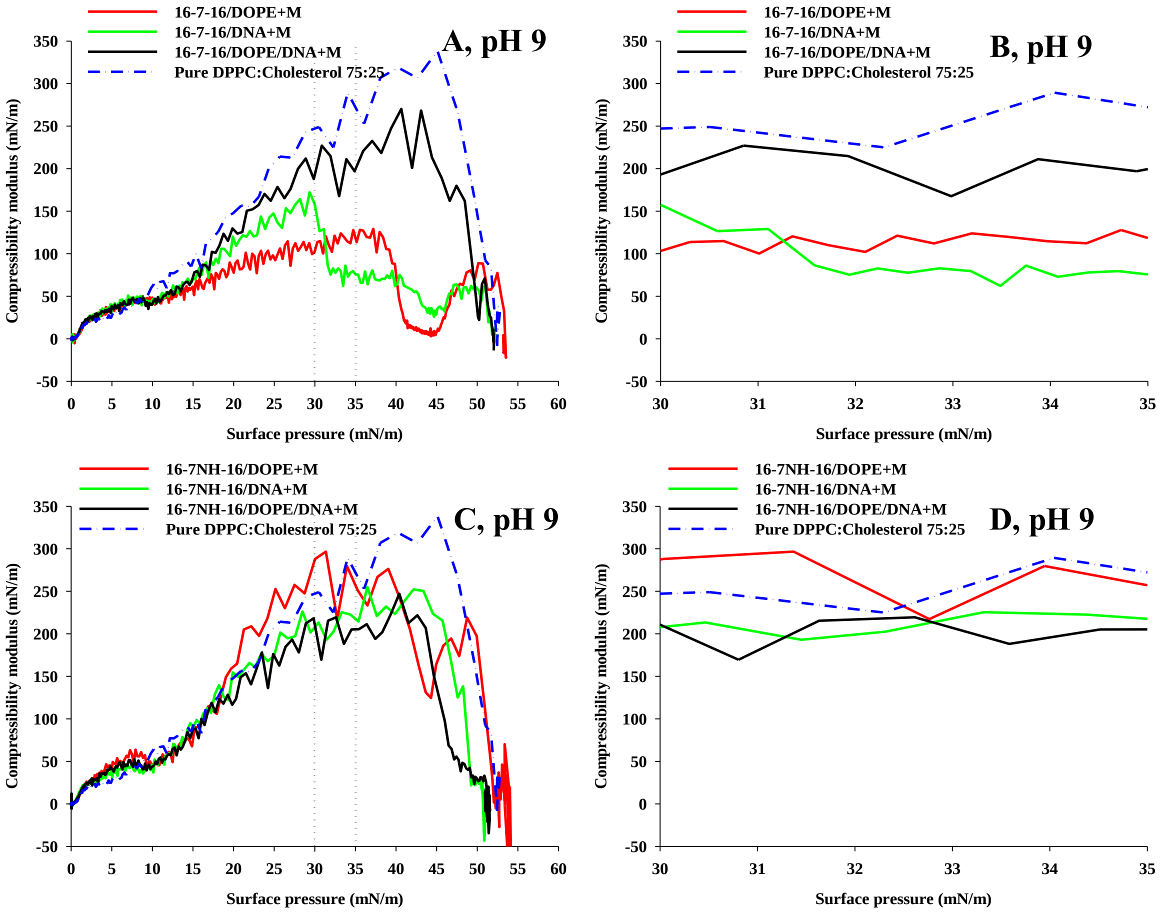

Figure 5.11. Compressibility modulus for the 16-7-16-based system (A, B) and 16-7NH-16-based system (C, D) in pH 9. M=model membrane (DPPC/cholesterol = 75/25 %).

5.1.3. Effect of mixed 16-7-16 systems on the model membrane

The 16-7-16 based system and their interaction with model membrane is presented in Figure 5.6, and the corresponding compressibility modulus values in Figure 5.9 to 5.11. In the presence of 16-7-16/DOPE in the subphase, the DPPC/cholesterol isotherm shows the A_L ~ 102, 94 and 150Å^2 at pH 4, 7 and 9, respectively (Figure 5.6 and Table 5.2, 5.3 and 5.4). The A_∞ values are ~ 73.5, 75 and 71.2 Å^2/molecules at pH 4, 7 and 9, respectively; signifying the relatively condensed monolayer formation in all pHs. In comparison with the 16-7-16/DPPC/cholesterol system, the addition of DOPE caused condensation at the DPPC/cholesterol monolayer regardless of the pHs. At pH 4, in the presence of 16-7-16/DOPE, the DPPC/cholesterol monolayer undergoes a LE-LC phase transition at the surface pressure between 10-20 mN/m and reaches a LC phase > 32 mN/m. The 16-7-16/DOPE system induces fluidization of the model membrane, since an S phase of the model membrane reduced into LE-LC or LC phase in the 30-35 mN/m range. On the other hand, at pH 7 (Figure 5.10 A and B), the 16-7-16/DOPE system induces similar phase transition at the DPPC/cholesterol monolayer to pH 4; however, it remained at the LC phase at surface pressure approximately ≥ 18mN/m. This suggests that the 16-7-16/DOPE with the model membrane forms relatively rigid monolayer at pH 7 than at pH 4. At the surface pressure range of plasma membrane (30-35 mN/m), 16-7-16/DOPE/DPPC/cholesterol shows the presence of LC phase (C_s^{-1} = ~193 to 180 mN/m), which is relatively higher than that of pH 4 (C_s^{-1}= ~79.8 to 139.8 mN/m), (Table 5.2, Figure 5.10). At pH 7, the pure DPPC/cholesterol shows C_s^{-1} values of around 200 mN/m which was not reduced by the presence of 16-7-16/DOPE system. This signifies that there is subtle effect of this system in fluidization of the DPPC/cholesterol membrane. On the other hand, at pH 9, as can be seen from the isotherm and the compressibility modulus values (Figure 5.6C, 5.11 A and B; Table 5.3, 5.4), the 16-7-16 monolayer possess similar phase transitions to pH 7, and forms a LC phase at higher surface pressure (> 25 mN/m). Interestingly, at the 30-35 mN/m range, the monolayer exhibits a LC phase (C_s^{-1} = 100 mN/m) at the lower end of ideal LC phase values (100-250 mN/m for the LC phase [215]). Thus, at pH 9, the 16-7-16 induces fluidization of the model membrane. These results are consistent with the isotherm obtained for the pure 16-7-16/DOPE monolayer at pH 4, 7 and 9 (chapter IV, Figure 4.8). We have observed the most rigid monolayer formation at pH 7, whereas, at pH 4 was the most expanded one. In the current study, the trend of fluidization induced by the 16-7-16/DOPE is: pH4 > pH9 > pH7. BAM images of the DPPC/cholesterol monolayer in the presence of 16-7-16/DOPE system at pH 4 are shown in Figure 5.13. It is observed from the images, the circular domains on black background are present at the low surface pressure (~1-4 mN/m). At the 30-35 mN/m range, the BAM images shows the dot like domains, whereas the pure DPPC/cholesterol (Figure 5.5.) does not possess this domains. As we hypothesized before, the 16-7-16/DOPE can be adsorbed in the DPPC/cholesterol monolayer. This, could lead to the changes in the overall orientation of the DPPC/cholesterol molecules in the air/buffer interface. This images further supports the fluidization effect of the model membrane in presence of 16-7-16/DOPE. Similar BAM images are observed at pH 7 or 9 (Figure 5.16).

We have combined the DNA with the 16-7-16 to observe the interaction of this system with the DPPC/cholesterol model membrane (Figure 5.6, 5.9 to 5.11, Table 5.2, 5.3 and 5.4). From the isotherm it is observed that at the A_L =122.4, 138.2, 117.7 Å^2 at pH 4, 7 and 9, respectively. The $A\infty$ values are ~78, 96 and 95 Å^2/molecules at pH 4, 7 and 9, respectively; indicating relatively condensed monolayer formation at pH 4 than at pH 7 or 9. At pH 4, in presence of 16-7-16/DNA system, the DPPC/cholesterol monolayer undergoes LC phase transition at pressures ≥ 20 mN/m (Figure 5.9A). At the 30-35 mN/m surface pressure range, the presence of 16-7-16/DNA shows reduction in the C_s^{-1} values of the pure DPPC/cholesterol monolayer. Surprisingly, at pH 7 (Figure 5.10B), at 30-35 mN/m, the presence of 16-7-16/DNA dramatically reduced the C_s^{-1} values of the pure DPPC/cholesterol monolayer. Similar results are obtained at the pH 9 (Figure 5.11B). In general, these results suggests that 16-7-16/DNA system may induce fluidization in the DPPC/cholesterol monolayer. Interestingly, this effect is prominently observed at the 30-35 mN/m surface pressure range. The exact reason for this phenomena is not known, however, in chapter IV, Figure 4.12 we have shown that there is a strong electrostatic interaction between the gemini amine group and the DNA phosphate group at the surface pressure ~28-35 mN/m, and the compressibility modulus values were reduced to exhibit the G-LE phase transition. Figure 5.14 shows the BAM images of the model membrane in presence of 16-7-16/DNA system. The presence of circular domains at the low surface pressure (~0.03 to 2 mN/m) is indicative of the G-LE phase. Some small bright dots are observed at the 30-35 mN/m surface pressure indicating the monolayer remained at the LC phase with relatively less orientations of the DPPC/cholesterol. In comparison with the BAM images of the pure DPPC/cholesterol (Figure 5.5) with this system, it seems to have reduced the solid phase of the model membrane to a LC phase, which is an indication of fluidization. BAM images shows small bright domain formation at pH 7 and 9, which implies to the fluidization of the monolayer. Thus, BAM images of the DPPC/cholesterol monolayer in presence of 16-7-16/DNA system, are well correlated with the observed isotherm as compressibility modulus of these system in all pHs.

The DPPC/cholesterol monolayer behaviors in presence of 16-7-16/DOPE/DNA system are demonstrated in Figure 5.6, 5.9 to 5.11. The isotherm possess A_L = 99.1, 108.4, 92.6 Å^2 at pH 4, 7 and 9, respectively and the A_∞ values ~66.5, 73 and 62.6 Å^2/molecules at pH 4, 7 and 9, respectively. Once again the relatively condensed monolayer is formed at pH 4 than at pH 7 or 9. At the cell membrane surface pressure (30-35 mN/m), the 16-7-16/DOPE/DNA shows the C_s^{-1} values ~149.2 to 141.2 mN/m which was considerably lower than the pure DPPC/cholesterol monolayer (~ 287 to 256 mN/m) at pH 4 (Figure 5.9B and Table 5.2). Considering the C_s^{-1} values at the 30-35 mN/m range, 16-7-16/DOPE/DNA system also shows the fluidization effect at pH 7 (Figure 5.10B). Overall, the 16-7-16/DOPE/DNA system fluidized the model membrane follows the trend: pH4 > pH7 > pH9. We believe that the 16-7-16/DOPE/DNA complex may undergo overall net positive zeta potential [35], and cause electrostatic interaction with the phosphate or hydroxyl group of the

DPPC/cholesterol monolayer. By this way the complex system may adsorb at the model membrane and cause changes in the fluidity. We have not found any similar studies to our system as references. However, Lopes-Costa el *al.* have demonstrated the adsorption effect of the DNA on the octadecylamine (ODA) monolayers [263]. Their study revealed that the presence of DNA causes expansion in the ODA monolayer and also lowered the compressibility modulus. They have hypothesized that the electrostatic interaction between the phosphate group of DNA and the positive charge of ODA molecules are responsible for this phenomena. This study signifies that depending on the system (gemini/DNA which may undergo an electrostatic interaction and form a net positive charge) present at the subphase; the complex system (gemini/DNA) may adsorb or penetrate to the DPPC/cholesterol monolayer and cause the condensation or fluidization effects. Apart from the electrostatic interaction and adsorption of the 16-7-16/DOPE/DNA system on the DPPC/cholesterol monolayer, penetration of these system may also occur into the model membrane. The minimum cross sectional area of the pure DPPC/cholesterol is ~ 48, 49, 41 Å^2/molecules at pH 4, 7 and 9, respectively; whereas the presence of 16-7-16/DOPE/DNA increased the values to ~66.5, 73 and 62.6 Å^2/molecules, at corresponding pHs. Thus, there is approximately 1.5 times increase in the cross sectional area of the DPPC/cholesterol in presence of the 16-7-16/DOPE/DNA. This signifies two possibilities, 1. the adsorption of the complex might have disoriented the monolayer, and subsequently (2) penetration of the system into the monolayer. Based on the experimental results both are possible in our case. Cárdenas et *al.* showed that positively charged dioctadecyldimethylammonium bromide (DODAB) and DODAB/disteroylphosphatidylcholine (DSPC) monolayers were influenced by the presence of DNA at the subphase [99]. The electrostatic interaction was the major factor for the fluidization of the monolayer. Additionally, they have not found any penetration effect of DNA into the monolayer since the minimum cross sectional area was not increased substantially. Castano et *al.* have injected the DNA under the cationic bis(guanidinium)-tris(2-aminoethyl)amine-cholesterol (BGTC) or BGTC/DOPE monolayer air/water interface. Their study revealed that regardless of the charge (positive or negative) of the monolayer, the double strands of the DNA molecules oriented parallel to the lipid monolayer plane and adsorbed to the monolayer (Chapter I, Figure 1.14). Same research group further included zwitterionic 1,2-dimyristoyl-sn-glycero-3-phosphocholine (DMPC) with the BGTC lipid [264]. When DNA was injected into the subphase, it adsorbs to BGTC/DMPC monolayers regardless of the lipid monolayer composition.

The BAM images for 16-7-16/DOPE/DNA with model membrane revealed the presence of G-LE phase transition at the surface pressure of ~0.26 to 2.16 (Figure 5.15). The images at the 30-35 mN/m surface pressure is different than that of the pure DPPC/cholesterol BAM images. Similar BAM images are found for at the pH 7 and 9 (Figure 5.16). However, the extent of the fluidization effect is not possible to calculate from the BAM images. Further studies are required to elucidate the mechanism and extent of enhanced model membrane fluidization by the 16-7-16/DOPE/DNA system at pH 4 than at pH 7 or 9. Lopes-Costa et *al.* have shown that the presence of the DNA in the subphase changed the dendritic domains of the octadecylamine (ODA) at air/water interface [263]. The adsorption of the DNA to the ODA molecules caused these changes in the domains of the ODA. We also believe that the 16-7-16/DOPE/DNA may form complexes at the aqueous subphase with net positive charges, which may interact with the polar head group of the DPPC/cholesterol molecules and induces adsorption as well as the penetration of the complexed molecules to the membrane, and consequently reduced the rigidity. The penetration effect of the16-7-16/DOPE/DNA is crucial to disrupt the endosomal membrane and release the DNA into the cytoplasm.

Table 5.2: DPPC/cholesterol monolayer properties in presence of various mixed system in **pH 4**.

System	A_L(Å^2)	A_c (Å^2)	π_c (mN/m)	$A\infty$ (Å^2)	C_s^{-1}		
					30mN/m	35mN/m	Max
DPPC/Cholesterol	74.2	37.6	52.3	48.1	**287.3**	**256.6**	**315.2**
16-7-16	154.1	43.6	49.4	85.5	30.1	40.4	96.2
16-7-16/DOPE	102.7	43.6	50.7	73.5	79.8	139.8	178.7
16-7-16/DNA	122.4	53.7	48.0	78.0	149.2	155.3	168.9
16-7-16/DOPE/DNA	99.1	45.5	48.9	66.5	149.1	141.2	172.9
16-7NH-16	104.9	43.9	51.4	85.4	85.5	59.9	122.6
16-7NH-16/DOPE	101.04	50.7	51.3	74.3	139.7	181.7	216.4
16-7NH-16/DNA	116.1	49.9	52.5	81.6	136.9	120.6	184.1
16-7NH-16/DOPE/DNA	108.7	47.4	51.8	74.3	140.9	137.5	166.4

Parameters obtained from the π-A isotherms are liftoff area, A_L; molecular area at collapse, A_c; collapse pressure, π_c; minimum cross sectional area or limiting area, A_∞. Compressibility modulus (C_s^{-1}) at 30 mN/m, 35 mN/m surface pressure and the maximum compressibility modulus values.

Table 5.3: DPPC/cholesterol monolayer properties in presence of various mixed system in **pH 7.**

System	A_L (Å^2)	Ac (Å^2)	π_c (mN/m)	A∞ (Å^2)	C_s^{-1}		
					30mN/m	35mN/m	Max
DPPC/Cholesterol	74.3	38.2	52.1	49.0	**174.8**	**191.1**	**222.4**
16-7-16	115.1	43.7	51.2	83.0	131.5	120.8	153.0
16-7-16/DOPE	94.0	46.9	50.6	75.4	193.7	180.0	193.7
16-7-16/DNA	138.2	52.1	51.1	96.9	137.4	36.3	143.4
16-7-16/DOPE/DNA	108.4	49.9	49.1	73.0	142.0	152.1	159.1
16-7NH-16	96.4	49.6	51.9	73.4	203.1	199.9	215.7
16-7NH-16/DOPE	83.8	45.0	50.3	62.7	182.0	204.4	238.5
16-7NH-16/DNA	95.3	48.0	50.5	63.7	176.2	189.3	214.3
16-7NH-16/DOPE/DNA	104.3	49.5	51.0	76.6	173.4	181.8	198.8

Table 5.4: DPPC/cholesterol monolayer properties in presence of various mixed system in **pH 9**.

System	A_L (Å^2)	A_c (Å^2)	π_c (mN/m)	A_∞ (Å^2)	C_s^{-1}		
					30mN/m	35mN/m	Max
DPPC/Cholesterol	64.4	34.3	52.3	41.4	**249.0**	**252.9**	**338.5**
16-7-16	116.4	48.5	53.5	75.4	169.0	135.7	177.0
16-7-16/DOPE	150.3	40.3	53.0	71.2	101.7	113.6	129.2
16-7-16/DNA	117.7	49.8	51.1	95.7	158.5	75.5	172.3
16-7-16/DOPE+DNA	92.6	47.7	51.8	62.6	187.9	197.0	270.2
16-7NH-16	88.7	51.0	51.8	67.4	258.8	251.2	304.4
16-7NH-16/DOPE	84.6	49.6	52.0	64.5	288.0	251.3	296.7
16-7NH-16/DNA	93.7	50.6	50.5	67.2	213.4	214.6	255.0
16-7NH-16/DOPE/DNA	94.5	47.1	51.5	68.1	218.1	205.4	247.0

Parameters obtained from the π-A isotherms are liftoff area, A_L; molecular area at collapse, A_c; collapse pressure, π_c; minimum cross sectional area or limiting area, A_∞. Compressibility modulus (C_s^{-1}) at 30 mN/m, 35 mN/m surface pressure and the maximum compressibility modulus values.

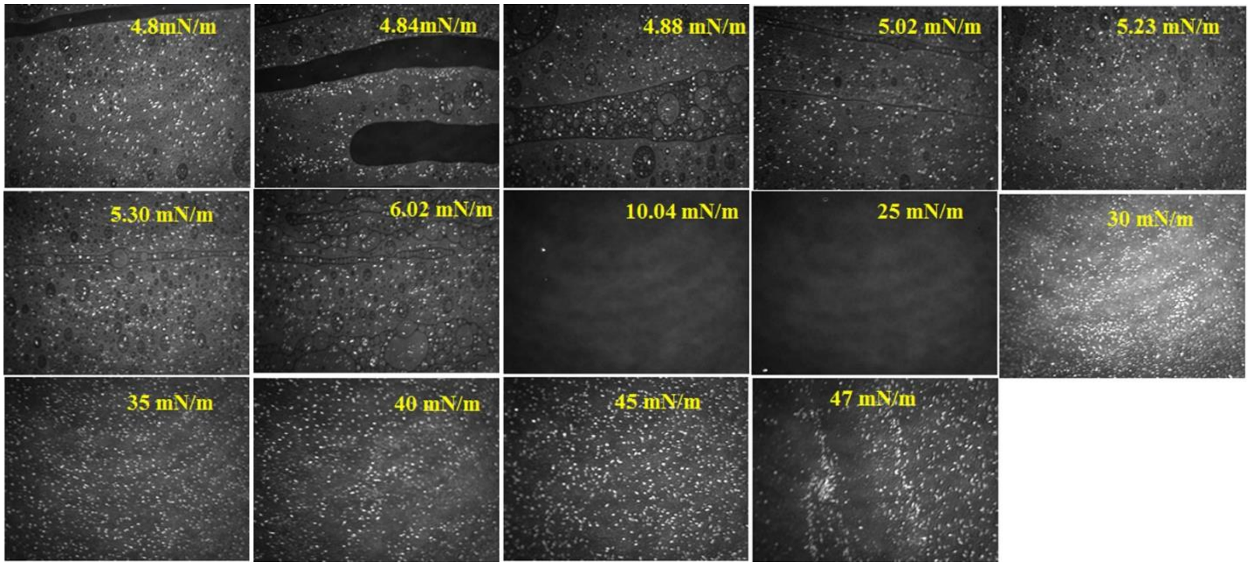

Figure 5.12. BAM images of DPPC/cholesterol monolayer at the air/buffer (**pH 4**) interface at in presence of pure 16-7-16 system on the subphase.

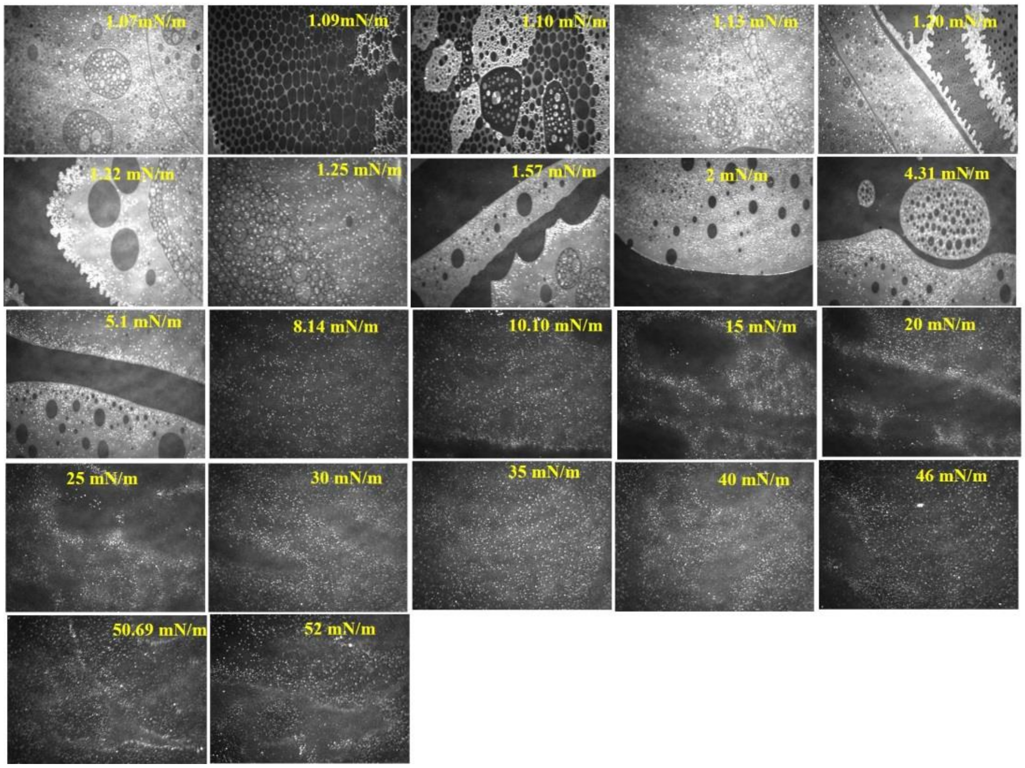

Figure 5.13. BAM image of DPPC/cholesterol monolayer at the air/buffer (**pH 4**) interface in presence of 16-7-16/DOPE system on the subphase.

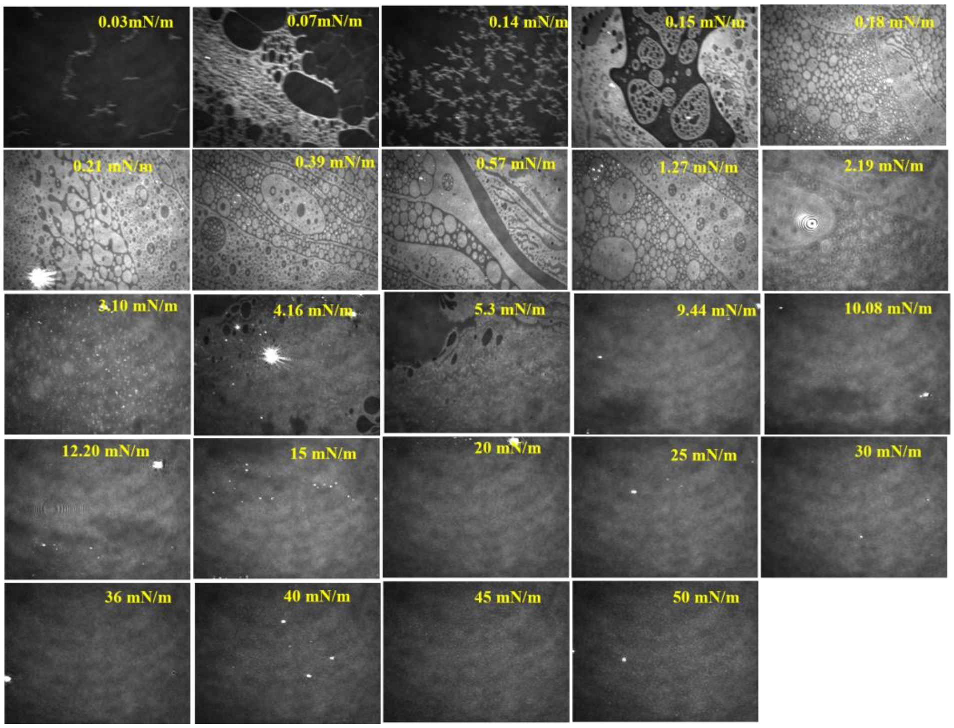

Figure 5.14. BAM image of DPPC/cholesterol monolayer at the air/buffer (**pH 4**) interface in presence of 16-7-16/DNA system on the subphase.

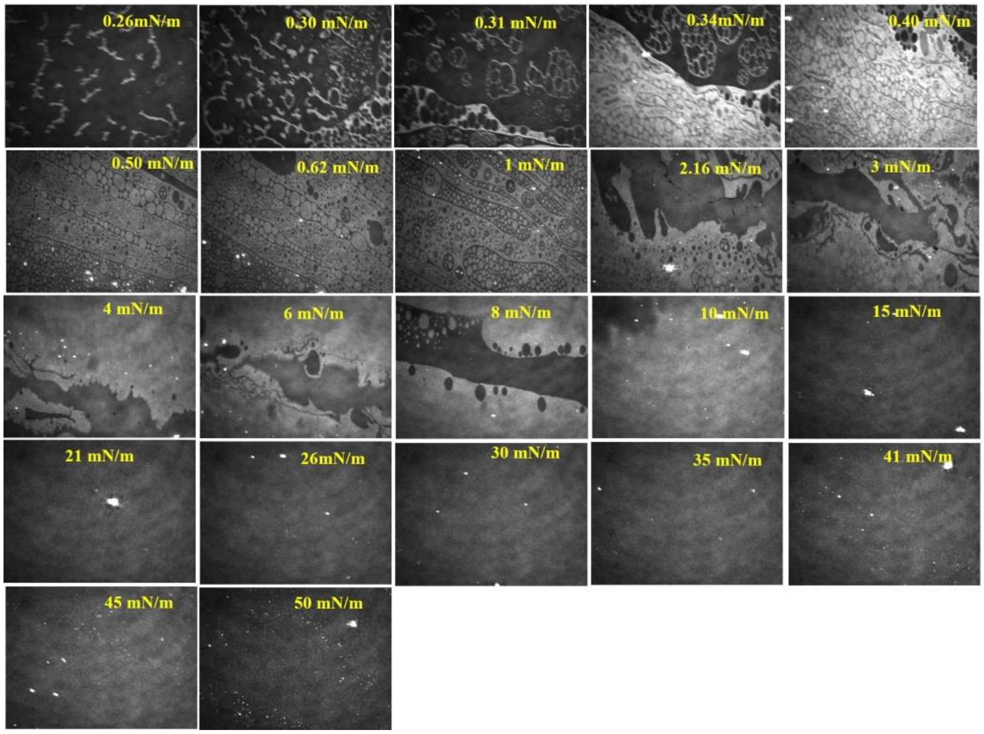

Figure 5.15. BAM image of DPPC/cholesterol monolayer at the air/buffer (**pH 4**) interface in presence of 16-7-16/DOPE/DNA system on the subphase.

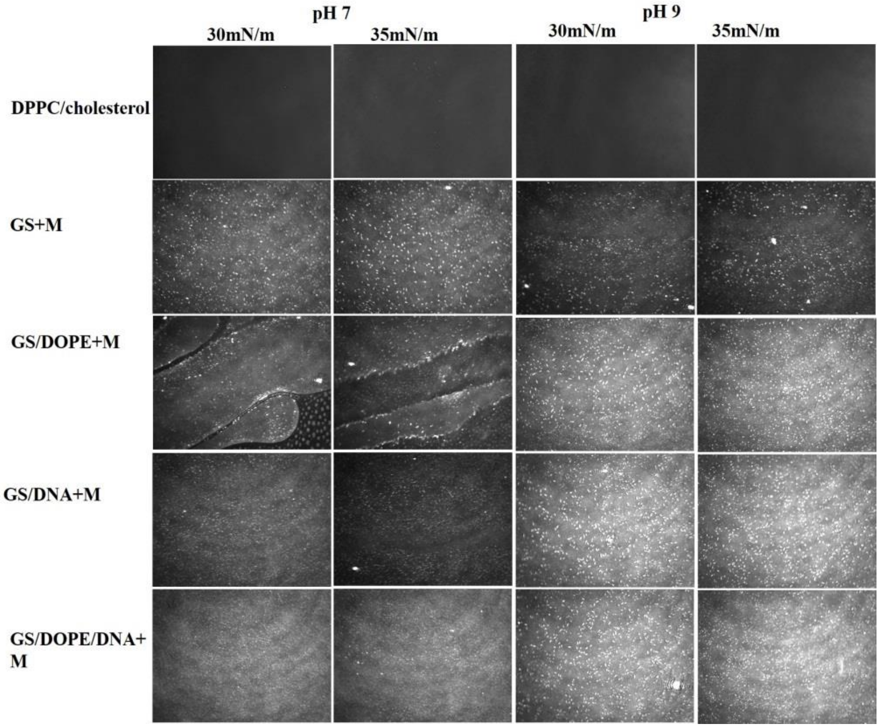

Figure 5.16. BAM image of DPPC/cholesterol monolayer at the air/buffer (pH 7 and 9) interface in presence of 16-7-16 system on the subphase. GS = 16-7-16, M = model membrane (DPPC/cholesterol = 75/25 %). The images are presented at the 30-35 mN/m surface pressure.

5.1.4. Effect of mixed 16-7NH-16 systems on the model membrane

The π-A isotherm and C_s^{-1}-π curve of the DPPC/cholesterol monolayer in presence of mixed 16-7NH-16 systems are mentioned at Figure 5.8 and 5.9 to 5.11, respectively. At pH 4, the 16-7NH-16/DOPE possess a lift-off are of ~101, 83.8 and 84.6 Å^2 at pH 4, 7 and 9, respectively (Table 5.2, 5.3, 5.4). Thus, the monolayer is expanded at pH 4 than at pH 7 or 9. The A_∞ is ~ 74.3 62.7, 64.5 Å^2/molecules at pH 4, 7 and 9, respectively. This implies that the DPPC/cholesterol forms relatively condensed monolayer at all pHs. At the 30-35 mN/m surface pressure, the DPPC/cholesterol shows the presence of LC phase transition (C_s^{-1} = 139.7 to 181.7 mN/m) at pH 4 (Figure 5.9 B). Similar LC phase transition was observed at pH 7 and 9 (Figure 5.10 B and 5.11 B), however, the values of the C_s^{-1} are higher in case of pH 7 and 9 than pH 4. While comparing the C_s^{-1} values of the pure DPPC/cholesterol monolayer, presence of 16-7-16/DOPE substantially reduced the rigidity of the pure monolayer (Figure 5.9B). As mentioned earlier, this is an indication of the membrane fluidization. In comparison, the 16-7NH-16/DOPE system could not induce any significant changes in the C_s^{-1} values of the pure DPPC/cholesterol at pH 7 and 9 (Figure 5.10 and 5.11). This result is consistent to the hypothesis that 16-7NH-16 protonates at pH 4, and induces more fluidization to the model membrane [35]. Additionally, Figure 5.17 represents the BAM images of the DPPC/cholesterol monolayer in presence of the 16-7NH-16 system. The small circular domains on dark images are indicative of the G-LE phase at low surface pressure (~2-4.29 mN/m). As the monolayer is further compressed the LE-LC phase transition is visible with the appearance of small dot like domains on the dark LE phase (> 7 mN/m). At the cell membrane surface pressure (30-35 mN/m), the presence of 16-7NH-16 induced substantial small dot like domains at the DPPC/cholesterol monolayer, which was not observed at the pure DPPC/cholesterol monolayer at pH 4 (Figure 5.5). Thus, the S phase of the pure DPPC/cholesterol was reduced to the LC phase, indicating the membrane fluidization. At pH 7 or 9, the BAM images showed more condensed and small domains, which might be indication of presence of higher ordering of the DPPC/cholesterol monolayer at those pHs (data not shown).

16-7NH-16/DNA with the model membrane is shown in Figure 5.8. Based on the lift-off area (Table 5.2, 5.3 and 5.4), the 16-7NH-16/DNA system causes expansion of the DPPC/cholesterol monolayer at pH 4 than at pH 7 or 9. At the 30-35 mN/m surface pressure range, in presence of 16-7NH-16/DNA the DPPPC/cholesterol monolayer exhibits a LC phase transition than the S phase transition (for the pure DPPC/cholesterol), Figure 5.9B. This substantial reduction in the S phase to a LC phase by the 16-7NH-16/DNA system implies that the mixed system interacts with the DPPC/monolayer at low pH. As mentioned earlier, the protonation of the 16-7NH-16 helps in strong binding of the 16-7NH-16 with the DNA molecule. We have observed a plateau for the 16-7NH-16/DNA monolayer at this surface pressure range (chapter IV, Figure 4.12) due to the electrostatic interaction between the 16-7NH-16 with DNA. Thus, 16-7NH-16/DNA complex may adsorb or penetrate to the DPPC/cholesterol monolayer. This phenomena was not observed at pH 7 or 9, indicating the strong effect of pH on the fluidization of the 16-7NH-16/DNA system on the model membrane. In presence of the 16-7NH-16/DNA system, the DPPC/cholesterol monolayer also showed the domains of G-LE phase transition at low surface pressure (0.2-2 mN/m), Figure 5.18. At 30-35 mN/m, the images possess relatively small bright domains, which might be the indication of the LC phase than S phase. Both at pH 7 and 9, condensed monolayer with the bright domains are observed (Figure 5.20). Thus, 16-7NH-16/DNA might have induced fluidization at pH 4 but not at pH 7 or 9 and further supports the surface pressure area isotherm results.

To our greatest interest, in presence of the complete system (16-7NH-16/DOPE/DNA), the DPPC/cholesterol monolayer showed reduction of the rigidity (Figure 5.9). At the 30-35 mN/m surface pressure, the C_s^{-1} values of the DPPC/cholesterol monolayer were substantially reduced from 287 mN/m to ~ 140 mN/m in absence or presence of 16-7NH-16/DOPE/DNA system, respectively. This suggests that the model membrane is fluidized by the 16-7NH-16/DOPE/DNA at pH 4. On the other hand, there were no effect of this system at pH 7 (Figure 5.10). There were subtle reduction of the C_s^{-1} values at pH 9 (Figure 5.11). Thus, the results resembles the strong pH dependent membrane fluidization of the 16-7NH-16/DOPE/DNA system. Additionally, in presence of 16-7NH-16/DOPE/DNA system the DPPC/cholesterol resembles the A_∞ values approximately 74.3, 76.6, 68.1 Å^2/molecules at pH 4, 7 and 9, respectively. Once again, these values are ~ 1.5 times higher than the pure DPPC/cholesterol at the corresponding pHs (Table 5.2, 5.3, 5.4). Increase in the cross sectional area of the hydrocarbon chains of the DPPC/cholesterol monolayer signifies the disorientation of the molecules at the air/buffer interface [119]. Which might have induced by the penetration of the complex to the monolayer [99]. Furthermore, the BAM images of the DPPC/cholesterol monolayer in presence of 16-7NH-16/DOPE/DNA at pH 4 is presented at the Figure 5.19. As can be seen, the G-LE phase transitions are visible at the BAM images at the surface pressure of 0.21 to 2.02 mN/m. Upon further compression, the monolayer undergoes LE-LC phase transition, and remains at the LC phase at higher surface pressure (> 14mN/m). At this stage, the homogeneous film with small bright dot like domains are visible in the BAM images until the monolayer collapse. At 30-35 mN/m, the images are substantially different form the pure DPPC/cholesterol (Figure 5.5), and indicative of the monolayer fluidization. However, at pH 7 and 9, more bright BAM images with homogenous dot like domains are observed. This could be the indication of highly condensed monolayer formation at pH 7 or 9 (Figure 5.20). Overall, the BAM images further supports the isotherm results and signifies that the 16-7NH-16 based system reduced the rigidity of the DPPC/cholesterol monolayer in a pH dependent manner.

In general, the 16-7NH-16/DOPE/DNA complexes may carry net positive charges due to protonation of the 16-7NH-16 at pH 4. Subsequently this complex may be adsorbed at the DPPC/cholesterol monolayer due to the electrostatic interaction of the positively charged complex with the negatively charged phosphate or hydroxyl group DPPC and cholesterol molecules or some of the complex may penetrate into the monolayer, and ultimately fluidized the membrane. Adsorption of DNA to the octadecylamine (ODA) monolayer was evaluated by Lopes-Costa et *al.* [263] and Hansda et *al.* [265]. In another study by Gromelski and Brezesinski showed that the presence of cation (Mg^{2+}, Ca^{2+}) in subphase mediated strong adsorption of the calf thymus DNA into the zwitterionic lipid 1,2- dimyristoyl-phosphatidylethanolamine (DMPE) monolayer [266]. They also showed that at low lateral pressure, the DNA partially penetrated into the lipid monolayer, however, it squeezed out at high pressure. They have proposed that the divalent cations may interact with the DMPE lipid, and the head group become positively charged, therefore, it interacts with the DNA in the form of electrostatic interaction. This study may not directly be applicable to our system; however, this suggests that the gemini/DOPE/DNA complex may undergo probable electrostatic as well as hydrophobic interaction to the DPPC/cholesterol monolayer; and adsorption as well as penetration may occur. From the zeta potential measurement it was observed that the 16-7NH-16/DOPE/DNA complex possess ~ +62 mV at pH 4 whereas at pH 9 it was just above 0 mV [35]. Also the particle size was substantially larger at low pH than at high pHs. It was believed that the protonation of this surfactant helps in disruption of the endosomal membrane, and enhanced transfection efficiency at COS-7 and PAM 212 cells [35]. Thus, our current results correlated well with the *in vitro* results [35].

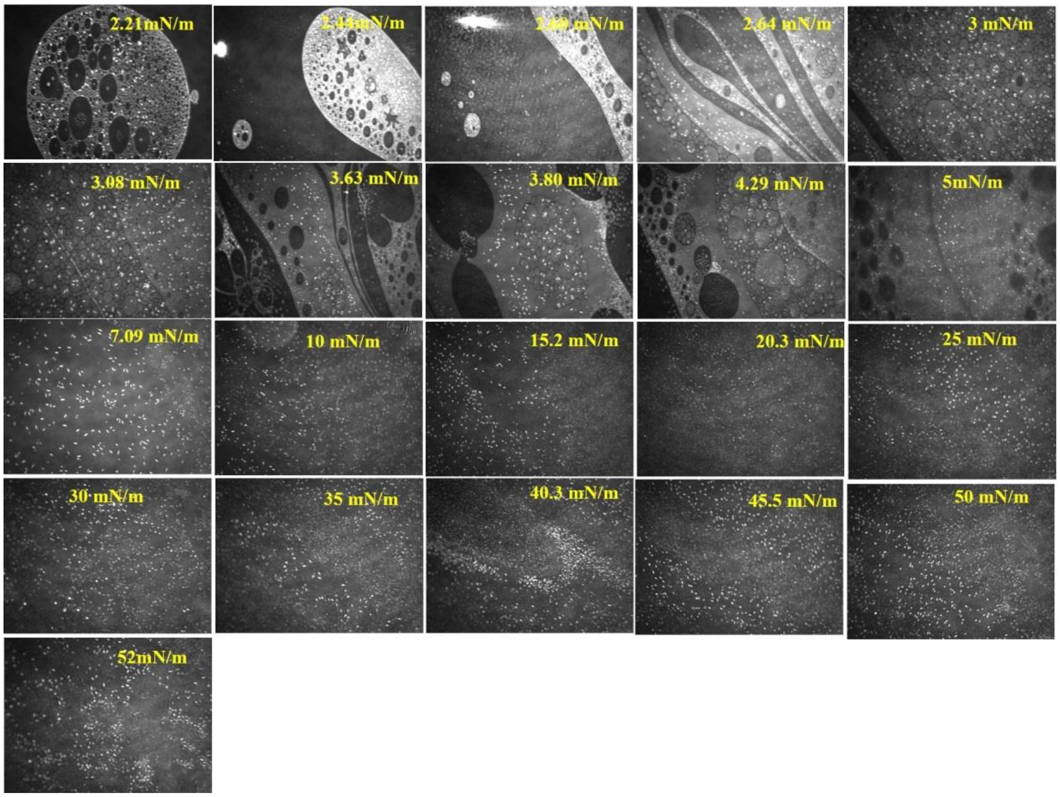

Figure 5.17. BAM image of DPPC/cholesterol monolayer at the air/buffer (**pH 4**) interface in presence of 16-7NH-16 system on the subphase.

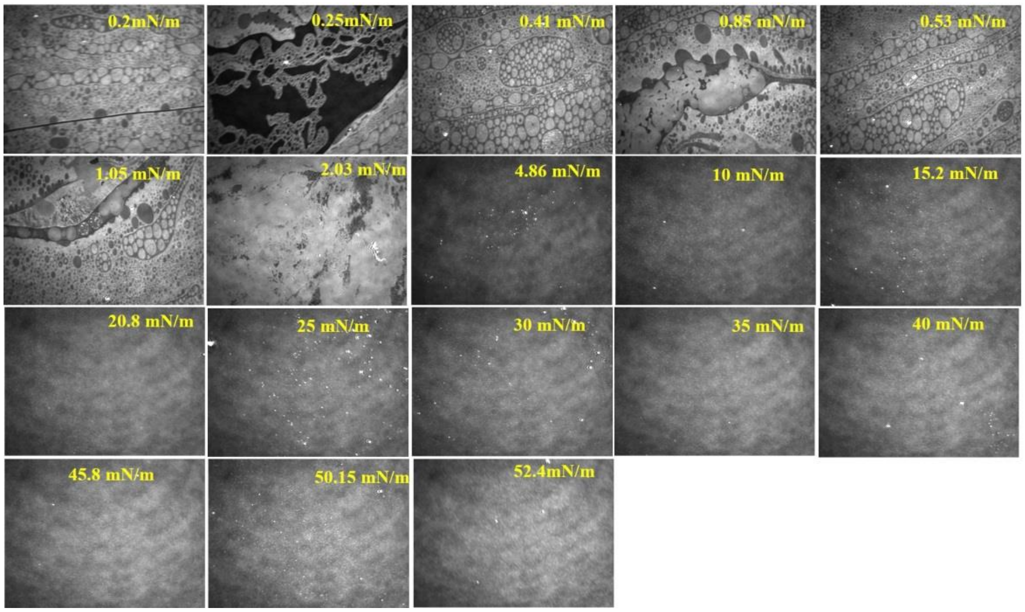

Figure 5.18. BAM image of DPPC/cholesterol monolayer at the air/buffer (**pH 4**) interface in presence of 16-7NH-16/DNA system on the subphase.

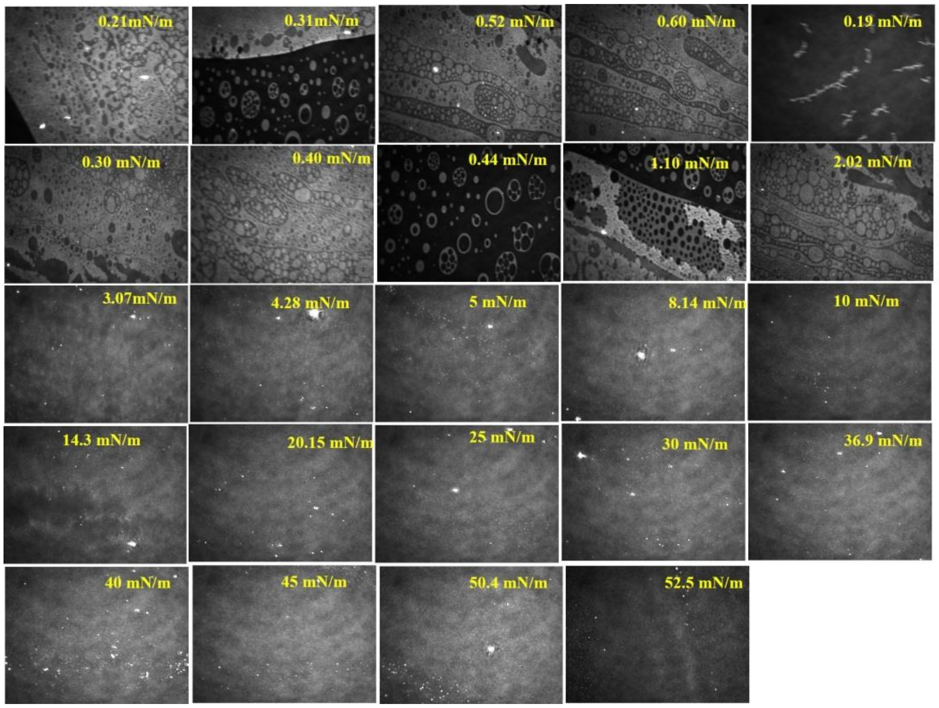

Figure 5.19. BAM image of DPPC/cholesterol monolayer at the air/buffer (**pH 4**) interface in presence of 16-7NH-16/DOPE/DNA system on the subphase.

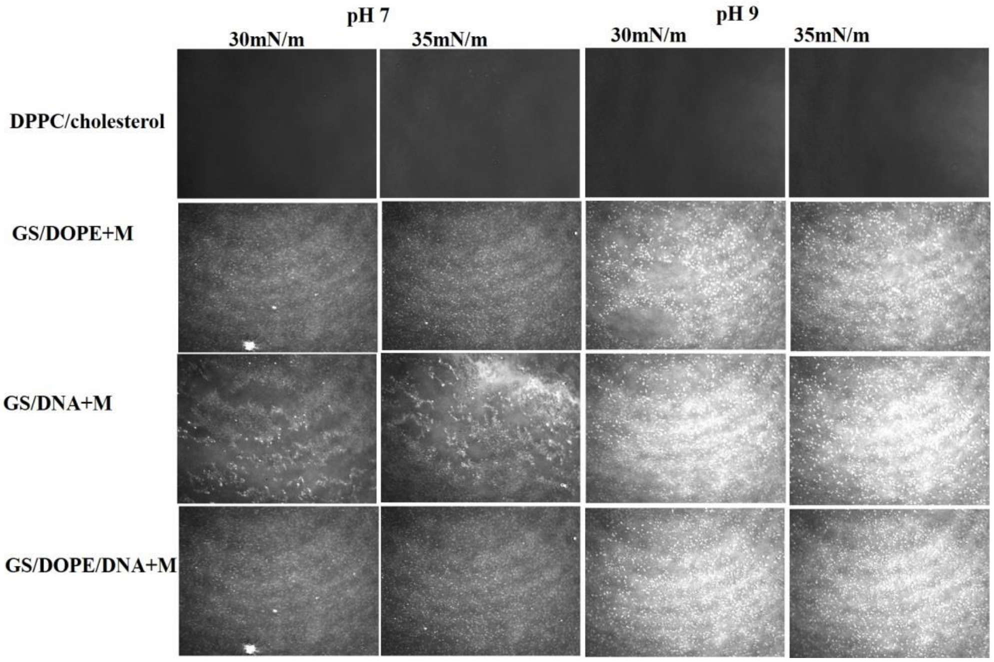

Figure 5.20. Comparative images of the DPPC/cholesterol monolayer in presence of mixed 16-7NH-16 systems at pH 7 and 9 at surface pressure 30-35 mN/m. GS = 16-7-16, M = model membrane (DPPC/cholesterol = 75/25 %).

5.1.5. PM-IRRAS studies of the pure DPPC, Cholesterol or their mixture

We have conducted PM-IRRAS studies of the mixed gemini/DOPE/DNA system to have further insight of the interaction mechanism of these system on DPPC/cholesterol model membrane. As mentioned earlier in **chapter IV**, section 4.2.10, the characteristic symmetric stretch $v_s(CH_2)$ is observed at around 2850 cm^{-1} and asymmetric stretch $v_a(CH_2)$ at around 2920 cm^{-1}. The frequencies of these bands are sensitive to the conformation of the phospholipid acyl chains. Therefore, these bands provide substantial information about the molecular orientation of the lipid acyl chains at the air/water interface [210, 234-237]. In general, if the obtained values are lower (red shift) than 2920 and 2850 cm^{-1}, it indicates higher chain ordering in the film. In contrary, the higher values (blue shift) indicates the chain disordering [238, 239]. Our literature review suggests that the $v_a(CH_2)$ is often found at narrow ranges from 2915 to 2918 cm^{-1}, and $v_s(CH_2)$ from 2846 to 2850 cm^{-1} for all-trans conformations of the fully extended tail chains [54]. Noteworthy, the red shift denotes for the ordered all-trans conformation of the chain, whereas blue shift stands for the chain disordering with the gauche conformation [238]. As can be seen from Figure 5.21 that the pure DPPC at pH 4 possess $v_a(CH_2)$ band ~2924 cm^{-1} and $v_s(CH_2)$ at ~ 2851 cm^{-1} at surface pressure 30 and 35 mN/m. This suggests that the slightly disordered acyl chains of lipid in presence of LC or LE-LC phase. The isotherm and compressibility modulus results (Figure 5.1 A and B) in which pure DPPC monolayer at pH 4 remained mostly at LC phase, are in good agreement with the PM-IRRAS results. Similar results with slightly higher wave number of the alkyl tails bands are reported in the literature for the DPPC monolayer [213, 235, 240, 267-269]. The characteristics ester groups ν(C=O) are found at ~1720 cm^{-1}. The asymmetric ($\nu_a(PO_2^-)$) and symmetric phosphate ($\nu_s(PO_2^-)$) stretches are observed at ~ 1230 and 1088 cm-1, respectively. The pure cholesterol monolayer shows (Figure 5.22) the characteristics $\nu_a(CH_2)$ band at around 2928 cm^{-1} and $\nu_s(CH_2)$ at ~ 2852 cm^{-1} and the CH_3 symmetric stretch at ~ 2887 cm^{-1} [249]. The mixed DPPC/cholesterol PM-IRRAS spectra is observed at Figure 5.23. The $\nu_a(CH_2)$ and $\nu_s(CH_2)$ has shifted to the lower values than the ideal 2920 and 2850 cm^{-1}. This implies to the higher ordering (almost vertical orientation of the alkyl tails to the plane) of the molecules at the biologically relevant surface pressure (30- 35mN/m). From the isotherm (Figure 5.1A and 5.2A), it was observed that DPPC/cholesterol forms the S phase at this surface pressure. The minimum cross sectional area of the DPPC/cholesterol system at pH 4 was around 48 Å^2/molecules (Table 5.1). These values remained less than 48 Å^2/molecules regardless of the pH of the subphase which indicates the closely packed vertically oriented DPPC/cholesterol molecules at the air/buffer interface. Thus, PM-IRRAS results strongly correlates to the obtained results of isotherm. The ν(C=O) band shifted from 1720 cm^{-1} (pure DPPC) to 1730 cm^{-1} (DPPC/cholesterol), indicating the probable hydrogen bonding between the DPPC and cholesterol molecule. Similar hydrogen bonding was observed for the DPPC/cholesterol mixture in presence of photosensitizer at the subphase which was attributed to the higher shift of ν(C=O) band. Additionally, Lewis et *al.* have shown that the ν(C=O) band is sensitive to hydrogen bonding and shifts to higher wave number upon the bond formation [270]. Moreover, the asymmetric ($\nu_a(PO_2^-)$) and symmetric phosphate ($\nu_s(PO_2^-)$) stretches also are observed at around 1216, 1248 and 1087 and 1097 cm^{-1}. There is a clear shift of the phosphate band to the higher values which are indicative of interactions. The $\nu_a(PO_2^-)$ is sensitive to hydration and ion binding [235]. An IRRAS study of the diphosphoryl Lipid A (a precursor of lipopolysaccharide) revealed the presence of three overlapped features at the asymmetric phosphate band region. The 1225, 1238 1258 cm^{-1} corresponded to the dihydrated, monohydrated, and unhydrated phosphate groups, respectively. This was attributed to the accessibility of Lipid A molecules to nearby water molecules [235]. Thus, there might be two possibilities in our results: intramolecular hydrogen bonding between the two adjacent DPPC molecules and the hydrogen bonds between the DPPC polar head groups with the cholesterol hydroxyl group. This bonding caused the closer packing of the DPPC/cholesterol molecules at the air/buffer interface, consequently resulted in the S phase at the monolayer. Similar effects was observed for the DPPC/cholesterol monolayer at pH 7 and 9 (data not shown).

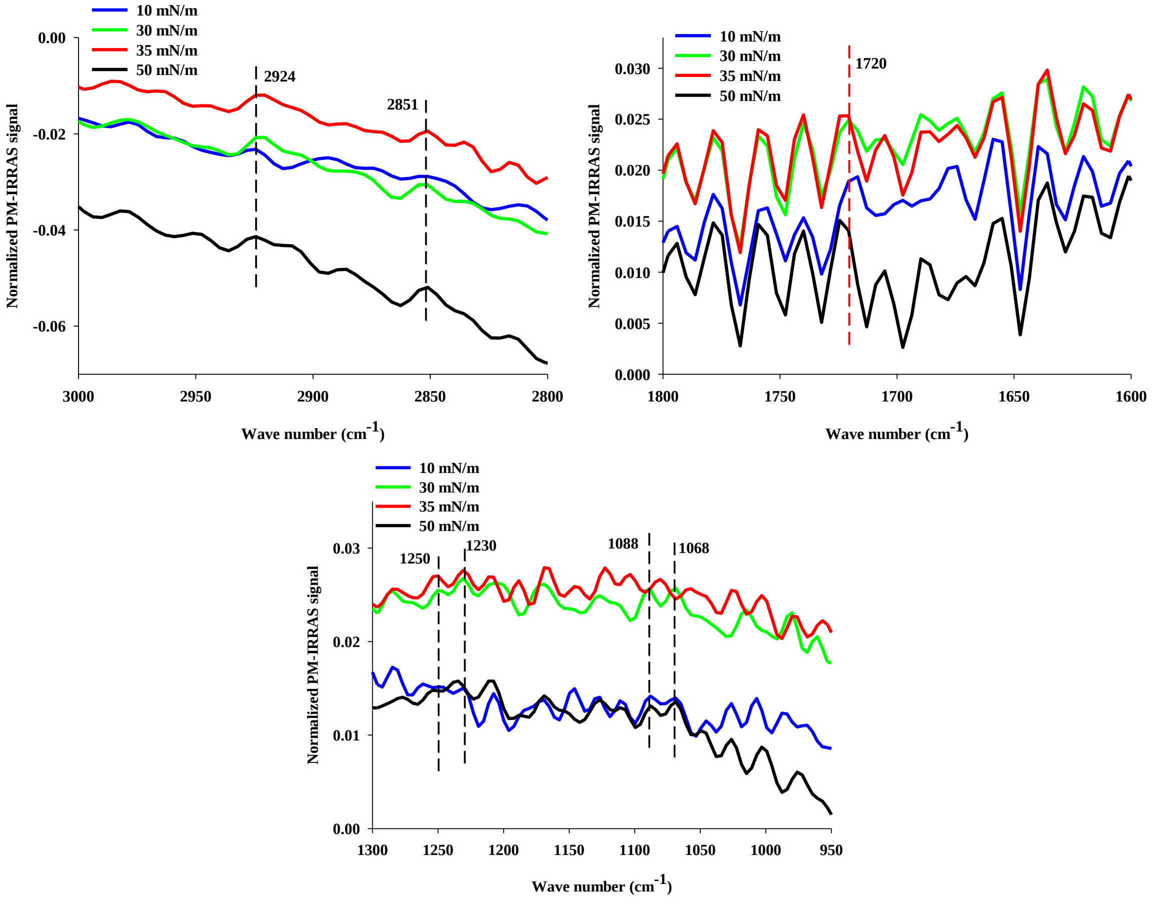

Figure 5.21. PM-IRRAS spectra of the pure DPPC at air/buffer (pH 4) interface.

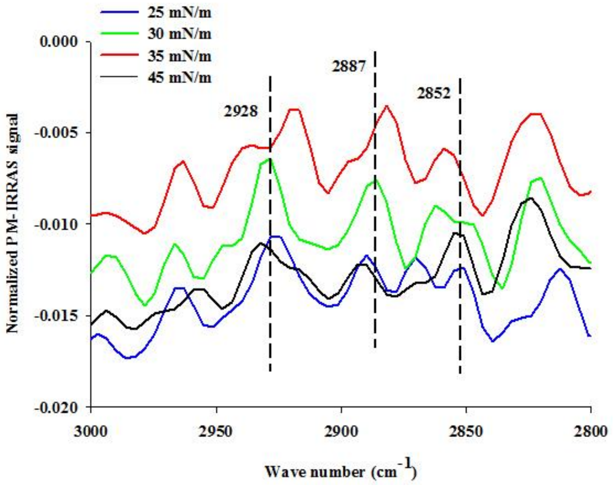

Figure 5.22. PM-IRRAS spectra of the pure cholesterol at air/buffer (pH 4) interface.

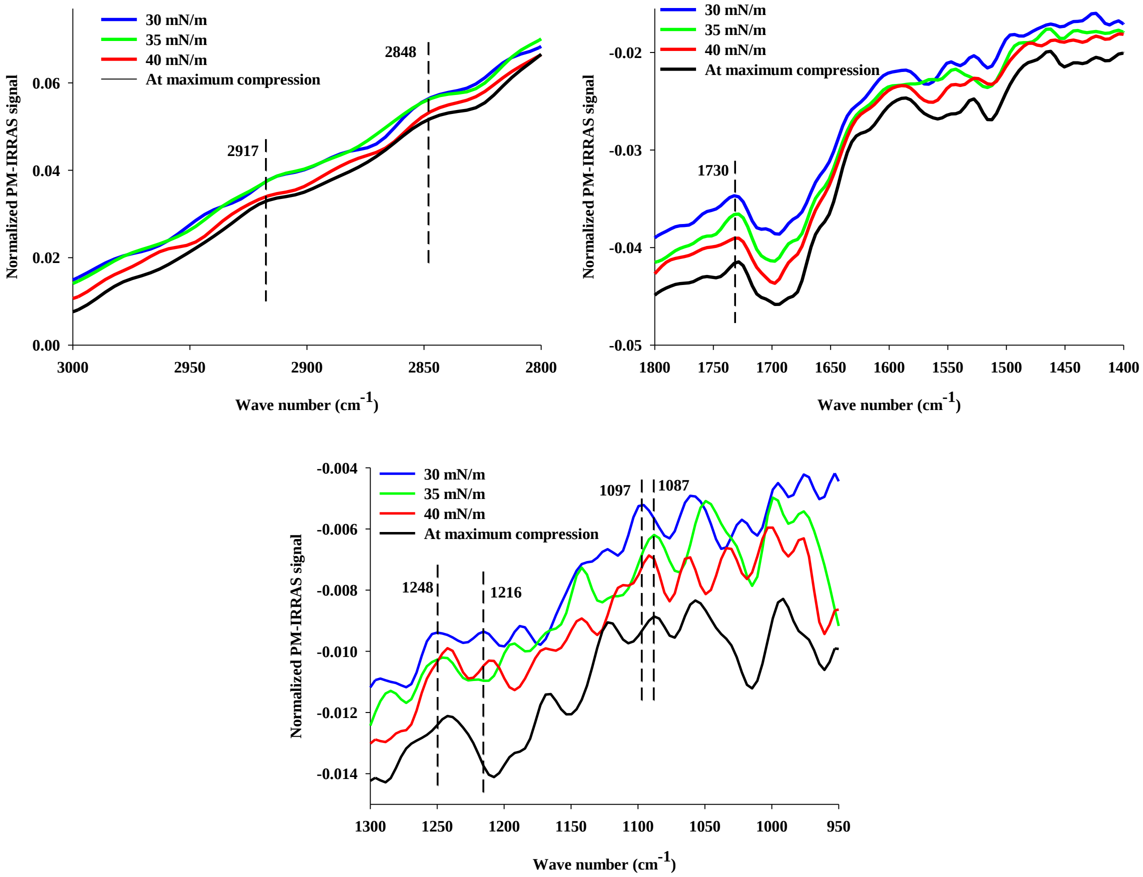

Figure 5.23. PM-IRRAS spectra of the pure DPPC/cholesterol at air/buffer (pH 4) interface.

As can be seen form Figure 5.24, in presence of 16-7NH-16/DOPE/DNA the DPPC/cholesterol monolayer showed characteristic $v_a(CH_2)$ band ~ 2922.5 cm^{-1} and $v_s(CH_2)$ band at ~ 2851 cm^{-1} at surface pressure 30 mN/m. Comparing with the pure DPPC/cholesterol (Figure 5.23), the observed bands are shifted to higher values, which is indicative of the disordered acyl chains of the lipids. Thus, the highly ordered transzigzag conformation of alkyl chain may have changed the conformation to the gauche conformations [271, 272]. This further indicates that the S phase of pure DPPC/cholesterol monolayer might be reduced into LC phase. This is a clear indication of membrane fluidization in presence of 16-7NH-16/DOPE/DNA system at pH 4. At pH 7 the $v_a(CH_2)$ and $v_s(CH_2)$ band remained constant with regards to the pure DPPC/cholesterol band (data not shown). This signifies that the monolayer is unaffected at pH 7 and it may have remained at the S phase. On the other hand, v(C=O) band of the monolayer was not affected by the system. As mentioned in **chapter IV**, the B form of DNA possess guanine/thymine carbonyl (C=O) stretch at 1715 cm^{-1}, thymine aromatic amine stretch (1328 cm^{-1}), $v_s(PO_2^-)$ and $v_a(PO_2^-)$ stretches at ~1088 and 1222 cm^{-1}, respectively; and a strongly coupled sugar-phosphodiester signal at approximately 970 cm^1 [241]. From Figure 5.24 it is observed that there are two band at 1606 and 1581 cm^{-1} which are attributed to the vibrational band of adenine. Marty et *al.* have reported that cationic ion−base interaction can induce changes in the vibrational band of adenine 1609-1606 cm^{-1} towards lower values [242], in our case 1581 cm^{-1}. Neault et *al.* showed that the bands observed at 1606 and 1590 cm−1 was attributed to the aspirin-DNA interaction [243]. Thus, the observed band at 1606 and 1581 cm^{-1} (Figure 5.24) might be due to the interactions of the quaternary ammonium head groups of gemini surfactant with the dipoles of bases (adenine N7 atoms or thymine O2). Even though the 16-7NH-16/DOPE/DNA was in the subphase, this characteristic DNA band is clearly observed at the monolayer. It is only possible if the part of the 16-7NH-16/DOPE/DNA adsorbs and penetrates the model membrane. This findings further supports that the 16-7NH-16/DOPE/DNA system may have penetrated the DPPC/cholesterol, and the PM-IRRAS signal detected those bands. Additionally, these spectral features (band at 1606 and 1581 cm^{-1}) are suggestive of the presence of ion−dipole interaction in the gemini/DOPE/DNA complex monolayers.

The symmetric and asymmetric $v(PO_2^-)$ band is contributed from DPPC, may also be attributed to the DOPE and DNA (due to the adsorption and penetration); thus it is not easy to exactly elucidate the mechanism of interaction at the $v(PO_2^-)$ in presence of 16-7NH-16/DOPE/DNA system. Interestingly, the sugar-phosphodiester signal of the DNA observed at around 983 cm^{-1} further shows the presence of DNA in the monolayer. In general, there is complex interaction occurring on between the DPPC/cholesterol and the 16-7NH-16/DOPE/DNA system. The mixed system adsorbed on as well as penetrated the model membrane, which was the major factor for membrane fluidization (as observed in the isotherm results at 30-35 mN/m surface pressure). At pH 7 or 9, the alkyl tail band at the 2920 and 2850 cm^{-1} remained unchanged, indicating the overall S phase of the DPPC/cholesterol monolayer at higher pHs (Appendix Figure A5.7 and A5.8). Thus, our study further suggests that the 16-7NH-16/DOPE/DNA system induces membrane fluidity in a pH dependent manner.

Finally, we have introduced the 16-7-16/DOPE/DNA system on the subphase of DPPC/cholesterol monolayer at pH 4 (Figure 5.25). At surface pressure 30 mN/m, the characteristic $v_a(CH_2)$ band is at ~2916 cm^{-1} and $v_s(CH_2)$ band is ~2847 cm^{-1}. This implies that the presence of 16-7-16/DOPE/DNA might not induce substantial changes at the orientation of the alkyl tails even though the compressibility modulus values showed LC phase for this system (Figure 5.9). Similar results was observed at pH 7 and 9 (data not shown). The PM-IRRAS results confirms that the membrane fluidization effect is much stronger for the 16-7NH-16/DOPE/DNA system than the 16-7-16/DOPE/DNA system at pH 4. The C=O band remained unchanged. Interestingly, Figure 5.25 shows the merged band at 1600 to 1584 cm^{-1}, indicating the adsorption or penetration of the complex into the subphase. However, the extent of penetration of the 16-7-16/DOPE/DNA system is unknown.

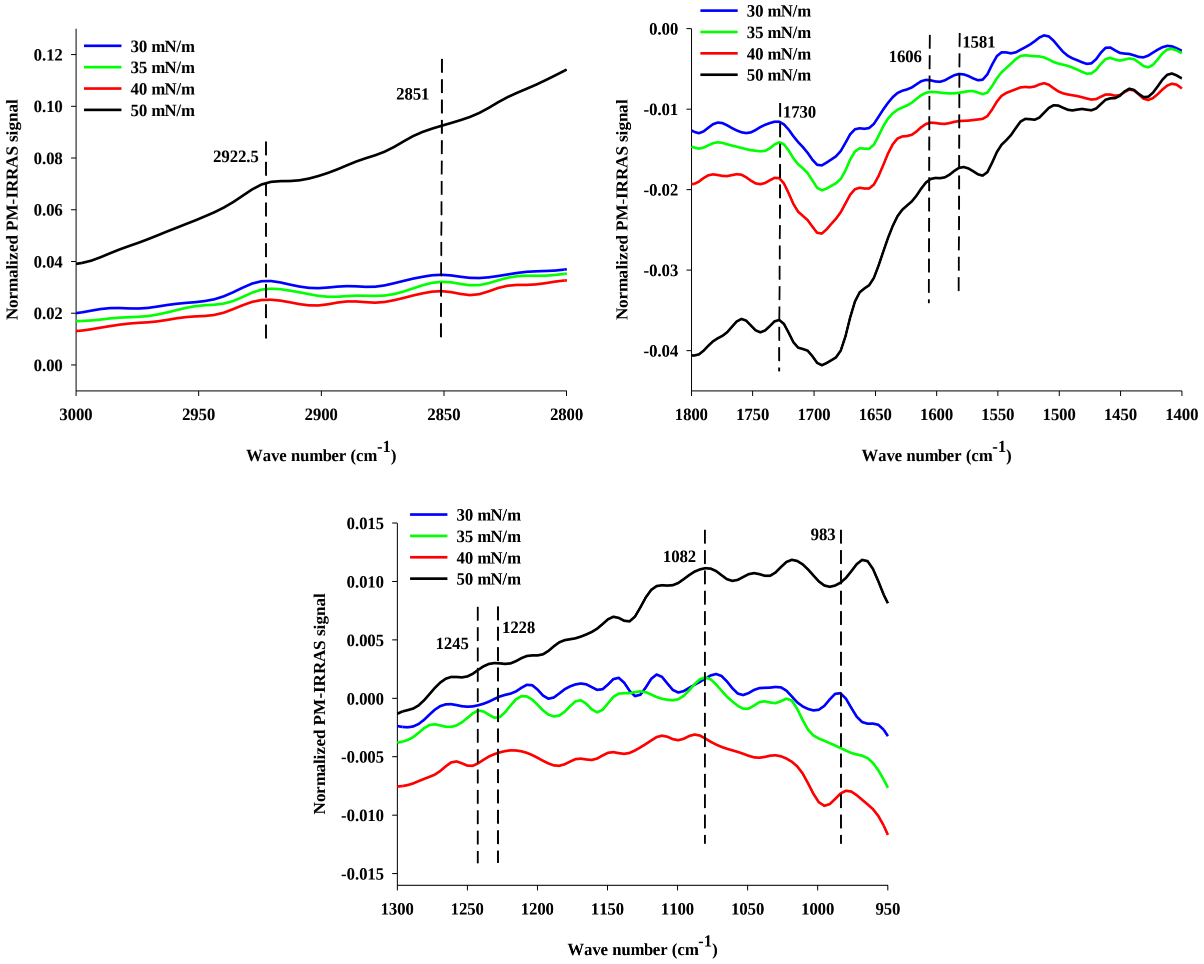

Figure 5.24. PM-IRRAS spectra of the pure 16-7NH-16/DOPE/DNA with DPPC/cholesterol model membrane at air/buffer (pH 4) interface.

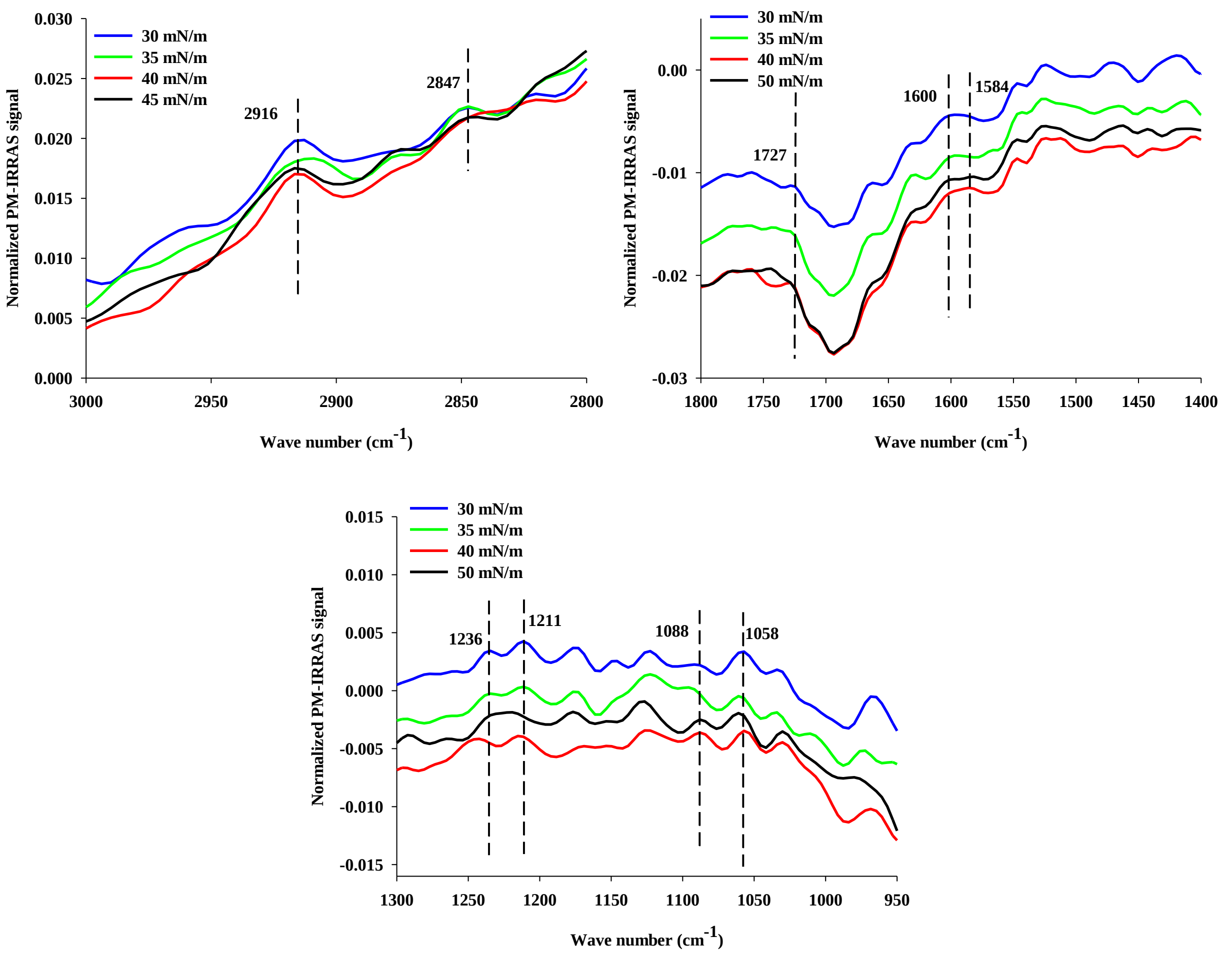

Figure 5.25. PM-IRRAS spectra of the pure 16-7-16/DOPE/DNA with DPPC/cholesterol model membrane at air/buffer (pH 4) interface.

At pH 4, based on the compressibility modulus and isotherm results, both 16-7NH-16/DOPE/DNA and 16-7-16/DOPE/DNA showed similar fluidization effect on the DPPC/cholesterol model membrane (Figure 5.9). However, the PM-IRRAS results confirm that the 16-7NH-16/DOPE/DNA is superior to the later system in terms of interaction which induces more alkyl tail disorientation. Moreover, the fluidization effect was much prominent at pH 4 than at pH 7 or 9. This is in good agreement with the isotherm and compressibility modulus results (Figure 5.9 to 5.11). Thus, our current system resembles the membrane fluidization at the real biological cell membrane surface pressure (30-35 mN/m) at pH 4. Therefore, this results further clarifies the fact that 16-7NH-16 system (due to protonation at low pH), may induce the adsorption to the endosomal membrane, cause penetration and ultimately disrupt the membrane and release the DNA into cytoplasm, subsequently, enhanced the transfection efficiency [35].

5.2 Summary

In the current study, we have successfully characterized the model endosomal membrane by DPPC/cholesterol = 75/25 %. The mixed monolayer showed solid phase at the natural cell membrane surface pressure (30-35 mN/m) at pH 4, indicating the rigid structure of the membrane. Interestingly, introducing the mixed 16-7-16 and 16-7NH-16 based system substantially reduced the rigidity of the membrane and induced fluidity. This was not only attributed to the adsorption of the gemini/DOPE/DNA system, but also to the penetration of this system into the model endosomal membrane. The fluidization effect of 16-7NH-16 based system was strongly pH dependent (at low pH more fluidization). This was due to the protonation of the 16-7NH-16 molecules at pH 4, and hence causes enhanced interaction with the DNA, and ultimately interacts with the membrane through adsorption and penetration. PM-IRRAS results also revealed that the membrane fluidization was prominent with the16-7NH-16 based system than the 16-71-16 systems. Our study, directly correlates to the *in vitro* transfection efficiency results in which 16-7NH-16 showed enhanced transfection due to the protonation and strong interaction with the endosomal membrane [35].

Chapter VI

Conclusion and future direction

In the current project, we have characterized non-viral gene therapy lipoplexes based on gemini surfactants (16-7-16 and 16-7NH-16) along with the helper lipid DOPE, using the Langmuir monolayer technique. Combining the π-A isotherm, compressibility modulus, BAM images, AFM and KFPM images and the PM-IRRAS results, we can conclude that the gemini/DOPE/DNA system possess a complex mixing behavior. The 16-7NH-16 surfactant undergoes strong electrostatic interaction with the DNA at the natural cell membrane surface pressure (30-35 mN/m) at pH 4 due to the protonation of the central secondary amine group. This was further evident from the formation of fibril type complex structures, observed at higher resolution using AFM and KPFM. Unfortunately, the exact role of DOPE in this transfection system remains unclear. Generally, DOPE causes condensation of the gemini surfactant monolayers; however whether or not this is due specifically the DOPE and gemini surfactant is unclear.

Subsequently, we have evaluated the effect of gemini/DOPE/DNA system on the model endosomal membrane (DPPC/cholesterol = 75/25 %). Mixed DPPC/cholesterol monolayer formed homogenous film at the natural cell membrane surface pressure indicating the presence of rigid and solid phase. Interestingly, injecting the mixed 16-7-16 and 16-7NH-16 based system in presence of DNA substantially reduced the rigidity of the membrane and caused fluidity. The mixed system was adsorbed at the DPPC/cholesterol membrane. The increase in the minimum cross sectional area of the DPPC/cholesterol molecules indicates the penetration of the gemini/DOPE/DNA system into the monolayer. The fluidization effect of 16-7NH-16 based system was strongly pH dependent (at low pH more fluidization). PM-IRRAS results also revealed that the membrane fluidization and penetration was prominent with the 16-7NH-16/DOPE/DNA system than the 16-71-16/DOPE/DNA systems. Our study, suggests that there may be a correlation to the *in vitro* transfection efficiency results in which 16-7NH-16 showed enhanced transfection due to the protonation and strong interaction with the endosomal membrane [35].

Further studies are required with the AFM and KPFM to understand the exact role of the DOPE in the endosomal membrane fluidization in the current system. To elucidate the exact mechanism of the membrane fluidization of the current GS/DOPE/DNA system, further studies with the AFM and KPFM are required.

For future studies, the 16-7-16/DOPE/DNA and 16-7NH-16/DOPE/DNA based system may be subjected to the model cancer cell membrane using the POPC/cholesterol = 75/25 %. Additionally, different types of gemini surfactants such as phy-3-m and phy-7NH-m (m = 12, 16, and 18) could be used since this system has shown better transfection efficiency in our recent study and relatively more hydrophobic than the 16-s-16 series [34, 48]. We may introduce some C22 containing gemini surfactant for better monolayer studies due to their higher hydrophobicity. The effect of specific buffer components on the GS/DOPE/DNA system may also be investigated. In our current study we have used double stranded salmon sperm DNA to produce the GS/DOPE/DNA system. However, a comparative study between the single stranded (ssDNA), double stranded (dsDNA) and circular plasmid DNA (pDNA) may be evaluated along with the salmon DNA to mimic the real biological condition, and application of these system(s) in gene therapy. Based on the literature, it is suggested that the cholesterol level reduces from plasma membrane to the lysosomal membrane. In lysosomal membrane it is almost 15 %. Therefore, a systematic study of different membrane compartment may be evaluated e.g. DPPC/cholesterol = 70/30 %, 75/25 %, 85/15 % to mimic the plasma membrane, early endosomal membrane and late endosomal membrane or lysosomal membrane, respectively. In addition to this, the outer leaflet of plasma membrane contains more sphingomyelin, phosphatidylcholine and cholesterol. Thus, a complex monolayer with the phosphatidylcholine/cholesterol/sphingomyelin = 75/20/5 % may be studied to mimic the outer layer of the plasma membrane. Another important study could be done with the negatively charged phosphatidylserine and phosphatidylinositol to mimic the negative charge of the plasma membrane. This lipids are specifically present in the inner leaflet of the plasma membrane. Additionally the late endosome is rich in lysobisphosphatidic acid (LBPA) or bis(monoacyl glycero)phosphate (BMP) and a lysosome specific lipid which is not found elsewhere in the cells. Thus incorporating LBPA along with cholesterol could be a good model membrane study for the late endosome.

Bibliography

1. Griffith F. The significance of pneumococcal types. *J. Hyg. (Lond)* 27(02), 113-159 (1928).
2. Miller AD. Human gene therapy comes of age. *Nature* 357(6378), 455-460 (1992).
3. Anderson WF. Human gene therapy. *Nature* 392 (Suppl.), 25-30 (1998).
4. Verma IM, Weitzman MD. Gene therapy: Twenty-first century medicine. *Ann. Rev. Biochem.* 74(1), 711-738 (2005).
5. Wirth T, Parker N, Ylä-Herttuala S. History of gene therapy. *Gene* 525(2), 162-169 (2013).
6. Ibraheem D, Elaissari A, Fessi H. Gene therapy and DNA delivery systems. *Int. J. Pharm.* 459(1-2), 70-83 (2014).
7. Gene therapy clinical trials worldwide (2015). Www.Wiley.Com/legacy/wileychi/genmed/clinical/.
8. Thomas CE, Ehrhardt A, Kay MA. Progress and problems with the use of viral vectors for gene therapy. *Nat. Rev. Genet.* 4(5), 346-358 (2003).
9. Lehrman S. Virus treatment questioned after gene therapy death. *Nature* 401(6753), 517-518 (1999).
10. Marshall E. What to do when clear success comes with an unclear risk? *Science* 298(5593), 510-511 (2002).
11. Branca MA. Gene therapy: Cursed or inching towards credibility? *Nat. Biotechnol.* 23(5), 519-521 (2005).
12. Felgner PL, Gadek TR, Holm M *et al*. Lipofection: A highly efficient, lipid-mediated DNA-transfection procedure. *Proc. Natl. Acad. Sci. U. S. A.* 84(21), 7413-7417 (1987).
13. Li S-D, Huang L. Non-viral is superior to viral gene delivery. *J. Control. Release* 123(3), 181-183 (2007).
14. Cian M M, Helen O M. *Cancer gene therapy – key biological concepts in the design of multifunctional non-viral delivery systems, in: Gene therapy - tools and potential applications*. InTech, Croatia, 213-48 (2013).
15. Wong SY, Pelet JM, Putnam D. Polymer systems for gene delivery—past, present, and future. *Prog. Polym. Sci.* 32(8–9), 799-837 (2007).
16. Wiethoff CM, Middaugh CR. Barriers to nonviral gene delivery. *J. Pharm. Sci.* 92(2), 203-217 (2003).
17. Zuhorn I, Engberts JFN, Hoekstra D. Gene delivery by cationic lipid vectors: Overcoming cellular barriers. *Eur. Biophys. J.* 36(4-5), 349-362 (2007).
18. Gottfried LF, Dean DA. *Extracellular and intracellular barriers to non-viral gene transfer, in: Novel gene therapy approaches*. Ming Wei, David Good (Ed.), InTech, Croatia, 75-88 (2013).
19. Giacca M. *Methods for gene delivery*. *In: Gene therapy*. Springer Milan, Italy, 47-137 (2010).
20. Miyata K, Nishiyama N, Kataoka K. Rational design of smart supramolecular assemblies for gene delivery: Chemical challenges in the creation of artificial viruses. *Chem. Soc. Rev.* 41(7), 2562-2574 (2012).

21. Xiang S, Tong H, Shi Q *et al*. Uptake mechanisms of non-viral gene delivery. *J. Control. Release* 158(3), 371-378 (2012).
22. Scholz C, Wagner E. Therapeutic plasmid DNA versus sirna delivery: Common and different tasks for synthetic carriers. *J. Control. Release* 161(2), 554-565 (2012).
23. Simoes S, Moreira JN, Fonseca C, Duzgunes N, De Lima MC. On the formulation of ph - sensitive liposomes with long circulation times. *Adv Drug Deliv Rev* 56(7), 947-965 (2004).
24. Donkuru M, Badea I, Wettig S, Verrall R, Elsabahy M, Foldvari M. Advancing nonviral gene delivery: Lipid- and surfactant-based nanoparticle design strategies. *Nanomedicine* 5(7), 1103-1127 (2010).
25. Sérgio Simões AF, Henrique Faneca, Miguel Mano, Nuno Penacho, Nejat Düzgünes, Maria Pedroso De Lima. Cationic liposomes for gene delivery. *Expert Opin. Drug Deliv.* 2(2), 237-254 (2005).
26. Tros De Ilarduya C, Sun Y, Duzgunes N. Gene delivery by lipoplexes and polyplexes. *Eur. J. Pharm. Sci.* 40(3), 159-170 (2010).
27. Ewert KK, Samuel CE, Safinya CR. Lipid–DNA interactions: Structure–function studies of nanomaterials for gene delivery. In: *DNA interactions with polymers and surfactants*, Dias. R,Lindman. B (Ed.^(Eds). John Wiley & Sons, Inc., Boston, MA 377-404 (2007).
28. Tresset G. The multiple faces of self-assembled lipidic systems. *PMC biophysics* 2(1), 3 (2009).
29. Audouy S, Hoekstra D. Cationic lipid-mediated transfection in vitro and in vivo (review). *Mol. Membr. Biol.* 18(2), 129-143 (2001).
30. Ewert K, Slack NL, Ahmad A *et al*. Cationic lipid-DNA complexes for gene therapy: Understanding the relationship between complex structure and gene delivery pathways at the molecular level. *Curr. Med. Chem.* 11(2), 133-149 (2004).
31. Koltover I, Salditt T, Rädler JO, Safinya CR. An inverted hexagonal phase of cationic liposome-DNA complexes related to DNA release and delivery. *Science* 281(5373), 78-81 (1998).
32. Rädler JO, Koltover I, Salditt T, Safinya CR. Structure of DNA-cationic liposome complexes: DNA intercalation in multilamellar membranes in distinct interhelical packing regimes. *Science* 275(5301), 810-814 (1997).
33. Foldvari M, Badea I, Wettig S, Verrall R, Bagonluri M. Structural characterization of novel gemini non-viral DNA delivery systems for cutaneous gene therapy. *J. Exp. Nanosci.* 1(2), 165-176 (2006).
34. Wang H, Kaur T, Tavakoli N, Joseph J, Wettig S. Transfection and structural properties of phytanyl substituted gemini surfactant-based vectors for gene delivery. *Phys. Chem. Chem. Phys.* 15(47), 20510-20516 (2013).
35. Donkuru M, Wettig SD, Verrall RE, Badea I, Foldvari M. Designing ph-sensitive gemini nanoparticles for non-viral gene delivery into keratinocytes. *J. Mater. Chem.* 22(13), 6232-6244 (2012).

36. Wettig SD, Badea I, Donkuru M, Verrall RE, Foldvari M. Structural and transfection properties of amine-substituted gemini surfactant-based nanoparticles. *J. Gene Med.* 9(8), 649-658 (2007).
37. Barran-Berdon AL, Misra SK, Datta S *et al*. Cationic gemini lipids containing polyoxyethylene spacers as improved transfecting agents of plasmid DNA in cancer cells. *J. Mater. Chem. B* 2(29), 4640-4652 (2014).
38. Pietralik Z, Krzyszton R, Kida W, Andrzejewska W, Kozak M. Structure and conformational dynamics of dmpc/dicationic surfactant and dmpc/dicationic surfactant/DNA systems. *Int. J. Mol. Sci.* 14(4), 7642-7659 (2013).
39. Mintzer MA, Simanek EE. Nonviral vectors for gene delivery. *Chem. Rev.* 109(2), 259-302 (2008).
40. Menger FM, Littau CA. Gemini-surfactants: Synthesis and properties. *J. Am. Chem. Soc.* 113(4), 1451-1452 (1991).
41. Menger FM, Keiper JS. Gemini surfactants. *Angew. Chem. Int. Edit.* 39(11), 1906-1920 (2000).
42. Wettig SD, Verrall RE, Foldvari M. Gemini surfactants: A new family of building blocks for non-viral gene delivery systems. *Curr. Gene. Ther.* 8(1), 9-23 (2008).
43. Kirby AJ, Camilleri P, Engberts JBFN *et al*. Gemini surfactants: New synthetic vectors for gene transfection. *Angew. Chem. Int. Edit.* 42(13), 1448-1457 (2003).
44. Zana. R, Xia. J. *Gemini surfactants: Synthesis, interfacial and solution-phase behavior, and applications*. CRC Press, New York, U.S.A. 117, (2003).
45. Kumar M, Jinturkar K, Yadav MR, Misra A. Gemini amphiphiles: A novel class of nonviral gene delivery vectors. *Crit. Rev. Ther. Drug Carrier. Syst.* 27(3), 237-278 (2010).
46. Bombelli C, Giansanti L, Luciani P, Mancini G. Gemini surfactant based carriers in gene and drug delivery. *Curr. Med. Chem.* 16(2), 171-183 (2009).
47. Badea I, Verrall R, Baca-Estrada M *et al*. In vivo cutaneous interferon-gamma gene delivery using novel dicationic (gemini) surfactant-plasmid complexes. *J. Gene Med.* 7(9), 1200-1214 (2005).
48. Wang H, Wettig SD. Synthesis and aggregation properties of dissymmetric phytanyl-gemini surfactants for use as improved DNA transfection vectors. *Phys. Chem. Chem. Phys.* 13(2), 637-642 (2011).
49. Li X, Wettig SD, Wang C, Foldvarib M, Verrall RE. Synthesis and solution properties of gemini surfactants containing oleyl chains. *Phys. Chem. Chem. Phys.* 7, 3172-3178 (2005).
50. Jiang N, Li P, Wang Y, Wang J, Yan H, Thomas RK. Micellization of cationic gemini surfactants with various counterions and their interaction with DNA in aqueous solution. *J. Phys. Chem. B* 108(39), 15385-15391 (2004).
51. Cardoso AM, Morais CM, Silva SG, Marques EF, De Lima MC, Jurado MA. Bis-quaternary gemini surfactants as components of nonviral gene delivery systems: A comprehensive study from physicochemical properties to membrane interactions. *Int. J. Pharm.* 474(1-2), 57-69 (2014).

52. Cardoso AM, Morais CM, Cruz AR *et al*. New serine-derived gemini surfactants as gene delivery systems. *Eur. J. Pharm. Biopharm.* 89, 347-356 (2015).
53. Muñoz-Úbeda M, Misra SK, Barrán-Berdón AL *et al*. How does the spacer length of cationic gemini lipids influence the lipoplex formation with plasmid DNA? Physicochemical and biochemical characterizations and their relevance in gene therapy. *Biomacromolecules* 13(12), 3926-3937 (2012).
54. Chen Q, Kang X, Li R *et al*. Structure of the complex monolayer of gemini surfactant and DNA at the air/water interface. *Langmuir* 28(7), 3429-3438 (2012).
55. Zhou T, Xu G, Ao M, Yang Y, Wang C. DNA compaction to multi-molecular DNA condensation induced by cationic imidazolium gemini surfactants. *Colloids Surf. A. Physicochem. Eng. Asp.* 414(0), 33-40 (2012).
56. Misra SK, Muñoz-Ubeda M, Datta S *et al*. Effects of a delocalizable cation on the headgroup of gemini lipids on the lipoplex-type nanoggregates directly formed from plasmid DNA. *Biomacromolecules*, (2013).
57. Aleandri S, Bombelli C, Bonicelli MG *et al*. Fusion of gemini based cationic liposomes with cell membrane models: Implications for their biological activity. *BBA. Biomembranes* 1828(2), 382-390 (2013).
58. Zhi D, Zhang S, Cui S, Zhao Y, Wang Y, Zhao D. The headgroup evolution of cationic lipids for gene delivery. *Bioconjug. Chem.* 24(4), 487-519 (2013).
59. Simberg D, Danino D, Talmon Y *et al*. Phase behavior, DNA ordering, and size instability of cationic lipoplexes. Relevance to optimal transfection activity. *J. Biol. Chem.* 276(50), 47453-47459 (2001).
60. Zuidam NJ, Barenholz Y, Minsky A. Chiral DNA packaging in DNA-cationic liposome assemblies. *FEBS Lett.* 457(3), 419-422 (1999).
61. Caracciolo G, Pozzi D, Caminiti R *et al*. Enhanced transfection efficiency of multicomponent lipoplexes in the regime of optimal membrane charge density. *J. Phys. Chem. B* 112(36), 11298-11304 (2008).
62. Ewert KK, Evans HM, Zidovska A, Bouxsein NF, Ahmad A, Safinya CR. A columnar phase of dendritic lipid-based cationic liposome-DNA complexes for gene delivery: Hexagonally ordered cylindrical micelles embedded in a DNA honeycomb lattice. *J. Am. Chem. Soc.* 128(12), 3998-4006 (2006).
63. Ma B, Zhang S, Jiang H, Zhao B, Lv H. Lipoplex morphologies and their influences on transfection efficiency in gene delivery. *J. Control. Release* 123(3), 184-194 (2007).
64. Misra SK, Biswas J, Kondaiah P, Bhattacharya S. Gene transfection in high serum levels: Case studies with new cholesterol based cationic gemini lipids. *PloS one* 8(7), e68305 (2013).
65. Bajaj A, Kondaiah P, Bhattacharya S. Synthesis and gene transfer activities of novel serum compatible cholesterol-based gemini lipids possessing oxyethylene-type spacers. *Bioconjug. Chem.* 18(5), 1537-1546 (2007).
66. Betker JL, Kullberg M, Gomez J, Anchordoquy TJ. Cholesterol domains enhance transfection. *Ther. Deliv.* 4(4), 453-462 (2013).

67. Bajaj A, Kondaiah P, Bhattacharya S. Effect of the nature of the spacer on gene transfer efficacies of novel thiocholesterol derived gemini lipids in dfferent cell lines: A structure–activity investigation. *J. Med. Chem.* 51(8), 2533-2540 (2008).

68. Meekel Arthur aP, Wagenaar A, Šmisterová J *et al*. Synthesis of pyridinium amphiphiles used for transfection and some characteristics of amphiphile/DNA complex formation. *Eur. J. Org. Chem.* 2000(4), 665-673 (2000).

69. Ilies MA, Seitz WA, Johnson BH *et al*. Lipophilic pyrylium salts in the synthesis of efficient pyridinium-based cationic lipids, gemini surfactants, and lipophilic oligomers for gene delivery. *J. Med. Chem.* 49(13), 3872-3887 (2006).

70. Bhadani A, Kataria H, Singh S. Synthesis, characterization and comparative evaluation of phenoxy ring containing long chain gemini imidazolium and pyridinium amphiphiles. *J. Colloid Interface Sci.* 361(1), 33-41 (2011).

71. Quagliotto P, Viscardi G, Barolo C *et al*. Gemini pyridinium surfactants: Synthesis and conductometric study of a novel class of amphiphiles1. *J. Org. Chem.* 68(20), 7651-7660 (2003).

72. Bhadani A, Singh S. Novel gemini pyridinium surfactants: Synthesis and study of their surface activity, DNA binding, and cytotoxicity. *Langmuir* 25(19), 11703-11712 (2009).

73. Maslov MA, Kabilova TO, Petukhov IA *et al*. Novel cholesterol spermine conjugates provide efficient cellular delivery of plasmid DNA and small interfering rna. *J. Control. Release* 160(2), 182-193 (2012).

74. Bajaj A, Kondiah P, Bhattacharya S. Design, synthesis, and in vitro gene delivery efficacies of novel cholesterol-based gemini cationic lipids and their serum compatibility: A sructure−activity investigation. *J. Med. Chem.* 50(10), 2432-2442 (2007).

75. Yang P, Singh J, Wettig S, Foldvari M, Verrall RE, Badea I. Enhanced gene expression in epithelial cells transfected with amino acid-substituted gemini nanoparticles. *Eur. J. Pharm. Biopharm.* 75(3), 311-320 (2010).

76. Mohammed-Saeid W, Michel D, El-Aneed A, Verrall RE, Low NH, Badea I. Development of lyophilized gemini surfactant-based gene delivery systems: Influence of lyophilization on the structure, activity and stability of the lipoplexes. *J. Pharm. Pharm. Sci.* 15(4), 548-567 (2012).

77. Perrone S, Usai M, Lazzari P, Tucker SJ, Wallace HM, Zanda M. Efficient cell transfection with melamine-based gemini surfactants. *Bioconjug. Chem.* 24(2), 176-187 (2013).

78. Sharma VD, Aifuwa EO, Heiney PA, Ilies MA. Interfacial engineering of pyridinium gemini surfactants for the generation of synthetic transfection systems. *Biomaterials* 34(28), 6906-6921 (2013).

79. Sharma VD, Lees J, Hoffman NE *et al*. Modulation of pyridinium cationic lipid–DNA complex properties by pyridinium gemini surfactants and its impact on lipoplex transfection properties. *Mol. Pharm.* 11(2), 545-559 (2013).

80. Huang YC, Riddle K, Rice KG, Mooney DJ. Long-term in vivo gene expression via delivery of pei-DNA condensates from porous polymer scaffolds. *Hum. Gene Ther.* 16(5), 609-617 (2005).

81. Badea I, Wettig S, Verrall R, Foldvari M. Topical non-invasive gene delivery using gemini nanoparticles in interferon-gamma-deficient mice. *Eur. J. Pharm. Biopharm.* 65(3), 414-422 (2007).
82. Badea I, Virtanen C, Verrall RE, Rosenberg A, Foldvari M. Effect of topical interferon-[gamma] gene therapy using gemini nanoparticles on pathophysiological markers of cutaneous scleroderma in tsk/+ mice. *Gene Ther.* 19(10), 978-987 (2012).
83. Badea I, Shaterian N, Foldvari M. Topical gene delivery in mice using gemini surfactant -lipid nanoparticles with and without tape electrode electroporation. *Drug Deliv. Lett.* 1(1), 62-66 (2011).
84. Alqawlaq S, Sivak JM, Huzil JT *et al.* Preclinical development and ocular biodistribution of gemini-DNA nanoparticles after intravitreal and topical administration: Towards non-invasive glaucoma gene therapy. *Nanomedicine*, (2014).
85. Markov OO, Mironova NL, Maslov MA *et al.* Novel cationic liposomes provide highly efficient delivery of DNA and rna into dendritic cell progenitors and their immature offsets. *J. Control. Release* 160(2), 200-210 (2012).
86. Koynova R, Wang L, Macdonald RC. An intracellular lamellar–nonlamellar phase transition rationalizes the superior performance of some cationic lipid transfection agents. *Proc. Natl. Acad. Sci. U. S. A.* 103(39), 14373-14378 (2006).
87. Hafez IM, Maurer N, Cullis PR. On the mechanism whereby cationic lipids promote intracellular delivery of polynucleic acids. *Gene Ther.* 8(15), 1188-1196 (2001).
88. Kawakami S, Harada A, Sakanaka K *et al*. In vivo gene transfection via intravitreal injection of cationic liposome/plasmid DNA complexes in rabbits. *Int. J. Pharm.* 278(2), 255-262 (2004).
89. Ciani L, Ristori S, Salvati A, Calamai L, Martini G. Dotap/dope and dc-chol/dope lipoplexes for gene delivery: Zeta potential measurements and electron spin resonance spectra. *Biochim. Biophys. Acta* 1664(1), 70-79 (2004).
90. Zhi D, Zhang S, Wang B, Zhao Y, Yang B, Yu S. Transfection efficiency of cationic lipids with different hydrophobic domains in gene delivery. *Bioconjug. Chem.* 21(4), 563-577 (2010).
91. Kikuchi A, Aoki Y, Sugaya S *et al*. Development of novel cationic liposomes for efficient gene transfer into peritoneal disseminated tumor. *Hum. Gene Ther.* 10(6), 947-955 (1999).
92. Zuidam NJ, Barenholz Y. Characterization of DNA–lipid complexes commonly used for gene delivery. *Int. J. Pharm.* 183(1), 43-46 (1999).
93. Sheikh M, Feig J, Gee B, Li S, Savva M. In vitro lipofection with novel series of symmetric 1,3-dialkoylamidopropane-based cationic surfactants containing single primary and tertiary amine polar head groups. *Chem. Phys. Lipids* 124(1), 49-61 (2003).
94. Kearns MD, Donkor A-M, Savva M. Structure−transfection activity studies of novel cationic cholesterol-based amphiphiles. *Mol. Pharm.* 5(1), 128-139 (2007).
95. Maitani Y, Igarashi S, Sato M, Hattori Y. Cationic liposome (dc-chol/dope=1:2) and a modified ethanol injection method to prepare liposomes, increased gene expression. *Int. J. Pharm.* 342(1–2), 33-39 (2007).

96. Kaneshiro TL, Wang X, Lu Z-R. Synthesis, characterization, and gene delivery of poly-l-lysine octa(3-aminopropyl)silsesquioxane dendrimers: Nanoglobular drug carriers with precisely defined molecular architectures. *Mol. Pharm.* 4(5), 759-768 (2007).
97. Symietz C, Schneider M, Brezesinski G, Möhwald H. DNA alignment at cationic lipid monolayers at the air/water interface. *Macromolecules* 37(10), 3865-3873 (2004).
98. Mcloughlin D, Dias R, Lindman B *et al*. Surface complexation of DNA with insoluble monolayers. Influence of divalent counterions. *Langmuir* 21(5), 1900-1907 (2005).
99. Cárdenas M, Nylander T, Jönsson B, Lindman B. The interaction between DNA and cationic lipid films at the air–water interface. *J. Colloid Interface Sci.* 286(1), 166-175 (2005).
100. Gromelski S, Brezesinski G. DNA condensation and interaction with zwitterionic phospholipids mediated by divalent cations. *Langmuir* 22(14), 6293-6301 (2006).
101. Erokhina S, Berzina T, Cristofolini L, Konovalov O, Erokhin V, Fontana MP. Interaction of DNA oligomers with cationic lipidic monolayers: Complexation and splitting. *Langmuir* 23(8), 4414-4420 (2007).
102. Cristofolini L, Berzina T, Erokhina S, Konovalov O, Erokhin V. Structural study of the DNA dipalmitoylphosphatidylcholine complex at the air−water interface. *Biomacromolecules* 8(7), 2270-2275 (2007).
103. Ulman A. *An introduction to ultrathin organic films: From langmuir-blodgett to self-assembly*. Academic Press: London, London. (1991).
104. Rubio-Magnieto J, Luis SV, Orlof M, Korchowiec B, Sautrey G, Rogalska E. Effects of gemini amphiphilic pseudopeptides on model lipid membranes: A langmuir monolayer study. *Colloids Surfac. B. Biointerfaces* 102(0), 659-666 (2013).
105. Brezesinski G, Möhwald H. Langmuir monolayers to study interactions at model membrane surfaces. *Adv. Colloid Interface Sci.* 100–102(0), 563-584 (2003).
106. Peetla C, Stine A, Labhasetwar V. Biophysical interactions with model lipid membranes: Applications in drug discovery and drug delivery. *Mol. Pharm.* 6(5), 1264-1276 (2009).
107. Corvis Y, Barzyk W, Brezesinski G *et al*. Interactions of a fungistatic antibiotic, griseofulvin, with phospholipid monolayers used as models of biological membranes. *Langmuir* 22(18), 7701-7711 (2006).
108. Hidalgo AA, Tabak M, Oliveira Jr ON. The interaction of meso-tetraphenylporphyrin with phospholipid monolayers. *Chem. Phys. Lipids* 134(2), 97-108 (2005).
109. Korchowiec B, Salem AB, Corvis Y, Korchowiec J, Rogalska E. Calixarenes in a membrane environment: A monolayer study on the miscibility of three p-tert-butylcalix[4]arene β-lactam derivatives with 1,2-dimyristoyl-sn-glycero-3-phosphoethanolamine. *J. Phys. Chem. B* 111(46), 13231-13242 (2007).
110. Korchowiec B, Paluch M, Corvis Y, Rogalska E. A langmuir film approach to elucidating interactions in lipid membranes: 1,2-dipalmitoyl-sn-glycero-3-phosphoethanolamine/cholesterol/metal cation systems. *Chem. Phys. Lipids* 144(2), 127-136 (2006).

111. Korchowiec B, Orlof M, Sautrey G *et al.* The mechanism of metal cation binding in two nalidixate calixarene conjugates. A langmuir film and molecular modeling study. *J. Phys. Chem. B* 114(32), 10427-10435 (2010).

112. Brockman H. Lipid monolayers: Why use half a membrane to characterize protein-membrane interactions? *Curr. Opin. Struc. Biol.* 9(4), 438-443 (1999).

113. Barnes G, Gentle I. *Interfacial science: An introduction*. (2nd). Oxford University Press, United States. 10-38, 76-84, 107-144, 289-310 (2011).

114. M Eeman MD. From biological membranes to biomimetic model membranes. *Biotechnol. Agron. Soc. Environ.* 14(4), 719-736 (2010).

115. Moghaddam B, Ali MH, Wilkhu J *et al.* The application of monolayer studies in the understanding of liposomal formulations. *Int. J. Pharm.* 417(1-2), 235-244 (2011).

116. Dupuy N, Pasc A, Baros F, Gérardin C. Langmuir isotherm analysis of novel branched perfluorinated surfactants and their interactions with single stranded DNA. *J. Fluorine Chem.* 132(11), 892-897 (2011).

117. Vollhardt D, Fainerman VB. Progress in characterization of langmuir monolayers by consideration of compressibility. *Adv. Colloid Interface Sci.* 127(2), 83-97 (2006).

118. Saupe A. Interfacial phenomena. Von j. T. Davies und e. K. Rideal. Academic press, new york-london 1963. 2. Aufl., viii, 480 s., zahlr. Abb. U. Tab., geb. $ 15.—. *Angewandte Chemie.* 77(6), 276-276 (1965).

119. Chen Q, Zhang D, Li R, Liu H, Hu Y. Effect of the spacer group on the behavior of the cationic gemini surfactant monolayer at the air/water interface. *Thin Solid Films* 516(23), 8782-8787 (2008).

120. Castano S, Delord B, Fevrier A, Lehn JM, Lehn P, Desbat B. Brewster angle microscopy and pmirras study of DNA interactions with bgtc, a cationic lipid used for gene transfer. *Langmuir* 24(17), 9598-9606 (2008).

121. Grueso E, Kuliszewska E, Prado-Gotor R, Perez-Tejeda P, Roldan E. Improving the understanding of DNA-propanediyl-1,3-bis(dodecyldimethylammonium) dibromide interaction using thermodynamic, structural and kinetic approaches. *Phys. Chem. Chem. Phys.* 15(46), 20064-20074 (2013).

122. Donlon L, Penaherrera A, Frankel D. Probing interactions of the hiv protein gp120 with lipids and cd4 receptors. *Soft Matter* 9(10), 2803-2809 (2013).

123. Donlon L, Nordin D, Frankel D. Complete unfolding of fibronectin reveals surface interactions. *Soft Matter* 8(38), 9933-9940 (2012).

124. Miyazawa N, Sakaue T, Yoshikawa K, Zana R. Rings-on-a-string chain structure in DNA. *J. Chem. Phys.* 122(4), (2005).

125. Chen X, Wang J, Shen N *et al*. Gemini surfactant/DNA complex monolayers at the air−water interface: Effect of surfactant structure on the assembly, stability, and topography of monolayers. *Langmuir* 18(16), 6222-6228 (2002).

126. Chen X, Wang J, Liu M. Influence of surfactant molecular structure on two-dimensional surfactant–DNA complexes: Langmuir balance study. *J. Colloid Interface Sci.* 287(1), 185-190 (2005).

127. Alami E, Beinert G, Marie P, Zana R. Alkanediyl-.Alpha.,.Omega.-bis(dimethylalkylammonium bromide) surfactants. 3. Behavior at the air-water interface. *Langmuir* 9(6), 1465-1467 (1993).
128. Sezgin E, Schwille P. Model membrane platforms to study protein-membrane interactions. *Mol. Membr. Biol.* 29(5), 144-154 (2012).
129. Bangham AD, Horne RW. Negative staining of phospholipids and their structural modification by surface-active agents as observed in the electron microscope. *J. Mol. Biol.* 8, 660-668 (1964).
130. Singer SJ, Nicolson GL. The fluid mosaic model of the structure of cell membranes. *Science* 175(4023), 720-731 (1972).
131. Simons K, Ikonen E. Functional rafts in cell membranes. *Nature* 387(6633), 569-572 (1997).
132. Parton RG, Simons K. Digging into caveolae. *Science* 269(5229), 1398-1399 (1995).
133. Lingwood D, Kaiser HJ, Levental I, Simons K. Lipid rafts as functional heterogeneity in cell membranes. *Biochem. Soc. Trans.* 37(Pt 5), 955-960 (2009).
134. Pike LJ. Lipid rafts: Bringing order to chaos. *J. Lipid Res.* 44(4), 655-667 (2003).
135. Lingwood D, Simons K. Lipid rafts as a membrane-organizing principle. *Science* 327(5961), 46-50 (2010).
136. Vereb G, Szollosi J, Matko J *et al*. Dynamic, yet structured: The cell membrane three decades after the singer-nicolson model. *Proc. Natl. Acad. Sci. U. S. A.* 100(14), 8053-8058 (2003).
137. Helms JB, Zurzolo C. Lipids as targeting signals: Lipid rafts and intracellular trafficking. *Traffic (Copenhagen, Denmark)* 5(4), 247-254 (2004).
138. Simons K, Sampaio JL. Membrane organization and lipid rafts. *Cold Spring Harb. Perspect. Biol.* 3(10), a004697 (2011).
139. Ikonen E. Roles of lipid rafts in membrane transport. *Curr. Opin. Cell Biol.* 13(4), 470-477 (2001).
140. Bissig C, Gruenberg J. Lipid sorting and multivesicular endosome biogenesis. *Cold Spring Harb. Perspect. Biol.* 5(10), a016816 (2013).
141. Gruenberg J. Lipids in endocytic membrane transport and sorting. *Curr. Opin. Cell Biol.* 15(4), 382-388 (2003).
142. Scott CC, Vacca F, Gruenberg J. Endosome maturation, transport and functions. *Semin. Cell Dev. Biol.* 31, 2-10 (2014).
143. Mukherjee S, Maxfield FR. Role of membrane organization and membrane domains in endocytic lipid trafficking. *Traffic (Copenhagen, Denmark)* 1(3), 203-211 (2000).
144. Van Meer G, Sprong H. Membrane lipids and vesicular traffic. *Curr. Opin. Cell Biol.* 16(4), 373-378 (2004).
145. Blom T, Somerharju P, Ikonen E. Synthesis and biosynthetic trafficking of membrane lipids. *Cold Spring Harb. Perspect. Biol.* 3(8), a004713 (2011).
146. Jovic M, Sharma M, Rahajeng J, Caplan S. The early endosome: A busy sorting station for proteins at the crossroads. *Histol. Histopathol.* 25(1), 99-112 (2010).

147. Van Meer G, Voelker DR, Feigenson GW. Membrane lipids: Where they are and how they behave. *Nature reviews. Molecular cell biology* 9(2), 112-124 (2008).
148. Canton I, Battaglia G. Endocytosis at the nanoscale. *Chem. Soc. Rev.* 41(7), 2718-2739 (2012).
149. El-Sayed A, Harashima H. Endocytosis of gene delivery vectors: From clathrin-dependent to lipid raft-mediated endocytosis. *Mol. Ther.* 21(6), 1118-1130 (2013).
150. Doherty GJ, Mcmahon HT. Mechanisms of endocytosis. *Annu. Rev. Biochem.* 78, 857-902 (2009).
151. Marsh M, Mcmahon HT. The structural era of endocytosis. *Science* 285(5425), 215-220 (1999).
152. Khalil IA, Kogure K, Akita H, Harashima H. Uptake pathways and subsequent intracellular trafficking in nonviral gene delivery. *Pharmacol. Rev.* 58(1), 32-45 (2006).
153. Thakur G, Micic M, Leblanc RM. Surface chemistry of alzheimer's disease: A langmuir monolayer approach. *Colloids Surf. B. Biointerfaces* 74(2), 436-456 (2009).
154. Yetukuri L, Ekroos K, Vidal-Puig A, Oresic M. Informatics and computational strategies for the study of lipids. *Mol. Biosyst.* 4(2), 121-127 (2008).
155. Escriba PV, Gonzalez-Ros JM, Goni FM *et al*. Membranes: A meeting point for lipids, proteins and therapies. *J. Cell. Mol. Med.* 12(3), 829-875 (2008).
156. Miñones Jr J, Pais S, Miñones J, Conde O, Dynarowicz-Łątka P. Interactions between membrane sterols and phospholipids in model mammalian and fungi cellular membranes — a langmuir monolayer study. *Biophys. Chem.* 140(1–3), 69-77 (2009).
157. Kenny J. Mammalian cell membranes. Vol. 2. The diversity of membranes: Edited by g. A. Jamieson and d. M. Robinson. Pp 364. Butterworths, london and boston, 1976. £18.00. *Biochemical Education* 6(1), 22-22 (1978).
158. Jamieson GA, Robinson DM. *Mammalian cell membranes: Volume 2: The diversity of membranes*. Elsevier Science, (2014).
159. Maxfield FR, Menon AK. Intracellular sterol transport and distribution. *Curr. Opin. Cell Biol.* 18(4), 379-385 (2006).
160. Guha S, Rajani M, Padh H. Identification and characterization of lipids from endosomes purified by electromagnetic chromatography. *Indian J. Biochem. Biophys.* 44(6), 443-449 (2007).
161. Barwicz J, Tancrede P. The effect of aggregation state of amphotericin-b on its interactions with cholesterol- or ergosterol-containing phosphatidylcholine monolayers. *Chem. Phys. Lipids* 85(2), 145-155 (1997).
162. Loose M, Schwille P. Biomimetic membrane systems to study cellular organization. *J. Struct. Biol.* 168(1), 143-151 (2009).
163. Nagle JF. Theory of lipid monolayer and bilayer phase transitions: Effect of headgroup interactions. *J. Membr. Biol.* 27(3), 233-250 (1976).
164. Feng S-S. Interpretation of mechanochemical properties of lipid bilayer vesicles from the equation of state or pressure−area measurement of the monolayer at the air−water or oil−water interface. *Langmuir* 15(4), 998-1010 (1999).

165. Sessa G, Weissmann G. Phospholipid spherules (liposomes) as a model for biological membranes. *J. Lipid Res.* 9(3), 310-318 (1968).

166. Pignatello R, Musumeci T, Basile L, Carbone C, Puglisi G. Biomembrane models and drug-biomembrane interaction studies: Involvement in drug design and development. *J. Pharm. Bioallied Sci.* 3(1), 4-14 (2011).

167. Piknova B, Schram V, Hall SB. Pulmonary surfactant: Phase behavior and function. *Curr. Opin. Struct. Biol.* 12(4), 487-494 (2002).

168. Wustneck R, Perez-Gil J, Wustneck N, Cruz A, Fainerman VB, Pison U. Interfacial properties of pulmonary surfactant layers. *Adv. Colloid Interface Sci.* 117(1-3), 33-58 (2005).

169. Gzyl-Malcher B, Handzlik J, Klekowska E. Interaction of prazosin with model membranes--a langmuir monolayer study. *Bioelectrochemistry (Amsterdam, Netherlands)* 87, 96-103 (2012).

170. Misiak P, Wilk KA, Kral T *et al*. New gluconamide-type cationic surfactants: Interactions with DNA and lipid membranes. *Biophys. Chem.* 180–181(0), 44-54 (2013).

171. Colomer A, Perez L, Pons R *et al*. Mixed monolayer of dppc and lysine-based cationic surfactants: An investigation into the antimicrobial activity. *Langmuir* 29(25), 7912-7921 (2013).

172. Hermans E, Vermant J. Interfacial shear rheology of dppc under physiologically relevant conditions. *Soft Matter* 10(1), 175-186 (2014).

173. Torrano AA, Pereira AS, Oliveira ON, Jr., Barros-Timmons A. Probing the interaction of oppositely charged gold nanoparticles with dppg and dppc langmuir monolayers as cell membrane models. *Colloids Surf. B. Biointerfaces* 108, 120-126 (2013).

174. Pavinatto FJ, Pavinatto A, Caseli L *et al*. Interaction of chitosan with cell membrane models at the air-water interface. *Biomacromolecules* 8(5), 1633-1640 (2007).

175. Pavinatto FJ, Caseli L, Pavinatto A *et al*. Probing chitosan and phospholipid interactions using langmuir and langmuir-blodgett films as cell membrane models. *Langmuir* 23(14), 7666-7671 (2007).

176. Preetha A, Huilgol N, Banerjee R. Comparison of paclitaxel penetration in normal and cancerous cervical model monolayer membranes. *Colloids Surf. B. Biointerfaces* 53(2), 179-186 (2006).

177. Preetha A, Huilgol N, Banerjee R. Effect of fluidizing agents on paclitaxel penetration in cervical cancerous monolayer membranes. *J. Membr. Biol.* 219(1-3), 83-91 (2007).

178. Bennett WF, Tieleman DP. Computer simulations of lipid membrane domains. *Biochim. Biophys. Acta* 1828(8), 1765-1776 (2013).

179. Mcconlogue CW, Vanderlick TK. A close look at domain formation in dppc monolayers. *Langmuir* 13(26), 7158-7164 (1997).

180. Wnetrzak A, Latka K, Dynarowicz-Latka P. Interactions of alkylphosphocholines with model membranes-the langmuir monolayer study. *J. Membr. Biol.* 246(6), 453-466 (2013).

181. Arczewska M, Gagos M. Molecular organization of antibiotic amphotericin b in dipalmitoylphosphatidylcholine monolayers induced by k(+) and na(+) ions: The langmuir technique study. *Biochim. Biophys. Acta* 1808(11), 2706-2713 (2011).

182. Szczes A, Jurak M, Chibowski E. Stability of binary model membranes--prediction of the liposome stability by the langmuir monolayer study. *J. Colloid Interface Sci.* 372(1), 212-216 (2012).
183. Zhao L, Feng SS, Go ML. Investigation of molecular interactions between paclitaxel and dppc by langmuir film balance and differential scanning calorimetry. *J. Pharm. Sci.* 93(1), 86-98 (2004).
184. Brun A, Brezesinski G, Möhwald H, Blanzat M, Perez E, Rico-Lattes I. Interaction between phospholipids and new gemini catanionic surfactants having anti-hiv activity. *Colloids Surf. A. Physicochem. Eng. Asp.* 228(1–3), 3-16 (2003).
185. Almeida JaS, Marques EF, Jurado AS, Pais AaCC. The effect of cationic gemini surfactants upon lipid membranes. An experimental and molecular dynamics simulation study. *Phys. Chem. Chem. Phys.* 12(43), 14462-14476 (2010).
186. Castillo JA, Pinazo A, Carilla J *et al*. Interaction of antimicrobial arginine-based cationic surfactants with liposomes and lipid monolayers. *Langmuir* 20(8), 3379-3387 (2004).
187. Kida W, Kozak M. Structural changes of dppc bilayers induced by gemini surfactant. *Acta Phys. Pol. A* 121(4), 893-898 (2012).
188. Teixeira CV, Blanzat M, Koetz J, Rico-Lattes I, Brezesinski G. In-plane miscibility and mixed bilayer microstructure in mixtures of catanionic glycolipids and zwitterionic phospholipids. *Biochim. Biophys. Acta* 1758(11), 1797-1808 (2006).
189. Klock JC, Pieprzyk JK. Cholesterol, phospholipids, and fatty acids of normal immature neutrophils: Comparison with acute myeloblastic leukemia cells and normal neutrophils. *J. Lipid Res.* 20(7), 908-911 (1979).
190. Peetla C, Vijayaraghavalu S, Labhasetwar V. Biophysics of cell membrane lipids in cancer drug resistance: Implications for drug transport and drug delivery with nanoparticles. *Adv. Drug Deliver. Rev.* 65(13-14), 1686-1698 (2013).
191. Kojima K. Molecular aspects of the plasma membrane in tumor cells. *J. Med. Sci.* 56, 1-18 (1993).
192. Matti V, Saily J, Ryhanen SJ *et al*. Characterization of mixed monolayers of phosphatidylcholine and a dicationic gemini surfactant ss-1 with a langmuir balance: Effects of DNA. *Biophys. J.* 81(4), 2135-2143 (2001).
193. Fan J, Sammalkorpi M, Haataja M. Formation and regulation of lipid microdomains in cell membranes: Theory, modeling, and speculation. *FEBS Lett.* 584(9), 1678-1684 (2010).
194. Heczkova B, Slotte JP. Effect of anti-tumor ether lipids on ordered domains in model membranes. *FEBS Lett.* 580(10), 2471-2476 (2006).
195. Serro AP, Galante R, Kozica A *et al*. Effect of tetracaine on dmpc and dmpc+cholesterol biomembrane models: Liposomes and monolayers. *Colloids Surf. B. Biointerfaces* 116C, 63-71 (2013).
196. Korchowiec B, Korchowiec J, Hato M, Rogalska E. Glycolipid-cholesterol monolayers: Towards a better understanding of the interaction between the membrane components. *Biochim. Biophys. Acta* 1808(10), 2466-2476 (2011).

197. Sakamoto S, Nakahara H, Uto T, Shoyama Y, Shibata O. Investigation of interfacial behavior of glycyrrhizin with a lipid raft model via a langmuir monolayer study. *Biochim. Biophys. Acta* 1828(4), 1271-1283 (2013).
198. Wang C, Li X, Wettig SD, Badea I, Foldvari M, Verrall RE. Investigation of complexes formed by interaction of cationic gemini surfactants with deoxyribonucleic acid. *Phys. Chem. Chem. Phys.* 9(13), 1616-1628 (2007).
199. Medina-Kauwe LK, Xie J, Hamm-Alvarez S. Intracellular trafficking of nonviral vectors. *Gene Ther.* 12(24), 1734-1751 (2005).
200. Akbar J, Tavakoli N, Gerrard Marangoni D, Wettig SD. Mixed aggregate formation in gemini surfactant/1,2-dialkyl-sn-glycero-3-phosphoethanolamine systems. *J. Colloid Interface Sci.* 377(1), 237-243 (2012).
201. Wettig SD, Wang C, Verrall RE, Foldvari M. Thermodynamic and aggregation properties of aza- and imino-substituted gemini surfactants designed for gene delivery. *Phys. Chem. Chem. Phys.* 9(7), 871-877 (2007).
202. Wettig SD, Verrall RE. Thermodynamic studies of aqueous m-s-m gemini surfactant systems. *J. Colloid Interface Sci.* 235(2), 310-316 (2001).
203. Springer DL, Auberry DL, Ahram M *et al.* Characterization of plasma membrane proteins from ovarian cancer cells using mass spectrometry. *Dis. Markers.* 19(4-5), 219-228 (2003).
204. Moores B, Hane F, Eng L, Leonenko Z. Kelvin probe force microscopy in application to biomolecular films: Frequency modulation, amplitude modulation, and lift mode. *Ultramicroscopy* 110(6), 708-711 (2010).
205. Zerweck U, Loppacher C, Otto T, Grafström S, Eng LM. Accuracy and resolution limits of kelvin probe force microscopy. *Physical Review B* 71(12), 125424 (2005).
206. Dluhy RA. Quantitative external reflection infrared spectroscopic analysis of insoluble monolayers spread at the air-water interface. *J. Phys. Chem.* 90(7), 1373-1379 (1986).
207. Dluhy RA, Cornell DG. In situ measurement of the infrared spectra of insoluble monolayers at the air-water interface. *J. Phys. Chem.* 89(15), 3195-3197 (1985).
208. Blaudez D, Buffeteau T, Cornut JC *et al.* Polarization-modulated ft-ir spectroscopy of a spread monolayer at the air/water interface. *Appl. Spectrosc.* 47(7), 869-874 (1993).
209. Mendelsohn R, Brauner JW, Gericke A. External infrared reflection absorption spectrometry of monolayer films at the air-water interface. *Ann. Rev. Phys. Chem.* 46(1), 305-334 (1995).
210. Mendelsohn R, Flach CR. Infrared reflection – absorption spectrometry of monolayer films at the air – water interface. In: *Handbook of vibrational spectroscopy,* (Ed.^(Eds). John Wiley & Sons, Ltd, (2006).
211. Blaudez D, Buffeteau T, Desbat B, Marie Turlet J. Infrared and raman spectroscopies of monolayers at the air–water interface. *Curr. Opin. Colloid Interface Sci.* 4(4), 265-272 (1999).
212. Dluhy RA, Stephens SM, Widayati S, Williams AD. Vibrational spectroscopy of biophysical monolayers. Applications of ir and raman spectroscopy to biomembrane model systems at interfaces. *Spectrochim Acta A Mol. Biomol. Spectrosc.* 51(8), 1413-1447 (1995).

213. Blaudez D, Buffeteau T, Cornut JC *et al*. Polarization modulation ftir spectroscopy at the air-water interface. *Thin Solid Films* 242(1–2), 146-150 (1994).
214. Kvs-Nima. Http://www.Ksvnima.Com/products/pm-irras-infrared#specifications. 2014(01 March), (2014).
215. E R, J D. *Interfacial phenomena*. Academic Press, New York. (1963).
216. Fahey D, Small DM. Phase behavior of monolayers of 1,2-dipalmitoyl-3-acyl-sn-glycerols. *Langmuir* 4(3), 589-594 (1988).
217. Qibin C, Xiaodong L, Shaolei W, Shouhong X, Honglai L, Ying H. Cationic gemini surfactant at the air/water interface. *J. Colloid Interface Sci.* 314(2), 651-658 (2007).
218. Alejo T, Merchán MD, Velázquez MM. Specific ion effects on the properties of cationic gemini surfactant monolayers. *Thin Solid Films* 519(16), 5689-5695 (2011).
219. Li R, Chen Q, Zhang D, Liu H, Hu Y. Mixed monolayers of gemini surfactants and stearic acid at the air/water interface. *J. Colloid Interface Sci.* 327(1), 162-168 (2008).
220. Cheng L, Jiang Z, Dong J *et al*. Monolayers of novel gemini amphiphiles with phthalimide headgroups at the air/water interface: Ph and alkyl chain length effects. *J. Colloid Interface Sci.* 401, 97-106 (2013).
221. Montis C, Sostegni S, Milani S, Baglioni P, Berti D. Biocompatible cationic lipids for the formulation of liposomal DNA vectors. *Soft Matter* 10(24), 4287-4297 (2014).
222. Petelska AD, Naumowicz M, Figaszewski ZA. The influence of ph on phosphatidylethanolamine monolayer at the air/aqueous solution interface. *Cell Biochem. Biophys.* 65(2), 229-235 (2013).
223. Xu M, Spinney R, Allen HC. Water structure at the air-aqueous interface of divalent cation and nitrate solutions. *J. Phys. Chem. B* 113(13), 4102-4110 (2009).
224. Xu M, Tang CY, Jubb AM, Chen X, Allen HC. Nitrate anions and ion pairing at the air−aqueous interface†. *J. Phys. Chem. C* 113(6), 2082-2087 (2009).
225. Zaitsev SY, Baryshnikova EA, Sergeeva TA *et al*. Monolayers of the photosensitive benzodithia-15-crown-5 derivative. *Colloids and Surfaces A: Physicochemical and Engineering Aspects* 171(1–3), 283-290 (2000).
226. Tachibana R, Harashima H, Shono M *et al*. Intracellular regulation of macromolecules using ph-sensitive liposomes and nuclear localization signal: Qualitative and quantitative evaluation of intracellular trafficking. *Biochem. Biophys. Res. Commun.* 251(2), 538-544 (1998).
227. Hafez IM, Cullis PR. Roles of lipid polymorphism in intracellular delivery. *Adv. Drug Deliver. Rev.* 47(2–3), 139-148 (2001).
228. Farhood H, Serbina N, Huang L. The role of dioleoyl phosphatidylethanolamine in cationic liposome mediated gene transfer. *BBA. Biomembranes* 1235(2), 289-295 (1995).
229. Wang CY, Huang L. Ph-sensitive immunoliposomes mediate target-cell-specific delivery and controlled expression of a foreign gene in mouse. *Proc. Natl. Acad. Sci. U. S. A.* 84(22), 7851-7855 (1987).
230. Zhang YP, Sekirov L, Saravolac EG *et al*. Stabilized plasmid-lipid particles for regional gene therapy: Formulation and transfection properties. *Gene Ther.* 6(8), 1438-1447 (1999).

231. Hirsch-Lerner D, Zhang M, Eliyahu H, Ferrari ME, Wheeler CJ, Barenholz Y. Effect of “helper lipid” on lipoplex electrostatics. *BBA. Biomembranes* 1714(2), 71-84 (2005).
232. Henderson RDE. Nanoscale physics of surfactant gene delivery. PhD thesis, (2015).
233. Stuart BH. *Infrared spectroscopy: Fundamentals and applications*. Wiley, (2004).
234. Snyder RG, Strauss HL, Elliger CA. Carbon-hydrogen stretching modes and the structure of n-alkyl chains. 1. Long, disordered chains. *J. Phys. Chem.* 86(26), 5145-5150 (1982).
235. Mendelsohn R, Mao G, Flach CR. Infrared reflection-absorption spectroscopy: Principles and applications to lipid-protein interaction in langmuir films. *Biochimica et biophysica acta* 1798(4), 788-800 (2010).
236. Frey BL, Corn RM, Weibel SC. Polarization-modulation approaches to reflection–absorption spectroscopy. In: *Handbook of vibrational spectroscopy*, (Ed.^(Eds). John Wiley & Sons, Ltd, (2006).
237. Macphail RA, Strauss HL, Snyder RG, Elliger CA. Carbon-hydrogen stretching modes and the structure of n-alkyl chains. 2. Long, all-trans chains. *J. Phys. Chem. B* 88(3), 334-341 (1984).
238. Meister A, Kerth A, Blume A. Interaction of sodium dodecyl sulfate with dimyristoyl-sn-glycero-3-phosphocholine monolayers studied by infrared reflection absorption spectroscopy. A new method for the determination of surface partition coefficients. *J. Phys. Chem. B* 108(24), 8371-8378 (2004).
239. Tolstoy VP, Chernyshova I, Skryshevsky VA. *Handbook of infrared spectroscopy of ultrathin films*. Wiley, (2003).
240. Blaudez D, Turlet J-M, Dufourcq J, Bard D, Buffeteau T, Desbat B. Investigations at the air/water interface using polarization modulation ir spectroscopy. *J. Chem. Soc., Faraday Trans.* 92(4), 525-530 (1996).
241. Braun CS, Jas GS, Choosakoonkriang S, Koe GS, Smith JG, Middaugh CR. The structure of DNA within cationic lipid/DNA complexes. *Biophys. J.* 84(2 Pt 1), 1114-1123 (2003).
242. Marty R, N'soukpoe-Kossi CN, Charbonneau DM, Kreplak L, Tajmir-Riahi HA. Structural characterization of cationic lipid-trna complexes. *Nucleic Acids Res.* 37(15), 5197-5207 (2009).
243. Neault JF, Naoui M, Manfait M, Tajmir-Riahi HA. Aspirin-DNA interaction studied by ftir and laser raman difference spectroscopy. *FEBS Lett.* 382(1-2), 26-30 (1996).
244. Ramsey CRM, Joshua D. Analysis of cationic-lipid?Plasmid-DNA complexes. *Anal. Chem.* 79(19), 7240-7248 (2007).
245. Matulis D, Rouzina I, Bloomfield VA. Thermodynamics of cationic lipid binding to DNA and DNA condensation: Roles of electrostatics and hydrophobicity. *J. Am. Chem. Soc.* 124(25), 7331-7342 (2002).
246. Seoane R, Miñones J, Conde O, Miñones J, Casas M, Iribarnegaray E. Thermodynamic and brewster angle microscopy studies of fatty acid/cholesterol mixtures at the air/water interface. *J. Phys. Chem. B* 104(32), 7735-7744 (2000).

247. Takano E, Ishida Y, Iwahashi M, Araki T, Iriyama K. Surface chemical and morphological study on monolayers of cholesterol, cholestanol, and their derivatives conjugated with amino acid. *Langmuir* 13(21), 5782-5786 (1997).

248. Baglioni P, Cestelli O, Dei L, Gabrielli G. Monolayers of cholesterol at water-air interface: Mechanism of collapse. *Journal of Colloid and Interface Science* 104(1), 143-150 (1985).

249. Arima AA, Pavinatto FJ, Oliveira Jr ON, Gonzales ERP. The negligible effects of the antifungal natamycin on cholesterol-dipalmitoyl phosphatidylcholine monolayers may explain its low oral and topical toxicity for mammals. *Colloids Surf. B. Biointerfaces* 122, 202-208 (2014).

250. Sabatini K, Mattila J-P, Kinnunen PKJ. Interfacial behavior of cholesterol, ergosterol, and lanosterol in mixtures with dppc and dmpc. *Biophysical Journal* 95(5), 2340-2355 (2008).

251. Duncan SL, Larson RG. Comparing experimental and simulated pressure-area isotherms for dppc. *Biophys. J.* 94(8), 2965-2986

252. Minones J, Jr., Munoz M, Minones Trillo J, Haro I, Busquets MA, Alsina MA. Miscibility and langmuir studies of the interaction of e2 (279-298) peptide sequence of hepatitis g virus/gb virus-c with dipalmitoylphosphatidyl choline and dimiristoylphosphatidyl choline phospholipids. *Langmuir*, (2015).

253. Weidemann G, Vollhardt D. Long-range tilt orientational order in phospholipid monolayers: A comparative study. *Biophys. J.* 70(6), 2758-2766 (1996).

254. Gong K, Feng S-S, Go ML, Soew PH. Effects of ph on the stability and compressibility of dppc/cholesterol monolayers at the air–water interface. *Colloids and Surfaces A: Physicochemical and Engineering Aspects* 207(1–3), 113-125 (2002).

255. Seoane R, Miñones J, Conde O, Casas M, Iribarnegaray E. Interaction between amphotericin b and sterols in monolayers. Mixed films of ergosterol−amphotericin b. *Langmuir* 15(10), 3570-3573 (1999).

256. Minones J, Jr., Rey Gomez-Serranillos I, Conde O, Dynarowicz-Latka P, Minones Trillo J. The influence of subphase temperature on miltefosine-cholesterol mixed monolayers. *J. Colloid Interface Sci.* 301(1), 258-266 (2006).

257. Kim K, Kim C, Byun Y. Preparation of a dipalmitoylphosphatidylcholine/cholesterol langmuir−blodgett monolayer that suppresses protein adsorption. *Langmuir* 17(16), 5066-5070 (2001).

258. Kim S-R, Choi S-A, Kim J-D. The monolayer behavior and transfer characteristics of phospholipids at the air/water interface. *Korean J. Chem. Eng.* 13(1), 46-53 (1996).

259. Zhao L, Feng SS. Effects of cholesterol component on molecular interactions between paclitaxel and phospholipid within the lipid monolayer at the air-water interface. *J. Colloid Interface Sci.* 300(1), 314-326 (2006).

260. Serro AP, Galante R, Kozica A *et al*. Effect of tetracaine on dmpc and dmpc+cholesterol biomembrane models: Liposomes and monolayers. *Colloids Surf. B. Biointerfaces* 116, 63-71 (2014).

261. Wnętrzak A, Lipiec E, Łątka K, Kwiatek W, Dynarowicz-Łątka P. Affinity of alkylphosphocholines to biological membrane of prostate cancer: Studies in natural and model systems. *J. Membrane Biology* 247(7), 581-589 (2014).

262. Romão RIS, Maçôas E, Martinho JMG, Gonçalves Da Silva AMPS. Interaction of toremifene with dipalmitoyl-phosphatidyl-glycerol in monolayers at the air–water interface followed by fluorescence microscopy in langmuir–blodgett films. *Thin Solid Films* 534, 584-590 (2013).

263. Lopes-Costa T, Gamez F, Lago S, Pedrosa JM. Adsorption of DNA to octadecylamine monolayers at the air-water interface. *J. Colloid Interface Sci.* 354(2), 733-738 (2011).

264. Castano S, Delord B, Fevrier A, Lehn JM, Lehn P, Desbat B. Asymmetric lipid bilayer formation stabilized by DNA at the air/water interface. *Biochimie* 91(6), 765-773 (2009).

265. Hansda C, Hussain SA, Bhattacharjee D, Paul PK. Adsorption behavior of DNA onto a cationic surfactant monolayer at the air–water interface. *Surf. Sci.* 617, 124-130 (2013).

266. Gromelski S, Brezesinski G. DNA condensation and interaction with zwitterionic phospholipids mediated by divalent cations. *Langmuir* 22(14), 6293-6301 (2006).

267. Gravier J, Korchowiec B, Schneider R, Rogalska E. Interaction of amphiphilic chlorin-based photosensitizers with 1,2-dipalmitoyl-sn-glycero-3-phosphocholine monolayers. *Chem. Phys. Lipids* 158(2), 102-109 (2009).

268. Gagos M, Arczewska M. Ftir spectroscopic study of molecular organization of the antibiotic amphotericin b in aqueous solution and in dppc lipid monolayers containing the sterols cholesterol and ergosterol. *Eur Biophys J* 41(8), 663-673 (2012).

269. Blaudez D, Buffeteau T, Cornut JC *et al.* Polarization-modulated ft-ir spectroscopy of a spread monolayer at the air/water interface. *Appl. Spectrosc.* 47(7), 869-874 (1993).

270. Lewis RN, Mcelhaney RN, Pohle W, Mantsch HH. Components of the carbonyl stretching band in the infrared spectra of hydrated 1,2-diacylglycerolipid bilayers: A reevaluation. *Biophys. J.* 67(6), 2367-2375 (1994).

271. Porter MD, Bright TB, Allara DL, Chidsey CED. Spontaneously organized molecular assemblies. 4. Structural characterization of n-alkyl thiol monolayers on gold by optical ellipsometry, infrared spectroscopy, and electrochemistry. *J. Am. Chem. Soc.* 109(12), 3559-3568 (1987).

272. Byrd H, Whipps S, Pike JK, Ma J, Nagler SE, Talham DR. Role of the template layer in organizing self-assembled films: Zirconium phosphonate monolayers and multilayers at a langmuir-blodgett template. *J. Am. Chem. Soc.* 116(1), 295-301 (1994).

Appendix

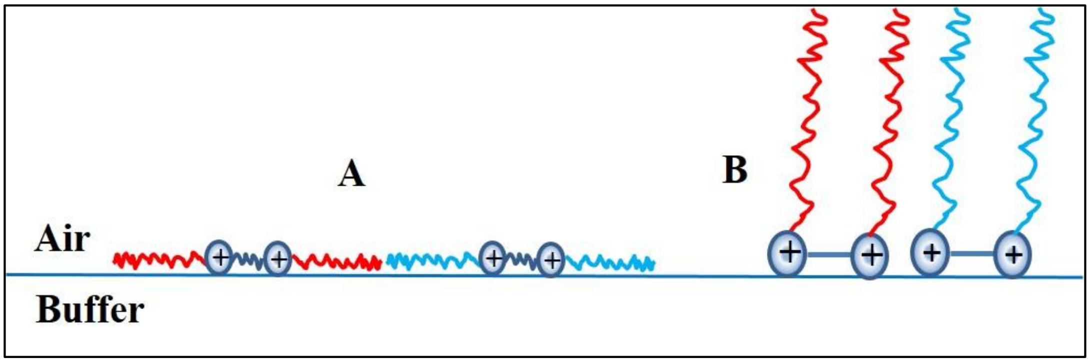

Figure A4.1. Schematic representation of the 16-7-16 molecules (A) having hydrophobic interactions between two alkyl tails, and the flexible spacer length provides the alkyl tails to lie flat on the air/buffer interface. (B). The short spacer length of the surfactant restricts the alkyl tail to remain flat on the surface, rather they remains slightly tilted at the air/buffer interface and occupies smaller molecular area.

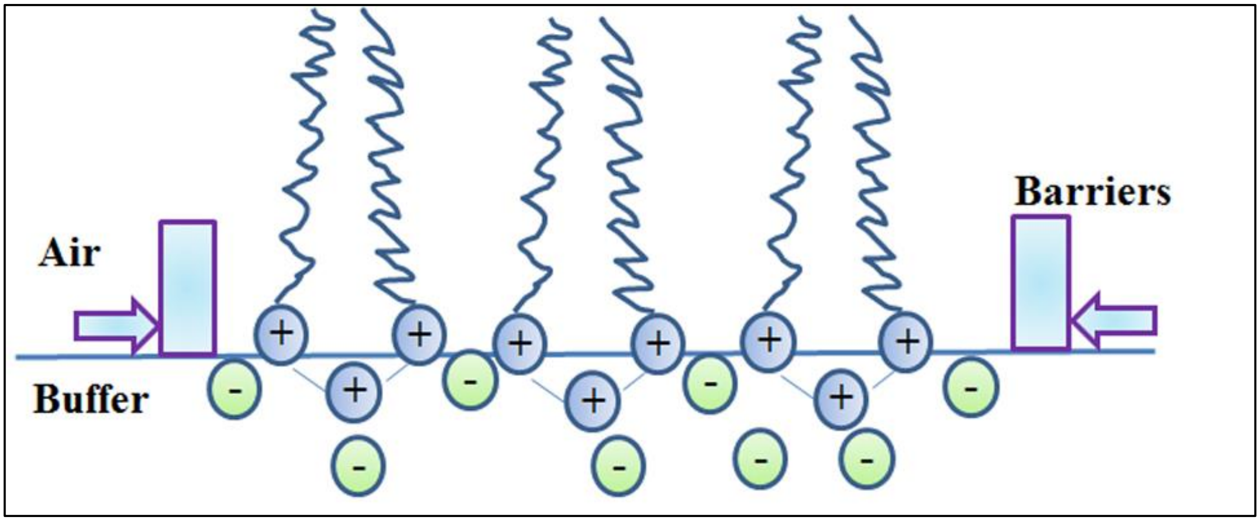

Figure A4.2. Schematic representation of the 16-7NH-16 monolayer at pH 4. The acetate buffer components resides in-between the positively charged 16-7NH-16 molecules, reduces the overall repulsions forces of the surfactant molecules, and consequently the monolayer may be compressed to smaller molecular area. During this charge neutralization by the acetate components, the monolayer undergoes a LE → G phase transition.

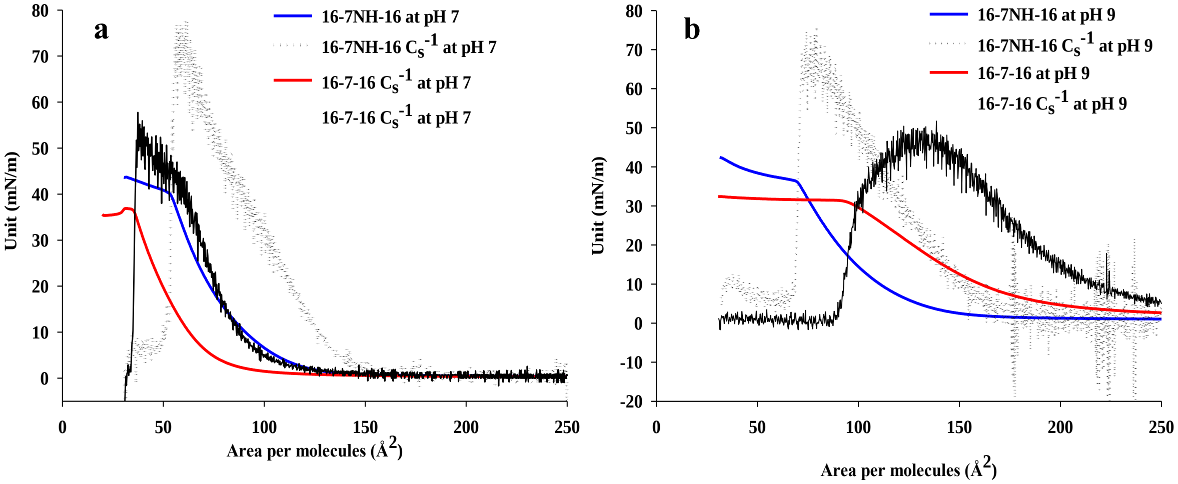

Figure A4.3. Compressibility modulus and surface pressure (Y axis) as a function of mean molecular area of the pure gemini surfactants at pH 7 (a) and 9 (b). The blue and red continuous line represents surface; and black continuous and dotted line represents values of the compressibility modulus of respective gemini surfactants.

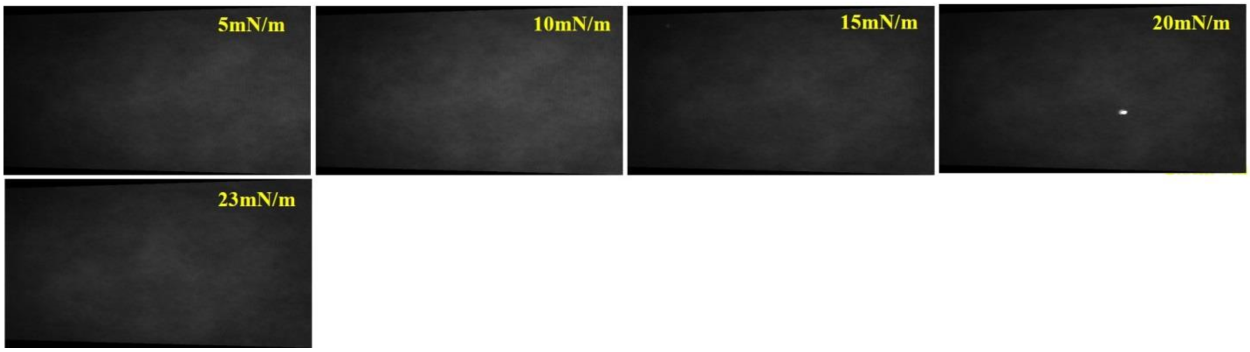

Figure A4.4. BAM image of 16-7-16 in pH 4 buffer.

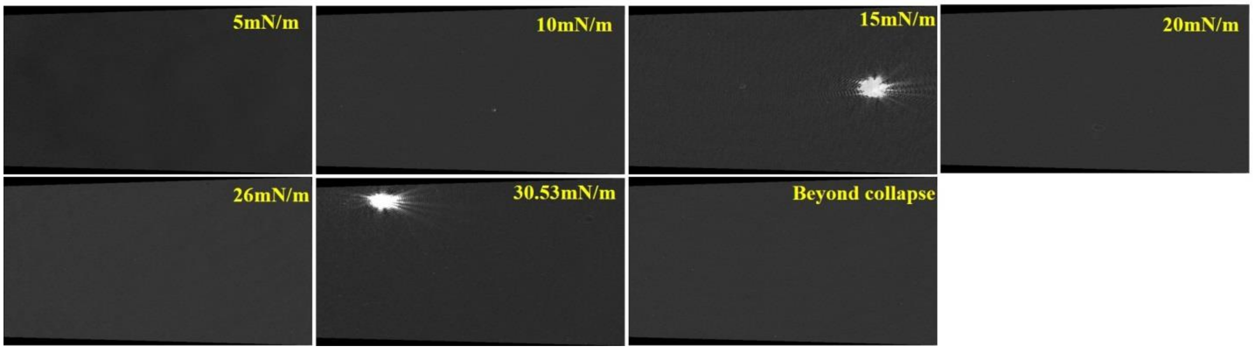

Figure A4.5. BAM image of 16-7-16 in pH 7 buffer.

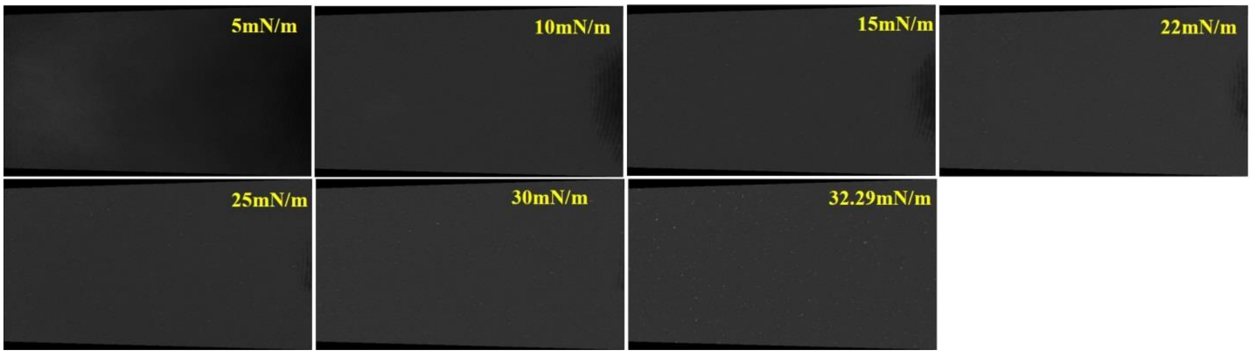

Figure A4.6. BAM image of 16-7-16 in pH 9 buffer.

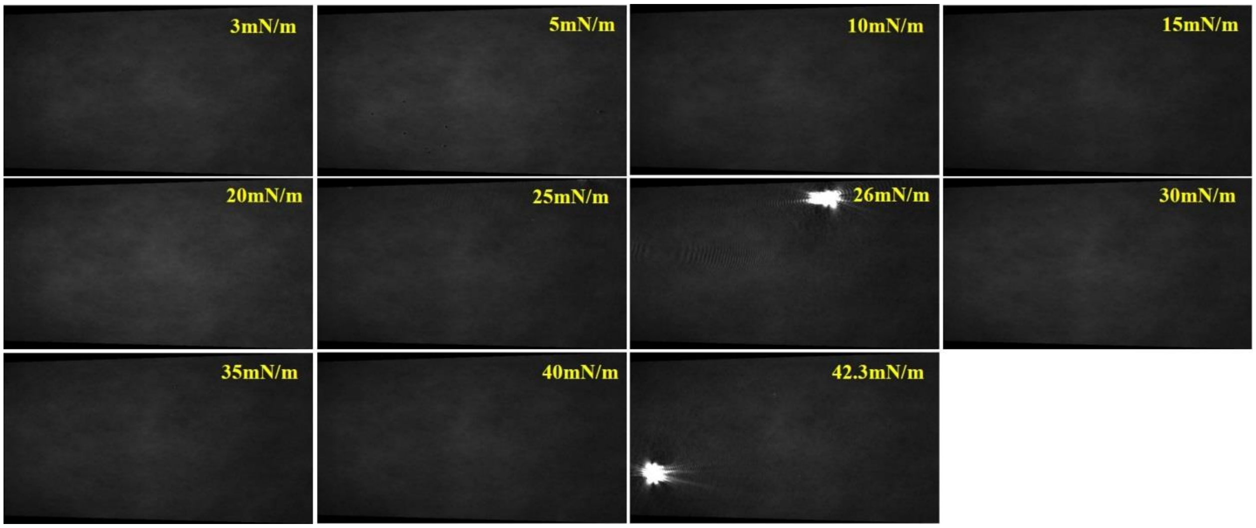

Figure A4.7. BAM image of 16-7NH-16 at pH 4.

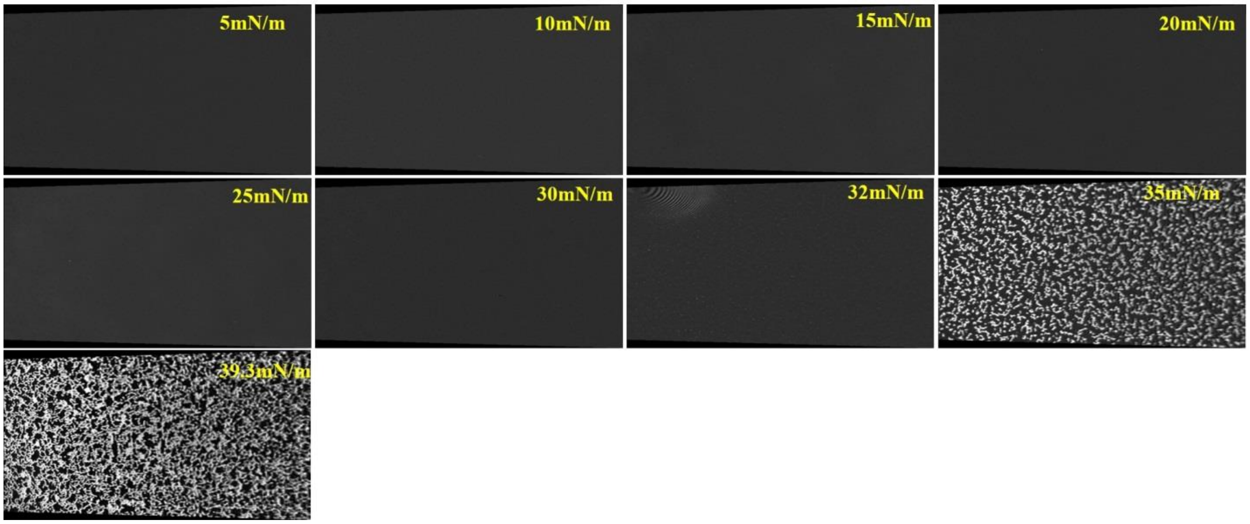

Figure A4.8. BAM image of 16-7NH-16 in pH 7 buffer.

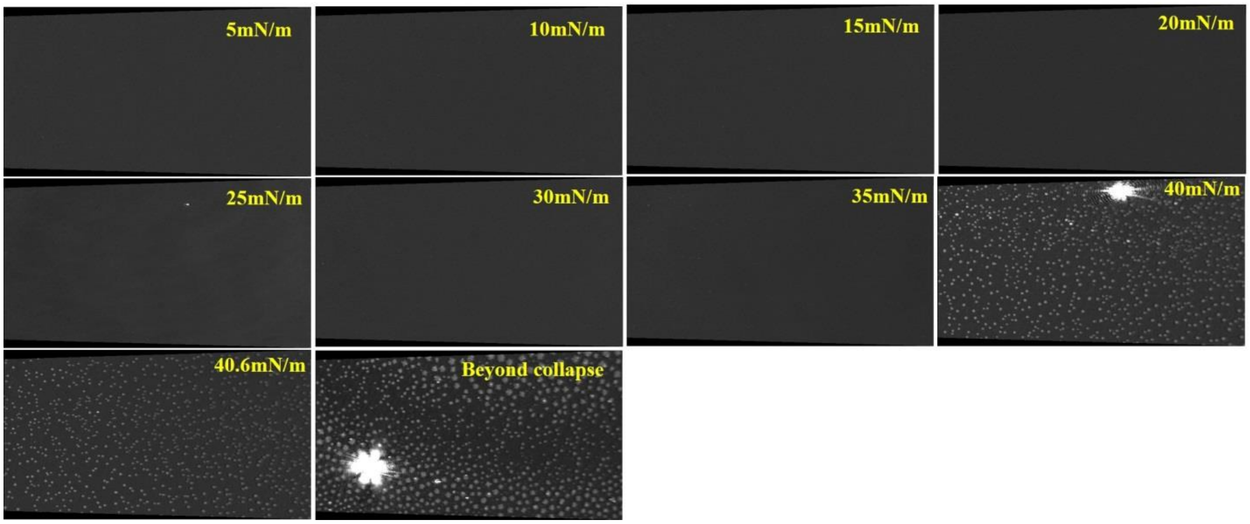

Figure A4.9. BAM image of 16-7NH-16 in pH 9 buffer.

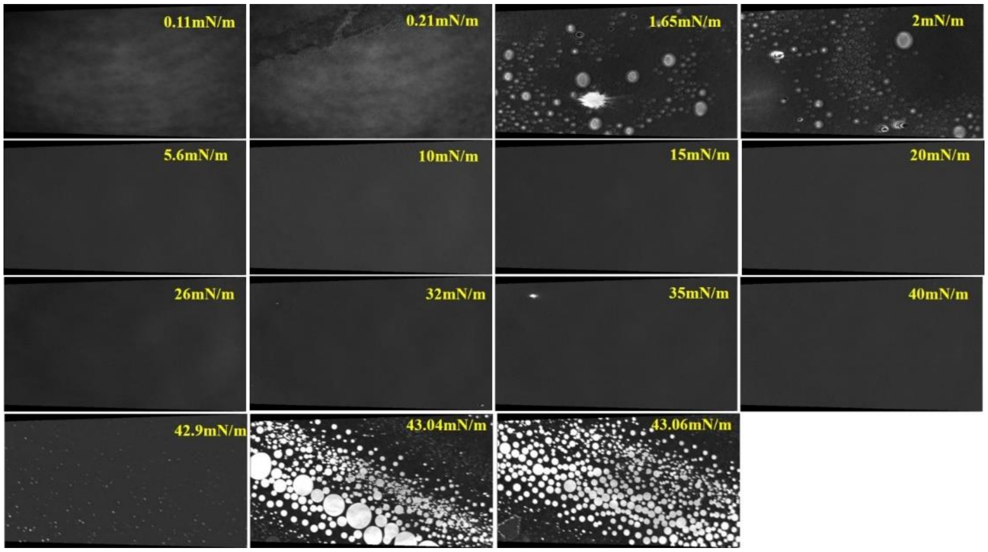

Figure A4.10. BAM image of DOPE at pH 4.

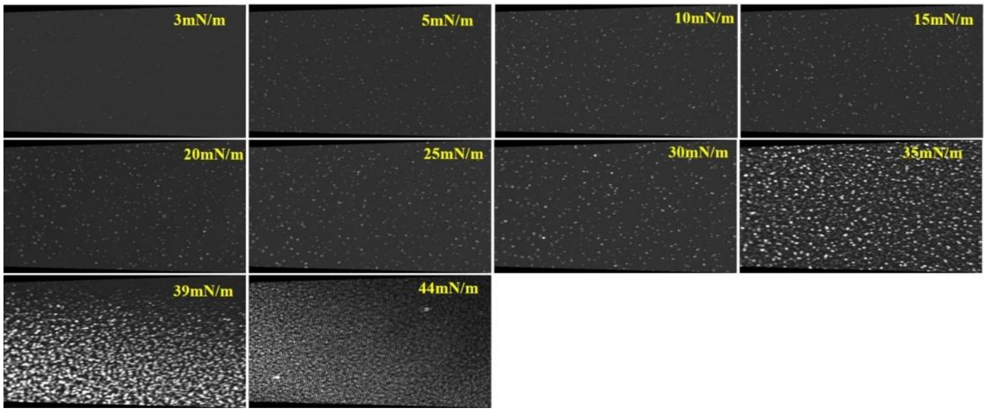

Figure A4.11. BAM image of DOPE in pH 7 buffer.

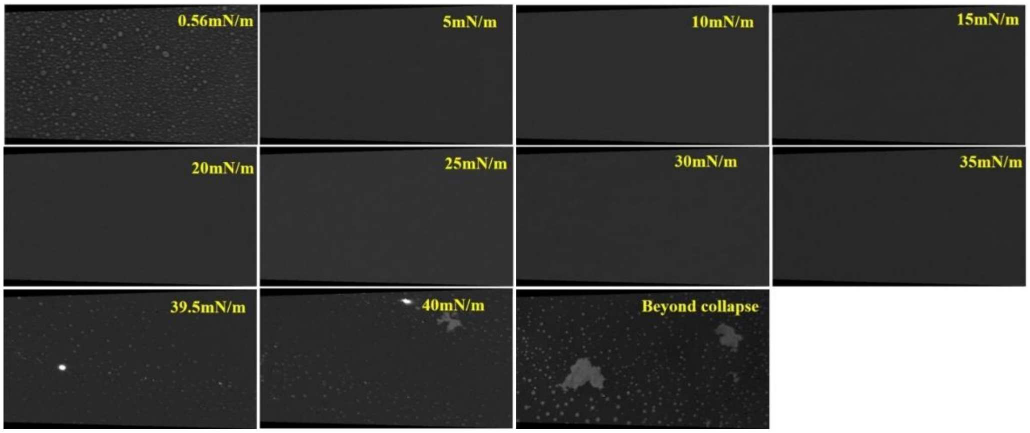

Figure A4.12. BAM image of DOPE in pH 9 buffer.

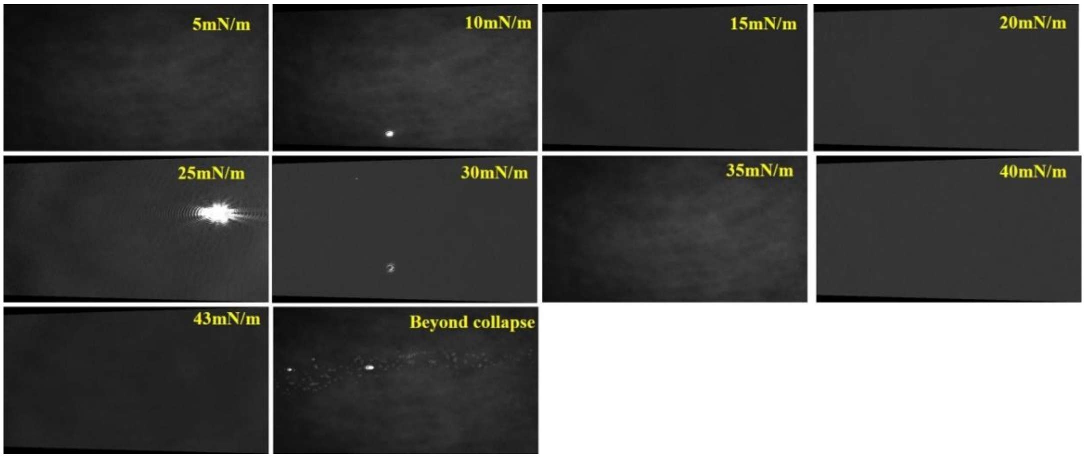

Figure A4.13. BAM image of 16-7-16/DOPE at pH 4 buffer.

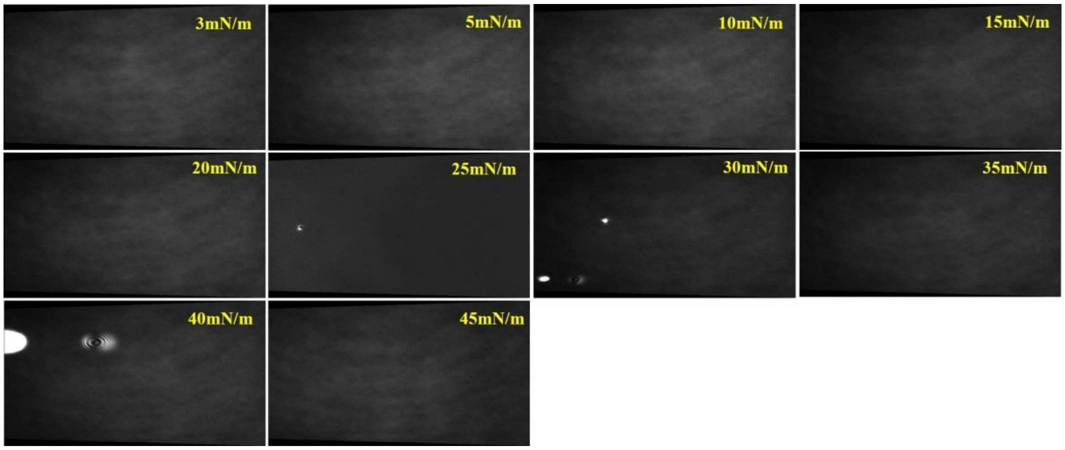

Figure A4.14. BAM images of 16-7NH-16/DOPE at pH 4 buffer.

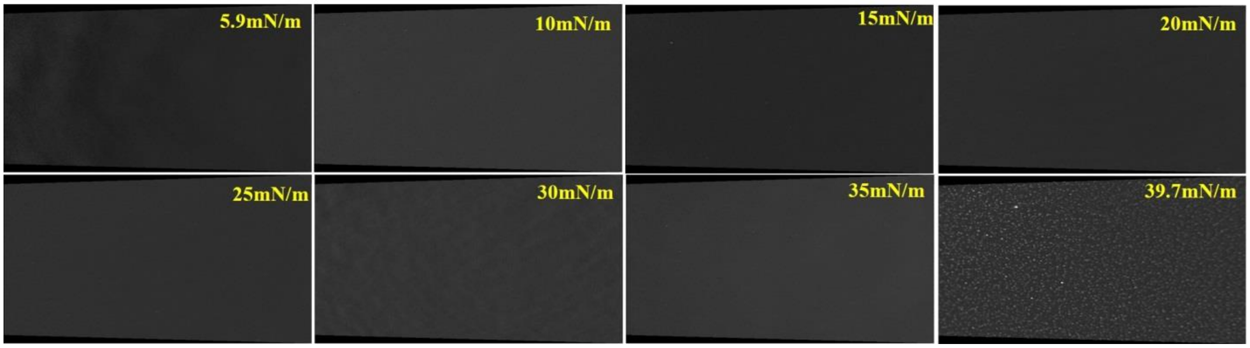

Figure A4.15. BAM image of 16-7-16/DOPE in pH 7 buffer.

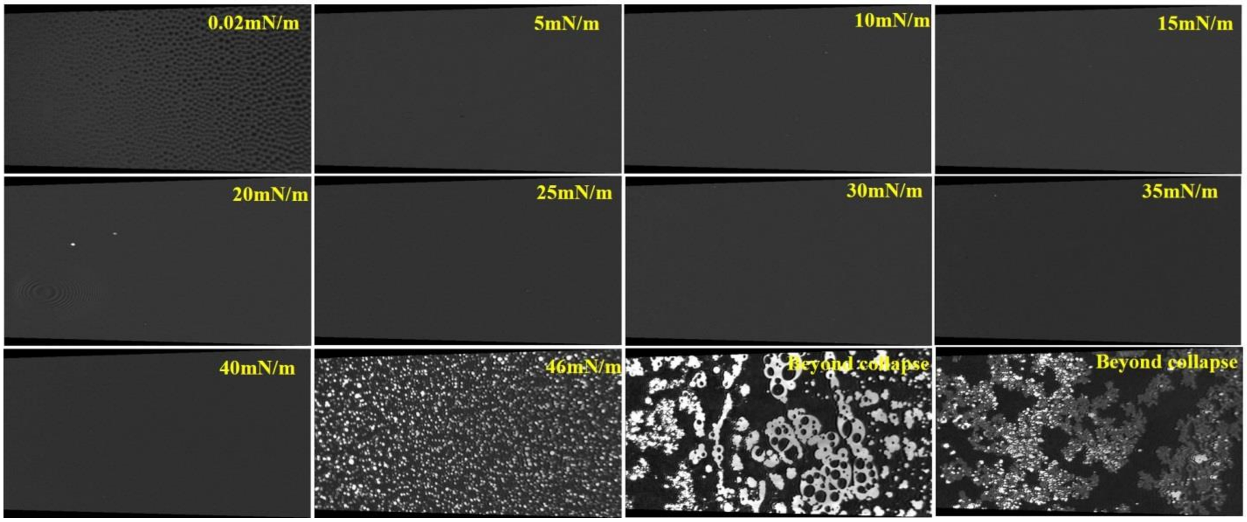

Figure A4.16. BAM image of 16-7NH-16/DOPE in pH 7 buffer.

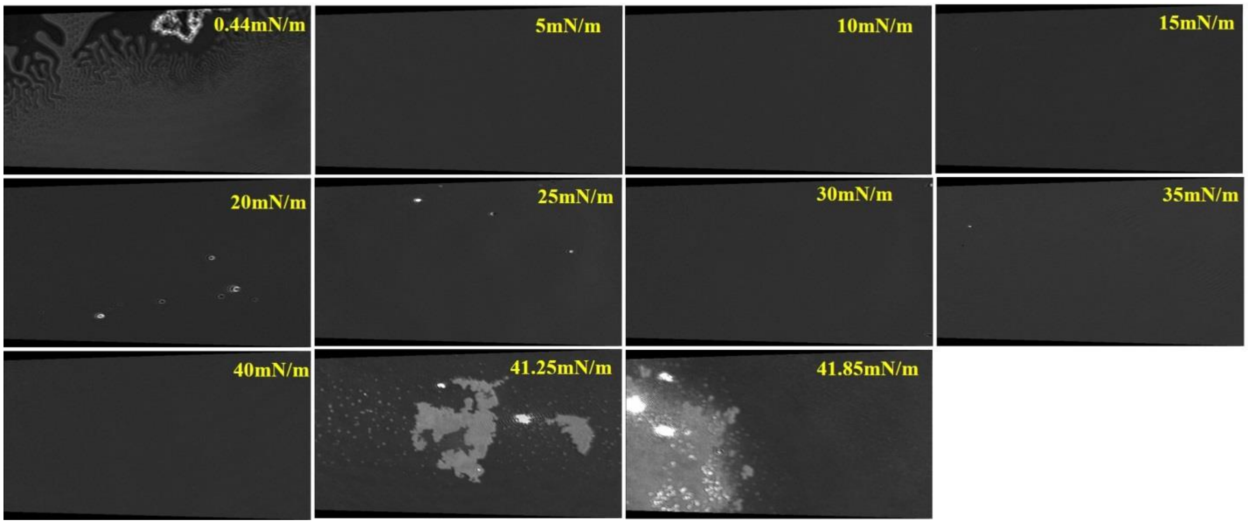

Figure A4.17. BAM image of 16-7-16/DOPE in pH 9 buffer.

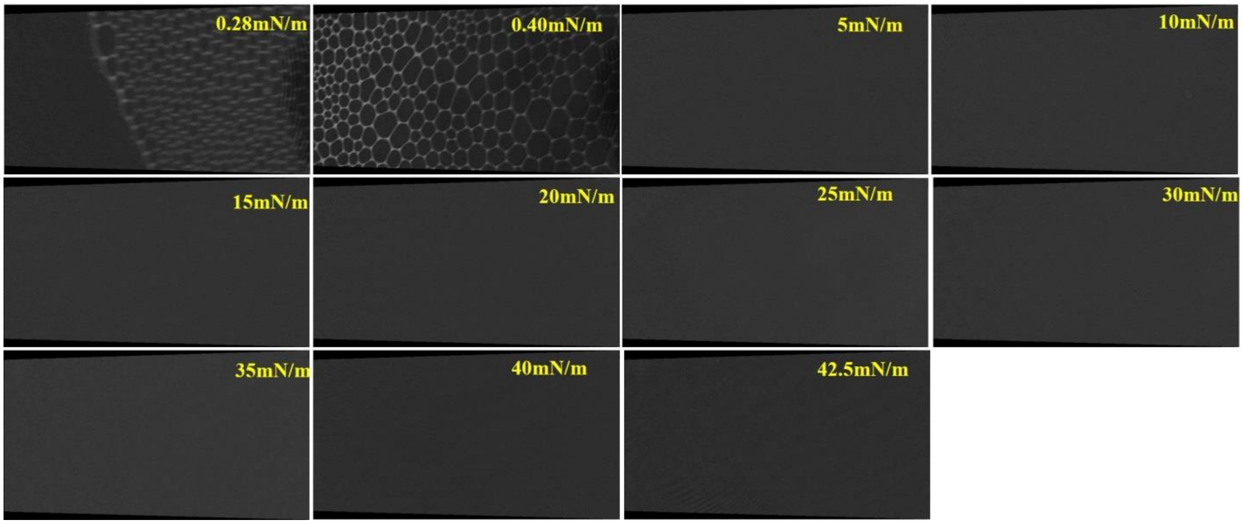

Figure A4.18. BAM image of 16-7NH-16/DOPE in pH 9 buffer.

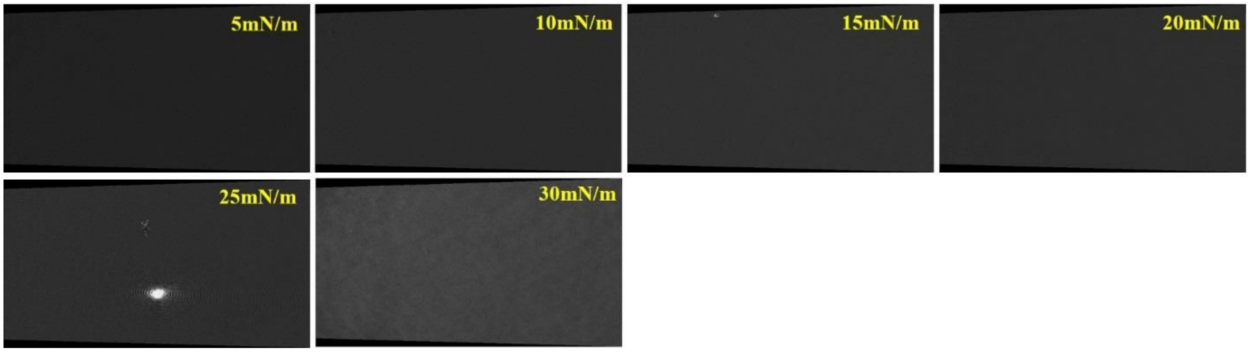

Figure A4.19. BAM image of 16-7-16/DNA in pH 4 buffer.

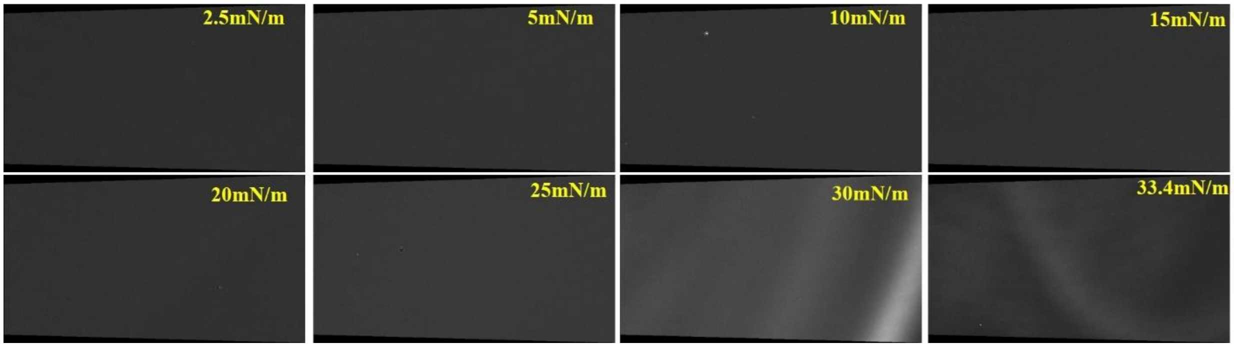

Figure A4.20. BAM image of 16-7NH-16/DNA in pH 4 buffer.

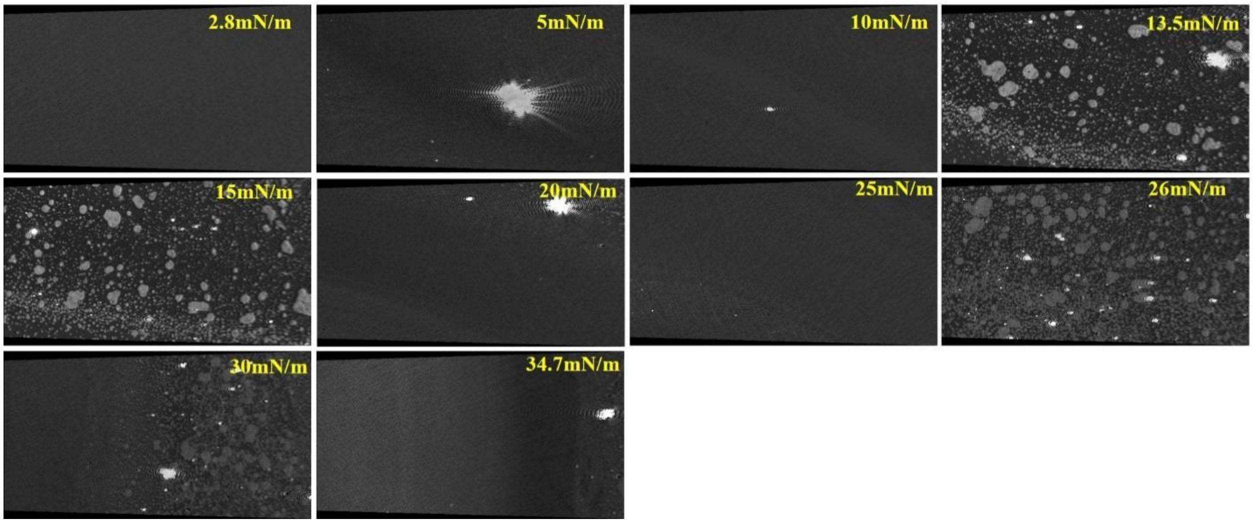

Figure A4.21. BAM image of 16-7-16/DNA in pH 7 buffer.

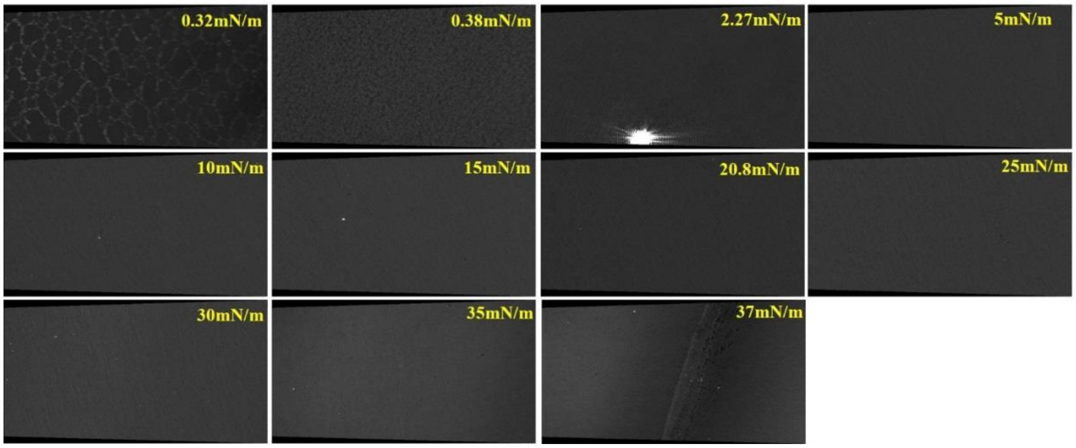

Figure A4.22. BAM image of 16-7NH-16/DNA in pH 7 buffer.

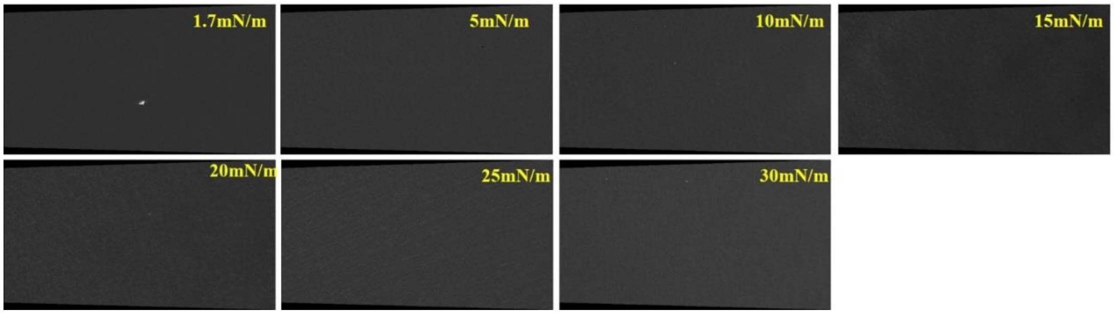

Figure A4.23. BAM image of 16-7-16/DNA in pH 9 buffer.

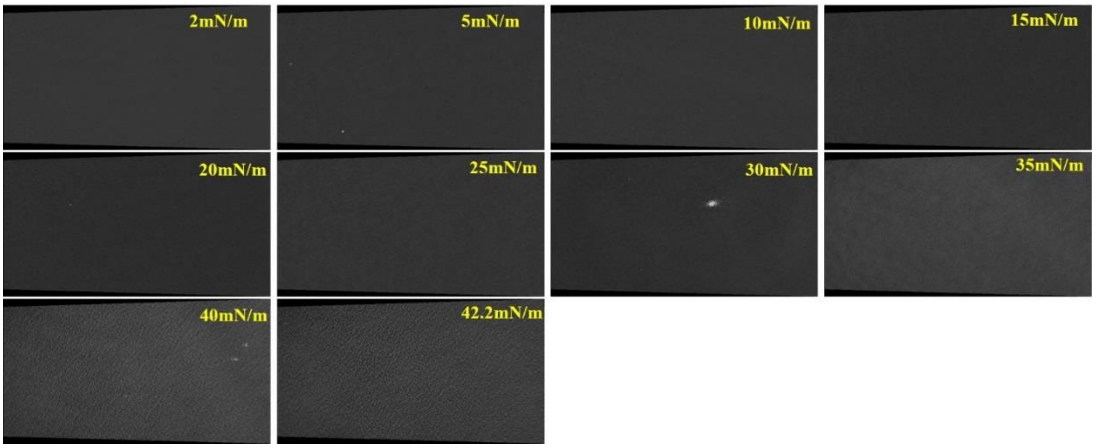

Figure A4.24. BAM image of 16-7NH-16/DNA in pH 9 buffer.

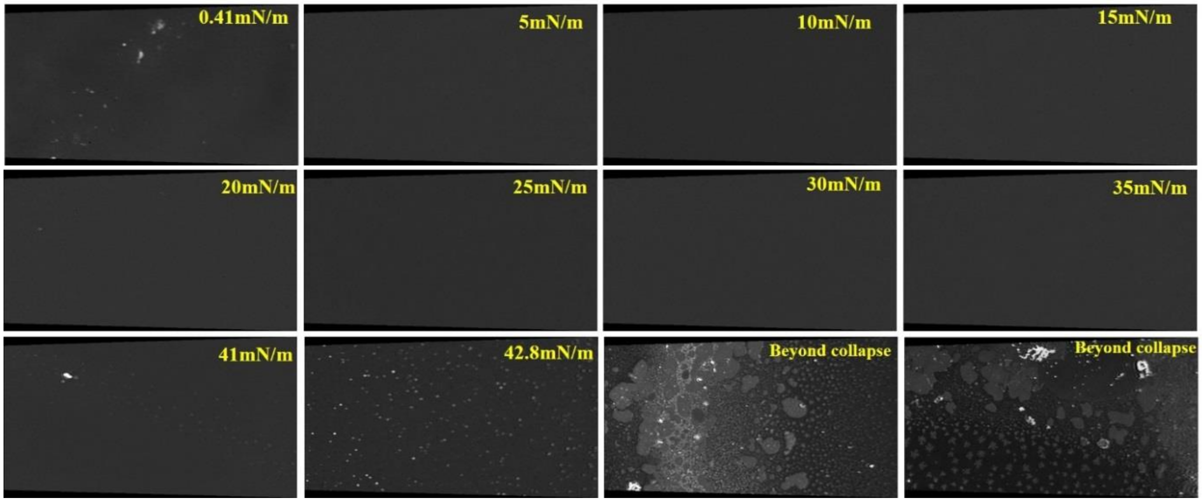

Figure A4.25. BAM image of DOPE/DNA in pH 4 buffer.

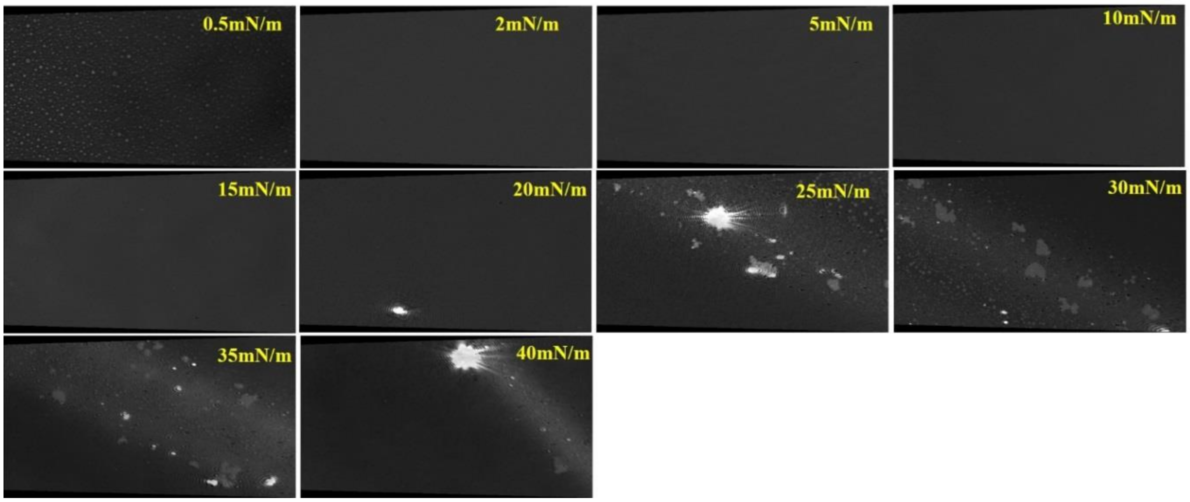

Figure A4.26. BAM image of DOPE/DNA in pH 7 buffer.

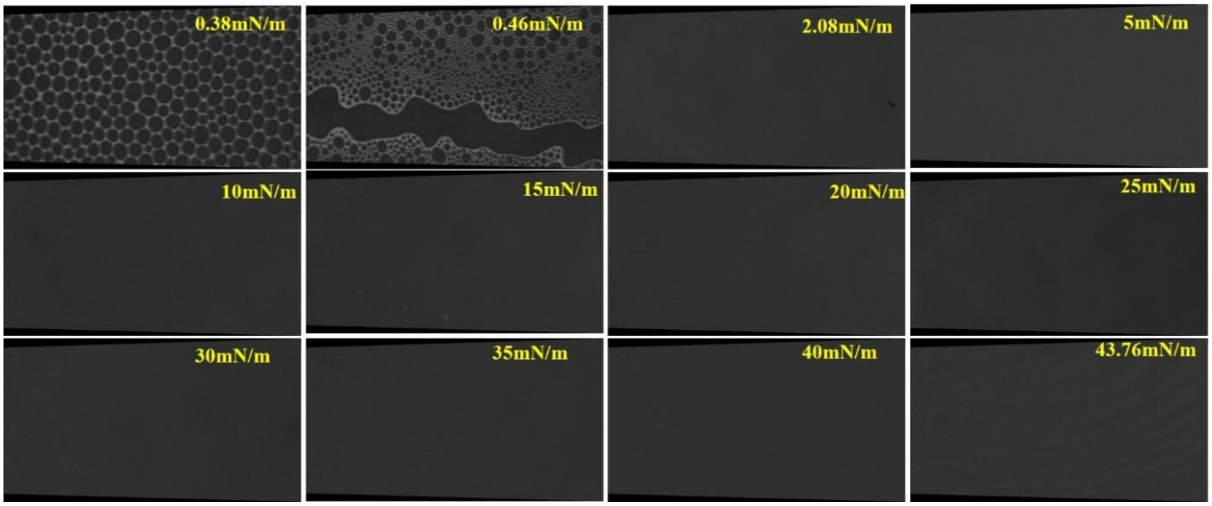

Figure A4.27. BAM image of DOPE/DNA in pH 9 buffer.

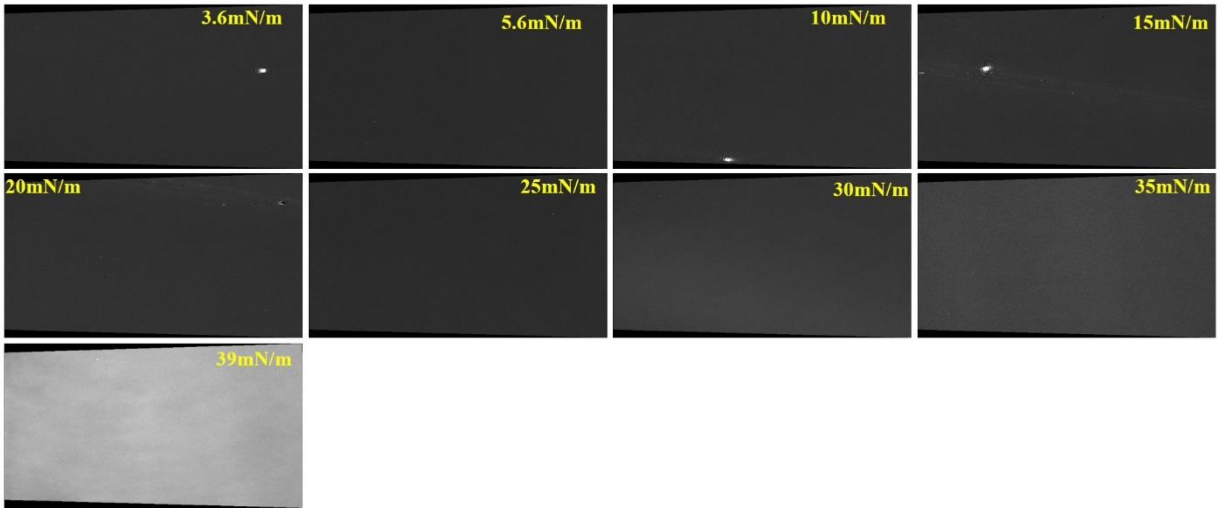

Figure A4.28. BAM image of 16-7-16/DOPE/DNA in pH 4 buffer.

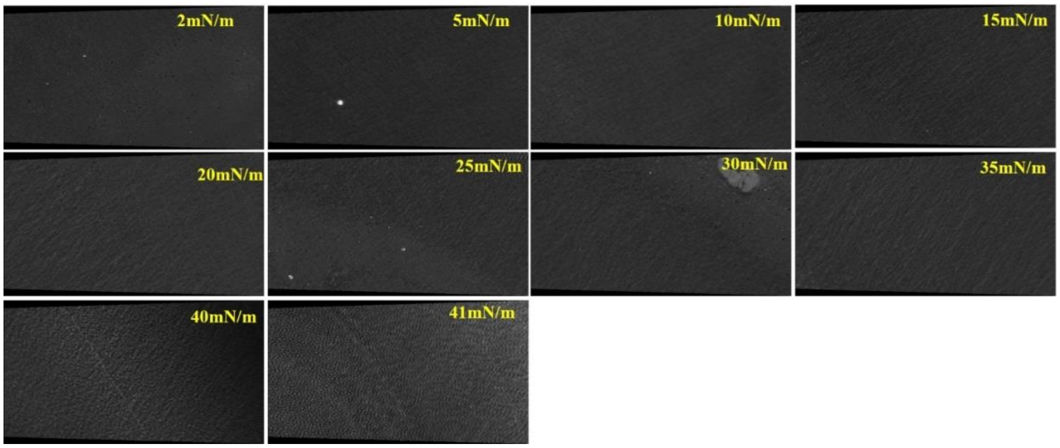

Figure A4.29. BAM image of 16-7-16/DOPE/DNA in pH 7 buffer.

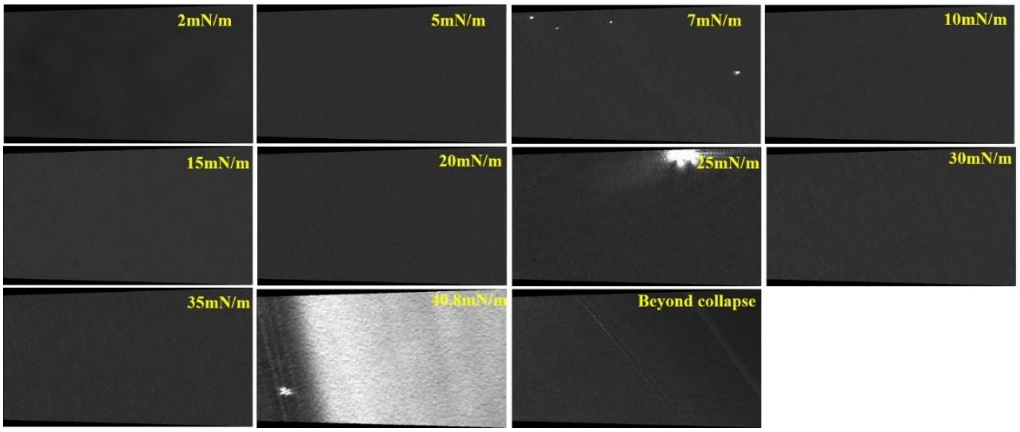

Figure A4.30. BAM image of 16-7-16/DOPE/DNA in pH 9 buffer.

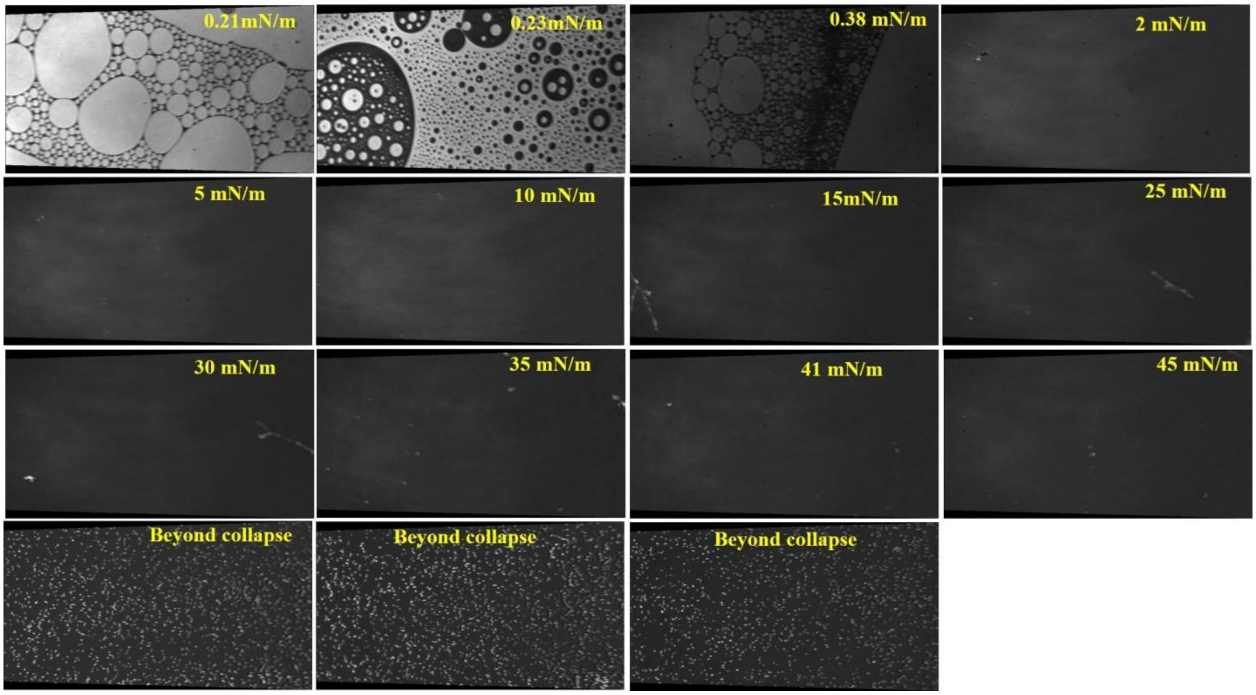

Figure A 5.1. BAM image of cholesterol at the air/buffer (pH 7) interface at different surface pressures.

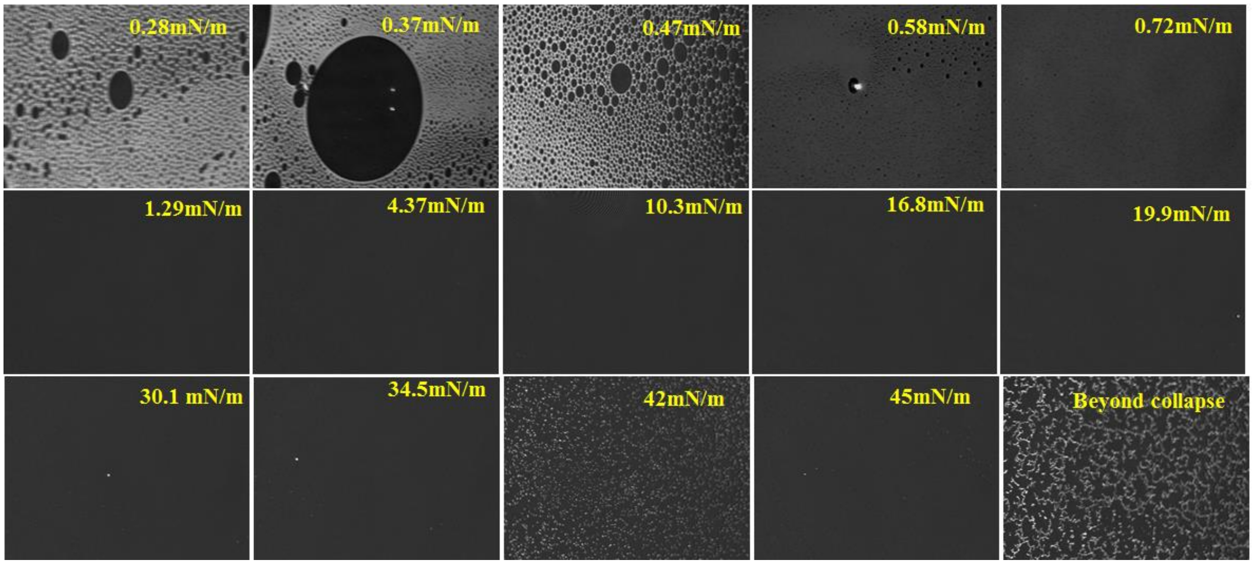

Figure A 5.2. BAM image of cholesterol at the air/buffer (pH 9) interface at different surface pressures.

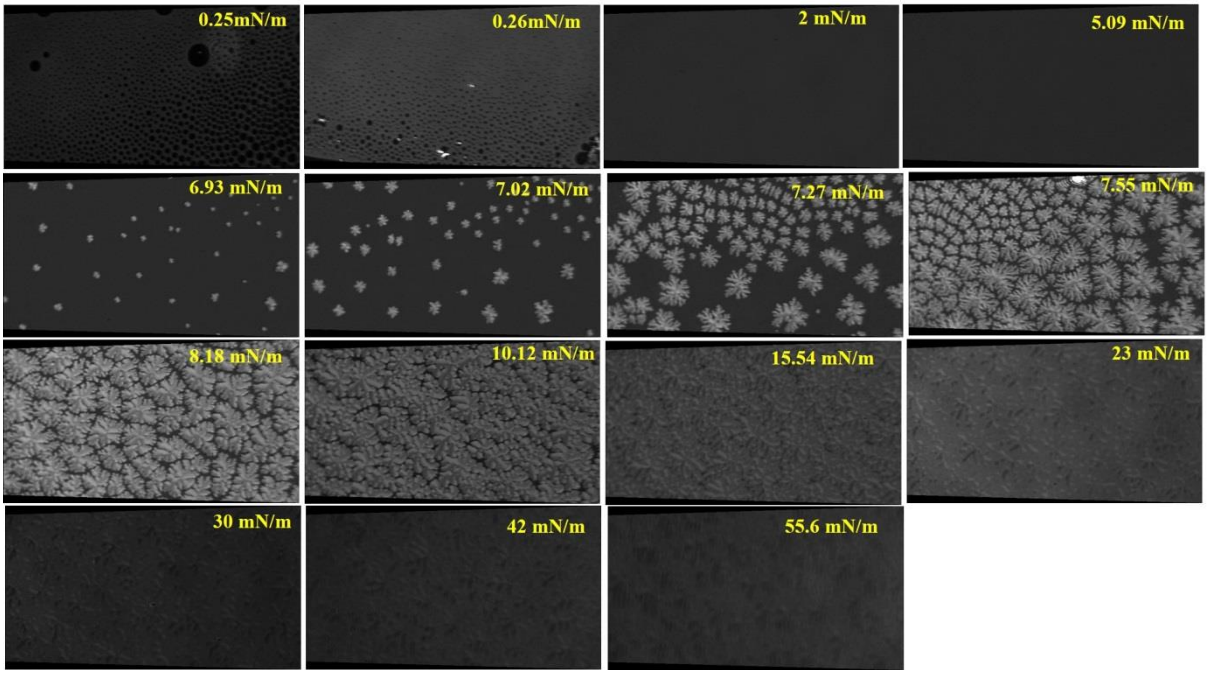

Figure A 5.3. BAM image of DPPC at the air/buffer (pH 7) interface at different surface pressures.

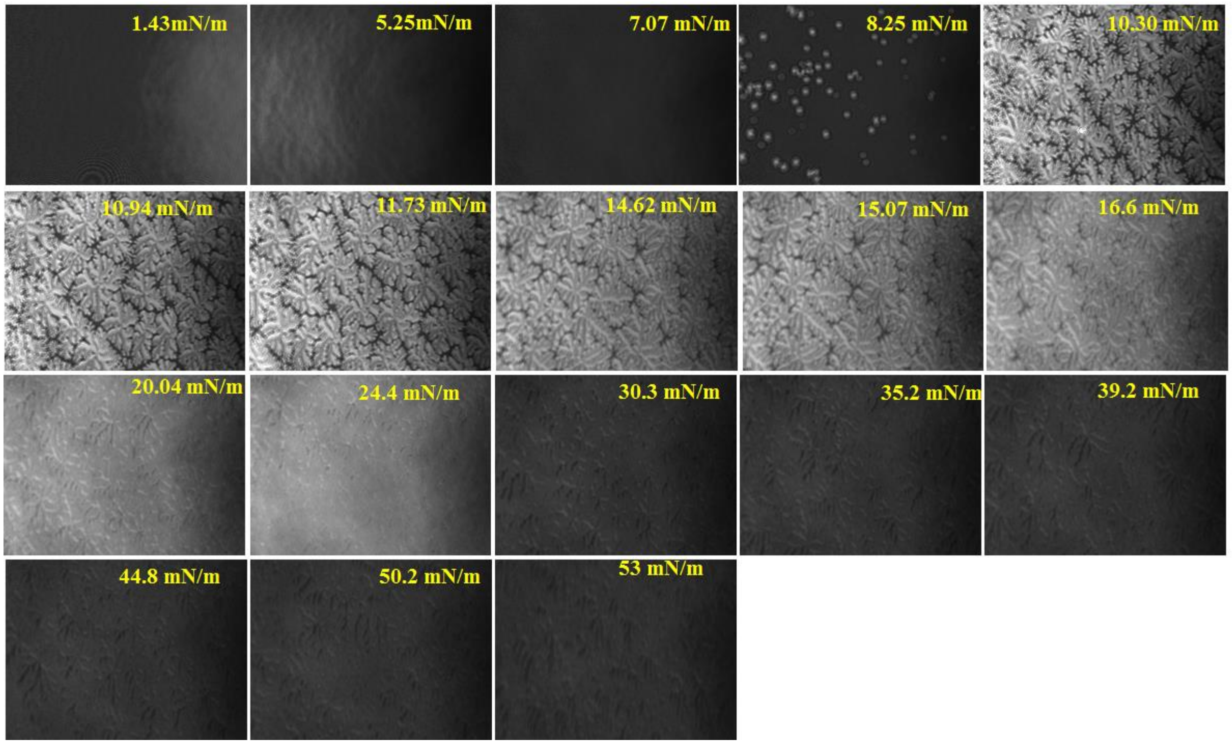

Figure A 5.4. BAM image of DPPC at the air/buffer (pH 9) interface at different surface pressures.

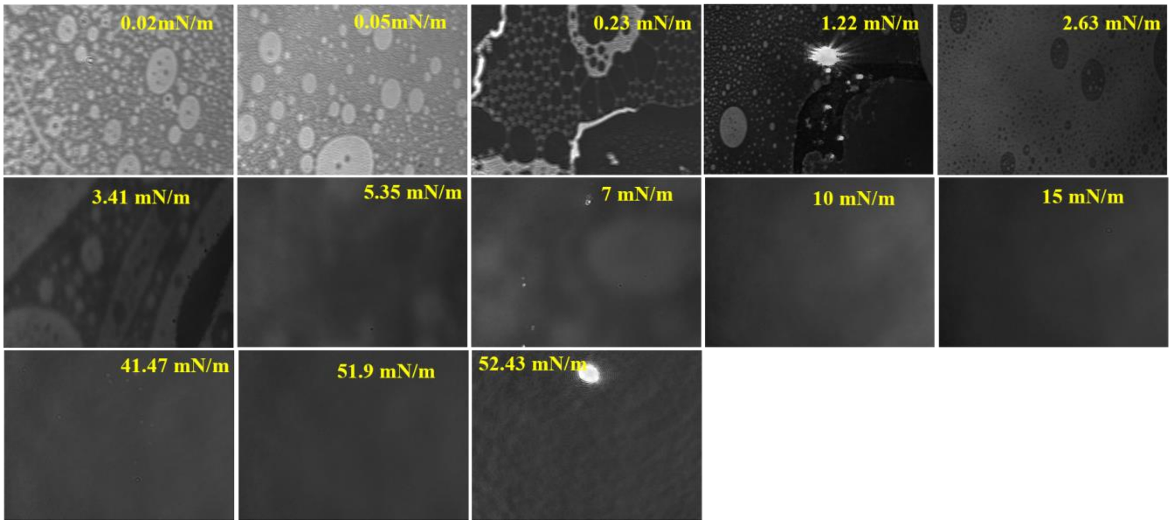

Figure A5.5. BAM image of model membrane (DPPC/cholesterol = 75/25 %) at the air/buffer (pH 7) interface at different surface pressures.

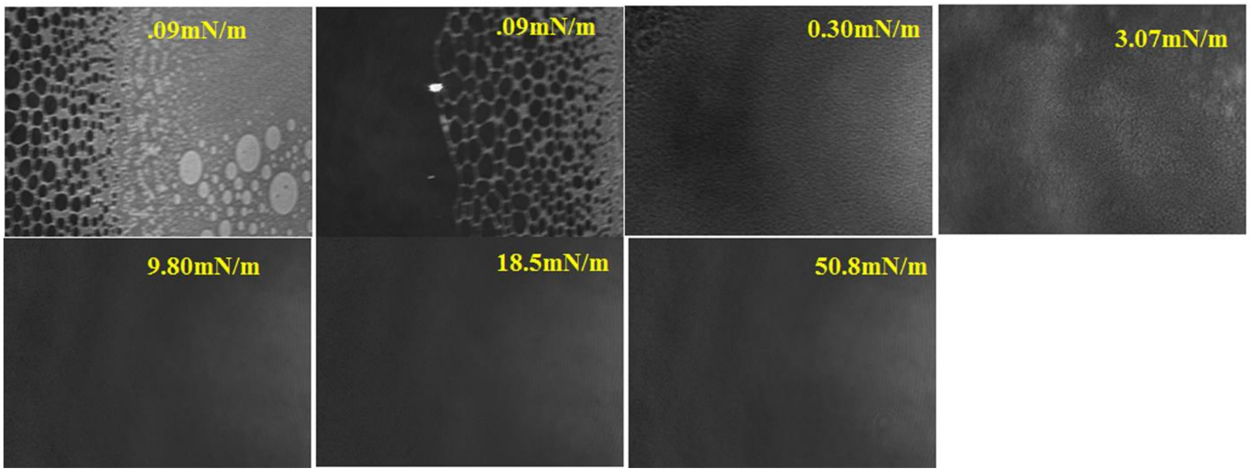

Figure A5.6. BAM image of model membrane (DPPC/cholesterol=75/25 %) at the air/buffer (pH 9) interface at different surface pressures.

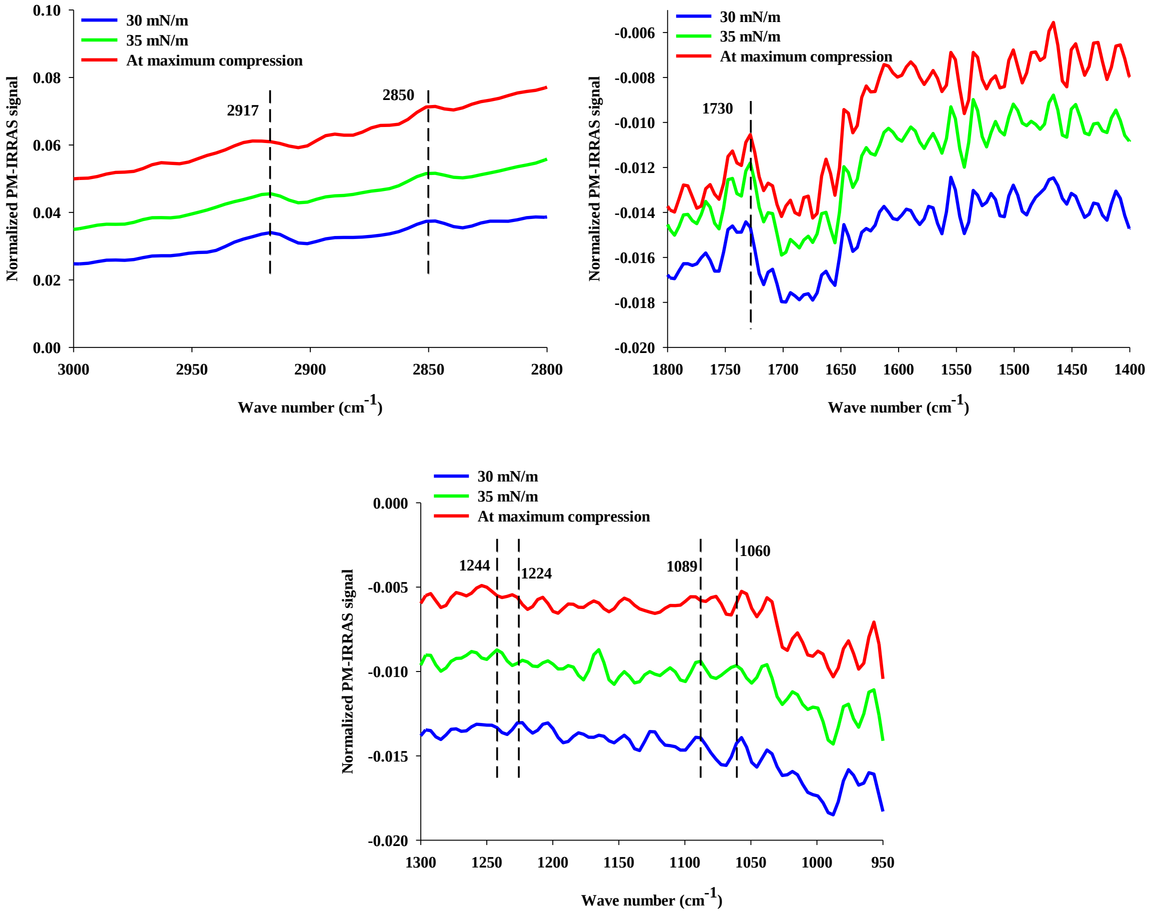

Figure A5.7. PM-IRRAS spectra of the pure 16-7NH-16/DOPE/DNA with DPPC/cholesterol model membrane at air/buffer (pH 7) interface.

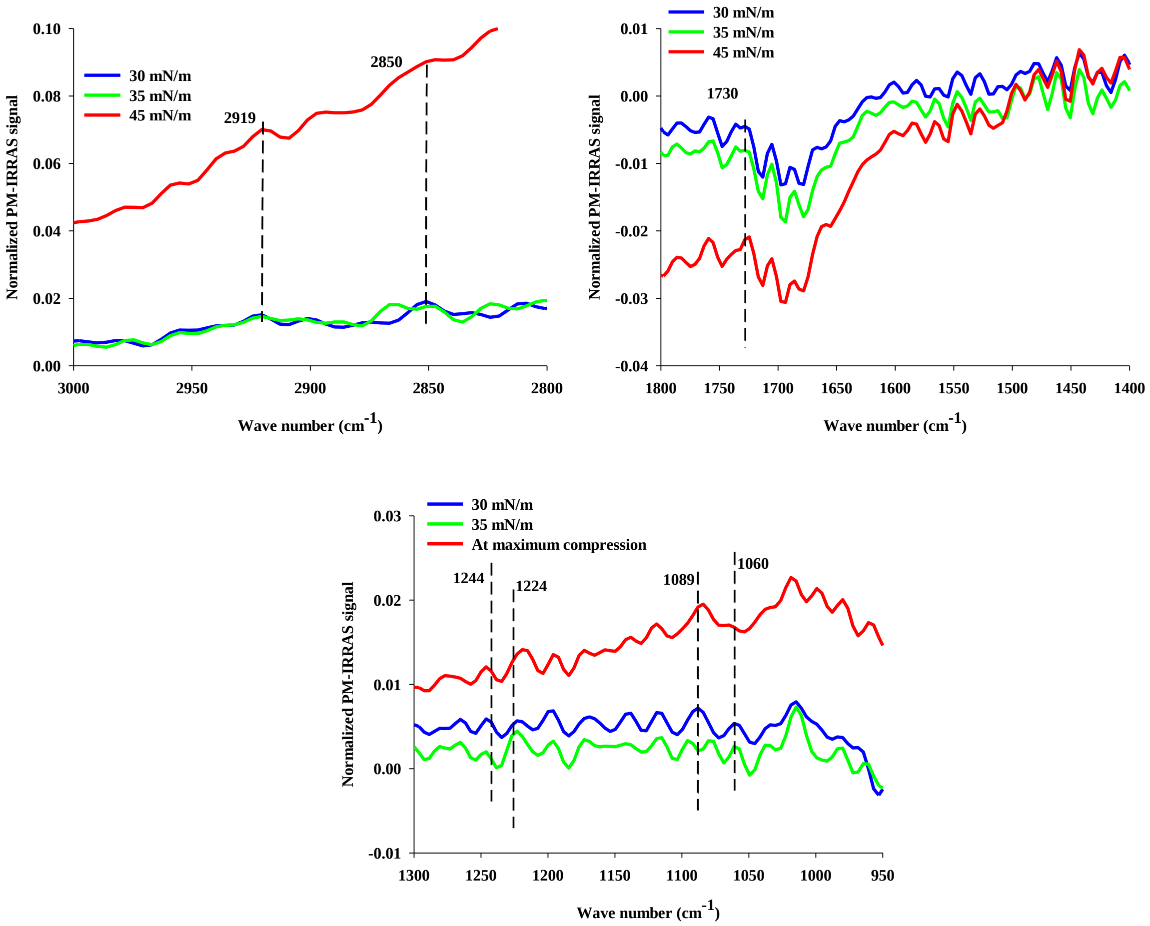

Figure A5.8. PM-IRRAS spectra of the pure 16-7NH-16/DOPE/DNA with DPPC/cholesterol model membrane at air/buffer (pH 7) interface.

Copyright Permissions

Figure 1.6:

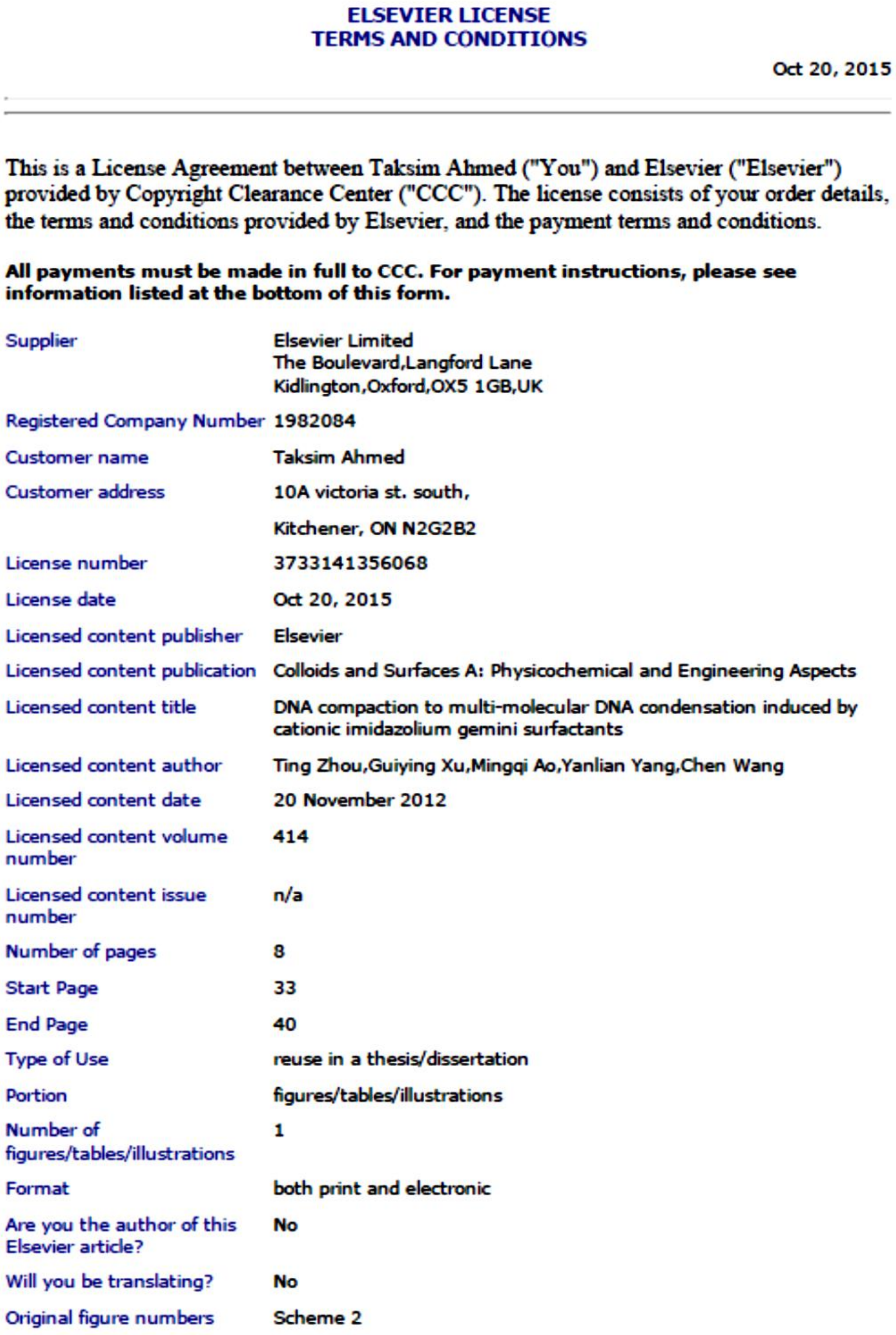

ELSEVIER LICENSE
TERMS AND CONDITIONS

Oct 20, 2015

This is a License Agreement between Taksim Ahmed ("You") and Elsevier ("Elsevier") provided by Copyright Clearance Center ("CCC"). The license consists of your order details, the terms and conditions provided by Elsevier, and the payment terms and conditions.

All payments must be made in full to CCC. For payment instructions, please see information listed at the bottom of this form.

Supplier	Elsevier Limited The Boulevard,Langford Lane Kidlington,Oxford,OX5 1GB,UK
Registered Company Number	1982084
Customer name	Taksim Ahmed
Customer address	10A victoria st. south, Kitchener, ON N2G2B2
License number	3733141356068
License date	Oct 20, 2015
Licensed content publisher	Elsevier
Licensed content publication	Colloids and Surfaces A: Physicochemical and Engineering Aspects
Licensed content title	DNA compaction to multi-molecular DNA condensation induced by cationic imidazolium gemini surfactants
Licensed content author	Ting Zhou,Guiying Xu,Mingqi Ao,Yanlian Yang,Chen Wang
Licensed content date	20 November 2012
Licensed content volume number	414
Licensed content issue number	n/a
Number of pages	8
Start Page	33
End Page	40
Type of Use	reuse in a thesis/dissertation
Portion	figures/tables/illustrations
Number of figures/tables/illustrations	1
Format	both print and electronic
Are you the author of this Elsevier article?	No
Will you be translating?	No
Original figure numbers	Scheme 2

Figure 1.10:

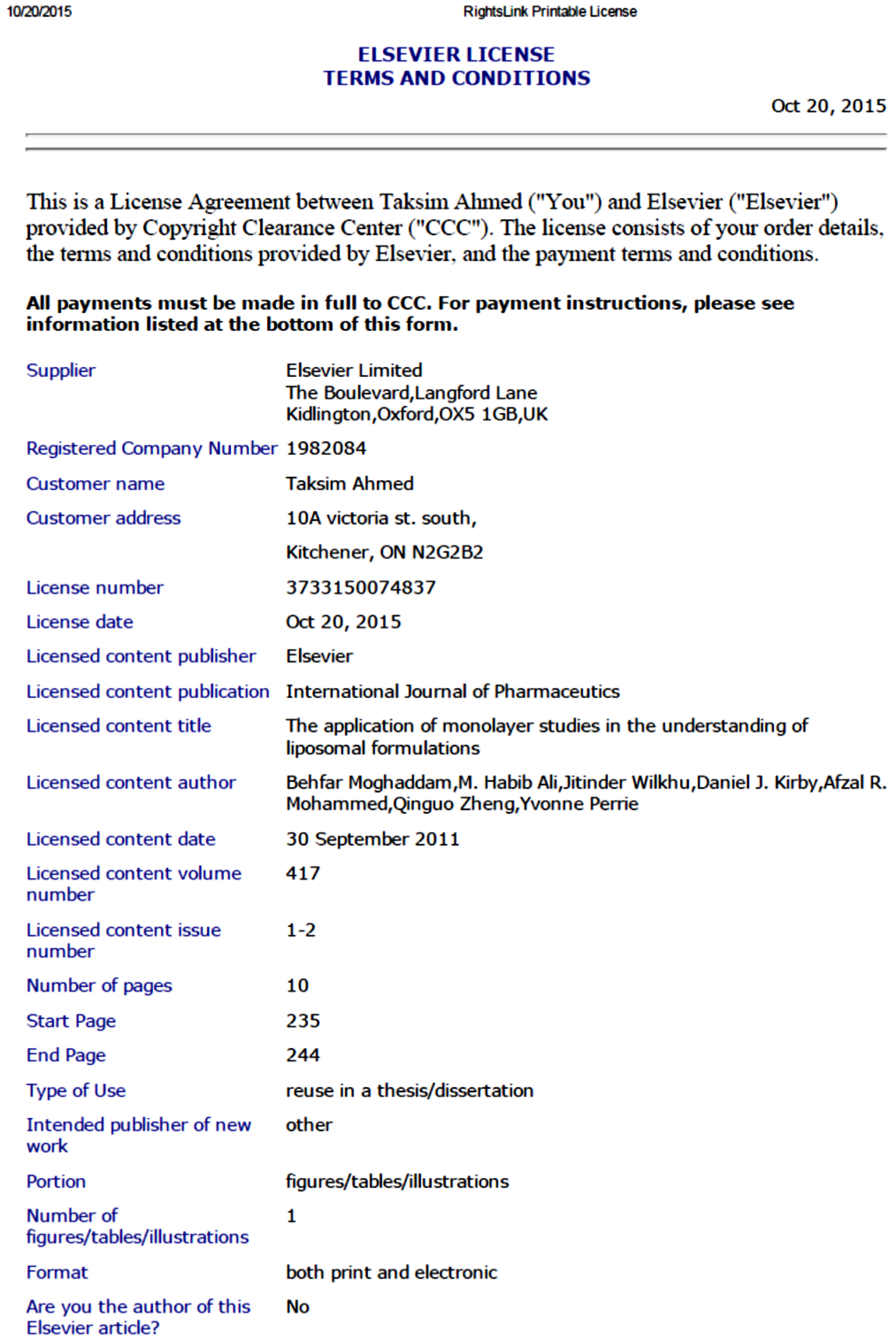

10/20/2015 RightsLink Printable License

ELSEVIER LICENSE
TERMS AND CONDITIONS

Oct 20, 2015

This is a License Agreement between Taksim Ahmed ("You") and Elsevier ("Elsevier") provided by Copyright Clearance Center ("CCC"). The license consists of your order details, the terms and conditions provided by Elsevier, and the payment terms and conditions.

All payments must be made in full to CCC. For payment instructions, please see information listed at the bottom of this form.

Supplier	Elsevier Limited The Boulevard,Langford Lane Kidlington,Oxford,OX5 1GB,UK
Registered Company Number	1982084
Customer name	Taksim Ahmed
Customer address	10A victoria st. south, Kitchener, ON N2G2B2
License number	3733150074837
License date	Oct 20, 2015
Licensed content publisher	Elsevier
Licensed content publication	International Journal of Pharmaceutics
Licensed content title	The application of monolayer studies in the understanding of liposomal formulations
Licensed content author	Behfar Moghaddam,M. Habib Ali,Jitinder Wilkhu,Daniel J. Kirby,Afzal R. Mohammed,Qinguo Zheng,Yvonne Perrie
Licensed content date	30 September 2011
Licensed content volume number	417
Licensed content issue number	1-2
Number of pages	10
Start Page	235
End Page	244
Type of Use	reuse in a thesis/dissertation
Intended publisher of new work	other
Portion	figures/tables/illustrations
Number of figures/tables/illustrations	1
Format	both print and electronic
Are you the author of this Elsevier article?	No

Figure 1.11, 1.12 and 1.13:

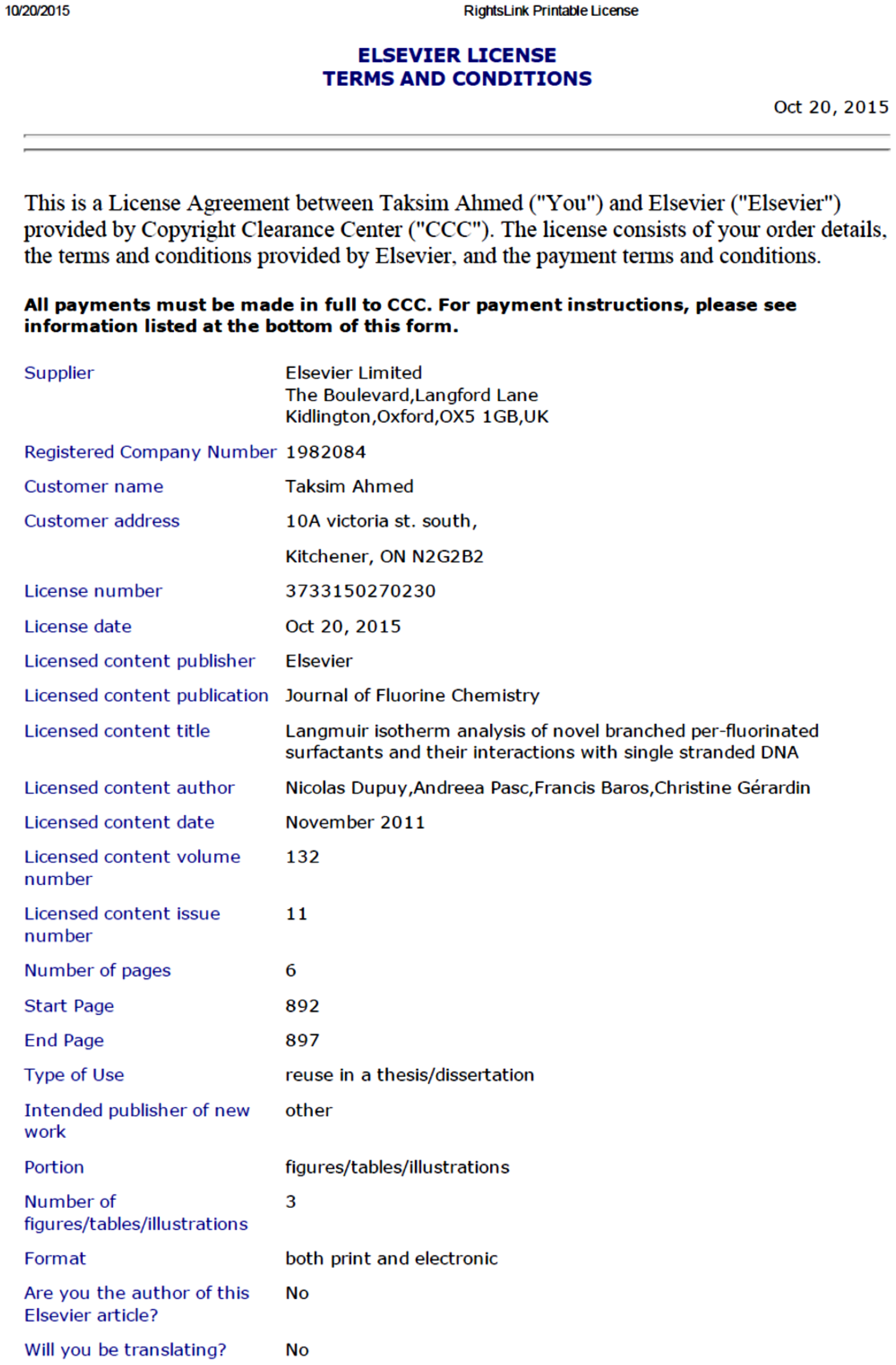

10/20/2015 RightsLink Printable License

ELSEVIER LICENSE
TERMS AND CONDITIONS

Oct 20, 2015

This is a License Agreement between Taksim Ahmed ("You") and Elsevier ("Elsevier") provided by Copyright Clearance Center ("CCC"). The license consists of your order details, the terms and conditions provided by Elsevier, and the payment terms and conditions.

All payments must be made in full to CCC. For payment instructions, please see information listed at the bottom of this form.

Supplier	Elsevier Limited The Boulevard,Langford Lane Kidlington,Oxford,OX5 1GB,UK
Registered Company Number	1982084
Customer name	Taksim Ahmed
Customer address	10A victoria st. south, Kitchener, ON N2G2B2
License number	3733150270230
License date	Oct 20, 2015
Licensed content publisher	Elsevier
Licensed content publication	Journal of Fluorine Chemistry
Licensed content title	Langmuir isotherm analysis of novel branched per-fluorinated surfactants and their interactions with single stranded DNA
Licensed content author	Nicolas Dupuy,Andreea Pasc,Francis Baros,Christine Gérardin
Licensed content date	November 2011
Licensed content volume number	132
Licensed content issue number	11
Number of pages	6
Start Page	892
End Page	897
Type of Use	reuse in a thesis/dissertation
Intended publisher of new work	other
Portion	figures/tables/illustrations
Number of figures/tables/illustrations	3
Format	both print and electronic
Are you the author of this Elsevier article?	No
Will you be translating?	No

Figure 1.16:

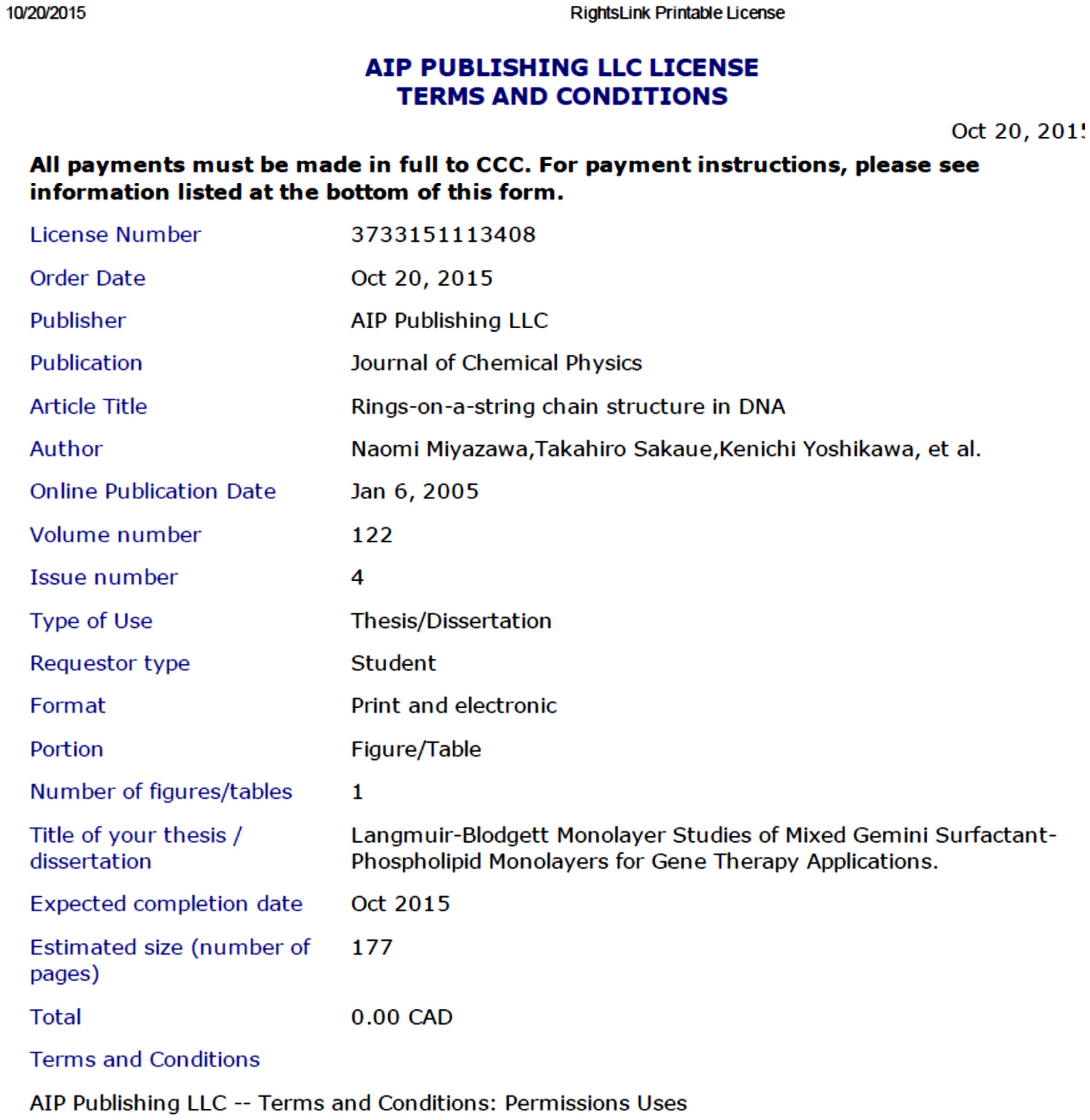

10/20/2015 RightsLink Printable License

AIP PUBLISHING LLC LICENSE
TERMS AND CONDITIONS

Oct 20, 201

All payments must be made in full to CCC. For payment instructions, please see information listed at the bottom of this form.

License Number	3733151113408
Order Date	Oct 20, 2015
Publisher	AIP Publishing LLC
Publication	Journal of Chemical Physics
Article Title	Rings-on-a-string chain structure in DNA
Author	Naomi Miyazawa,Takahiro Sakaue,Kenichi Yoshikawa, et al.
Online Publication Date	Jan 6, 2005
Volume number	122
Issue number	4
Type of Use	Thesis/Dissertation
Requestor type	Student
Format	Print and electronic
Portion	Figure/Table
Number of figures/tables	1
Title of your thesis / dissertation	Langmuir-Blodgett Monolayer Studies of Mixed Gemini Surfactant-Phospholipid Monolayers for Gene Therapy Applications.
Expected completion date	Oct 2015
Estimated size (number of pages)	177
Total	0.00 CAD
Terms and Conditions	

AIP Publishing LLC -- Terms and Conditions: Permissions Uses

Figure 1.18:

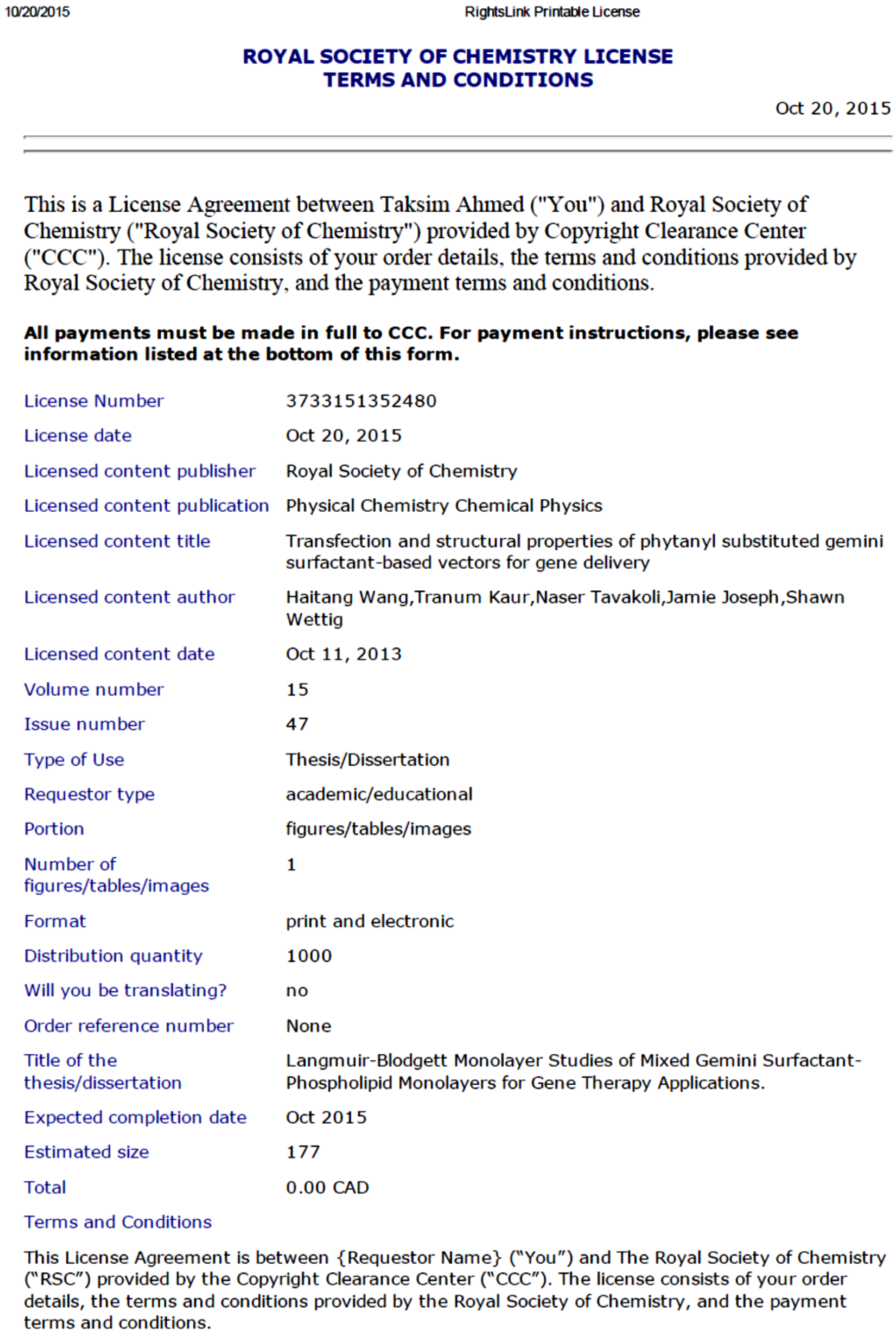

ROYAL SOCIETY OF CHEMISTRY LICENSE TERMS AND CONDITIONS

Oct 20, 2015

This is a License Agreement between Taksim Ahmed ("You") and Royal Society of Chemistry ("Royal Society of Chemistry") provided by Copyright Clearance Center ("CCC"). The license consists of your order details, the terms and conditions provided by Royal Society of Chemistry, and the payment terms and conditions.

All payments must be made in full to CCC. For payment instructions, please see information listed at the bottom of this form.

License Number	3733151352480
License date	Oct 20, 2015
Licensed content publisher	Royal Society of Chemistry
Licensed content publication	Physical Chemistry Chemical Physics
Licensed content title	Transfection and structural properties of phytanyl substituted gemini surfactant-based vectors for gene delivery
Licensed content author	Haitang Wang,Tranum Kaur,Naser Tavakoli,Jamie Joseph,Shawn Wettig
Licensed content date	Oct 11, 2013
Volume number	15
Issue number	47
Type of Use	Thesis/Dissertation
Requestor type	academic/educational
Portion	figures/tables/images
Number of figures/tables/images	1
Format	print and electronic
Distribution quantity	1000
Will you be translating?	no
Order reference number	None
Title of the thesis/dissertation	Langmuir-Blodgett Monolayer Studies of Mixed Gemini Surfactant-Phospholipid Monolayers for Gene Therapy Applications.
Expected completion date	Oct 2015
Estimated size	177
Total	0.00 CAD

Terms and Conditions

This License Agreement is between {Requestor Name} ("You") and The Royal Society of Chemistry ("RSC") provided by the Copyright Clearance Center ("CCC"). The license consists of your order details, the terms and conditions provided by the Royal Society of Chemistry, and the payment terms and conditions.